Faculdade de Ciências Médicas
Universidade Nova de Lisboa

Doctoral Thesis

Impact of using different radiation therapy techniques in breast cancer: contralateral breast dose

Author:
Cecília Borges

Supervisors:
Nuno José Teixeira
José Pedro Vaz

A thesis submitted in fulfillment of the requirements for the degree of Doctor of Philosophy

in the

Department of Life Sciences

March 2014

Declaration of Authorship

I, Cecília Borges, declare that this thesis titled, 'Impact of using different radiation therapy techniques in breast cancer: contralateral breast dose' and the work presented in it are my own. I confirm that:

- This work was done wholly or mainly while in candidature for a PhD degree at this University.
- Where I have consulted the published work of others, this is always clearly attributed.
- Where I have quoted from the work of others, the source is always given. With the exception of such quotations, this thesis is entirely my own work.
- I have acknowledged all main sources of help.

Signed: _____

Date: _____

"If you talk to a man in a language he understands, that goes to his head. If you talk to him in his language, that goes to his heart."

Mandela

Abstract

Breast cancer is the most frequent in women. Scientific knowledge and technology have created many and different strategies to treat this pathology. Radiotherapy (RT) is in the actual standard guidelines for most of breast cancer treatments. However, radiation is a two-sword weapon: although it may heal cancer, it may also induce secondary cancer. The contralateral breast (CLB) is a susceptible organ to absorb doses with the treatment of the other breast, being at significant risk to develop a secondary tumor.

New radiation related techniques, with more complex delivery strategies and promising results are being implemented and used in radiotherapy departments. However some questions have to be properly addressed, such as: Is it safe to move to complex techniques to achieve better conformation in the target volumes, in breast radiotherapy? What happens to the target volumes and surrounding healthy tissues? How accurate is dose delivery? What are the shortcomings and limitations of currently used treatment planning systems (TPS)?

The answers to these questions largely rely in the use of Monte Carlo (MC) simulations using state-of-the-art computer programs to accurately model the different components of the equipment (target, filters, collimators, etc.) and obtain an adequate description of the radiation fields used, as well as the detailed geometric representation and material composition of organs and tissues.
This work aims at investigating the impact of treating left breast cancer using different radiation therapy (RT) techniques f-IMRT (forwardly-planned intensity-modulated), inversely-planned IMRT (IMRT2, using 2 beams; IMRT5, using 5 beams) and dynamic conformal arc (DCART) RT and their effects on the whole-breast irradiation and in the undesirable irradiation of the surrounding healthy tissues.
Two algorithms of iPlan BrainLAB TPS were used: Pencil Beam Convolution (PBC) and commercial Monte Carlo (iMC). Furthermore, an accurate Monte Carlo (MC) model of the linear accelerator used (a Trilogy® VARIAN®) was done with the EGSnrc MC code, to accurately determine the doses that reach the CLB. For this purpose it was necessary to model the new High Definition multileaf collimator that had never before been simulated. The model developed was then included on the EGSnrc MC package of National Research Council Canada (NRC). The linac was benchmarked with water measurements and later on validated against the TPS calculations.

The dose distributions in the planning target volume (PTV) and the dose to the organs at risk (OAR) were compared analyzing dose-volume histograms; further statistical analysis was performed using IBM SPSS v20 software.

For PBC, all the techniques provided adequate coverage of the PTV. However, statistically significant dose differences were observed between the techniques, in the PTV, OAR and also in the pattern of dose distribution spreading into normal tissues. IMRT5 and DCART spread low doses into greater volumes of normal tissue, right breast, right lung, heart and even the left lung than tangential techniques (f-IMRT and IMRT2). However, IMRT5 plans improved distributions for the PTV, exhibiting better conformity and homogeneity in target and reduced high dose percentages in ipsilateral OAR. DCART did not present advantages over any of the techniques investigated. Differences were also found comparing the calculation algorithms: PBC estimated higher doses for the PTV, ipsilateral lung and heart than the MC algorithms predicted. The MC algorithms presented similar results (within 2% differences). The PBC algorithm was considered not accurate in determining the dose in heterogeneous media and in build-up regions. Therefore, a major effort is being done at the clinic to acquire data to move from PBC to another calculation algorithm. Despite better PTV homogeneity and conformity there is an increased risk of CLB cancer development, when using non-tangential techniques.

The overall results of the studies performed confirm the outstanding predictive power and accuracy in the assessment and calculation of dose distributions in organs and tissues rendered possible by the utilization and implementation of MC simulation techniques in RT TPS.

Keywords:

Monte Carlo simulations, External Beam Radiotherapy, Intensity Modulated Radiotherapy, Contralateral Breast Doses

Resumo

O cancro de mama é o mais frequente diagnoticado a indivíduos do sexo feminino. O conhecimento científico e a tecnologia têm permitido a criação de muitas e diferentes estratégias para tratar esta patologia. A Radioterapia (RT) está entre as diretrizes atuais para a maioria dos tratamentos de cancro de mama. No entanto, a radiação é como uma arma de dois canos: apesar de tratar, pode ser indutora de neoplasias secundárias. A mama contralateral (CLB) é um órgão susceptível de absorver doses com o tratamento da outra mama, potenciando o risco de desenvolver um tumor secundário.

Nos departamentos de radioterapia têm sido implementadas novas técnicas relacionadas com a radiação, com complexas estratégias de administração da dose e resultados promissores. No entanto, algumas questões precisam de ser devidamente colocadas, tais como: É seguro avançar para técnicas complexas para obter melhores índices de conformidade nos volumes alvo, em radioterapia de mama? O que acontece aos volumes alvo e aos tecidos saudáveis adjacentes? Quão exata é a administração de dose? Quais são as limitações e vantagens das técnicas e algoritmos atualmente usados?

A resposta a estas questões é conseguida recorrendo a métodos de Monte Carlo para modelar com precisão os diferentes componentes do equipamento produtor de radiação (alvos, filtros, colimadores, etc), afim de obter uma descrição apropriada dos campos de radiação usados, bem como uma representação geométrica detalhada e a composição dos materiais que constituem os órgãos e os tecidos envolvidos.

Este trabalho visa investigar o impacto de tratar cancro de mama esquerda usando diferentes técnicas de radioterapia f-IMRT (intensidade modulada por planeamento direto), IMRT por planeamento inverso (IMRT2, usando 2 feixes; IMRT5, com 5 feixes) e DCART (arco conformacional dinâmico) e os seus impactos em irradiação da mama e na irradiação indesejada dos tecidos saudáveis adjacentes.

Dois algoritmos do sistema de planeamento iPlan da BrainLAB foram usados: *Pencil Beam Convolution* (PBC) e Monte Carlo comercial *iMC*. Foi ainda usado um modelo de Monte Carlo criado para o acelerador usado (Trilogy da VARIAN Medical Systems), no código EGSnrc MC, para determinar as doses depositadas na mama contralateral. Para atingir este objetivo foi necessário modelar o novo colimador multi-lâminas *High-Definition* que nunca antes havia sido simulado. O modelo desenvolvido está agora disponível no pacote do código EGSnrc MC do National Research Council Canada (NRC). O acelerador simulado foi validado com medidas realizadas em água e posteriormente com cálculos realizados no sistema de planeamento (TPS).

As distribuições de dose no volume alvo (PTV) e a dose nos órgãos de risco (OAR) foram comparadas através da análise de histogramas de dose-volume; análise estatística complementar foi realizads usando o *software* IBM SPSS v20.

Para o algoritmo PBC, todas as técnicas proporcionaram uma cobertura adequata do PTV. No entanto, foram encontradas diferenças estatisticamente significativas entre as técnicas, no PTV, nos OAR e ainda no padrão da distribuição de dose pelos tecidos sãos. IMRT5 e DCART contribuem para maior dispersão de doses baixas pelos tecidos normais, mama direita, pulmão direito, coração e até pelo pulmão esquerdo, quando comparados com as técnicas tangenciais (f-IMRT e IMRT2). No entanto, os planos de IMRT5 melhoram a distribuição de dose no PTV apresentando melhor conformidade e homogeneidade no volume alvo e percentagens de dose mais baixas nos órgãos do mesmo lado. A técnica de DCART não apresenta vantagens comparativamente com as restantes técnicas investigadas. Foram também identificadas diferenças entre os algoritmos de cálculos: em geral, o PBC estimou doses mais elevadas para o PTV, pulmão esquerdo e coração, do que os algoritmos de MC. Os algoritmos de MC, entre si, apresentaram resultados semelhantes (com dferenças até 2%). Considera-se que o PBC não é preciso na determinação de dose em meios homogéneos e na região de *build-up*. Nesse sentido, atualmente na clínica, a equipa da Física realiza medições para adquirir dados para outro algoritmo de cálculo. Apesar de melhor homogeneidade e conformidade no PTV considera-se que há um aumento de risco de cancro na mama contralateral quando se utilizam técnicas não-tangenciais.

Os resultados globais dos estudos apresentados confirmam o excelente poder de previsão com precisão na determinação e cálculo das distribuições de dose nos orgãos e tecidos das técnicas de simulação de Monte Carlo usados.

Palavras-Chave:

Simulações de Monte Carlo, Radioterapia Externa, Radioterapia de Intensidade Modulada, Doses na Mama Contralateral

Acknowledgements

The present work could not have been done without the cooperation of different people and institutions.

I would like to specially thank Professor Doctor Nuno Teixeira for his availability, guidance and opportunity for doing this interesting work.

To Professor Doctor Pedro Vaz, I want to acknowledge for the constant support, cooperation and interest throughout all this investigation, having had an essential contribution for the accomplishment of this thesis.

I also want to thank Professor Doctor Maria Isabel Monteiro-Grillo for the support and interest in this work.

I want to express my gratitude to all the team at the service and to Medical Consult SA for giving me the opportunity to perform this work . To all their fundamental support and collaboration and encouragement, for all the patience, help and many discussions throughout the work. To all, my deepest acknowledgment.

To Emily Heath for all the help and contribution in modeling the HDMLC CM.

To Professor Gilda Cunha, I thank the availability, many discussions and guidance in the statistical analysis of the data.

To Professor Antonio Leal from Universidad de Sevilla for lending NAOMI phantom to perform measurements;

To Nuno Sol, for his help with iPlan BrainLAB TPS and constant availability.

To Professor Wayne Newhauser from M.D. Anderson for having sent their phase space files from the simulations of a linac.

To VARIAN Medical Systems for having provided the detailed data of the linac head constitution.

To Centro Oncológico Dra Natália Chaves for having provided all the conditions to perform the experimental part of this work.

To Centro de Física Nuclear from Universidade de Lisboa for permitting performing the Monte Carlo calculations in ALFC cluster at their facilities.

To Hospital de Santa Maria for having lent the RandoAlderson phantom to make a plaster mold for the breast experimental measurements.

To all the colleagues at CTN/IST for all the encouragement and their kindness throughout these years.

A very special acknowledgment to Miriam Zarza-Moreno for being a constant support and help along this work but most of all for her friendship and presence at all times.

To my family, to whom I dedicate this thesis, for the unconditional support, for comprehension of my absence and their constant presence: Mum, Dad and my dearest brother Paulo, for everything!

Contents

List of Figures

List of Tables

Abbreviations

AAA	Anisotropic Analytical Algorithm
ALN	Axillary Lymph Nodes
AP	anterior-posterior
ASCII	American Standard Code for Information Interchange
BC	Breast Cancer
BCS	Breast Conserving Surgery
BCT	Breast Conserving Therapies
BEV	Beam's Eye View
CDF	Cumulative Distribution Function
CH	Condensed History
CI	Conformity Index
CLB	Contralateral Breast
CM	Component Module
CN	Conformation Number
CRT	Conformal Radiation Therapy
CT	Computerized Tomography
CTV	Clinical TargetVolume
DBS	Directional Bremsstrahlung Splitting
DCART	Dynamic Conformal Arc Radiotherapy
DCIS	Ductal Carcinoma *in situ*
DICOM	Digital Imaging and Communication in Medicine
DRR	Digitally Reconstructed Radiographs
DTA	Distance To Agreement
DVH	Dose Volume Histogram
EBRT	External Beam Radiation Therapy

EDW	Enhanced Dynamic Wedges
f-IMRT	forward - Intensity Modulated Radiation Therapy
FDA	Food and Drug Adminsitration
FF	Flattening Filter
FFT	Fast Fourier Technique
FWHM	Full Width Half Maximum
GTV	Gross Tumor Volume
H	Equivalent dose
HDMLC	High Definition Multileaf Collimator
HDR	High Dose Rate
HI	Homogeneity Index
HU	Hounsfield Units
IC	Ionization Chamber
iMC	iPlan Monte Carlo
IMC	Internal Mammary Chain
IMRT	Intensity Modulated Radiation Therapy
IORT	Intra Operative Radiation Therapy
IV	Irradiated Volume
HDR	High Dose Rate
LABC	Locally Advanced Breast Cancer
LCIS	Lobular Carcinoma *in situ*
LDR	Low Dose Rate
LINAC	LINear ACcelerator
MB	Modified Batho
MC	Monte Carlo
MLC	Multileaf Collimator
MMC	Macro Monte Carlo
MRI	Magnetic Resonance Imaging
MU	Monitor Units
NNT	Number Needed to Treat
NRC	National Research Council Canada
OAR	Organs At Risk
OD	Optical Density

OIS	Oncology Information System
PBC	Pencil Beam Convolution
PBI	Partial Breast Irradiation
PD	Prescribed Dose
PDD	Profile Depth Dose
PDF	Probability Distribution Function
PET	Positron Emission Tomography
PS	Power Supply
PSF	Phase Space File
PTV	Planning Target Volume
RCT	Randomized Control Trials
RF	RadioFrequency
ROI	Region Of Interest
RT	Radiation Therapy or RadioTherapy
SAR	Scatter-Air Ratio
SBS	Selective Bremsstrahlung Splitting
SERM	Selective estrogen-receptor modulators
SLN	Sentinel Lymph Node
SSD	Source to Skin Distance
STOPS	Simultaneous Transport of Particle Sets
TERMA	Total Energy Released per unit MAss
TLD	ThermoLuminescent Detectors
TPS	Treatment Planning Systems
TV	Treated Volume
UBS	Uniform Bremsstrahlung Splitting
VMAT	Volumetric Modulated Arc Therapy
VRT	Variance Reduction Technique
WBI	Whole Breast Irradiation
Z	atomic number
γ	gamma

I dedicate this thesis to Mum, Dad and Paulo.

Introduction

1. Technology and Monte Carlo simulations in support of improved clinical practice in RT

In the recent decades, the radiotherapy (RT) techniques went through major developments, namely with conformational RT and intensity modulated RT (IMRT). These technical and technological evolutions were made possible due to the advances in the linear accelerator (linac) technology and the development and implementation of dose calculation treatment planning systems (TPS).

The modern linacs permit the accurate delivery of a prescribed dose, even in large 3D volumes, with the possibility of following the movement of the target volume and other organs during the treatments. The treatment planning algorithms and systems are nowadays an important tool in RT and are of paramount importance for estimating the doses.

The calculation algorithms are becoming increasingly more accurate allowing dose distributions in the patient's organs and tissues closer to real. Such techniques bring along an improvement of the treatment quality for the tumors in deeper and radiosensitive locations, such as in the breast, lung and head and neck cases.

Considering the dose calculation, there are two main difficulties when willing to perform patient dose calculations: on one side, it is necessary the modeling of the patient's complex anatomy with a detailed description of the geometry and materials composition of organs and tissues; on the other side there is the modeling of the physical processes of energy deposition and absorbed dose within the patient's body. On what the modeling of the patients anatomy is concerned, computed tomography (CT) offers the possibility to model the patient's organs and tissues, discretizing their volumes into small volume elements, called *voxels*. Each voxel is associated to a value known as Hounsfield units (HU) that is representative of the average electronic density of the material that constitutes each specific element volume. This method permits determining the attenuation power of the medium for the specific radiation beam. To model the physical processes of energy transfer and absorption, dose calculation methods and algorithms were developed to determine an accurate representation of the dose delivered by the treatment beams.

The calculated dose entails different types of uncertainties associated to the TPS and the calculation algorithms. The *slightly miscalculated* doses can reduce the treatments' efficacy or increase the risk of complications in the healthy tissues. Reduction in the dose uncertainties leads to more predictable and reproducible results to the prescribed dose, given the individual variability of the patients. In practice, the radiation oncologist validates the dose calculated by an algorithm, if it is within a theoretical acceptable range. The dose calculation method should be as accurate as possible in order to decrease its uncertainty in the dose prediction associated to the treatment.

The dose calculation algorithms calculate the energy deposition and the absorbed dose in the voxels that model the patient's organs and tissues, by the treatment radiation beams. These calculation models are models represent approximations made for the energy deposition calculation and for the representation of the patient. Consequently, these provide an approximate representation of the dose distribution in the patient.

Dose calculation algorithms play a central role for the clinical practice of radiation therapy. They are the basis for any treatment plan optimization, requirement of paramount importance with the development of complex techniques such as IMRT. The increased accuracy of calculation tools such as superposition algorithms or Monte Carlo (MC) simulations offer substantial advantages for clinical cases which involve calculations within heterogeneous tissue, but are time-consuming making them still unpractical for clinical routine.

The remarkable accuracy of MC dose calculation algorithms led to the widely accepted view that these methods already play a central role in existing RT TPS and their importance will be even higher in future TPS, heavily based in MC simulations and modeling. The advantages of using MC clinically are particularly evident for radiation fields passing through inhomogeneities, such as lung and air cavities, and for small fields, including those used in IMRT. Many research groups have however reported significant differences between MC and conventional TPS algorithms in such complex situations.

Algorithms that use MC methods are known to more realistically model the energy transfer and deposition mechanisms in the medium. They are efficient tools to model the patient and the radiation source, and to, calculate the dose distribution. However, MC methods need significant calculation times, making them still incompatible for routine clinical practice.

Radiation delivery techniques continue to evolve, with arc therapy and other advanced delivery techniques which widespread utilization for clinical use in the coming years is anticipated. Some researchers consider that the combination of a fast, gold standard, MC dose calculation algorithm in the planning stages of advanced radiotherapy delivery will represent a powerful tool for radiotherapy treatment.

On the other hand, since the 1990's, existing general purpose MC computer codes (such as MCNP(x), FLUKA, GEANT, PENELOPE, EGS) have been adapted to feature to allow medical physics-related, and particularly radiotherapy calculations. At the end of the 1990's, a special computational platform, PEREGRINE, was develop aiming at the implementation, in clinical environment of Real Time Treatment Planning systems in RT. Other computer programs and algorithms, such as DPM, PENFAST, MCDOSE, VMC, XVMC, VMC++, MMC, etc, were developed to perform fast, but accurate, MC simulations especially suited for treatment planning calculations. By 2009, it was estimated that all equipment manufacturers had developed and incorporated MC based algorithms in TPS. Other computer programs such as EGSnrc and the associated BEAMnrc became powerful and sophisticated Monte Carlo simulation tools widely used by the community of experts to perform the modeling and simulation of linacs and to accurate compute particle fluences and dose distributions in external radiotherapy treatments.

The dissemination of the use of MC techniques and simulations for Radiotherapy Treatment Planning is also shown by the dramatic increase in recent years of the number of peer reviewed scientific articles published yearly, as displayed in the following figure extracted from Emiliano Spezi [1].

2. Breast cancer treatment and dose in the CLB

At present, it is possible to detect breast cancer in early stages due to improved screening techniques and great awareness from the medical community and the public in general. Breast cancer mortality has therefore decreased in the last years due to its increasingly more accurate detection in precocious stages. Moreover, this permits using techniques to preserve the breast and avoid radical solutions such as mastectomy (complete breast removal surgically). The use of breast-conserving treatment approaches for breast cancer has, for some time now, become a standard option for early stage disease. More than ever, the general public is more aware and thereby involved in the therapeutical decision, thus being important to identify and quantify the risks of the conservative approaches.

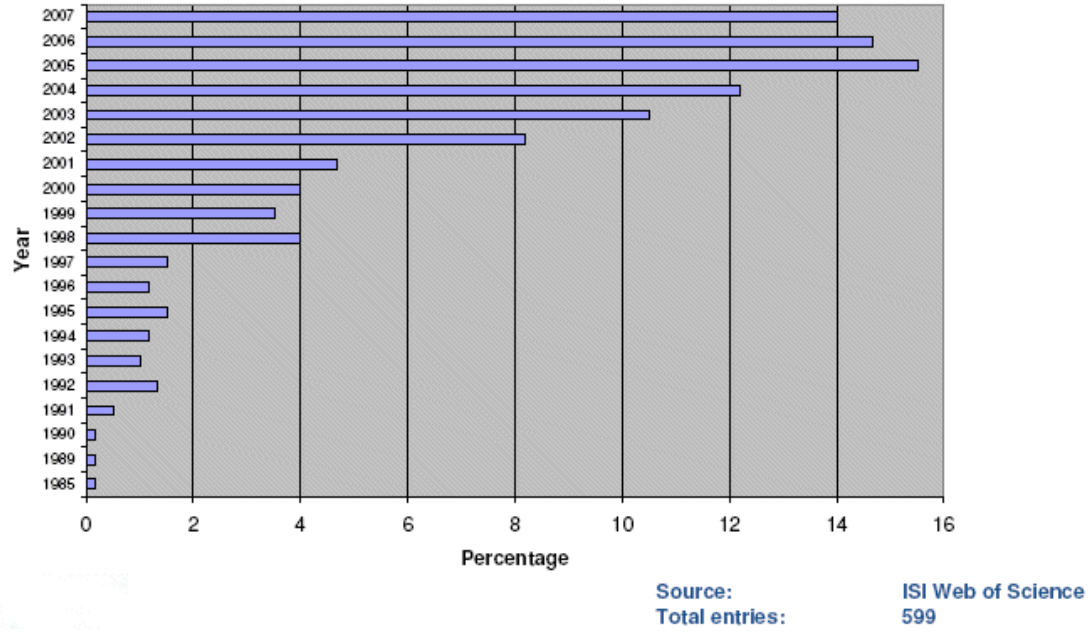

FIGURE 1: Monte Carlo papers publication evolution until 2008 (when this investigation started).[1]

RT is the standard treatment technique after breast conservative surgery, reducing the chances of local relapse and mortality, mainly for young women. This therapeutic strategy has proven to increase the probability of free-disease survival. Several randomized studies have shown equivalent or better results of lumpectomy followed by RT compared to mastectomy, in the management of breast cancer. These improvements in overall survival are also achieved due to new and sophisticated equipment and techniques dedicated to RT. More specifically: Cobalt-60 machines were replaced by linear accelerators and TPS has evolved from 2D to 3D using computed tomography (CT) based images with the complete anatomical information. With these improvements, the tumor volume is irradiated with greater accuracy; on the contrary, for the healthy organs surrounding the tumor, efforts are put forward so that these are irradiated with lower doses.

The breast is a particularly complex site to treat due to its concave shape, the different media that surround it (bones, lung, soft tissue) and its proximity to the external body contour. Furthermore, the breast moves with breathing, varying its position during treatment. Breast treatment plans often present heterogeneous dose distributions, with parts of the breast receiving higher doses than prescribed. To achieve better irradiation and conformation to the tumor volume, special collimators, named multileaf collimators (MLC), were designed. These complex collimators allowed the rising of new techniques such as field-in-field, step-and-shoot and dynamic (sliding-window) MLC conformation. The goal of these techniques

is ultimately to homogenize and improve the dose coverage in the tumor volume. Despite the documented importance of RT, normal-tissue toxicities, including secondary radiogenic cancer, can disturb the quality of life and limit the survival rate.

One concern that has arisen is related to contralateral breast (CLB) cancer after breast radiotherapy. Although most studies do not show statistically significant evidence that patients treated with breast RT have an increased risk of developing CLB cancer when compared to control groups treated with mastectomy alone, the available data clearly shows that the amount of scattered radiation absorbed by the CLB during a routine course of breast radiotherapy is considerable (several Gy) and is therefore within the range that one might be concerned about radiogenic contralateral tumors.

3. Monte Carlo simulations in support of breast cancer RT (this work)

This work aims at estimating the doses in CLB when considering primary breast irradiation. The following external beam techniques using a linear accelerator were investigated: forward-intensity modulated RT (f-IMRT), IMRT using two and five modulated fields using inverse planning - IMRT2 and IMRT5, respectively - and dynamic conformal arc RT (DCART).

A 2300C/D Trilogy VARIAN (Medical Systems, Palo Alto, CA) linac used for RT treatment equipped with a High Definition micro multileaf collimator (HDMLC) was considered for the purpose of this work. The treatment planning system (TPS) used for this work was iPlan (BrainLAB AG, Feldkirchen, Germany) TPS v. 4.1, using two calculation algorithms, Pencil Beam Convolution (PBC) and commercial Monte Carlo (iMC). A detailed comparison of the techniques was performed and the main results were published in an article in Physica Medica journal in March 2014.

Regarding the MC independent model of the linac, the first task consisted in applying an efficient method for the determination of the optimal intensity distribution of the pre-target electron beam able to accurately reproduce a set of measured photon field profiles and incident electron beam energy, for the linac structure used throughout this work. The independent MC model of the linac was created using BEAMnrc/EGSnrc and DOSXYZnrc/EGSnrc and was later on validated against measurements for a 6 MV photon beam, at first, for the beam only with the jaws collimation and then including the modeled micro multileaf

collimator, HDMLC. The results of the first simulations of the HDMLC modeled were published in Medical Physics journal, in January 2012.

The main goal of these independent MC calculations is to verify the TPS calculations using both algorithms, for the breast irradiation techniques. The simulation results were validated against measurements performed in breast-shaped phantoms. The EGSnrc MC calculations were compared against the TPS calculations.

The ultimate goal was to assess the CLB doses and to estimate the risk of using the different conformal techniques. The results are presented in this thesis and were presented in September 2013 in the International Conference in Medical Physics, in Brighton (UK).

This dissertation is organized in seven chapters. The first chapter is about breast cancer and the actual therapeutic approaches. In the second chapter, the fundamentals regarding radiotherapy are provided. MC techniques and the first modeling, simulation and validation results, in equivalent water phantoms, are presented in the third chapter. In the fourth chapter, the breast irradiation techniques investigated and the TPS algorithms are explored. In the following chapter, the optimized treatment plans were simulated using the Monte Carlo validated model both for phantoms and patient data and the results are presented. In the sixth chapter, the contralateral breast doses were assessed and further investigated comparing both the irradiation techniques and algorithms. The main conclusions of this work and what is left to do are put forward in this last chapter.

Introdução

1. Influência das novas tecnologias e simulações de Monte Carlo na clínica prática em Radioterapia

Nas últimas décadas, as técnicas de radioterapia (RT) sofreram grandes desenvolvimentos, com o aparecimento da RT convencional 3D e as técnicas de intensidade modulada (IMRT). Estes avanços foram possíveis com a construção de aceleradores lineares e o desenvolvimento de sistemas de planeamento para cálculos de dose.

Os aceleradores lineares modernos usados em RT permitem a administração de dose com elevada precisão, mesmo em grandes volumes que são passíveis de ser observados em 3D, e até acompanhar o movimento dos volumes alvo e de outros órgãos durante os tratamentos. Os sistemas de planeamento (TPS) e os algoritmos neles implementados assumem atualmente uma importância primordial em RT para a determinação das doses.

Os algoritmos de cálculo são cada vez mais precisos através de representações cada vez mais realistas dos pacientes. Todas estas técnicas contribuem para a melhoria da qualidade dos tratamentos, em localizações profundas e radiosensíveis, como a mama, pulmão ou cabeça e pescoço.

Para a realização de cálculos de dose em pacientes, há fundamentalmente duas dificuldades: por um lado é necessário a modelação da complexa geometria do paciente através de uma descrição detalhada da geometria e composição dos órgãos e tecidos; por outro lado é essencial a modelação dos processos físicos envolvidos na deposição de energia e absorção de dose no paciente. No que diz respeita à modelação dos pacientes, as tomografias computerizadas atuais permitem modelar o paciente, discretizando o volume do paciente em pequenos elementos de volume, chamados *voxels*. A cada voxel é associado um valor conhecido por *unidades de Hounsfield* que é representativo da densidade eletrónica média do material que compõe cada elemento específico de volume. Este método permite a determinação do poder de atenuação do meio para o feixe de radiação em questão. Para simular os processos físicos de transferência e deposição de energia foram desenvolvidos os modelos de cálculos de dose, para determinar uma representação precisa do dose administrada pelos feixes de tratamento.

O cálculo de dose compreende tipos diferentes de incertezas associadas ao TPS e aos próprios algoritmos de cálculo. As *imprecisões* no cálculo podem reduzir a

eficácia do tratamento ou aumentar os riscos de complicação nos tecidos saudáveis. Consequentemente, a redução das incertezas conduz a resultados previsíveis e reprodutíveis à dose prescrita, apesar da variabilidade individual das reações dos pacientes. Na prática, o radioterapeuta valida a dose calculada por um algoritmo de cálculo de dose, considerando este cálculo aproximado, dentro de limites teoricamente aceites. Assim, é importante que o método do cálculo de dose seja o mais exato possível para diminuir as incertezas no cálculo de dose associado ao tratamento.

Os algoritmos de cálculo de dose determinam a dose depositada pelos feixes de tratamento, nos *voxels* que modelam o paciente. Todos estes modelos de cálculo são, apesar de tudo, modelos; o que quer dizer que representam aproximações feitas para o cálculo da absorção de energia e para a representação do paciente. Consequentemente, o resultado final, a distribuição de dose, será uma representação aproximada do que acontece na absorção de dose no paciente. Este grau de aproximação é variável dependendo do algoritmo de cálculo.

A precisão notável que é possível obter através de algoritmos de MC é consensual quanto ao papel fundamental que estes métodos desempenham em TPS atuais e na sua importância quanto à continuidade da sua utilização em TPS. As vantagens de usar MC clinicamente são evidentes em situações que o feixe de radiação atravessa heterogeneidades, como cavidades de ar (pulmão) e para campos pequenos, como os de IMRT. Vários grupos publicaram já diferenças significativas entre cálculos MC e outros algoritmos convencionais usados em TPS, em situações complexas.

Algoritmos que usem métodos MC são conhecidos por serem modelos mais realistas no que respeita à modelação da transferência e deposição de energia no meio. Estas são ferramentas eficientes na modelação do paciente e da fonte de radiação para, posteriormente, calcular a distribuição de dose. No entanto, os métodos de MC precisam de muito tempo para a realização dos cálculos, não permitindo ainda a sua utilização na rotina clínica, sendo necessário estabelecer um compromisso entre a precisão e o tempo de cálculo.

As técnicas de irradiação têm evoluído, com técnicas como a RT em arco conformacional e outras técnicas avançadas e a sua utilização em prática clínica nos próximos anos pode ser agora antecipada. Alguns investigadores defendem que a combinação de um algoritmo MC com maior velocidade de cálculo seria a solução ideal para melhorar a precisão no cálculo de dose a usar nos TPS.

Desde os anos 1990, os códigos gerais de MC (tais como MCNP(x), FLUKA, GEANT, PENELOPE, EGSnrc, etc) têm sido desenvolvidos e adaptados para a prática física-médica, nomeadamente nos cálculos de dose em RT. No final dos anos 90, uma plataforma computacional denominada PEREGRINE foi desenvolvida visando a implementação de TPS em tempo real em RT. Outros programas de computador e algoritmos, como o DPM, PENFAST, MCDOSE, VMC, XVMC, VMC++, MMC, etc., foram desenvolvidos para realizar simulações rápidas e precisas, para cálculos de RT. Em 2009 estimava-se que todos os fabricantes de equipamentos tivessem desenvolvido e incorporado algoritmos baseados em MC nos TPS. Outros programas, tal como o EGSnrc e o BEAMnrc associado tornaram-se ferramentas de simulação MC muito usadas por comunidades de investigadores para modelar e simular aceleradores lineares e para determinar computacionalmente com precisão as fluências das partículas e as distribuições de dose, para tratamentos de EBRT.

A disseminação do uso de técnicas de MC e simulações para planeamento dos tratamentos de RT é também mostrado pelo aumento dramático de publicações científicas publicadas anualmente, tal como apresentado na figure 1, extraída no trabalho de Emiliano Spezi [1].

2. Tratamento de cancro de mama e dose na mama contralateral

Atualmente, devido à implementação de programas de rastreio e ao desenvolvimento das técnicas de diagnóstico, uma maior percentagem de casos são detetados em estadios iniciais, com tamanho reduzido e ainda sem quaisquer gânglios positivos. A taxa de mortalidade por cancro de mama tem vindo a diminuir, nos últimos anos. A deteção precoce permite, muitas vezes, a preservação da mama e evitar o recuso a soluções radicais que podem envolver a remoção completa da mama (técnica cirúrgica denominada por mastectomia).

O uso de técnicas de conservação da mama, em cancro de mama, tem vindo a tornar-se a opção standard nos casos de doença detetado em estadios iniciais. Mais do que nunca, o público está mais desperta e atenta a este problema, estando inevitavelmente também mais envolvida na decisão clínica, sendo portanto importante identificar e quantificar os riscos destas abordagens conservadoras. Neste tipo de abordagem, a RT é a técnica standard após a cirurgia de remoção do tumor (tumorectomia), reduzindo a probabilidade de recidiva local e mortalidade, especialmente em mulheres mais jovens. Esta estratégia terapêutica tem provas dadas de aumentar a probabilidade de sobrevivência com remissão da doença.

Vários estudos provaram resultados equivalentes ou melhores com tumorectomia seguida de RT comparativamente com mastectomia. Estes resultados positivos têm sido observados devido aos novos equipamentos e às novas técnicas especializadas e dedicadas à RT, sendo que: máquinas de cobalto-60 foram substituídas por aceleradores lineares e os sistemas de planeamento evoluiram de 2D para 3D usando imagens de tomografia computorizadas. Com tudo isto, os volumes tumorais são agora encontrados com maior precisão; por outro lado, empreendem-se esforços para que os tecidos saudáveis recebam menos doses.

A mama é uma localização particularmente complexa de irradiar devido à sua forma côncava, junto à grelha costal, e aos diferentes tipos de tecidos envolventes (osso, pulmão e tecido mole) e à sua proximidade com o limite do contorno externo do corpo. Esta localização tem ainda a dificuldade acrescida do movimento de toda a caixa torácica devido à respiração, variando o posicionamento durante o tratamento. As planimetrias dos tratamentos de mama apresentam frequentemente distribuições de dose heterogéneas, em que algumas partes da mama recebem dose mais elevada que a dose prescrita. Para se conseguirem planos de irradiação mais homogéneos e melhor conformados ao volume tumoral, foram desenvolvidos colimadores especiais, denominados colimadores multi-lâminas. Estes colimadores complexos permitiram o aparecimento de técnicas novas conformacionais como o *field-in-field*, *step-and-shoot* ou *sliding-window*, que visam homogeneizar a distribuição de dose no volume do tumor.

Apesar da importância justificada da RT, esta abordagem terapêutica pode ter implicações na qualidade de vida e até limitar a taxa de sobrevivência das pacientes devido a aumento da toxicidade, incluindo tumores secundários induzidos pela radiação.

Uma das preocupações que tem surgido com o aparecimento das novas técnicas está relacionada com o cancro na mama contralateral. Apesar da maioria dos estudos não evidenciar diferenças significativas entre doentes tratados com terapias conservadoras da mama que incluem RT de mama e doentes tratados por mastectomia radical no que respeita ao risco acrescido de desenvolvimento de cancro na mama contralateral, há dados que mostram claramente que a quantidade de radiação dispersa absorvida pela mama contralateral no decurso de um tratamento de radioterapia é considerável (podendo ser de vários Gy), estando portanto no intervalo de doses que eleva os riscos associados a cancros na mama contralateral induzidos por radiação. Com o aumento da sobrevivência que atualmente se verifica em doentes de cancro de mama é urgente seguir o princípio 'ALARA' (*as low*

as reasonably achievable) numa tentativa de minimização da radiação dispersa na mama contralateral para todos os doentes que realizem RT.

3. Simulações de Monte Carlo: suporte aos tratamentos de RT de cancro de mama

Este trabalho tem como principal objetivo a determinação de doses na mama contralateral quando se considera a irradiação primária da mama. Foram estudadas quatro técnicas de irradiação com feixes de fotões passíveis de serem tratados num acelerador linear: *forward-intensity modulated* RT (f-IMRT), planeamento direto para intensidade modulada; IMRT usando planeamento inverso para 2 e 5 campos modulados - IMRT2 e IMRT5, respetivamente; e arco dinâmico conformacional RT (DCART).

Todo o estudo foi realizado para o acelerador linear 2300 C/D Trilogy VARIAN (Medical Systems, Palo Alto, CA) usando para tratamentos de radioterapia externa, equipado com o *High Definition* colimador micro multilâminas (HDMLC) que foi explorado para o propósito deste trabalho. O sistema de planeamento (TPS) utilizado foi o iPlan (BrainLAB AG, Feldkirchen Alemanha) v. 4.1, usando dois algoritmos de cáluclo distintos, o *Pencil Beam Convolution* (PBC) e o Monte Carlo comercial (iMC). As técnicas de irradiação de mama foram exploradas e aplicadas neste TPS. Foi realizada uma comparação detalhada das técnicas de irradiação e dos algoritmos de cálculo do TPS. Os resultados foram apresentados num artigo publicado no *journal Physica Medica*, em Março de 2014.

Uma parte do trabalho subjacente a esta dissertação consistiu em aplicar um método eficiente para determinação da distribuição de intensidade ótima do feixe de eletrões antes do alvo, para, com mais precisão reproduzir perfis de vários campos de fotões com diferentes configurações para a energia usada neste estudo (6 MV) e a estrutura do acelerador linear utilizado ao longo deste trabalho. Um modelo independente, usando técnicas de Monte Carlo através do sistema BEAMnrc/EGSnrc e DOSXYZnrc/EGSnrc do acelerador Trilogy foi criado e validado com medidas experimentais para o feixe de 6 MV. Numa primeira fase, o modelo foi validado até ao colimador primário (jaws); o colimador multi-lâminas, HDMLC foi introduzido apenas numa fase posterior. A simulação deste colimador foi um trabalho pioneiro, tendo estes resultados sido apresentados no *journal Medical Physics*, num artigo publicado em Janeiro de 2012.

O principal objetivo destes cálculos independentes de MC consiste em verificar os cálculos realizados no TPS, para os dois algoritmos que este utiliza, para as técnicas de IMRT. Os resultados simulados foram validados com medições realizadas em fantomas com forma semelhante à da mama, na mulher.

O objetivo final consiste em determinar as doses na mama contralateral, sendo este dado essencial para estimar o risco de utilizar técnicas conformacionais mais complexas. Os resultados são apresentados nesta dissertação e foram apresentados em Setembro de 2013, na conferência *International Conference on Medical Physics*, em Brighton, UK.

Esta dissertação está organizada em sete capítulos. No primeiro capítulo aborda-se a problemático do cancro de mama e as possíveis abordagens terapêuticas. No segundo capítulo são mencionados os fundamentos essenciais sobre radioterapia, necessários à compreensão desta tese. As técnicas de Monte Carlo e os resultados da modelação, simulação e validação do acelerador Trilogy e do colimador micro multi-lâminas (HDMLC) em fantomas de água são apresentados, no capítulo 3. No quarto capítulo, as técnicas de irradiação e os algoritmos do TPS são explorados e os resultados são apresentados. No capítulo seguinte simularam-se os planos de tratamento otimizados usando o modelo de Monte Carlo validado, em fantoma e em imagens de pacientes e apresentam-se os resultados. No sexto capítulo, calcularam-se as doses na mama contralateral para as várias técnicas de irradiação e algoritmos. As conclusões deste trabalho e o trabalho futuro são discutidos no sétimo e último capítulo.

Publications

Articles

- March 2014 - C Borges, G Cunha, I Monteiro-Grillo, P Vaz, N Teixeira; Comparison of different breast planning techniques and algorithms for radiation therapy treatment. Physica Medica: European Journal of Medical Physics 30, (2): 160-70
- May 2013 - C Borges; G Cunha; N Teixeira; Comparação de diferentes técnicas de irradiação de mama em radioterapia com recurso a acelerador linear em modo de fotões; Radioterapia SAÚDE & TECNOLOGIA (2013), 9: 33-9 - Artigo vencedor de melhor artigo publicado nesta revista.
- June 2012 - Abstract publication: Borges C, Zarza-Moreno M, Teixeira N, Vaz P; Monte Carlo simulations on clinical applications using the new HDMLC BEAMnrc component module; Physica Medica: European Journal of Medical Physics Vol. 28Supplement 1, Pages S8-S9 June 2012
- January 2012 - C Borges, M Zarza-Moreno, E Heath, N Teixeira, P Vaz; Monte Carlo modeling and simulations of the High Definition (HD120) micro MLC and validation against measurements for a 6 MV beam, Med Phys (2012), 39 (1): 415-23.

Presentations

- September 2013 - Oral presentation: C Borges, M Zarza Moreno, N Teixeira, P Vaz; Assessment of whole-breast radiotherapy (RT) treatments using Pencil Beam Convolution and Monte Carlo algorithms: dosimetric consequences; Conferência de Protecção Radiológica na Saúde 2013 (PRS2013); in Lisboa (Portugal)
- September 2013 - Poster: C Borges, M Zarza-Moreno, N Teixeira, P Vaz; How much dose does the contralateral breast receive using breast external beam RT techniques?; 20^{th} International Conference on Medical Physics;in Brighton (United Kingdom)
- March 2013 - Poster: C Borges; M Zarza-Moreno; G Cunha; P Vaz; N Teixeira; Comparação de técnicas de irradiação de mama baseado em algoritmos de convolução e Monte Carlo: implicações e riscos em cancros secundários; 5º Congresso da Sociedade Portuguesa de Radioterapia Oncologia, in Coimbra

- September 2012 - Oral presentation: C Borges, M Zarza-Moreno, N Teixeira, P Vaz; Simulações Monte Carlo de tratamentos de Radioterapia em patologia primária de esófago – comparação de técnicas de irradiação; 18ª Conferência Nacional de Física e 22º Encontro Ibérico para o Ensino da Física, in Aveiro

- June 2012 - Oral presentation: Borges C, Zarza-Moreno M, Teixeira N, Vaz P; Monte Carlo simulations on clinical applications using the new HDMLC BEAMnrc component module; 51ème Journées Scientifiques, organized by the Sociéte Française de Physique Médicale and EFOMP, in Strasbourg (France)

- May 2012 - Oral presentation: Borges C, Zarza-Moreno M, Teixeira N, Vaz P; "Assessing different conformal radiotherapy techniques for breast cancer treatments using Monte Carlo simulations" at the 3rd European Workshop Monte Carlo Treatment Planning organized by European Group on MCTP and EFOMP, in Seville (Spain)

- May 2012 – Poster: M Zarza-Moreno, C Borges, N Teixeira, A P Jesus, G Mora; "Assessing dose-to-medium to dose-to-water conversion for the Monte Carlo verification of 6 MV head and neck IMRT"; Radiotherapy and Oncology. Vol 103, Sup 1, S128

- February 2012 - Poster: P12: C Borges, G Cunha, P Vaz, N Teixeira; "Comparison of different irradiation techniques on breast cancer radiotherapy"; 1ª edição da Conferência International: Conference on Health Technology Assessment and Quality Management 2012 at Escola Superior de Tecnologia da Saúde in Lisboa

- October 2009 - Poster: Use of Monte Carlo simulations to assess contralateral breast doses in breast cancer treatments, at the 2^{nd} European Working Group of Monte Carlo Treatment Planning (MCTP), in Cardiff (United Kingdom).

Chapter 1

Breast Cancer

1.1 Breast cancer epidemiology

Cancer is responsible for a large percentage of deaths worldwide, every year. According to GLOBOCAN most recent studies [2], about 14.1 million new cases and 8.2 million deaths occurred only in 2012.

The term 'cancer' refers to various diseases characterized by two symptoms: the unregulated proliferation of cells and the spread of these cells through the body by the invasion and/or metastasis [3]. Cell proliferation typically results in the development of neoplasms (more commonly known as tumors).

Cancer develops as a result of genetic abnormalities in proto-oncogenes and tumor suppressor genes which translate genetic code into proteins that promote and suppress cell growth, respectively. These abnormalities can be the result of a mutagen altering genetic information or a spontaneous error in DNA replication. Substances responsible for these mutations are known as carcinogens [4].

Breast cancer is by far the most frequent cancer among women with an estimated 1.68 million new cancer cases diagnosed in 2012 (25% of all cancers), and ranks second overall (10.9% of all cancers). It is now the most common cancer both in developed and developing countries. Cancer incidence profile, in general, has changed from the 1990s in the USA and most western European countries mostly due to the improved screening tools and to a greater awareness about the disease leading to more frequent diagnosis of cancer at earlier stages (see figure 1.1).

The breast cancer risk is more common in the female gender and is associated with different factors such as: aging (particularly for women with more than 55

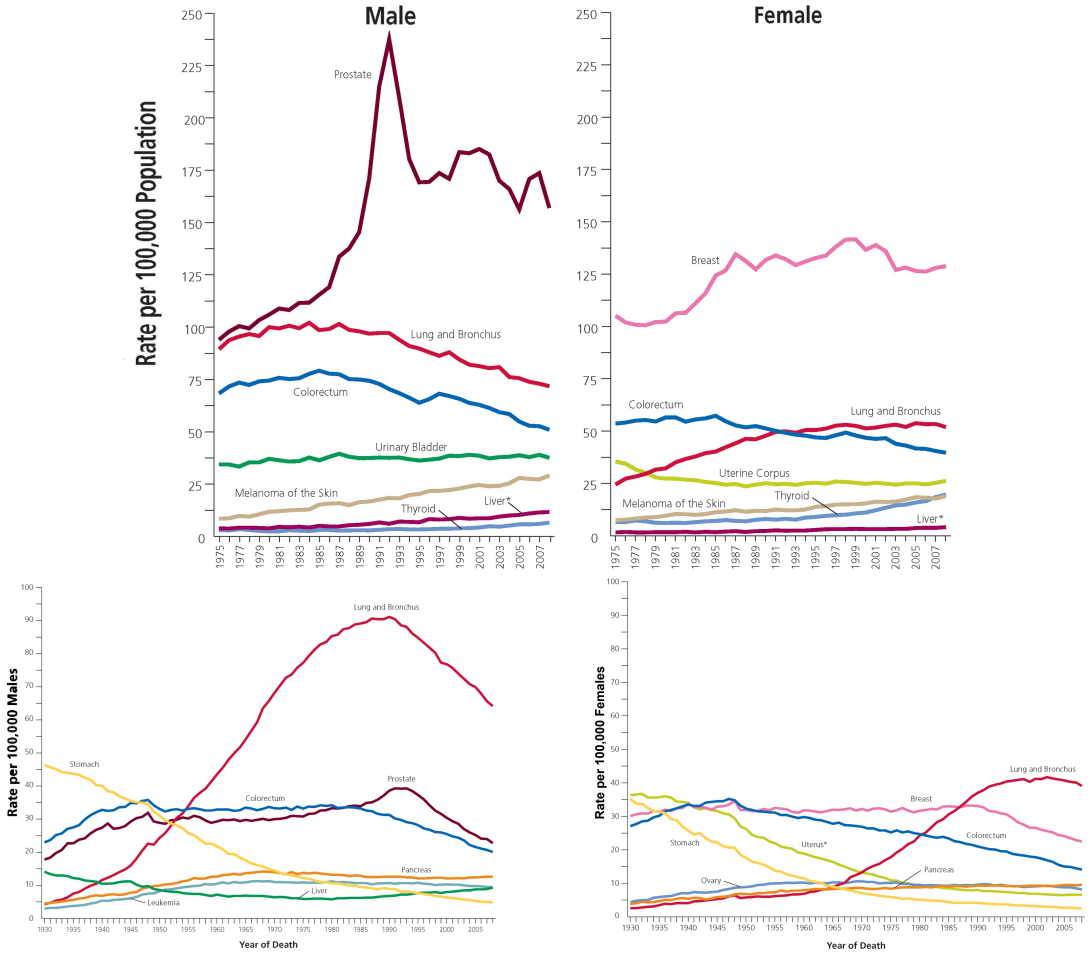

FIGURE 1.1: The first two graphs are related to screening rate per 100,000, in the United States, 1975 to 2008, for men on the left and women on the right. The graphs below represent the number of deaths, per 100,000, in the United States, from 1975 to 2008, for men on the left, and women, on the right. There is a notable increase of screening since the 80s; and a decrease of deaths since the 90s, in general.Study developed by the SEER program www.seer.cancer.org)[5].

years old), genetic factors (mutation in the suppressor genes of tumors BRCA1, BRCA2 and p53), the user of replacement hormonal therapy, family history, etc [6].

In the particular case of breast cancer, earlier diagnoses make it possible to apply breast conserving therapies. Nowadays there are several techniques for screening the breast [6]. Routine radiographic studies include bilateral mammograms. If clinically indicated, these may be complemented with ultrasounds, computerized tomography (CT) scans, magnetic resonance imaging (MRI), positron emission

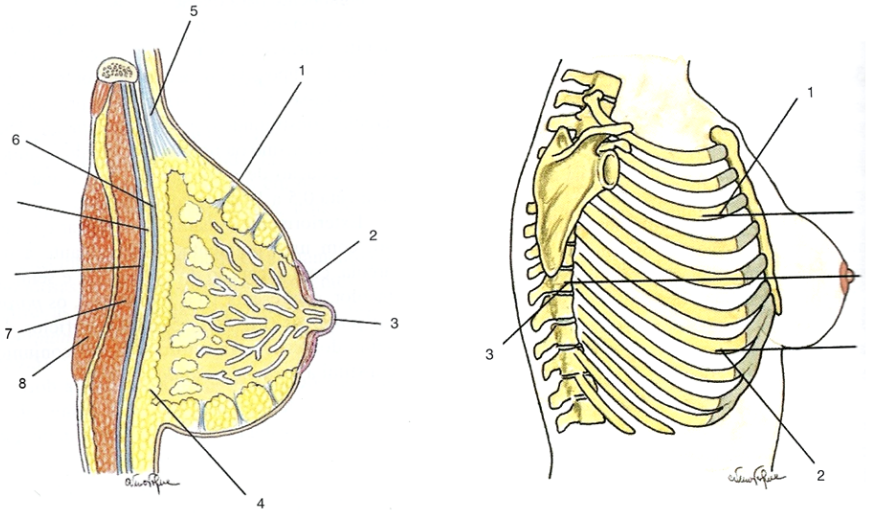

FIGURE 1.2: Breast constitution and location. On the left, 1 –skin of the peripheral zone; 2 –skin of the aureole; 3 –skin of the nipple; 4 –Retro–mammary zone of cells and fat; 5–Ligamentum suspensoria mammaria; 6 –Fascia superficialis; 7 –Pectoralis major muscle; 8 –Pectoralis minor muscle; on the right: 1 –3rd rib; 2 –7th rib; 3 –9th dorsal vertebrae.[8]

tomography (PET) or single photon emission tomography (SPECT) scans, bone scans and chest radiography.

Due to the generalized spread of screening programs, it is estimated that about two thirds of breast cancers are detected in early stages of the disease [7]. It is therefore possible to apply breast conserving therapies, preserving the breast, instead of adopting radical surgery, mastectomy. Despite the increasing breast cancer diagnosis, recent studies [5] show that the majority of these patients have, ever since, been treated successfully with long-term survival.

1.2 Breast anatomy

The breasts are organs that serve, in the women's lifetime, the main purpose of producing milk, to assure the baby-born feeding. A woman has two breasts, a left and a right. The female breast lies on the anterior chest wall superficial to the pectoralis major muscle. The breast can extend from the midline to near the midaxillary line and cranial-caudally, generally, from the third anterior rib to the seventh anterior rib. The upper-outer quadrant of the breast extends into the region of the low axilla and is frequently referred to as the axillary tail of Spence. This anatomical feature leads the upper–outer quadrant of the breast to contain a greater percentage of total breast tissue compared to other quadrants.

The breast is made of mammary gland, fat, blood vessels, nerves and lymphatics. The surface of the breast has deep attachments of fibrous septa, called Cooper's ligament, which run between the superficial fascia (attached to the skin) and the deep fascia (covering the pectoralis major and other muscles of the chest wall). The chest wall includes the ribs, intercostal muscles, and serratus anterior muscle, but not the pectoral muscles.
The breast parenchyma is composed of lobules and ducts. The function of the lobules is to produce milk whereas the ducts are responsible to transport lactation products to the nipple. The peripheral ducts converge into major lactiferous ducts, which then communicate with the nipple-areola complex.

The breast parenchyma is intermixed with connective tissue, which has a rich vascular and lymphatic network. Mammary gland lymphatics begin in the interlobular or prelobular spaces, follow the ducts, and end in the subareolar network of lymphatics of the skin. The predominant lymphatic drainage of the breast is to axillary lymph nodes, which is commonly described in three levels, based on the relationship of the lymph node regions to the pectoralis minor muscle. The level I axilla is caudal and lateral to the muscle, level II is beneath the muscle, and level III (also known as the infraclavicular region) is cranial and medial to the muscle. A standard axillary lymph node dissection resects the tissue and lymph nodes within levels I and II. It is very unusual to have involvement of level III of the axilla without disease in level I or II. The axillary lymph nodes continue underneath the clavicle to become the supraclavicular lymph nodes, which can be involved in locally advanced breast cancers.

Lymphatics can also drain directly into the internal mammary lymph node chain (IMC), which are intrathoracic structures located in the parasternal space. Although these nodes are not usually visualized on computed tomography (CT), the anatomical region of the IMC can be determined by the internal mammary artery and vein, which are easily visualized by CT and usually lay 3 to 4 cm lateral to midline. Regardless of the location within the breast, the axilla is the most common site of lymphatic involvement. However, breast cancers that develop in the medial, central, or lower breast more commonly drain to the IMC (in addition to the axilla) than those occurring in the lateral and upper quadrants.

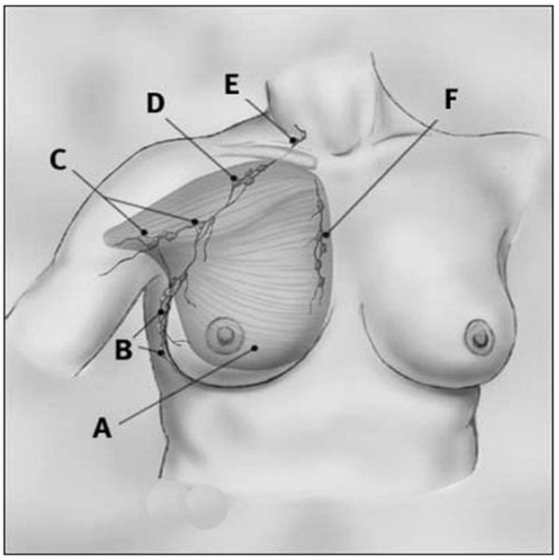

FIGURE 1.3: Pectoralis major muscle and major lymph nodes involved in the breast: A –Pectoralis major muscle; B –Axillary lymph nodes level I; C –Axillary lymph nodes level II; D –Axillary lymph nodes level III; E –Supraclavicular lymph nodes; F –Internal Mammary lymph nodes

1.3 Breast cancer therapeutic approaches

The location and stage of a tumor determine which the available treatment options can be adopted to treat the primary tumor. The therapeutic approach to be chosen depends largely on the TNM (tumor, node, metastasis) classification of the tumor:

- T describes the size of the original (primary) tumor and whether it has invaded nearby tissue,
- N describes nearby (regional) lymph nodes that are involved,
- M describes distant metastasis (spread of cancer from one part of the body to another).

Among the clinical options available, the most applied are surgical removal, chemotherapy, hormone therapy, immunotherapy and radiation therapy. These treatments may also be delivered as part of palliative care, where the aim is to improve the quality of life of the patient. In the following, these techniques are briefly summarized.

1.3.1 Surgery

Surgery was one of the first ways found to manage breast cancer. The most ancient evidence was found in an Edwin Smith papyrus dating from 3000 BC [9].

Surgery is the definitive treatment for breast cancer comprising either a breast (preferable) conserving operation, which removes the tumor with some surrounding tissue or mastectomy which involves removal of the whole breast. Both procedures are usually combined with sampling or removal of the axillary lymph nodes.

Historically, the treatment of breast cancer required mastectomy without exception. Mastectomy removes all tumor cells including microscopic residual disease and provides staging information. Nowadays, following mastectomy an immediate or delayed reconstruction may be performed.

In the 1980s, large randomized trials compared the efficacy of breast conserving therapy (BCT), in the form of tumorectomy,sentinel node investigation, axillary node dissection, in case of positive sentinel node, and radiation, with modified radical mastectomy [10, 11]. In early stage breast cancer, BCT options have shown to offer equivalent overall survival to mastectomy, improved cosmetic results and reduced psychological trauma [12–14].

1.3.2 Chemotherapy

Preoperative chemotherapy can be offered to facilitate breast conservation in patients with tumors of a significant size or in a location that made breast-conserving surgery unlikely to be done without a decrease in tumor size.

For patients with clinically uninvolved lymph nodes, sentinel lymph node biopsy and/or axillary nodal dissection generally is performed before initiation of neoadjuvant chemotherapy.

Patients at risk of distant metastasis are generally administered adjuvant chemotherapy, in accordance to the actual guidelines. Results of the Early Breast Cancer Trialists' Collaborative Group meta-analysis have shown that adjuvant chemotherapy improves breast cancer specific survival and overall survival [15].

1.3.3 Hormone therapy

Hormonal therapy is one of the major modalities of medical treatment for cancer. It involves the manipulation of the endocrine system through exogenous administration of specific hormones, particularly steroid hormones, or drugs which inhibit the production or activity of such hormones (hormone antagonists). Steroid hormones are powerful drivers of gene expression in certain cancer cells, changing the activity of certain hormones and therefore possibly causing certain cancers to cease growing, or even undergo cell death. Surgical removal of endocrine organs, such as oophorectomy can also be employed as a form of hormonal therapy.

Typically, the hormonal treatment is performed after surgery and it is not recommended concomitantly with chemotherapy.

Hormonal therapy is used for several types of cancers derived from hormonally responsive tissues, including the breast. One of the most frequent example of hormonal therapy in oncology is the use of the selective estrogen-response modulator (SERM), tamoxifen, for the treatment of breast cancer, although another class of hormonal agents, such as aromatase inhibitors, have an expanding role in this disease.

1.3.4 Radiation therapy

Radiotherapy (RT) in the breast cancer is a loco-regional technique, generally integrating the treatment after conserving surgery or after mastectomy when in respecting specific criteria, in order to eliminate the microscopic residual disease and to prevent local relapse. According to Holland et al [16], the surgical tumor bed and the mammary gland risk that contain microscopic disease must be removed with the breast conserving surgery and it is essential to irradiate locally to eradicate the residual disease. This technique is usually applied 4 weeks after surgery, after the healing. RT after surgery has proven efficacy with equivalent or superior free disease survival, when compared to mastectomy [12, 13, 17–19]. Several studies confirmed that surgery followed by RT reduces mortality among breast cancer women, 5 to 10 years after, being therefore essential to protect the normal tissues, keeping the severity of the secondary effects as low as possible [12, 13, 20].

The choice of the irradiation technique (external beam RT or brachytherapy), the dose to administer to the tumor depend on its location, size, histology, grade

TABLE 1.1: Breast cancer five-year survival by stage at diagnosis.

Cancer stage	Classification	Five-year survival rate (%)
0	*In situ*	100
I, IIa, IIb	Early invasive	98.0 (local); 83.6 (regional)
IIIa, IIIb, IIIc	Locally advanced	57
IV	Metastatic	23.4

and extension of the disease, the breast size, cosmetic expected result or patient preference. Adding an extra dose (frequently called a boost) either with photons or electrons, to the tumor bed, as determined from mammographic and surgical information, further reduces the risk of local relapse.

In the last years, with the growth and broader know-how of the biology and nature of the breast tumors, combined with the technological improvements in immobilization accessories (breast board, vacuum bed, etc), planning in 3-dimensional computed tomography (CT) images, the positioning verification imaging, permitted a great improvement in precision and reproducibility of the patient set up, in the definition of the target volumes and homogeneity of the dose distributions. The modern linacs are now equipped with complex collimator systems that permit a better field size control as well as modeling the beam intensity, conforming the dose distribution to the volumes to treat.

The goal of RT it is to adequately irradiate all the mammary gland, in initial stage breast cancer patients while trying to minimize the dose to the adjacent organs at risk (OAR).

1.4 Breast cancer classification

Breast cancer prognosis and treatment options are generally based on TNM, tumor-node-metastasis staging. Lymphovascular spread, histologic grade, hormone receptor status, ERBB2 over-expression, comorbidities and patient menopausal status and age are important factors. The staging at diagnosis can be classified according to the specification provided in table 1.1 [21, 22].

1.4.1 Stage 0: *in situ*

Lobular carcinoma *in situ* (LCIS) is an incident microscopic finding of abnormal tissue growth in the lobules of the breast, as represented in figure 1.4, on the left side. Ductal carcinoma *in situ* (DCIS) is found in the ducts (see figure 1.4, on the right side) and can progress to invasive breast cancer.

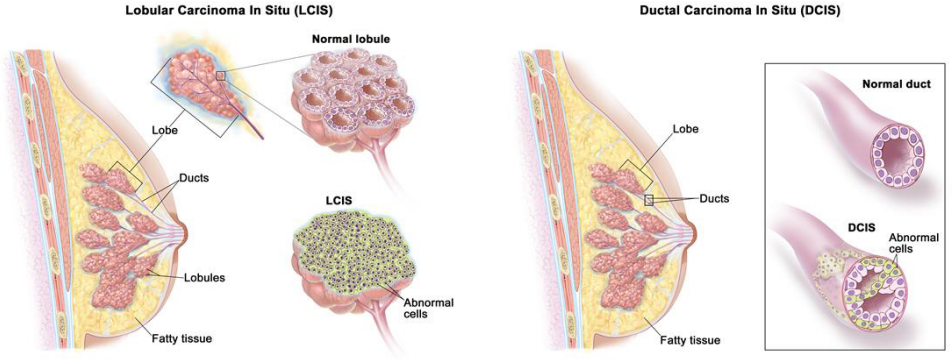

FIGURE 1.4: On the left, lobular carcinoma in situ (LCIS): abnormal cells are found in the lobules of the breast. On the right: ductal carcinoma in situ (DCIS): abnormal cells are found in the lining of a breast duct. Figures by Terese Winslow, http://www.cancer.gov/cancertopics/pdq/treatment/breast/Patient/page2.

1.4.2 Stages I and II: Early Stage Invasive

When classified as stage I or II, the abnormal cells have grown into bigger clusters and are classified according to their dimensions, as shown in figure 1.5.

In stage IA, the tumor is 2 centimeters or smaller. Cancer has not spread outside the breast. In stage IB, small clusters of breast cancer cells (larger than 0.2 cm but not larger than 2 cm) are found in the lymph nodes and either: no tumor is found in the breast; or the tumor is 2 centimeters or smaller.

Stage II is divided into stages IIA and IIB. In stage IIA, 1 to 3 positive lymph nodes are found in the axilla or near the breastbone and there is no tumor or it is smaller than 2 cm; or the tumor is 2 to 5 cm large without positive lymph nodes. In stage IIB, a tumor larger than 2 cm but not larger than 5 cm is found in the breast and there are 1 to 3 positive axillary lymph nodes or in the lymph nodes near the breastbone; or the tumor is larger than 5 cm (with no positive lymph nodes).

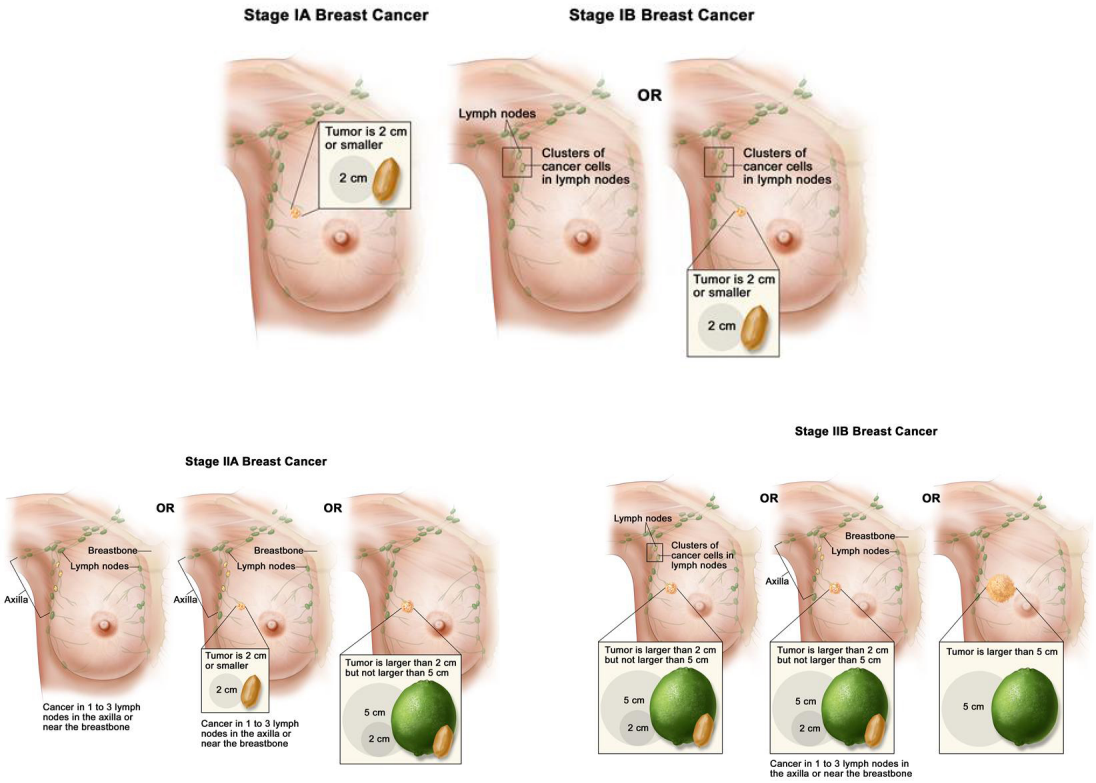

FIGURE 1.5: Representation of breast cancer in stages I and II . Figures by Terese Winslow, http://www.cancer.gov/cancertopics/pdq/treatment/breast/Patient/page2.

1.4.3 Stage III: Locally Advanced

Locally advanced breast cancer (LABC) includes tumors larger than 5 cm, extensive regional lymph node involvement, direct involvement of underlying chest wall or skin, tumors considered inoperable but without distant metastases, and inflammatory breast cancer.

Induction chemotherapy followed by local therapy (surgery, RT, or both) is becoming the standard of care. Five-year survival can be achieved in 55% of patients presenting with non-inflammatory LABC. The most important prognostic factors are response to induction chemotherapy and lymph node status.
The Stage III can be classified in 3 categories (A, B or C), as represented in figure 1.6.

In stage IIIA:

- no tumor is found in the breast or the tumor may be of any size. Cancer is found in 4 to 9 axillary lymph nodes or in the lymph nodes near the breastbone (found during imaging tests or a physical exam); or

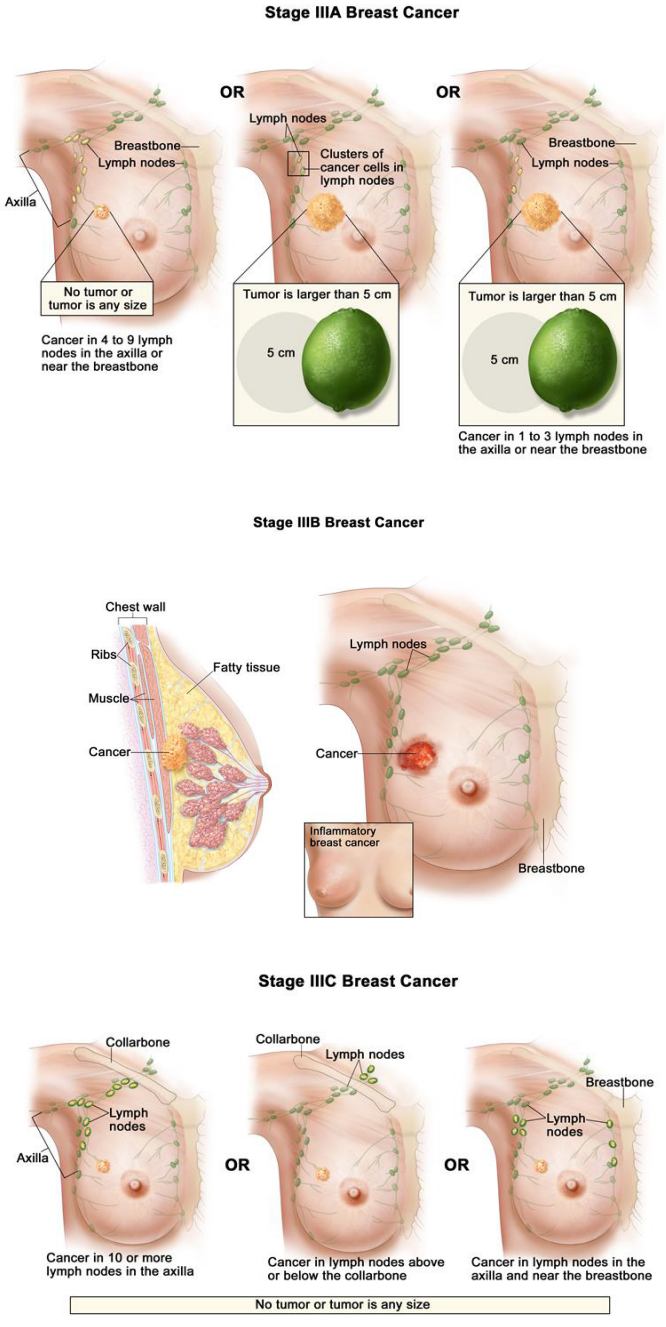

FIGURE 1.6: Stage III: A, on top; B, in the middle; and C, in the bottom. Figures by Terese Winslow, http://www.cancer.gov/cancertopics/pdq/treatment/breast/Patient/page2.

- the tumor is larger than 5 centimeters. Small clusters of breast cancer cells (larger than 0.2 centimeter but not larger than 2 centimeter) are found in the lymph nodes; or
- the tumor is larger than 5 centimeters. Cancer has spread to 1 to 3 axillary lymph nodes or to the lymph nodes near the breastbone (found during a sentinel lymph node biopsy).

In stage IIIB, the tumor may be of any size and cancer has spread to the chest wall and/or to the skin of the breast and caused swelling or an ulcer. Also, cancer may have spread to:

- up to 9 axillary lymph nodes; or;
- the lymph nodes near the breastbone.

Cancer that has spread to the skin of the breast may also be inflammatory breast cancer.

In stage IIIC, no tumor is found in the breast or the tumor may be any size. Cancer may have spread to the skin of the breast and caused swelling or an ulcer and / or has spread to the chest wall. Also, cancer has spread to:

- 10 or more axillary lymph nodes; or
- lymph nodes above or below the collarbone; or
- axillary lymph nodes and lymph nodes near the breastbone.

Cancer that has spread to the skin of the breast may also be inflammatory breast cancer. For treatment, stage IIIC breast cancer is divided into operable and inoperable stage IIIC.

1.4.4 Stage IV: Metastatic

In stage IV, cancer has spread to other organs of the body, most often the bones, lungs, liver, or brain, as represented in figure 1.7.

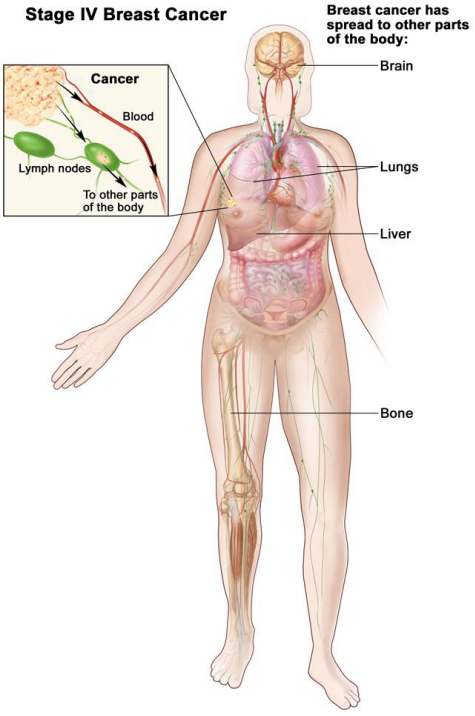

FIGURE 1.7: Stage IV: cancer has spread to other organs of the body, most often the bones, lungs, liver, or brain. Figures by Terese Winslow, http://www.cancer.gov/cancertopics/pdq/treatment/breast/Patient/page2.

1.5 Management of breast cancer

According to Maughan et al [22], the treatment options to treat breast cancer are given according to the cancer stage and type as presented in table 1.2. Different and more detailed options according to several other indicators such as evaluation of axillary and regional nodes, dimension and extension of the lesion(s), specific hormone receptor status, can be found in other references such as NCCN (National Comprehensive Cancer Network, http://www. nccn.org) guidelines, for instance.

1.5.1 Stage 0: *in situ*

It does not progress to, but increases the risk of, subsequent invasive breast cancer in either breast by approximately 7% over 10 years. Local and systemic therapies are not indicated, but affected women should undergo rigorous breast cancer surveillance. The National Comprehensive Cancer Network recommends annual mammography and clinical breast examination every six months. Patients should be offered information about chemoprevention with SERM, such as tamoxifen.

Cancer stage and type	Primary treatment	Node evaluation	Adjuvant therapy: Hormone negative receptor	Adjuvant therapy: Hormone positive receptor	Adjuvant therapy: ERBB2 overexpression
Stage 0: *in situ*					
Lobular carcinoma *in situ*	No treatment or consider prophylaxis with tamoxifen				
Ductal carcinoma *in situ*	BCS (consider mastectomy for extensive or multifocal) and RT				
Stages I and II: early-stage invasive	BCS and RT	SLN biopsy and ALN dissection[1]	Chemotherapy [2]	Chemotherapy and endocrine therapy	Chemotherapy and trastuzumab (Herceptin)
Stages III: locally advanced					
Non-inflammatory	Induction chemotherapy, followed by BCS[3] and RT	ALN dissection or SLN biopsy	Induction chemotherapy	Induction chemotherapy and post-operative endocrine therapy	Induction chemotherapy and postoperative trastuzumab
Inflammatory	Induction chemotherapy, followed by mastectomyand RT	ALN dissection			
Stage IV: metastatic					
Initial or recurrent	Address patient's treatment goals; RT or biophosphonates for bone pain		Chemotherapy	Endocrine therapy with or without chemotherapy	Trastuzumab with or without chemotherapy
Recurrent					
Local after BCS	Mastectomy	ALN dissection[4]	Chemotherapy[5]	Chemotherapy and endocrine therapy[6]	Chemotherapy and trastuzumab
Local after mastectomy	Wide excision	ALN dissection[7]			
Local inoperable	Induction chemotherapy	ALN dissection			

ALN=axillary lymph node; SLN = sentinel lymph node

[1] - SLN biopsy of clinically negative nodes; otherwise, ALN dissection is recommended.

[2] - Except lowest risk (i.e., tumor ≤ 1 cm, node negative).

[3] - Mastectomy may be considered if tumor does not sufficiently respond to induction chemotherapy.

[4] - If nodes are clinically negative and SLN biopsy is done initially, SLN can be repeated; if nodes are clinically positive, ALN dissection is needed.

[5] - Local recurrence is often associated with distant metastasis; therefore prophylactic chemotherapy theoretically may be of benefit and is being studied.

[6] - Benefit of adjuvant therapy is uncertain and under investigation; until results are available, chemotherapy is generally recommended.

[7] - May not need to explore axilla if ALN dissection is done initially and there are clinically negative nodes with recurrence

TABLE 1.2: Treatment options for breast cancer by stage. Information compiled by Maughan et al [22].

Conversely, for DCIS, breast-conserving surgery followed by radiation therapy is standard treatment; however, mastectomy may be recommended for extensive or multifocal disease. Pathologic lymph node evaluation is not usually performed because nodal metastasis is rare. There is conflicting evidence regarding endocrine therapy with tamoxifen in women with DCIS. Given the risks of tamoxifen and the low risk of recurrence of DCIS, routine use of tamoxifen in women with DCIS is not recommended.

1.5.2 Stages I and II: Early Stage Invasive

1.5.2.1 Surgery

Modified radical mastectomy has traditionally been the standard of care for early-stage invasive breast cancers. However, breast-conserving surgery has been favored more recently. This therapy involves removing the tumor without removing excess healthy breast tissue, with the outcome of a breast that is more aesthetically acceptable to the patient than the outcome from radical mastectomy. Radiation therapy following breast-conserving surgery decreases local recurrence and improves cancer-specific survival rates to rates equivalent to those with mastectomy [12, 13, 17–19]. Breast conserving surgery has the highest success rate in women with early-stage breast cancer, but it is not recommended for women at high risk of local recurrence.

1.5.2.2 Evaluation of regional lymph nodes

The status of axillary lymph nodes (ALN) determines the need for RT and adjuvant systemic therapy. ALN dissection at the time of surgery was standard care until the 1990s, but often resulted in pain, numbness, swelling, and decreased mobility in the affected arm. In patients with clinically negative nodes, a negative intraoperative sentinel lymph node (SLN) biopsy precludes the need for ALN dissection.

SLN biopsy reduces arm symptoms compared with ALN dissection. SLN biopsy has a sensitivity of 95% to 100%, a false-negative rate of 5.5%, and a negative predictive value of 98%. A prospective analysis provides evidence that patients with early-stage breast cancer who have a negative SLN have improved disease-free and overall survival compared with patients who have a negative ALN dissection. This is most likely because of more accurate axillary staging in patients from the

SLN group. ALN dissection is indicated for all women with palpable lymph nodes or a positive SLN [23].

SLN biopsy reduces arm symptoms compared with ALN dissection. SLN biopsy has a sensitivity of 95% to 100%, a false-negative rate of 5.5%, and a negative predictive value of 98%. A prospective analysis provides evidence that patients with early-stage breast cancer who have a negative SLN have improved disease-free and overall survival compared with patients who have a negative ALN dissection. This is most likely because of more accurate axillary staging in patients from the SLN group. ALN dissection is indicated for all women with palpable lymph nodes or a positive SLN [23].

The risk of microscopical invasion of the supraclavicular lymph nodes is highly influenced by the number of involved axillary nodes. According to Strom et al [24], with 4 or more nodes invaded or when level 3 of the axilla is invaded, the risk exceeds 15 –20%. Invasion of the internal mammary chain varies between 3% and 65% depending on tumor stage and position of the primary tumor in the breast [25].

There are several randomized trials going on to find out whether these lymph nodes should be treated with radiation, such as the SUPREMO (Selective Use of Post-operative Radiotherapy after Mastectomy) trial and the EORTC trial, AMAROS (Adjuvant Management of the Axilla, Radiotherapy of Surgery) [26] and results are expected from the EORTC trial 22922/10925, NCIC CTG (National Cancer Institute of Canada Clinical Trials Group) and SFRO (Société Française de Radiothérapie Oncologique) CMI.

1.5.2.3 Radiation therapy

Typically, whole-breast irradiation is performed following breast-conserving surgery to treat subclinical disease. A review of randomized controlled trials (RCT) comparing breast-conserving surgery with and without radiation showed that radiation in addition to surgery significantly reduced the five-year local recurrence rate, regardless of the use of adjuvant systemic therapy, and appeared to decrease the 15-year breast cancer mortality risk [27, 28]. According to a systematic review of three RCT, the sequencing of chemotherapy and radiation therapy does not appear to have a major effect on survival or recurrence as long as radiation is initiated within seven months of surgery. Radiation therapy is expensive and

time-consuming, and shorter therapies can be appealing. Five-year results appear favorable in studies evaluating brachytherapy and compressed schedules of radiation; however, long-term data are lacking.

1.5.2.4 Adjuvant systemic therapies

Most women with early-stage breast cancer receive adjuvant systemic therapies. Chemotherapy, endocrine therapy, and tissue targeted therapies enhance definitive local therapy (surgery, radiation therapy, or both), substantially decreasing cancer recurrence and disease-specific death. Node-positive disease benefits most from systemic therapy.

Chemotherapy Chemotherapy is the standard of care for women with node-positive cancer or with a tumor larger than 1 cm. Hormone receptor–negative disease derives more benefit from chemotherapy than hormone receptor–positive disease. Factors such as age and comorbidities also influence the decision to use chemotherapy. Most studies suggest a small benefit for treatment with anthracyclines or taxanes over other chemotherapies, particularly in women with tumors over expressing ERBB2. A systematic review of 12 studies demonstrated disease-free and overall survival advantages when using a taxane-containing regimen for premenopausal and postmenopausal women with early-stage breast cancer. A meta-analysis of 13 RCT determined that adding a taxane to ananthracycline-based regimen improved disease-free survival (5-year risk reduction of 5%) and overall survival (5-year risk reduction of 3%) [29].

Endocrine Therapy Endocrine therapies, such as SERM, aromatase inhibitors, and gonadotropin releasing hormone agonists, prevent estrogen production or block estrogen, thereby preventing stimulation of an estrogen-sensitive tumor. In premenopausal women, ovarian ablation or oophorectomy may be considered.

Endocrine therapy is not effective against cancers that are lacking hormone receptors. 5 years of treatment with tamoxifen reduces the breast cancer death rate (absolute risk reduction of 9.2% over 15 years) [29].

Aromatase inhibitors should be considered in all postmenopausal women with hormone receptor–positive breast cancer. They block the conversion of androgens to estrogen in postmenopausal women. Trials consistently show that aromatase

inhibitors reduce the risk of relapse of early-stage breast cancer both in direct comparison with and after completion of tamoxifen. Many women tolerate aromatase inhibitors better than tamoxifen. Aromatase inhibitors are not indicated for premenopausal women.

Tissue-Targeted Therapy Approximately 20 to 30% of early-stage breast cancers overexpress ErbB2. These cancers generally have a worse prognosis. A humanized anti-ErbB2 monoclonal antibody, trastuzumab (Herceptin), improves disease-specific and overall survival when added to anthracyclines and paclitaxel (Taxol) chemotherapy in women with node-positive and high-risk, node-negative breast cancers overexpressing ErbB2. The combination of trastuzumab and anthracyclines must be used with caution, however, because cardiac toxicity will develop in 2 to 3% of patients over two years of treatment.

1.5.3 Stage III: Locally Advanced

1.5.3.1 Induction systemic therapies

Induction Chemotherapy Patients with LABC who achieve an excellent response to induction chemotherapy have outcomes similar to those in patients with early stage disease. Preoperative chemotherapy downsizes the local tumor, facilitating breast-conserving surgery. With induction chemotherapy, 75% of the patients have a reduction in tumor size greater than 50%. Preoperative chemotherapy increases breast conservation rates, but also increases the rate of local recurrence. However, local recurrence is not increased as long as surgery remains part of the treatment, even after complete tumor regression. Mastectomy may be the best option in the case of poor response to induction chemotherapy, or based on patient preference.

Induction Endocrine Therapy Induction endocrine therapy (tamoxifen with or without aromatase inhibitors) is less effective than chemotherapy and may be most appropriate for older patients not willing to accept chemotherapy-related toxicity. Patients with hormone receptor–positive LABC are generally best served by combined induction chemotherapy and endocrine therapy following surgery.

Induction tissue-targeted therapy There are few solid data about the use of tissue-targeted therapy (trastuzumab) as induction therapy. Because of the benefit of adding trastuzumab to adjuvant chemotherapy in early stage breast cancer, 12 months of postoperative trastuzumab is recommended for patients who have LABC with ErbB2 overexpression.

1.5.3.2 Local therapy

Tumor response to induction chemotherapy determines local therapy, such as surgery (mastectomy or breast conserving surgery), radiation therapy, or both. Data from uncontrolled prospective studies indicate that 50 to 90% of women with LABC can be successfully treated with breast-conserving surgery after induction chemotherapy. In patients whose cancer does not respond to induction chemotherapy, surgery is appropriate only if a complete resection can be attained. Extensive lymph node involvement (i.e., more than three axillary, internal mammary, or clavicular nodes), residual pathologic tumors larger than 2 cm, multifocal residual disease, and lymphovascular invasion increase the rate of local recurrence following breast-conserving surgery after induction chemotherapy and, therefore, warrant mastectomy. Most patients presenting with LABC have clinically positive lymph nodes and require ALN dissection. In patients with LABC and clinically negative nodes, SLN biopsy following induction chemotherapy has been shown to have a similar detection rate as in early-stage breast cancer without induction chemotherapy. Even in patients who have clinically complete remission with induction chemotherapy, radiation therapy following surgery decreases the local recurrence rate.

1.5.3.3 Inflammatory breast cancer

Inflammatory breast cancer is relatively rare and is characterized by diffuse erythema and edema (peau d'orange), no palpable mass, early age at diagnosis, poor nuclear grade, negative hormone–receptor status, and poor survival outcome. Management is similar to that of non inflammatory LABC; however, because of the aggressiveness of inflammatory breast cancer, SLN biopsy and breast-conserving surgery are not recommended. After induction chemotherapy, patients are usually treated with mastectomy followed by chest wall radiation.

1.5.4 Stage IV: Metastatic

Some women, including those who relapse after treatment of early-stage breast cancer or LABC, will present metastatic disease. Five-year survival is attained in only 23.3% of these patients; therefore, it is important to understand the patient's treatment goals. Radiation therapy or bisphosphonates, along with endocrine therapy or chemotherapy, can ease pain from bony complications. Systemic treatment depends on hormone receptor status, rate of disease progression, and patient willingness to tolerate adverse effects of treatment. Endocrine therapy is generally better tolerated than chemotherapy. In women with rapidly progressive disease, it may be better to treat with chemotherapy, which is more likely to induce a timely response. Trastuzumab with or without chemotherapy is a reasonable choice for the initial treatment of metastatic disease overexpressing ErbB2. Trastuzumab can be used in combination with endocrine therapy for susceptible tumors.

1.5.5 Recurrent breast cancer

Following initial treatment, breast cancer can recur locally, regionally (nodes), or at distant metastatic sites. Approximately up to 20% of patients treated with adjuvant therapies develop locoregional recurrence within 5 - 10 years, respectively.

Locoregional recurrence is an indicator of an aggressive tumor, and early recurrence carries a poor prognosis. Recurrence without clinical metastases has a five-year survival of approximately 40%. Mastectomy is indicated for in-breast tumor recurrence after breast-conserving surgery, followed by repeat axillary staging. SLN biopsy is thought to be acceptable if lymph nodes were not removed initially and if there is no clinical evidence of lymph node involvement, although RCT are lacking.

Wide local excision of the recurrent tumor is recommended for an isolated chest wall recurrence. If unresectable, induction chemotherapy may facilitate successful local treatment. If there is evidence of axillary involvement without distant metastases, axillary evaluation is recommended. Radiation therapy is recommended only in the setting of inoperable or incompletely resected recurrent disease. The benefit of adjuvant systemic chemotherapy for patients with recurrence is uncertain, and a large randomized trial is underway. Until results are available, chemotherapy is recommended for recurrent cancer; endocrine therapy is recommend for hormone receptor–positive cancer; and trastuzumab is recommended for tumors overexpressing ErbB2.

1.6 Conclusions

Breast cancer is the most frequent cancer among women. Its classification depends on the type of tumor, location, extension to the lymph nodes, histology, etc. Based on that, at present, there are several different therapeutic approaches, that were reviewed in this chapter. The clinical decision depends on a multi disciplinary discussion between oncologists, surgeons, radiation physicians, and eventually gynecologists and other imaging specialists that may need to be involved.

RT is of utmost importance in actual standards for breast cancer treatment and it is adopted in different stages of the disease.

Chapter 2

Fundamentals of Radiotherapy

2.1 Context and goals

In the first part of this chapter, the basics about a linear accelerator are put forward. Then, the external beam RT techniques explored in this thesis as well as the main concepts underlying the RT fundamentals are presented. The dose calculation methods are also briefly introduced. Finally, some highlights on the vast theme of dosimetry are presented.

2.2 The modern medical linear accelerator

The medical linacs are cyclic accelerators that accelerate electrons to kinetic energies from 4 up to 25 MeV using non–conservative microwave radiofrequency (RF) fields.

The electrons are accelerated in structures called accelerating waveguides. The high power RF fields used for electron acceleration in the accelerating waveguides are produced through the process of decelerating electrons in retarding potentials in special evacuated devices called magnetrons and klystrons.

A typical modern high energy linac has two photon energies (6 MV and 15–18 MV) and several electron energies (e.g. 6, 9, 12, 15, 20 MeV).

2.2.1 General description of an electron linear accelerator

Linacs are machines as presented in figure 2.1. This linac is a Trilogy 2300 CD Varian Medical Systems equipment.

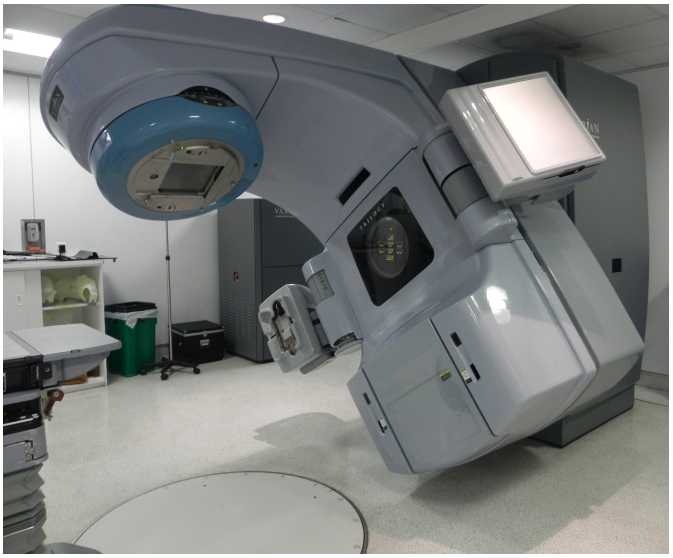

FIGURE 2.1: Example of a linac used in radiotherapy departments for clinical use.

They are typically mounted isocentrically and are mainly constituted by five major sections:

- computer control system;
- modulator cabinet;
- RF module and Stand drive;
- gantry;
- treatment couch.

In figure 2.2 a simplified scheme of the constitution of a linac is presented.

The main components for the beam production of a modern medical linac are:

- injection power;
- RF power generation system;
- accelerating waveguide;
- auxiliary system;

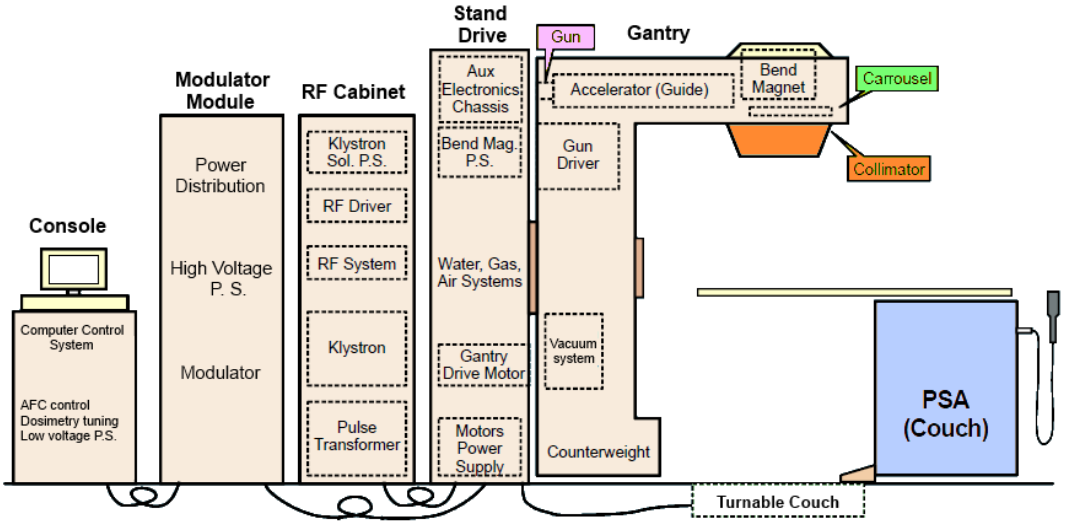

FIGURE 2.2: Simplified scheme of a medical linac used in RT. Image from Varian Medical Systems, Palo Alto, CA

- beam transport system; and
- beam collimation and beam monitoring system.

The injection system is the source of electrons and consists of a simple electrostatic accelerator called *electron gun*. Electrons are thermoionically emitted from the heated cathode towards the perforated anode through which they drift to enter the accelerating waveguide.

The acceleration of electrons in the medical linac is achieved through the application of microwaves (produced by the RF power generation system: RF power source and pulse modulator) that are confined and structured by the use of a waveguide. The input microwaves are generated through use of a klystron and are typically in the 3000 MHz range. The auxiliary system comprises four independent systems:

- vacuum pumping;
- water cooling for the accelerating guide, target, circulator and RF generator;
- optional air pressure systems; and
- shielding against leakage radiation.

Electrons originating in the electron gun are accelerated in the accelerating waveguide to the desired kinetic energy and then brought, in the form of a pencil beam,

through the beam transport system into the linac treatment head, where the clinical photon and electron beams are produced. The beam transport system includes bending and steering magnets, where to electrons emerging from the accelerating waveguide are directed to. In the case of the Varian linac series used for this work, the electrons are directed 270° toward the target (in case of photon production) or to the electron collimation system (for clinical electron beam production). This bending magnet system permits to filter out and prevent low energy contaminant electrons from reaching the target and allows a more compact accelerator design.

2.2.2 Production of X-rays

The linac head contains several components that influence the production, shaping, localizing and monitoring of the clinical photon or electron beams. Modern linacs are typically equipped with: several retractable x–ray targets; flattening filters and electron scattering foils; primary and adjustable secondary collimators; dual transmission ionization chambers; a range finder and a light to observe the field projection; retractable optional wedges and multileaf collimator (MLC). A simplified scheme of the linac head is presented in figure 2.3.

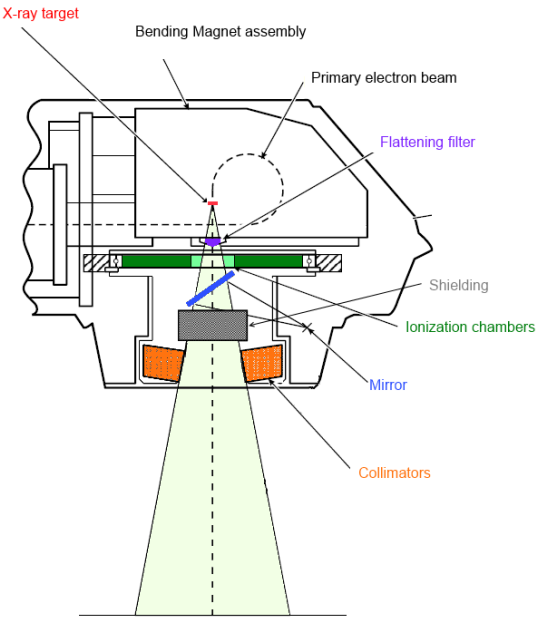

FIGURE 2.3: Simplified scheme of a medical linac head. Image adapted from Varian Medical Systems, Palo Alto, CA.

The primary electron beam enters the treatment head of the linac to be adapt into a therapeutically useful beam.

X-rays are produced from the accelerated electron beam predominantly through the bremsstrahlung process within a target placed in the electron beam path. The x–ray spectra generated depends strongly on the atomic number (Z) and thickness of the target. Actually, it is frequent to use targets made of two layers, the first with a high Z (tungsten, W or molybdenum, Mb) with an adequate thickness not to attenuate the average energy of the photons, and a second with a low Z (copper, Cu or aluminum, Al) to absorb the electrons produced and reduce their contribution. Flattening filters have low Z irrespective of beam energy. Nowadays, tungsten is commonly used in the first layer for both its high atomic number and resistance to heat deformation. The ability to resist heat deformation is important since in a typical tungsten target only about 1% of the incident electron energy emerges as bremsstrahlung photons. The remaining energy is lost to heat in the target. The heat is dissipated by the accelerator's cooling system. Copper is fused to the downstream face of the tungsten slab and placed in thermal contact with the accelerator's cooling system to aid in the heat dissipation and reduce secondary electron production.

Primary collimation of the photons emerging from the bremsstrahlung target is performed using a tungsten collimator. The conical beam exiting the primary collimator is cylindrically symmetric about the beam's central axis.

Bremsstrahlung photons emerging from the electron target and primary collimator are highly forward peaked, that is, the beam contains a significantly higher intensity of high energy photons directed along the beam's central axis.These forwardly-peaked photons will subsequently bombard a copper flattening filter. The flattening filter flattens the dose profiles in a water phantom under specific reference conditions [30]. The combination of target thickness/composition with flattening filter shape/composition gives rise to the spectral and penetration properties of the beam. In fact, different (in dimension and material) targets and filters are used for different energies.

2.2.3 Shaping, flattening and monitoring the beam

The photon beam collimation is achieved with the following collimation systems:

- primary collimator;
- secondary movable user-defined collimators; and
- MLC (optional)

The beam shaping takes place within the treatment head using a series of collimators. The primary collimator affects initial collimation of the bremsstrahlung photon beam before the photons reach the flattening filter.

The beam's symmetry, instantaneous dose rate and integral dose rate are all monitored using a gas filled transmission style ionization chamber. The chamber is divided into sectors to allow acquisition of beam balancing symmetry measurements. These measurements allow the feedback of alignment corrections to electron beam steering magnets located upstream within the bending magnet and accelerating waveguide structures.

Secondary beam collimation occurs on the flattened beam (photon and electron) using paired sets of tungsten blocks (jaws) and is intended to provide large area collimation of the beam to approximate treatment field sizes. The Trilogy Varian linac contains 2 sets of orthogonal adjustable opposed jaws, positioned after the flattening filter, capable of collimating the field into rectangular fields over a range from 3 cm up to 40 cm. Each jaw is limited to ± 20.0 cm of travel from the beam's central axis thereby allowing a maximum field size of $40.0 \times 40.0\ cm^2$ at a distance of 100 cm from the target.

2.2.4 Multileaf collimators (MLC)

Irregular shaping of the beam is performed with a multileaf collimator (MLC). These devices are made of several units, called *leaves*, organized side-by-side, in two opposed banks. Each leaf is controlled independently and the control of each leaf (driven independently by motors) allows complex outlines to be defined.

The tungsten leaves (located downstream of the secondary collimator) from the Varian Millennium MLC are shown in figure 2.4.

For radiotherapy delivery of some brain cancers (astrocytomas, glioblastoma multiforme, gliomas, etc.) and small cell lung cancers, MLC can be used in a process known as stereotactic radiosurgery. Such devices consist of narrow leaf banks ($\leq$ 2.5 mm width) driven by precision motors capable of highly precise delivery of radiation.

In our Trilogy Varian linac, such a MLC is installed with inner leaves of 2.5 mm and outer leaves of 5.0 mm projected at 100 cm. This MLC is the newest Varian MLC, the High-Definition with 120 leaves. This MLC permits a maximum MLC-defined field of 40 x 22 cm^2 at a distance of 100 cm from the target.

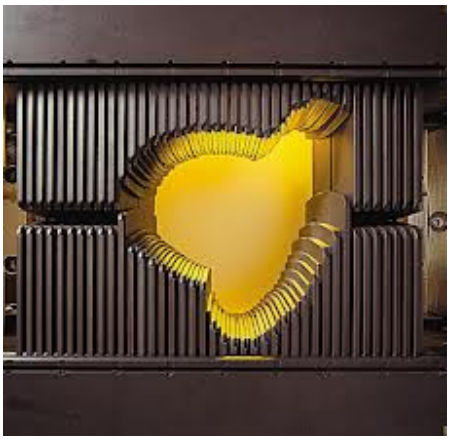

FIGURE 2.4: A Varian Millenium multileaf collimator with a leaf arrangement. Image from Varian Medical Systems, Palo Alto, CA

2.3 External Beam Radiotherapy

The purpose of external beam RT (EBRT) is to treat cancer by delivering the maximum dose of x-rays produced by linear accelerators (linac) to the tumor, sparing as much as possible the healthy tissues in the vicinities. Radiotherapy makes use of complex processes after the acquisition of the anatomic information of the patients before their treatment in the linac. The planning is an essential step in RT to define all the ballistic irradiation details such as the number of monitor units (MU) or the treatment time, the type of particles (photons and/or electrons) and the energy of the beams. The treatment plan is carried out using a computerized system (treatment planning system, TPS) which contains at least one algorithm[1] for dose calculation. In theory, these algorithms should be able to account for all the physical phenomena that are involved in the dose calculation in the patient. Nowadays, they are able to perform dose calculations in two modes: in *homogeneous* mode without tissue density correction; and in *heterogeneous* mode taking into consideration the effect of the heterogeneous tissues. The dosimetrist or radiophysicist uses the system for planning the treatments in an interactive way to calculate the dose distributions, optimize the beams orientations and the shape of the irradiation fields. After the radiophysicians' treatment plan approval, the treatment time is calculated according to the validated dose prescription. Then, the irradiation parameters and the reference images (Digitally Reconstructed Radiographs, DRR) are sent from the TPS to the linear accelerator through a management software able to track the parameters and all the irradiation actions, the OIS (Oncology Information System).

[1]algorithm: step-by-step finite procedure developed to solve a mathematical problem that frequently involves the repetition of an operation and may involve computer science to speed up the calculations

2.3.1 3D Conformal RT

Using 3D Conformal RT (3D CRT), the planning is made using static beams, in 3D CT images. In this kind of treatment plan, there is conformation to the target volumes and the beam incidences are chosen in order to guarantee an adequate irradiation of the target volumes and to avoid the OAR. This conformation is better achieved using the MLC. The MLC is fixed for each beam even though external beam modifiers (such as wedges) may be used.

2.3.2 Conformal RT using Modulated Intensity IMRT

Conformal RT using Modulated Intensity, IMRT, is a RT technique that consists in delivering the dose to the target volume by varying the intensity inside each beam (figure 2.5). This technique envisages increasing the dose to the target volume, to decrease the dose in the tissues in the vicinities of the irradiation target, to obtain an improved conformation of the delivered dose and, eventually, to obtain a more homogeneous dose distribution with the target volume. The most significant examples are the prostate and head and neck tumors [31, 32].

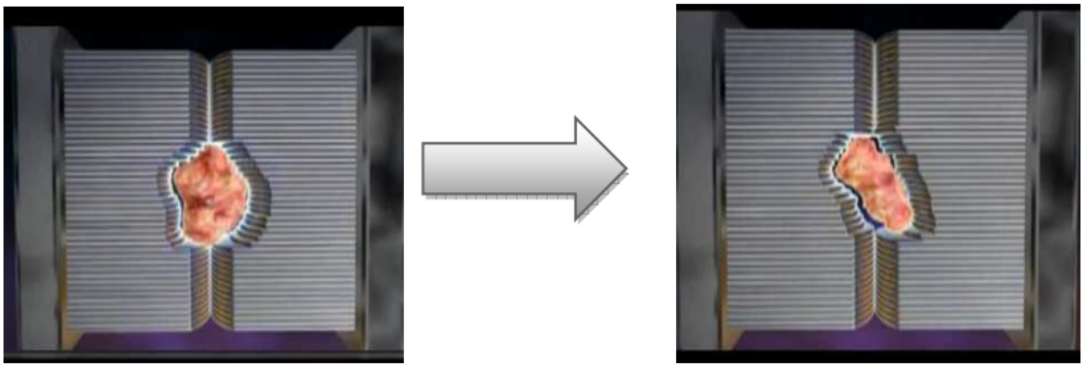

FIGURE 2.5: Modulated movement of the leaves of the MLC to conform, for each beam incidence, to the target volume, represented in red.

2.3.3 Arc Conformal RT

Dynamic conformal Arc RT (DCART) is an EBRT technique that uses the capability of MLC to conform to the target volume during beam on and includes gantry rotation while irradiating. An example is presented in figure 2.6, for a brain pathology. This technique is used in clinical routine for brain radiosurgery and extracranial lesions using stereotaxic RT.

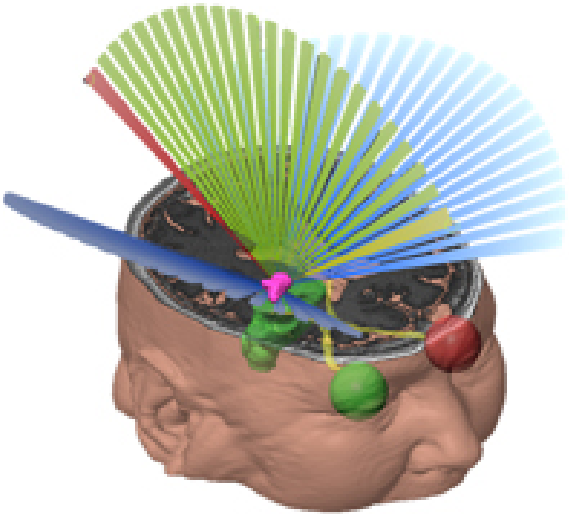

FIGURE 2.6: Dynamic conformal arc RT, DCART. Image from BrainLAB AG, Feldkirchen, Germany.

2.3.4 Planning procedures for RT treatments

The steps and procedures for planning a treatment are, succinctly, the following [33]:

- Choice of the immobilization system that will be adapted to the patient. The patient's position should be set so that it guarantees comfort to the patient and therefore treatment reproducibility during the several sessions and protection of the healthy tissues.
- Acquisition of the anatomic coordinates by a computerized tomography (CT) scanner and transfer of the images to the treatment planning system (TPS). The images are in DICOM (Digital Imaging and Communication in Medicine) format.
- Definition and contouring of the tumor volume(s) and the healthy tissues as organs at risk (OAR).
- Dosimetry encompasses the choice of the beams, energy, incidences, weight, conformation of the beams to the target volumes with the multileaf collimator and possible use of beam modifiers (wedges, bolus, etc).
- Dose calculation and dosimetric optimization which need the choice of the dose calculation algorithm, determining the number of monitor units and irradiation time for each beam.

- Evaluation of the treatment plan and dosimetric optimization. The treatment plan validation is performed by visual analysis of the dose distribution and evaluation of the dose-volume histogram (DVH), see subsection 2.3.6.
- Verification of the calculation of the monitor units for each field of the treatment plan; transfer of the treatment plan to the treatment machine.
- Positioning the patient in the linac.

2.3.5 ICRU recommendations for EBRT

The radiation oncologist uses all the clinical data available of the patient's tumor, such as histopathology, surgery, fibroscopy and radiological information to define the target volumes and the OAR. The target volume location can be determined in the CT, magnetic resonance imaging (MRI), and/or positron emission tomography (PET) images.

The definition of the target volumes and concepts of security margins were introduced by the International Commission on Radiation Units and Measurements, in the reports ICRU50 and ICRU62 [34, 35]. These reports are dedicated to the dose prescription, administration and aspects related to EBRT with photon beams.

2.3.5.1 Definition of the target volumes and security margins

Figure 2.7 represents the tumor volumes, the volume to treat and the irradiated volume. As target volumes, the recommendations indicate that the following target volumes should be contoured:

- GTV (Gross Target Volume): represents the macroscopic volume of the primary tumor, visible in the diagnostic images.
- CTV (Clinical Target Volume): a margin is given to the GTV to take into account the subclinical involvement of microscopic dimensions, considering the biologic features of the tumor and the metastasis ways.
- PTV (Planning Target Volume): it is a geometrical concept that accounts for all the geometric uncertainties and other uncertainties that may occur (due to positioning or respiration, for instance), to guarantee the prescribed dose is administered homogeneously to the CTV. Its shape depends not only on

the CTV but also on the internal movements of the organs (such as, cardiac movement, breathing, peristaltic movements, and so on) and the tumor, as well as the treatment technique used, which will affect the beam orientations and the patient immobilization.

Despite these volumes, ICRU also defined other non-anatomical volumes, based on the dose distribution and used for evaluation and plan optimization:

- Treated volume (TV): volume that receives at least the reference dose planned. It is usually delineated after the planning and verification of the irradiation parameters. It should permit the evaluation of possible recurrence causes (close or outside the target volume) and the complications in the normal tissues, usually located outside the PTV but within the treated volume.
- Irradiated volume (IV): tissue that receives a significant dose taking into consideration the tolerance dose of the OAR. This volume does substantially depend on the treatment technique used and this volume is usually increased with the number of fields. It is the radiation oncologist responsibility to choose the most adequate irradiation plan.

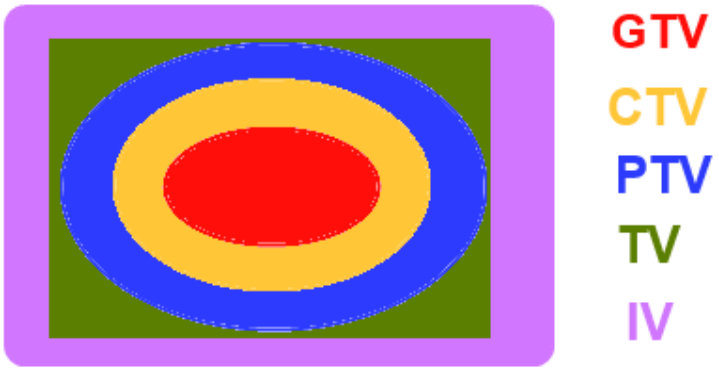

FIGURE 2.7: Schematic representation of the target volumes designation, as defined in ICRU Reports 50 and 62.

2.3.5.2 Organs at risk

The OAR or critical structures which are normal tissues with functional properties, adjacent to the target volume, can be included in the radiation fields. The radiation can irreversibly affect the normal function of these organs. Taking this

into consideration, it is important that these organs receive the lowest possible dose.

The total dose an organ receives, as well as the exposed volume to a determined dose are two important variables that can be used to predict the risk of late toxicity [36]. The late effects depend on the tissues irradiated, which can be categorized into:

- organs in series, whose complete functionality can be compromised even if a small portion receives more than the dose limit (eg. medulla, optic chiasm, optic nerve);
- organs in parallel, in which the damage in a part of an organ does not compromise its total function, unless a large volume of the organ is included within all the radiation fields (eg. liver or lung);
- a combination of both models: being a series-parallel structures (eg. heart, in which the coronary arteries are parallel and the myocardium is considered to be series).

The radiotherapy treatment aims at controlling locally the tumor, minimizing the acute and late effects due to radiation - *therapeutic ratio* concept. The goal of the treatment is often reached at some cost, considering the damage inflicted to the normal tissues, being essential to balance between guaranteeing that the tumor cells receive a lethal radiation dose and the secondary effects are tolerable [37].

The tolerance of different tissues and organs may vary, being the incidence and magnitude of the radiation induced complications dependent of some risk factors:[36–39]

- treatment related: total dose, dose per fraction, dose-volume relation (percentage of organ that receives a determined dose), dose rate, beam energy, treatment volume, technique used, radiation protector or other biologic modifiers, concomitant chemotherapy, time between fractions and treatment for re-irradiation patients;
- patient related: existence of other diseases (diabetes, hypertension, pre-existence of coronary or pulmonary disease, etc), radiation response and age;
- organ related: organs functionality, specific tissue radio-sensibility, organ functionality or loss before irradiation, development of severe acute toxicity

(leading to late effects), regional variation of radio-sensibility within an organ and its hierarchy organization;

- tumor related: type of treated tumor, its extension and influence on adjacent organs.

The OAR can be classified into three categories:

- Class 1. critical organs, susceptible to severe lesions that may cause death or severe morbidity;
- Class 2. OAR whose lesion can cause low to moderate lesion; and
- Class 3. OAR whose lesion may cause no or transitory morbidity.

2.3.6 Dose volume histograms

The dose volume histograms (DVH) are quantitative evaluation tools relating the dose and the contoured volumes. The x axis represents the dose received by a structure, in absolute dose or in %. The y axis represents the proportion of the total volume of the structures that receive a specific dose. The proportion of the volume is expressed in % or cm^3. They are used to estimate the dose each organ/structure receives during the RT treatment.
The DVH represents the relative or absolute volume of a structure that receives a dose equal or superior to a defined dose. Figure 2.8 presents a typical cumulative DVH used in routine for the planning in RT. The analysis of the HDV permits to compare: the average dose , the minimum dose, the maximum dose, the volumes (expressed in % or cm^3) that receive at least a determined dose (V_{dose}), and the dose (expressed in % or Gray) received by a given volume, expressed in percentage of target volume (D_{vol}).

2.3.6.1 Tumor volume analysis

The ideal treatment plan is characterized by 100% of the treatment volume receiving 100% of the prescribed dose. In fact, there is always a part of the volume that receives less or more than 100% of the prescribed dose. According to the ICRU there may be considered two volumes:

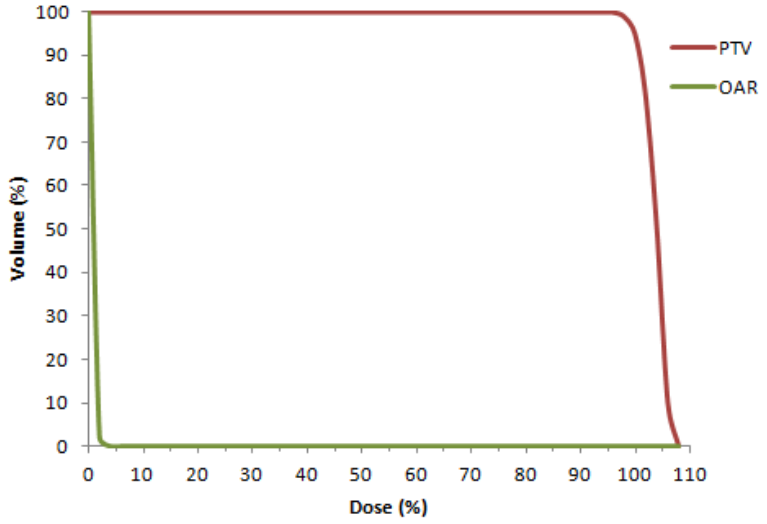

FIGURE 2.8: Typical DVH aimed for adequate PTV coverage.

- under dose volume - tumor volume receiving less than 95% of the prescribed dose;
- over dose volume - tumor volume that receives more than 107% of the prescribed dose.

2.3.6.2 Organs at risk analysis

Against to what was the PTV goal, the OAR should receive the minimum possible dose, as represented by the green curve in figure 2.8. The decision to choose a plan versus another is very often made based on the OAR analysis and the lower dose in the OAR may be preferred to a better PTV coverage. The decision depends on the radiation oncologist criteria.

2.3.7 The importance of accuracy in radiation delivery

Research efforts over the past decade have focused on techniques to minimize the normal tissue exposure during an EBRT treatment. The importance of accuracy in radiation delivery is most apparent by observing the probability of local tumor control and normal tissue complications as a function of the absorbed radiation dose in tissue. Predictive models derived from average population radiation therapy responses are shown in figure 2.9. From this figure, tumor control probability

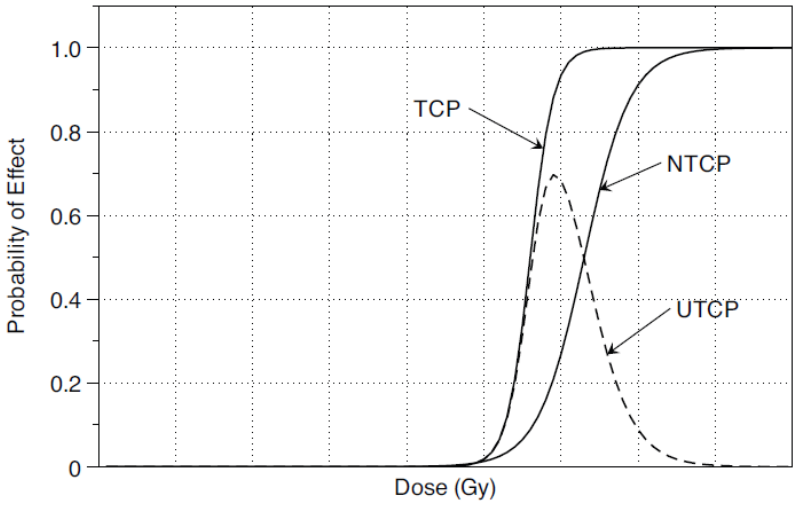

FIGURE 2.9: Qualitative plot depicting the predictive models of tumor control probability (TCP), normal tissue complication probability (NTCP) and uncomplicated tumor control probability (UTCP) with absorbed dose to tissue.

(TCP) is shown to sharply rise (sigmoid shape) starting from a particular absorbed dose. The normal tissue complication probability (NTCP) rises sharply at a slightly higher absorbed dose. A desirable radiotherapy plan is one that maximizes TCP while minimizes NTCP.

The highly sensitive nature of the TCP and NTCP dose responses combined with the potentially small differences in dose response curves demonstrate the need for accuracy in radiation delivery. Small differences in absorbed dose can be seen to have substantial effects on the treatment's TCP and NTCP outcomes. The uncomplicated tumor control probability (UTCP) is also plotted in figure 2.9. UTCP represents the probability of achieving local tumor control while having no complications and is simply calculated as TCP $\times$ (1-NTCP).

It should be noted that the standard deviations of TCP and NTCP predictive models have been estimated as high as 15-20%. In addition, the shapes and positions of the curves may vary between patients and/or tissue type. Recent radiobiological research is aimed at improving the understanding of factors affecting the TCP and NTCP functions of various patient and tissue response classes. A better understanding of patient dose response may allow adjustments of prescribed treatment doses based on individual patient dose response evaluation. There is also an individual variability in the dose response. With the development of molecular biology, the aim is to perform tailored-to-patient RT.

2.3.8 Errors in RT

The errors in RT can be of two types:

- systematic: occur when a patient is set up using an incorrect positioning information. This could be because information has been entered incorrectly into the record/verify system, or for instance, due to inaccurate determination of the isocenter in the bunker, or incorrect positioning of the lasers in the bunker.
- random: occur when the patient's position is incorrect due to daily fluctuations - for instance, the bladder is a bit fuller than the day before, or the temperature in the bunker is slightly different so the immobilization devices have a minor change in their size. Random errors fluctuate around a certain point.

2.3.9 Main dose uncertainties related to the TPS

The real dose delivered to the patient is not exactly the same as calculated by the TPS. There are uncertainties in the dose calculation that can be associated to the patient positioning and the organ's mobility, the mechanical uncertainties related to the linac (calibration of the different possible movements and distance source to the patient skin, field size, dose calibration of the machine) and the dose calculation mode in the TPS. These uncertainties are resumed in the IAEA 2004 Report, table 19 [40] and presented in table 2.1.

In 1999, Ahnesjö and Aspradakis evaluated the present and the envisaged uncertainties, in the future, in percentage for the dose delivered to the patient during the complete treatment course, using photon beams [41]. Their evaluation is presented in table 2.2.

Considering the authors' analysis, if the dose calculation is 1.0%, the overall uncertainty increases 0.1-0.2%; however if it is about 4.0%, the overall uncertainty can be 1.6% to 2.3% higher. The dose calculation uncertainty is, therefore important to decrease the overall uncertainty associated to RT treatments.

	Uncertainty consideration
Basic beam data	Measurement uncertainties (detector reading reproducibility) Detector resolution Detector sensitivity
Input–output devices	Digitizer co-ordinate location uncertainties Generation of contours from CT films Density assumptions when CT films are used for contours Image display resolution Inaccurate location of isodose lines on the display (an inaccurate display could result in an inaccurate placement of beams)
Data transfer	Inaccuracies relate to how the software writes and reads the data, especially for CT and MR scanners
Individual patient data	Reproducibility of patient set-up Organ motion during the different steps of the planning and treatment process Use of different imaging modalities, each with their own capabilities and limitations, for example MR distortions
Target volumes and beam parameters	Inter- and intra-observer variability in defining target volumes (different target volume definitions could result in a different choice of field sizes or even different optimization techniques)
Dose calculation limitations	Algorithms provide an approximate solution to complex physics Accuracy varies depending on the circumstances Deviations tend to be systematic Choice of calculation parameters such as grid spacing and pencil beam size have a significant impact on accuracy
Plan evaluation limitations	DVH accuracy is affected by the accuracy of volumes or doses DVH accuracy is dependent on the number and location of points used for DVH determination

TABLE 2.1: Main uncertainties related to the TPS [40].

	Present technique $100 \times \Delta D(1\sigma)/D$	Future development $100 \times \Delta D(1\sigma)/D$
Absorbed dose determination at the calibration point	2.0	1.0
Additional uncertainty for other points	1.1	0.5
Monitor stability	1.0	0.5
Beam flatness	1.5	0.8
Patient data uncertainties	1.5	1.0
Beam and patient set-up	2.5	1.6
Overall excluding dose calculation	**4.1**	**2.4**
Dose calculation	1.0 2.0 3.0 4.0 5.0	0.5 1.0 2.0 3.0 4.0
Resulting overall uncertainty	**4.2 4.6 5.1 5.7 6.5**	**2.4 2.6 3.1 3.8 4.7**

TABLE 2.2: Evaluation if the uncertainties of the dose delivered to the patient during all the sessions of the radiotherapy treatment [41].

2.4 Dose calculation methods

2.4.1 Concepts and physical quantities in medical radiation physics

The photons from a linac yield a cascade of interactions, not only in the patient but also in the treatment machine itself before the energy is absorbed as dose.

The primary photons energy is absorbed without previous interactions; scattered photons change their initial trajectory after one or several interactions. The most preponderant interactions of the high energy photons within the tissues is through the Compton effect. When treating with photons, the depth dose contributions are due to:

- primary photons radiant from the target (in the linac head);
- scattered photons originated in the linac head;
- photons scattered in the patient; and
- contaminant electrons from the linac head.

These different components deposit their energy contributing to the dose delivered, as represented in figure 2.10.

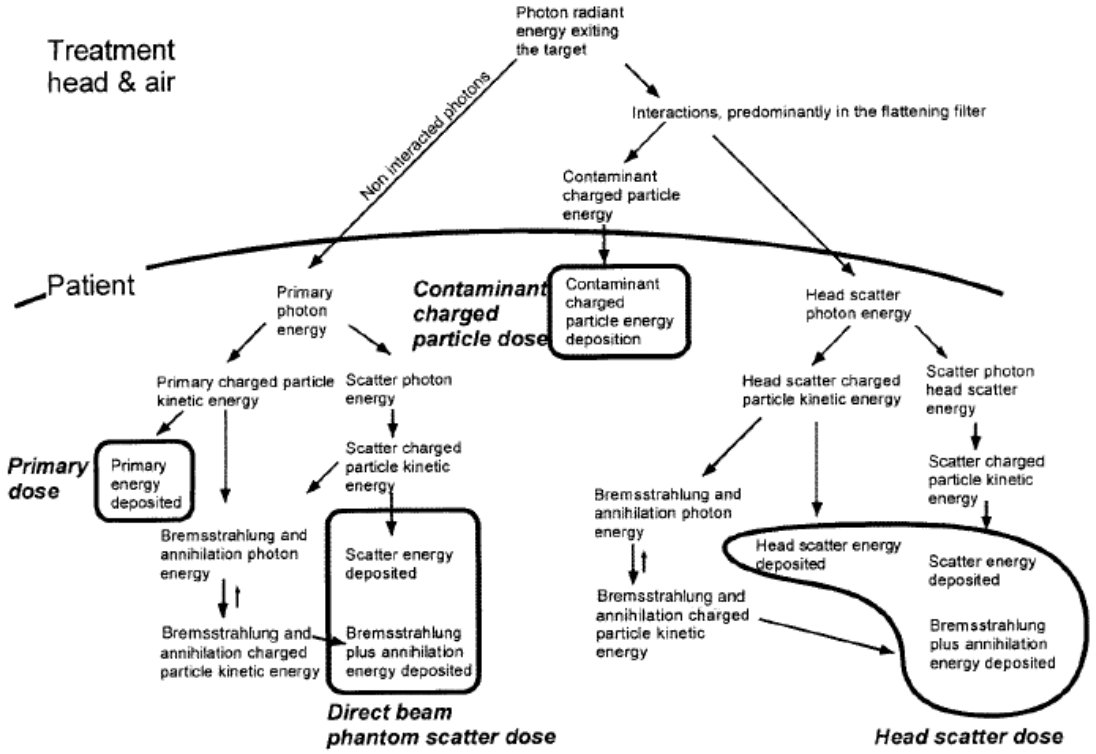

FIGURE 2.10: Interaction history of the four dose categories commonly referred to in dose calculations for treatment planning — primary dose, phantom scatter dose, contaminant charged particle dose and head scatter dose [41].

Physical quantities in medical radiation physics

Dose: is the absorbed energy (dE) per mass unit (dm), measured in Gy:

$$D = \frac{dE}{dm} \tag{2.1}$$

TERMA (Total energy released per unit mass): quantifies the total energy released per mass unit, in J/kg or gray (Gy). It is characterized by the linear attenuation coefficient[2], measured in cm^{-1}. It depends on the energy (E), the density (ρ) and the atomic number (Z):

$$TERMA = \Psi \left(\frac{\mu}{\rho} \right), \tag{2.2}$$

where Ψ is the energetic fluence of the beam.

KERMA (Kinetic energy released per unit mass): is the kinetic energy released and transferred from photons to the charged particles, in elemental mass of the medium dm, measured in Gy. It is characterized by the linear transfer coefficient in energy, measured in cm^{-1}.

$$K_{air} = \Psi \left(\frac{\mu_{tr}}{\rho} \right)_{air} \tag{2.3}$$

Monitor Unit (MU): in EBRT, the linac delivers the dose to the patient in this unit. The linear accelerator is calibrated to deliver a certain dose in reference conditions, which may be, for instance: 1 UM = 1 cGy for a 10×10 cm^2 field, at a source detector distance of 100 cm, at the maximum dose depth.

Beam interaction properties in a homogeneous medium

For dosimetry purposes, a water phantom is the basic element to investigate the beam properties for the treatment machine calibration and TPS configuration according to these properties. Several regions can be defined, as presented in figure 2.11.

Region:

[2] linear attenuation coefficient: interaction probability of the particle by path unit

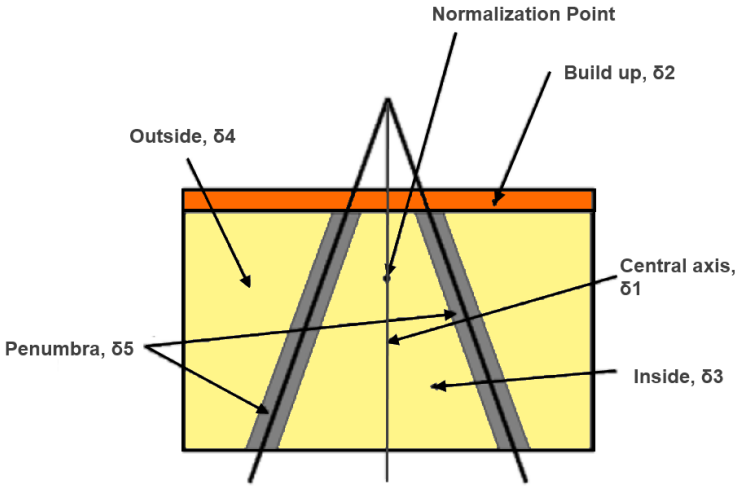

FIGURE 2.11: Definition of the different regions of a beam, according to the dose gradient in each region.

- $\delta_1$is for data points on the central beam axis beyond the depth of d_{max}, the high dose and small dose gradient region;
- δ_2 for data points in the build-up region, in the penumbra, and in regions close to interfaces of inhomogeneities: the high dose and large dose gradient region;
- δ_3 for data points beyond d_{max}, within the beam but outside the central beam axis: again this region is a high dose and small dose gradient region; and
- δ_4 for data points off the geometrical beam edges and below shielding blocks, generally beyond d_{max}: the region is a low dose and small dose gradient region, for instance below 7% of the central ray normalization dose.

Profiles determined in these regions look like those presented in figure 2.12 [42].

The process of energy deposition in the tissues can be divided into two steps, analyzing figure 2.12a:

1. *build-up*: represents the dose longitudinal electronic equilibrium achievement, related to the secondary electrons' displacement. The higher the energy is, more energy is transferred to the electrons, the further away occurs the maximum dose.
2. exponential decrease, according to the different attenuation coefficients of the traversed media.

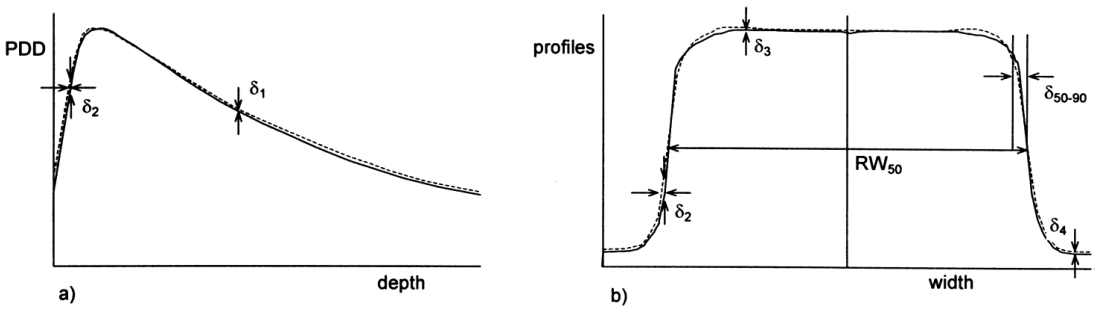

FIGURE 2.12: Representation of the different regions for comparison of measured and calculated dose: a. depth dose profile; b. dose profile [42]. δ_{50-90} is the distance between the 50% and the 90% point (relative to the maximum of the profile) in the penumbra, which is sometimes called 'beam fringe'; RW_{50} is the radiological width, defined as the width of a profile measured at half its height compared to the value at the beam axis.

When a photon beam interacts in a medium, the beam energy transfer to the electrons does not occur at the level of the photon with matter. This is due to the free mean path of the secondary electrons produced. In an ideal situation, in a medium, the energy losses due to the electrons that leave the volume of interest are compensated by the energy entering associated to the particles arriving from other sites: this phenomena is the condition of electronic equilibrium. However, the electronic equilibrium is not fulfilled at all points.

Beam interaction properties in a heterogeneous medium

At the surface or near the surface of a new medium, the energy absorbed is lower than the transferred energy (collision kerma): there is lack in electron equilibrium between the charged particles entering and exiting the region of interest. At a characteristic depth of the beam energy, the two components compensate: the collision kerma K_c is equal to the absorbed dose D. The equilibrium ratio or transitory equilibrium is characterized by the relation:

$$\beta = \frac{D}{K_c} \tag{2.4}$$

About the yield in depth, the electronic disequilibrium arises at the region of formal electronic equilibrium and the dose increases before the exponential decrease. Typically for the depths between the surface and the depth of maximum dose, there is $\beta \leq 1$ or $\beta \geq 1$. The degree of electronic equilibrium in the beam axis decreases with the field size.

This phenomena occurs at the air-skin interface and in the interfaces between different media with different densities composing an heterogeneous anatomic volume. The low density causes an increased flux of scattered photons and secondary electrons. This leads to a dose decrease in the nearby tissues, which depends on the energy and on the geometry and size of the beams.

2.4.2 Precision and tolerance of the dose calculation by an algorithm

The accurate and fast calculation of a 3D dose distribution within the patient is one of the most central procedures in modern radiation oncology. It creates the only reliable and verifiable link between the chosen treatment parameters, and the observed clinical outcome for a specific treatment technique, i.e., the prescribed dose level to the tumor, the number of therapeutic beams, their angles of incidence and a set of intensity amplitudes result in a distribution of absorbed dose which is the primary physical quantity available for an analysis of the achieved clinical effects of this specific treatment.

The dose calculation algorithms have twofold application:

- plan optimization in the treatment planning process; and
- establish the correlation between treatment parameters and clinical outcome.

They also have two conflicting goals in what the dose calculation is concerned:

- it has to be fast enough so that the treatment planning process can be accomplished in clinically acceptable time frames; and
- the result of the calculation has to be sufficiently accurate so that meaningful and reliable correlations between delivered dose and clinical effects are obtained.

The dose calculation algorithm should calculate the dose with good accuracy, as well as take into count the physical processes and the primary and secondary particles transport, to consider the patient tissue heterogeneities and at the interface tumor-tissue. The dose calculation accuracy depends directly on the accuracy of the algorithms' dose calculation which are implemented in the TPS. Their are meant to calculate the spatial dose distribution in the patient according to the radiation oncologists' dose prescription and the dosimetrist choices for planning the

treatment. The TPS contains the specific geometric and dosimetric characteristics (PDD, profiles, outputs, etc) of each specific linac. For the different regions considered in figure 2.11, Venselaar et al [42] proposed the tolerances and acceptability criteria presented in table 2.3.

Tolerance	(1) Homogeneous, simple geometry	(2) Complex geometry (wedge, inhomogeneity, asymmetry)	(3) More complex geometries, i.e. combinations of (2)
δ_1 (central beam axis data) high dose, small dose gradient	2%	3%	4%
δ_2[a] (build-up region of central beam axis, penumbra region of the profiles) high dose, large dose gradient	2 mm or 10%	3 mm or 15%	3 mm or 15%
δ_3 (outside central beam axis region) high dose, small dose gradient	3%	3%	4%
δ_4 (outside beam edges) low dose, small dose gradient	3%[b] (30%)	4%[b] (40%)	5%[b] (50%)
RW_{50}[a] (radiological width)	2 mm or 1%	2 mm or 1%	2 mm or 1%
δ_{50-90} (beam fringe)	2 mm	3 mm	3 mm

[a] These values are preferably expressed in mm. A shift of 1 mm corresponding to a dose variation of 5% is assumed to be a realistic value in the high dose, large dose gradient region.
[b] This percentage is applicable to equation $\delta = 100\% \times (D_{calc} - D_{meas})/D_{meas}$; the percentages between brackets refer to equation $\delta_4 = 100\% \times (D_{calc} - D_{meas})/D_{meas,cax}$

TABLE 2.3: Proposed values of the tolerances for δ for application in different test configurations [42].

It is inherently difficult to report the specific inner processes of commercial treatment plan optimization algorithms as the material is, in general, proprietary.

2.4.3 Classification of the dose calculation methods

2.4.3.1 Correction based algorithms

In the past, dose calculations for RT used to be performed strictly based on directly measured data such as lateral and percentage depth dose profiles for different field sizes and configurations, measured in water phantoms. These algorithms are being put aside and replaced by other methods.

2.4.3.2 Global methods based on the separation of primary and scattered radiation

This method was, some time ago, used by the TPS. It was developed by Clarkson (1941) [43] and later on by Cunningham (1972) [44, 45]. Cunningham introduced the concept of scatter-air ratio, SAR, that describes the scattered dose in the beam axis at a depth, z, of a square field, with s' width. This method consists in calculating separately the primary and scattered doses by decoupling the fields in circular sectors. The total dose in a point is the primary dose (P) and the scatter dose (S) contributions.

Primary dose calculation

Results from the first interaction of the photons in the phantom, can be mathematically translated by:

$$P = D_A \times TAR(z, 0) \times F, \tag{2.5}$$

, where D_A is the dose in the air;
$TAR(z, 0)$ is the tissue-air ration in the beam axis, at a z depth, extrapolated to a field of null size ($s' = 0$);
F represents the dose variation within the field, taking into account the penumbra.

Scatter dose calculation

Is the dose deposited by photons that interacted with the medium, at least, once. The irradiation field is decomposed in circular sectors with a center defined with an angle $\Delta\theta_i$ and radius r_i. The scattered contribution in a point is the sum of all the n scattered sectors. The SAR is given by:

$$SAR(z, s') = \frac{\Delta\theta}{2\pi} \sum_{i}^{n} SAR(z, r_i), \tag{2.6}$$

$SAR(z, s')$ - air-scatter ratio at the z depth for a s' field size;
$SAR(z, r_i)$- air-scatter ratio at the z depth for a circular field with radius r_i;
n - the number of sectors.

The scattered dose is:

$$S = D_A \times SAR(z, s') \tag{2.7}$$

Total dose calculation

The total dose is the sum of the primary and scattered dose, given by:

$$D(x, y, z) = P(x, y, z) + S(x, y, z) = D_A \times [TAR(z, 0) \times F + SAR(z, s')] \tag{2.8}$$

2.4.3.3 Methods based in fundamental physics

These algorithms calculate the dose deposition from fundamental physical phenomena related to the particles interactions. They take into consideration the anatomic information of the patients such as the geometry ant electronic density. Then can be divided into two categories:

- A. kernel[3] - superposition based models
- B. Monte Carlo methods

A. Superposition-convolution kernel based methods

Definition The convolution methods based in Pencil Beam were proposed in the beginning of the 1980's. These can be Monte Carlo based algorithms [46–50] and the dose is obtained in two steps that involve the calculation of the TERMA and the kernels:

- TERMA: transferred energy by all the primary photons in a unit of mass; and
- kernels: point spread functions, are the energy fraction by volume unit deposited by the secondary particles, photons and electrons.

This method takes into account the dose deposited by all the photon interactions. There are two types of kernels:

- Point Spread Kernel; and
- Pencil Beam Kernel.

1. Point Spread Kernel With this model, TERMA is determined by tracing the radiologic path of the particles along a line through a series of voxels, and given by equation 2.9.

$$TERMA = \frac{\mu}{\rho(x', y', z')} \times \Psi(x', y', z'), \tag{2.9}$$

[3]Kernel or core of energy deposition: describes the distribution of energy deposited in an infinite medium around a primary interaction site, known as *kernel-point*.

, where $\frac{\mu}{\rho(x',y',z')}\times$ is the mass attenuation coefficient of the medium (in $m^2.kg^{-1}$); and
$\Psi(x',y',z')$ is the energetic fluence in the point (in $J.m^{-2}$).

The dose $D(p)$ in a P point with coordinates (x,y,z), is obtained by the superposition of all the kernels at the points $q(x',y',z')$ with dV volume and the corresponding TERMA at point q by equation 2.10.

$$D(p) = \int\int\int T(q) \times K(x-x', y-y', z-z')dVq, \tag{2.10}$$

, where
- T= TERMA;
- K is the kernel; and
- $dVq = dx \times dy \times dz$ is the voxel of elementary volume.

The dose model can be calculated using the Monte Carlo method and generalized considering the spectral variations of the photon beams. Several methods were investigated to speed up the dose calculation, such as the Fast Fourier Technique, FFT [46], and a specific technique called Collapsed Cone Convolution [48].

Dose calculation in heterogeneous media

The application of this model in heterogeneous media is based on the TERMA calculation and scaled in all the poli-energetic point kernels by the average electronic density between the receiving medium ($\vec{r}$) and the source volume ($\vec{s}$) [51], expressed as:

$$D(r) = \sum_{s}^{volume} T(\vec{s})\frac{\rho(s)}{\rho_{water}}c^2(\vec{r},\vec{s}).h_{\rho_{water}}\left(c(\vec{r},\vec{s})(\vec{r}-\vec{s})\right).V_{\vec{s}} \tag{2.11}$$

, where
- $T(s)$ is the TERMA contribution;
- $h_{\rho_{water}}\left(c(\vec{r},\vec{s})(\vec{r}-\vec{s})\right)$ is the (monoenergetic) energy deposition kernel generated in water;
- $c^2(\vec{r},\vec{s})$ is the factor to calculate the mean density along the line between the interaction point and where the dose is deposited.

An assumption made is that the energy transport through the kernel between the interaction point to the dose point occurs through a straight line, i.e., within the kernel, an interval ray tracing is introduced. Along each internal ray, the

contribution of the kernel is scaled with the average electron density encountered along the line connecting the two points - density-scaled dose deposition kernels. The direct application of this is hypothetically represented in figure 2.13. It can be clearly seen that the kernel extends further from the interaction point if the internal energy transport encounters a medium with an electron density smaller than water on its way to the dose deposition point. The dimensions of the scaled dose kernel are shrinking in comparison with the original dose kernel in water if higher electron densities represent an additional obstacle for the energy transport within the dose kernel.

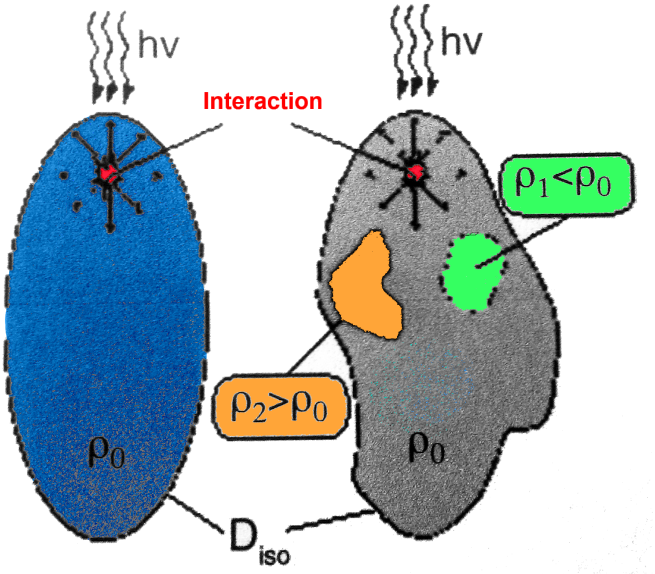

FIGURE 2.13: Isodose curves of density-scaled kernels of the superposition kernel. The tissue inhomogeneities are corrected in the dose kernels leading to a deformation of the isodose lines behind the inhomogeneities. Image adapted from Oelfke et al [52].

2. Pencil Beam Kernel Pencil Beam was introduced by Ahnesjö et al, in 1992 and the basic idea is to decompose the initial beam into elementary beams of semi-infinite section to reduce the calculation time. It relies on the pre-calculated kernel point along the path of the primary particles. The dose is given by:

$$D(p) = \int\int\int \Psi(E)(x', y')K_{PK}(E, x - x', y - y', z)dx'dy'dE, \tag{2.12}$$

with - $\Psi_E(x', y')$ being the energetic fluence of the primary photons at the point of coordinates (x', y') at the entrance of the phantom;
- K_{PK}, the pre-calculated mono-energetic Pencil Beam Kernel at the given medium.

Dose calculation in heterogeneous media

The idea is to calculate the 3D dose and apply a correction factor. Pencil Beam method is frequently used for the three-dimensional dose calculation. However, this algorithm is limited and is not accurate in non-homogeneous conditions: it does not consider the density variations along the beam axis, does not account for photons' lateral scattering; neglects the penumbra effect and does not consider scatter radiation.

In figure 2.14 [53], the depth dose curves obtained by the PBC algorithm without corrections (water phantom) and two correction based methods (ETAR and MB - Modified Batho) are presented in A and C, for a $4 \times 4\ cm^2$ field and in B and D, for a $10 \times 10\ cm^2$ posterior field for 8 MV (in A and B) and 15 MV (in C and D) energy beams, traversing a media composed of chest wall from the skin up to 3.5 cm in depth; lung, from 3.5 cm to 18.5 cm; and chest wall.

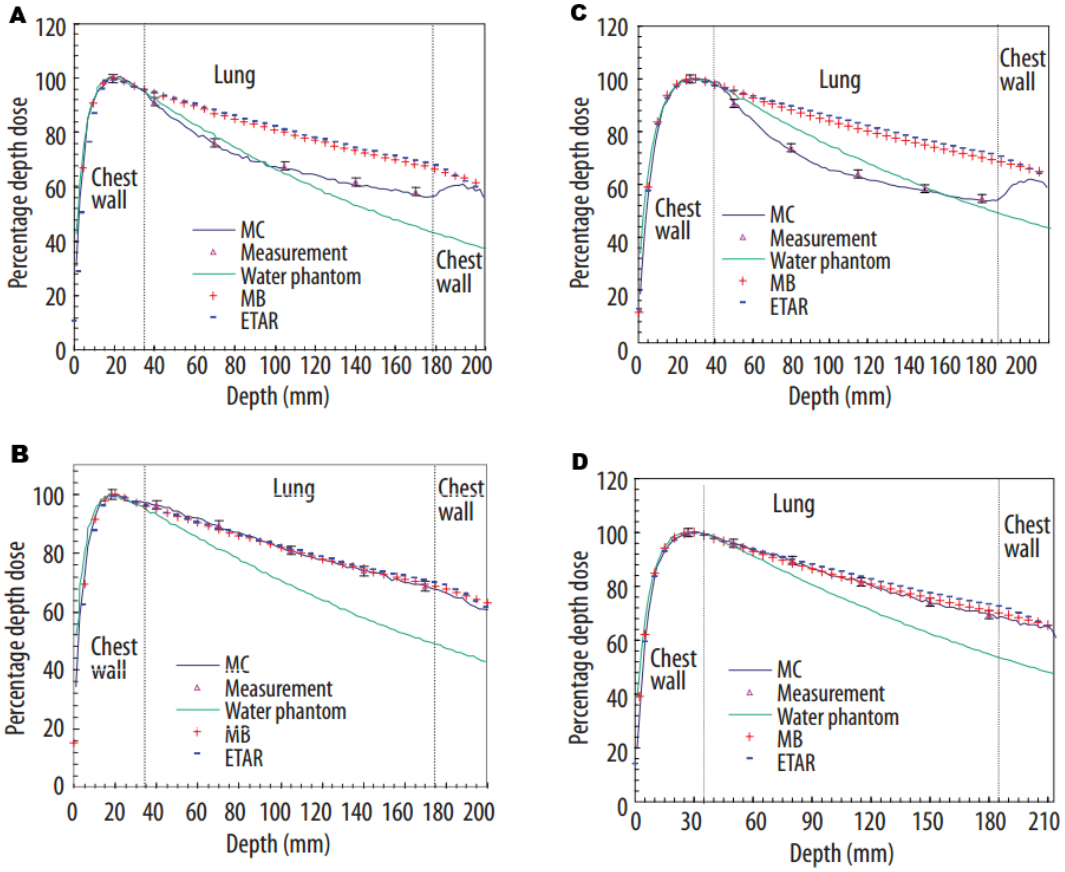

FIGURE 2.14: Comparison of percentage depth doses calculated by MB, ETAR and Monte Carlo methods and measurements for posterior lung irradiations by 8 ((A) and (B)) and 15 MV ((C) and (D)) photon beams. (A) and (C) Field size $= 4 \times 4cm^2$, (B) and (D) Field size $= 10 \times 10cm^2$ [53].

Mesbahi et al [53] showed that the first "build-up" is followed by a 'build-down", when the beam traverses the lung and enters the chest wall, for small field sizes. It is here proved that the Pencil Beam correction based methods are not capable of accurately predicting in the "build-down" region in the lungs. Concerning larger fields, the correction based methods present comparable curves to those obtained by Monte Carlo.

The conclusion from this study is that the PBC and the correction methods do not accurately model the dose for the tumors localized in heterogeneous regions or in the lung interface.

B. Monte Carlo methods The Monte Carlo method is the most accurate method for dose calculation. With this method histories of millions of photons and secondary electrons are simulated to calculate dose deposition based on the physics of interactions in matter.

The main photon interactions simulated are the photoelectric effect, Compton effect and pair production which lead to electron interactions (ionization, excitation, bremsstrahlung and ultimately dose deposition). There are other effects that contribute to dose such as neutron production which may or may not be modeled.

The MC method uses known probabilities and probability distributions in sampling to predict the interactions results. The MC obeys to the law of large numbers: the average of the results obtained from a large number of histories should be close to the expected value and will tend to become closer as more trials are performed. Programming subroutines and interaction probabilities are used to calculate dose.

The question that arises is 'if MC is the most accurate method for dose calculation, why to develop other algorithms?' The answer is time. Processing time makes MC calculations impractical for clinic within the TPS engine and for plan optimization. However, MC may be used for treatment plan verification. Moreover, with the reduction of the cost of higher performance computing over the last years, it is now possible to use more sophisticated algorithms employing MC calculations, with pre-calculated phase space files.

MC accuracy is highly dependent on the modeling of the components of the linac head. As input, the programmer needs to introduce the following information: finite photon source size characteristics; open fluence distribution; head scatter sources, flattening filter, collimators, wedges and monitor backscatter, when applicable; fluence modulation; and other specific details.

Patient dose calculation using MC can be done with the electrons exiting from the accelerator vacuum window and tracking them and their descendants through the linac head including the patient dependent beam configurations (collimation system) and then the patient geometry. This is, however, inefficient, since the first part of the linac is fixed for each beam energy and is not patient dependent. The radiation beam information can be stored in a phase space file [54], which contain a complete characterization of the particles, or a source model [55], at the plane below the fixed components of the linac head. The phase space data is generated by MC simulation; the source model is derived from the phase space data [55–59] or measured beam data[60].

MC-based algorithm calculations simulate the particle transport and interaction in the patient-dependent field-defining components in the treatment delivery system together with patient dose calculation. The particles (primary and descendants) are transported in the beam collimation system and through the patient geometry until they exhaust their energy or escape to the free space. Direct MC simulation of the particle transport through the collimation system is time consuming because most particles are absorbed before they can reach the patient geometry. To improve the simulation efficiency, a variety of strategies have been applied, such as using high-energy cutoffs for photon and electron particles or to disregard the secondary Compton scattering photons [61] or the secondary electrons because they deposit most of their energy locally.

Since the MC method is based on random sampling, the calculated doses always contain statistical uncertainties. The doses calculated using analytical methods do not have statistical uncertainties; however, they usually contain larger systematic errors in heterogeneous media compared to the MC method. Simulating a predetermined number of particles, the statistical uncertainty of a MC result can be reduced to values that are considered clinically insignificant (e.g.: inferior to 2%) but these results are clinically useful and meaningful.

The patient dose calculation can be reported whether as dose-to-water or dose to the local medium. By default, when considering MC, dose-to-medium is reported; in the conventional methods, it was excepted that these would report the results in dose-to-water, however, large discrepancies are usually observed, when MC dose-to-medium is converted to dose-to-water and compared to the dose determined by conventional algorithms.

2.4.4 Dose correction methods for photon beams

The density correction issue is well-known and several correction algorithms were developed. These algorithms can be grouped in different ways, considering how they take into account the density variations (heterogeneities): the correction dimension of the heterogeneities considered (1D or 3D) and how they handle the electron transport, as presented in table 2.15 [62].

	TERMA	**DOSE**
	Local energy deposition (No electron transport)	*Non-local energy deposition (Electron transport)*
1D	**Category 1**	**Category 3**
	1.1 Linear attenuation 1.2 Ratio of TAR (RTAR) (Equivalent path length, effective SSD, isodose shift) 1.3 Power law (Batho)	3.1 Convolution (pencil beam) 3.2 FFT techniques
3D	**Category 2**	**Category 4**
	2.1 Equivalent TAR (ETAR) 2.2 Differential SAR (DSAR) 2.3 Delta volume (DVOL) 2.5 3D Beam Subtraction Method	4.1 Superposition/Convolution 4.2 Monte Carlo 2.4 Differential TAR (dTAR)

FIGURE 2.15: Categorization of different inhomogeneity correction algorithms according to the level of anatomy sampled (1D or 3D) and the inclusion or exclusion of electron transport [62].

The correction methods use a factor to correct the dose in an heterogeneous medium. The dose calculation is performed in two steps:

- dose calculation supposing the patient is homogeneous with a density equivalent to the water density $\rho = 1g/cm^3$;
- correct the dose with a correction factor, F_c that depends on the correction method.

F_c is given by:

$$F_c = \frac{D_{heterogeneous}}{D_{homogeneous}} \tag{2.13}$$

There are several correction methods, such as Batho Power Law [62, 63], modified Batho Power Law [64, 65], ETAR (Equivalent Tissue Air Ratio) [66], and others.

Nonetheless, these correction methods do not take into account the secondary electrons transport. These electrons are most relevant for high-energy photon beams and within the low density tissues, such as in air cavities. Moreover, the dose calculation is not accurate in the build-up regions and in the interface tissue / tumor, which becomes more relevant for high energy beams and in case the tumor is located in the vicinities of air cavities and there can be loss of lateral and/or logitudinal electronic equilibrium [63].

The majority of treatment planning optimization algorithms have performed calculations of the dose delivered from each beam or fluence element using a *pencil beam convolution/ superposition type algorithm* [46, 47]. In this approach, the dose delivered is calculated at each calculation point within the patient using a convolution of the TERMA [30].

The accuracy of convolution/superposition pencil beam algorithms has been thoroughly investigated. In particular, their ability to correctly determine the dose in the presence of tissue inhomogeneities was examined. Ma et al [67] have shown a commercial implementation to miscalculate dose by up to 20% within the OAR where inhomogeneities exist. Significant differences with MC dose calculation have also been reported by Wang et al [68]. Cranmer-Sargison et al [69] have shown inaccuracies (overestimation of the dose to lung) in lateral profiles across a sharp lung-water interface by as much as 16%. Knoos and Wieslander [70, 71] have also observed differences in a mediastinum water-cork geometry by as much as 14%.

The above findings have recently prompted several improvements to commercial convolution pencil beam algorithm. For example, Varian's new anisotropic analytical algorithm (AAA) accounts for tissue heterogeneity anisotropically in the three dimensional neighborhood of an interaction site by using photon scatter kernels along multiple lateral directions [50]. Studies on the accuracy of the algorithm have found significant improvements. Confidence limits on the lung-water interface test was found to be within 4% [72]. Sterpin et al [73] has found the algorithm accurate to within 5% at interfaces and 1.7% differences in the mean planning target volume dose for a clinical case.

The improvements to the algorithm come at a computational cost. The algorithm cannot be implemented in the iterative stages of the optimization at present due to the required computational time. The algorithm is used only after the optimization completes as a final dose calculation.

2.5 Radiation detectors

There are many types of dosimeters such as ion chambers, solid state detectors, thermoluminescent detectors (TLD), radiographic or radiochromic films, among others. Each of these detectors features different suitability in radiotherapy applications. Depending on the situation, different requirements may be necessary such as high spatial and time resolution, very small dependence of response on photon or electron energy or good temperature and radiation type stability. In these devices, the absorbed energy has the capability of producing a measurable change in their properties, as for instance a change in the measured charge, in the ionization chambers; a visible chemical reaction, in photographic films; any light output, in TLD, and so on.

The exploited dosimeters in this work were mainly, ionization chambers and photographic films, which are briefly described next.

2.5.1 Ionization chamber dosimetry

In this work, the ionization chambers (IC) were responsible for absolute calibration and also for checking beam flatness and symmetry. These dosimeters have long-term stability, high accuracy, direct readout and are easy to use. The IC is a dosimeter which is available in a variety of designs such as free-air standard chamber for measuring of the exposure for primary calibrations, thimble air cavity chamber for measuring the absorbed dose and high-pressure IC for measuring the low intensity γ radiation or cosmic radiation, etc.

A typical ionization chamber used in RT is made of a thin wall of a specific material, generally graphite filled with a defined volume of gas, as depicted in figure 2.16. This specific chamber represents cylindrically shaped IC (also known as thimble or compact chambers) which are most commonly used in photon dosimetry. However, there are chambers in a variety of designs and sizes, related to the required sensitivity.

The following cylindrical IC, presented in figure 2.17 were used for the dosimetric measurements:

- Semiflex IC (model PTW 31010), with a sensitive volume of 0.125 cm^3 appropriate for measuring high-energy photon (nominal useful energy range from 30 kV to 50 MV) and electron (nominal useful energy range from 6 MeV

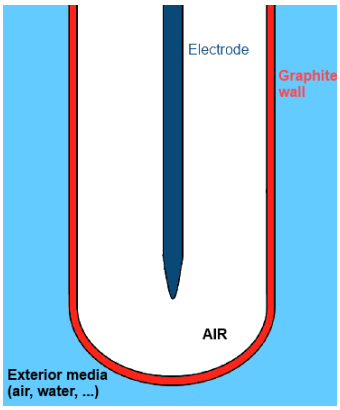

FIGURE 2.16: Scheme of an ionization chamber commonly used for radiation therapy purposes.

and 50 MeV) radiation in air, water and phantom material. Graphite is the wall material and it possesses a protective acrylic cover. This chamber is a good option for small size fields with reasonable spatial resolution and large sensitive volume for precise dose measurements. Furthermore it can be used for high precision absolute dose measurements and has no significant dose rate or energy dependence. Its usability is limited to fields larger than 3 x 3 cm^2, due to its dimensions.

- PinPoint IC (model PTW 31016), with a sensitive volume of 0.015 cm^3 this chamber was designed for application where superior spatial resolution is required. It consists of a 2 mm diameter and 5 mm long cylindrical air chamber with a central steel electrode with a PMMA (covered with graphite) wall. It is an adequate chamber for field measurement between 2 x 2 cm^2 and 10 x 10 cm^2.

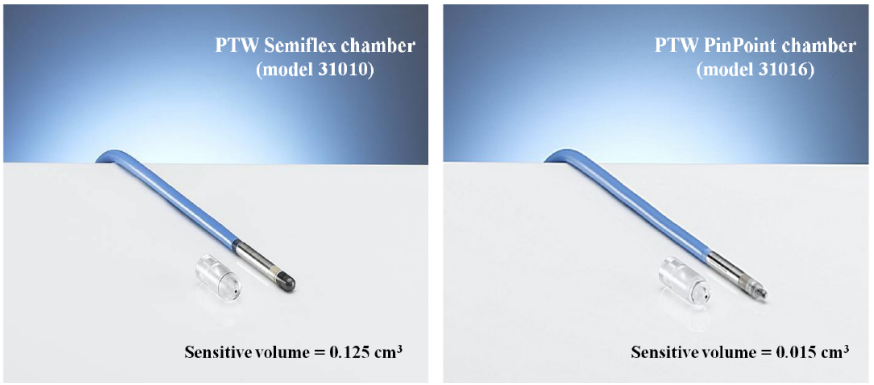

FIGURE 2.17: PTW Semiflex ionization chamber of 0.125 cm^3, on the left; and PTW PinPont chamber of 0.015 cm^3 on the right side. Images from www.ptw.de

Dosimetry protocols with ionization chambers

When measuring absorbed dose with an IC several corrections need to be made to ensure that the measurement of absorbed dose gives the same result regardless the operational conditions such as radiation quality, dose rate and ambient conditions (temperature, pressure, humidity, etc). The International Atomic Energy Agency (IAEA) and other institutions such as the American Association of Physicist in Medicine (AAPM) published dosimetry protocols for the dose determination in EBRT. These protocols define all the different correction factors needed to achieve a clinically relevant accuracy of the measurements of absorbed dose.

The IAEA TRS-398 code of practice [74] has been taken as a reference for the dosimetric measurements performed in the present work. A brief description of the methodology and recommendations given by this protocol are given next.

IC for absolute dosimetry are usually calibrated in secondary standard laboratories using reference conditions under a known field of radiation, usually a ^{60}Co beam. The calibration is based on determined absorbed dose in water by international primary standard laboratories in so-called standard conditions of pressure 1013.0 kPa and temperature 20°C. In order to use the IC in other conditions different from those of the chamber calibrations, it is essential to consider many issues concerning either the IC or the measurement circumstances and correct the measured signal for the specific conditions. The IAEA TRS-398 code of practice is based on a calibration factor N_{D,w,Q_0} in terms of absorbed dose to water for a reference beam of quality Q_0 (usually a ^{60}Co beam) and is applied to photon beams generated by electrons with energies in the range of 1 MeV to 50 MeV. According to this code, the absorbed dose in water for a megavoltage beam is given by:

$$D_{w,Q_0} = M_{Q_0} \times N_{D,w,Q_0} \tag{2.14}$$

where the N_{D,w,Q_0} calibration coefficient has been traceable from the standards laboratory and relates the reading of the dosimeter M_{Q_0}, formed by the IC and the electrometer, to dose to water D_{w,Q_0} in a reference field under reference conditions. These reference conditions are air pressure, temperature, field sizes, measurement depth, phantom size and quality index Q directly linked to the energy of the irradiation beam. In general, when a IC is used for clinical dosimetry, only a few of the defined reference conditions can be usually reproduced. Thus, deviations due to several influence quantities need to be accounted for by the application of a product of multiplicative factors of two classes. The first class of corrections accounts for changes in the beam quality, Q, compared to the reference beam quality Q_0. These corrections are represented by the beam quality correction factor which

is denoted as k_{Q,Q_0}. This factor corrects all differences from the ideal conditions of the Bragg-Gray cavity theory and includes the following parameters:
- p_{wall}: Correction for the non-medium equivalence of the chamber wall and the surrounding water where the chamber is placed.
- p_{cav}: Correction for scattering differences between the air cavity and the surrounding material, usually water.
- p_{cel}: Central electrode perturbation correction accounting for the central electrode in a thimble ionization chamber.
- p_{dis}: Factor accounting for the fact that the air cavity of a cylindrical chamber causes less attenuation or build-up than the water displaced by it and causes the upstream shift of the effective point of measurement. The effective point of a chamber is usually shifted from the position of the center towards the source by a distance which depends on the type of beam and chamber.
- $s^{\Delta}_{w,a}$: Restricted stopping power ratio of water to air considering the fraction of the total collision stopping power that includes all the soft collisions and those hard collisions resulting in δ-rays with energies less than a cutoff value Δ.
Extending these corrections to a function of beam quality leads to:

$$k_{Q,Q_0} = \frac{N_{D,w,Q}}{N_{D,w,Q_0}} = \frac{\left(s^{\Delta}_{w,a} p_{cel} \cdot p_{wall} \cdot p_{cav} \cdot p_{dis}\right)_Q}{\left(s^{\Delta}_{w,a} \cdot p_{cel} \cdot p_{wall} \cdot p_{cav} \cdot p_{dis}\right)_{Q_0}} \tag{2.15}$$

The second type of corrections relates to the reading of the electrometer and include:
- k_{elec}: Calibration factor of the electrometer.
- $k_{P,T}$: Temperature and pressure correction for the varying density and humidity of the air in the user facility with respect to the conditions specified by the standards laboratory.
- k_{pol}: Polarity correction for the effect of altering the measured charge.
- k_s: Recombination correction for ions that recombine before they reach the electrodes, leading to the incomplete collection of charge in the chamber.
In summary, the absorbed dose to water $D_{w,Q}$ in a user's beam, measured with an IC dosimeter, is determined by:

$$D_{w,Q} = M_C \times N_{D,w,Q_0} \times k_{Q,Q_0} \tag{2.16}$$

, where M_C is the reading of the electrometer corrected for the various influence factors previously mentioned:

$$M_C = M \prod k_i = M \times k_{elec} \times k_{P,T} \times k_{pol} \times k_s \tag{2.17}$$

The factor N_{D,w,Q_0} is a calibration factor valid under reference conditions for the quality Q_0 and it is obtained at a standards dosimetry laboratory under a set of well-established reference conditions. All these factors are generally provided by the protocol or the chamber manufacturer for the various IC and beam qualities, requiring to maintain the geometrical reference conditions.

2.5.2 Film dosimetry

Film dosimetry has been used extensively as a convenient and rapid mean of measuring dose distributions of therapeutic electron and photon beams. In radiation dosimetry, there are numerous problems associated with the measurements of two-dimensional dose distributions or depth-dose distributions in high-gradient dose regions, where automated dosimetry systems using IC cannot easily be employed. Dosimetry with films have resulted in a suitable solution to overcome these difficulties due to their high spatial resolution. The films are easy to develop and give a permanent record of dose distributions with an acceptable accuracy.

In film dosimetry, the effect produced in the film by the radiation is measured in terms of light opacity of the film using a densitometer. Opacity is defined as I_0/I, where I_0 is the light intensity measured in the absence of the film and I the intensity through the film in a direction perpendicular to its plane. Based on this relation of intensities, the optical density (OD) is defined as:

$$OD = -log_{10}\left(\frac{1}{T}\right) = log_{10}\left(\frac{I_0}{I}\right) \tag{2.18}$$

, where T is the transmittance defined as $\frac{I}{I_0}$.

A relationship between the OD and the dose is generally defined for each combination of film and densitometer or scanner. This relation is known as sensitometric curve and provides the characteristics of the film. This type of curves are also an important tool for quantifying contrast and dynamic range of a radiographic film and depend strongly on the processing conditions.

The radiochromic films used were EBT2 Gafchromic films from ISP (International Specialty Products: www.ispcorp.com).

In this work, all radiochromic films were scanned using the Epson Expression 10000XL flatbed scanner. The subsequent analysis of the data was performed with the software FilmQA.

Radiochromic film is a recent type of film for radiotherapy dosimetry. The radiochromic films (based on polydiacetylene) are most used when high spatial resolution, weak energy dependence are required.

According to the manufacturer, the GafChromic EBT2 film is composed of one adhesive layer of 25 μm, a top coat 5 μm thick and an active substrate layer of 30 μm. These layers are coated with two clear polyester sheets with different thicknesses: 50 μm, on top and 175 μm, at the bottom, as presented in figure 2.18.

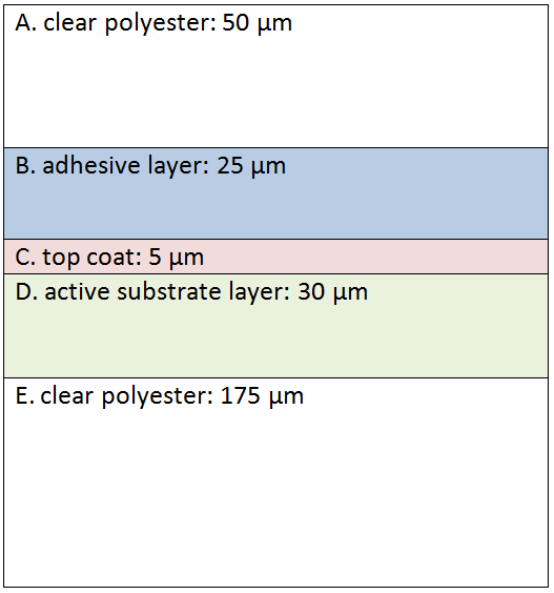

FIGURE 2.18: Composition of an EBT2 Gafchromic film.

The active component of EBT2 films is nearly tissue equivalent with an effective atomic number Z_{eff} of 6.84. Its overall atomic composition is H (40.85%), C (42.37%), O (16.59%), N (0.01%), Li (0.10%), K (0.01%), Br (0.01%) and Cl (0.04%). Radiochromic films are expected to be independent of the energy of the incident ionizing radiation. These kind of films contain a special yellow marker dye that is polymerized upon exposure to radiation. The polymer absorbs the light and the transmission of light through the film is measured with a densitometer.

The dosimetry with radiochromic films has several advantages compared with previous films, like radiographic films, such as ease of use, elimination of the need for

darkroom facilities and film processing, dose rate independence, better energy characteristics and (almost) insensitivity to ambient conditions. All these advantages have subsequently consequences in the accuracy of the dosimetry performed using these films. The uncertainty using radiochromic films is 2 - 3% [75].

Chapter 3

Monte Carlo

3.1 The Monte Carlo method

The Monte Carlo (MC) is a method of approximately solving mathematical and physical problems by the simulation of random variables [76]. Given a specific probability density function (PDF), the ability to generate random numbers according to the PDF provides a means to simulate physical systems. This is achieved in the MC method through the transformation of a set of uniformly distributed (pseudo) random numbers (easily generated on a modern computer) into the desired distribution of random numbers.

3.1.1 Transformation of random numbers by integral inversion

Considering the known probability density function (PDF) $p(x)$, for which random numbers X shall be generated, over the interval $[X_{min}, X_{max}]$, the values of X are given by

$$G = \int_{X_{min}}^{X} p(x)dx, \tag{3.1}$$

, where G is a set of uniformly distributed numbers, and X_{min} is the lower bound of the range of desired X values [76]. The example presented below demonstrates a method to transform a uniform random variable.

Integral inversion sampling of interaction probability

The following PDF determines the probability of interaction for a photon penetrating an infinitely thick slab of material:

$$p(x) = \mu e^{-\mu x},\ for\ 0 \leq x \leq \infty, \tag{3.2}$$

where μ is the sum of *linear attenuation coefficients* for all photon interaction types (e.g. pair production, Compton scattering, photoelectric effect, coherent scattering, triplet production, etc.) for a certain material and energy. The set of random numbers G with uniform PDF can be transformed into the set of numbers X with PDF $p(x)$ according to:

$$\begin{gathered} G = \int_0^X \mu e^{-\mu x} dx, \\ G = 1 - e^{-\mu X}, \\ X = -\tfrac{1}{\mu} ln(1 - G), \text{ for } 0 \leq G \leq 1. \end{gathered}$$

By binning X for a set of random numbers G, the resulting histogram is isomorphic to the shape of $p(x)$. However, $p(x)$ can not always be inverted to solve for X. An alternative method is the *acceptance-rejection* MC method.

3.1.2 Transformation of Random Numbers by Acceptance-Rejection

This transformation is used when it is not possible to obtain the inverse of $p(x)$. It was first used by George-Louis Leclerc, in the 18^{th} century in a technique known as Buffon's needle. This technique was later formalized by John von Neumann [77].

Given the PDF, $p(x)$, a rectangular sampling envelope is constructed which completely encloses the area under $p(x)$. Suppose N random points uniformly distributed over the sampling envelope, as represented in figure 3.1 are chosen by generating a pair of uniform random numbers G_1 and G_2 such that

$$\begin{gathered} x_{min} \leq G_1 \leq x_{max} \text{ and} \\ p_{min}(x) \leq G_2 \leq p_{max}(x) \end{gathered}$$

form the coordinates of the point (G_1,G_2). For each $x = G_1$ generated, $p(G_1)$ is evaluated and compared to G_2. If $G_2 \leq p(G_1)$, the random value is accepted, otherwise it is rejected and another set of G_1 and G_2 are generated. In this way, a random set of values G_1 distributed as $p(x)$ can be generated from two uniform distributions of random numbers. The disadvantage of this method is

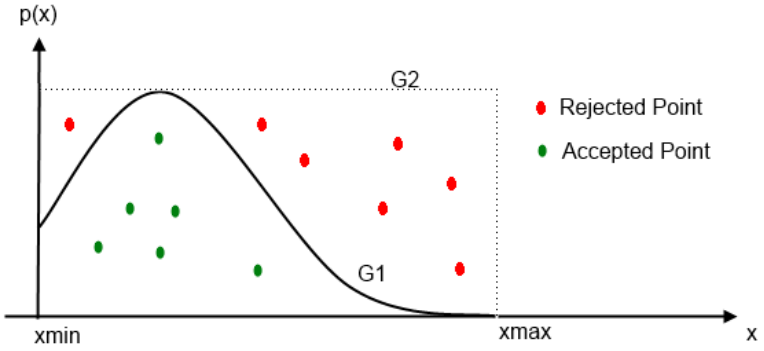

FIGURE 3.1: Representation of the Acceptance-Rejection method by transformation of random numbers. The green points represent the accepted numbers, that are contained with the function's envelope; the red points represent rejected numbers.

that a portion of random numbers are wasted and each accepted value requires two random numbers to be generated.

The approach of continually sampling PDF is inefficient, as many of the histories (and therefore computational time) will not contribute to the final result (the particles that for some reason do not reach the patient/phantom or travel out of field).

3.2 Monte Carlo codes for linac simulations

MC techniques were used in the early days of linac design in the 1970s to aid in the optimization of the photon beams [78]. The first simplified models of photon beams were presented by Patau et al [79], Nilsson and Brahme [80], Mohan et al [81]. Extensive literature review of modeling of photon beams was provided by Verhaegen and Seuntjens 2003 [82].

Clinical used photon beams in RT are usually within the energy range of 4 to 20 MeV. The linac essential modular structure is presented in figure 3.4 and are required in a MC model. The most commonly employed MC codes are EGS4 [83] or EGSnrc [84], in conjunction with the user interface BEAM [54], Penelope [85], MCNP [86] and GEANT4 [87].

EGSnrc simultaneously with BEAMnrc and DOSXYZnrc was used throughout this work for Monte Carlo simulation purposes.

3.3 Efficiency improvements and variance reduction techniques in Monte Carlo sampling

The clinical applications of MC techniques are, at a first glance, very attractive for the possibility of rigorous results regarding particle transport simulation. However, there are two major issues directly related to MC: the time to produce results and the efficiency.

Variance reduction is the application of techniques that attempt to improve this efficiency, that is, to achieve the desired statistical uncertainty with fewer simulations.

BEAMnrc has introduced several techniques to allow variance reduction and improve simulation efficiency. An overview of the most common techniques will now be presented.

The *unconditional acceptance probability* is calculated to be the ratio of particles accepted to those generated. Sampling is more efficient when the unconditional acceptance probability is high (equal to unity in integral inversion sampling). In acceptance-rejection sampling, the efficiency can be increased through careful choice of the sampling envelope, by constructing, for example, a non-rectangular envelope.

Other techniques have been developed in an effort to increase sampling efficiency such as the Ziggurat algorithm [88] and the Box-Muller transform [89]. In these cases although the unconditional acceptance probability is less than 1, computational tricks have been implemented to reduce their computation times.

3.3.1 Importance sampling

The variance in estimating the properties of a particular random distribution may be reduced, in some cases, through the use of an importance sampling technique. In this technique one samples from a distribution other than the uniform G of above. In importance sampling one attempts to avoid taking samples in regions where the PDF is less important to the problem at hand, and to concentrate on those regions contributing more to the problem. To account for this bias the samples are weighted appropriately by the inverse of the applied importance function. A careful choice of the biased distribution to encourage the important

regions of the input variables is imperative as the reward can be significant run-time savings. Poor choice of distribution can result in longer run times than sampling without importance sampling [90].

3.3.2 Calculation Efficiency

The accuracy of any MC calculated mean value is limited by its statistical uncertainty and is dependent of the number of histories, N, simulated. The uncertainty is given by the variance and provides a measure of the statistical fluctuations of the calculated mean value around the true value of that quantity. Thereby the concept of efficiency ε, establishing a relationship between the variance and calculation time is defined:

$$\varepsilon = \frac{1}{s^2 T} \tag{3.3}$$

, where T is the CPU simulation time and s^2 is an estimate of the statistical variance. Efficiency increasing methods can be classified as either reducing T, by increasing the CPU power available to the simulation, or reducing s^2, which is equivalent to requiring fewer simulations to attain the same level of statistical variance.

3.3.3 Variance Reduction techniques

MC calculations can be time consuming, especially for applications in RT. Therefore, it is essential to use variance reduction techniques (VRT) to speed up the simulations. VRT, by definition, must not influence the expected result of an infinitely long simulation not using VRT. However, in the literature, approximate methods are often denoted as VRT, as for example, condensed history (CH) technique.

3.3.3.1 Range Rejection

Most of the computation time in MC simulation is devoted to tracking electrons. Range rejection can allow significant time savings during computations of electron transport. In this technique, the residual range of each charged particle is calculated and the history is terminated if it cannot escape from its current region. The

threshold for cutoff is defined using ECUT (defined in MeV, including rest mass) which can be set independently in each region of the accelerator model. Because any potential photons (produced via bremsstrahlung) are assumed to deposit their energy within the current region, range rejection introduces an approximation into the simulation. Care must therefore be taken to select an appropriate value for ECUT [54]. As a general rule, ECUT is set such that an electron of energy ECUT has a range of less than $\frac{1}{3}$ of the smallest dimension of the geometric dose scoring region of interest. The ECUT used was 700keV, for BEAMnrc simulations.

Range rejection is a popular VRT that involves terminating histories where further simulation would not contribute to the final result. BEAMnrc applies this VRT for electrons traveling through the treatment head. Basically, the method consists in calculating the residual range of a charged particle and terminating its history if it cannot escape from the current region, not depositing there its energy. However, by terminating an electron's history preliminarily, no bremsstrahlung photons can be created or escape the region (depositing their energy somewhere else), possibly leading to an dose underestimation for high energies and high Z materials. Therefore, an energy threshold, ESAVE, is defined, above which no range rejection can occur. This parameter has to be chosen taking into account the Z of the medium (may vary from region to region) and so that the bremsstrahlung production at lower energies has a negligible effect. In this work, all simulations used ESAVE of 1 MeV, justified by a study of Rogers et al [54] as the best compromise between accuracy and simulation speed.

3.3.3.2 Uniform Particle Splitting

Photons are produced in a medical linac via bremsstrahlung within the electron target. A significant portion of the computations in a photon beam accelerator simulation involve tracking electrons within the target. A VRT called 'particle splitting' is often used to increase the number of bremsstrahlung photons created in the simulation geometry of a photon treatment machine. The statistical uncertainty in the photon fluence, for a given number of incident electrons, can be significantly reduced by sampling multiple bremsstrahlung photons at each bremsstrahlung interaction site [54].

This technique is often used for the simulation of an electron hitting the target of a medical linear accelerator and producing one bremsstrahlung photon. In general, several photons can be produced by one electron in the target. However,

for simplicity purposes, consider the case of one bremsstrahlung photon generated by one electron. In an analog MC simulation, this photon carries a statistical weight of $w = 1$. To statistically account for the split, each photon is weighted by the inverse of the number of photons split into (splitting factor). Considering, for instance a particle splitting factor of $N_{split} = 5$, instead of one, five independent bremsstrahlung photons are sampled from the same bremsstrahlung production distribution of the given electron. If all photons are created with the same probability independent of their energy, each carry a statistical weight of $w = 1/N_{split} = 1/5$, which means that one realistic photon is represented by five photons in the simulation to preserve the total weight. This strategy permits increasing the number of photons, increasing the the statistical accuracy by lowering the variance. As most of the electrons that hit the target are absorbed, they do not contribute to the final result.

The most efficient implementation is directional bremsstrahlung splitting (DBS) which is featured in EGSnrc/BEAMnrc. DBS combines particle splitting and range rejection, with the following aim: only photons that aim into a field of interest are split, saving calculation time by ignoring those that are unlikely to reach the scoring region. Further details in Rogers et al [91].

3.3.3.3 Russian Roulette

Together with bremsstrahlung splitting, Russian Roulette can be used to restrict the number of electrons produced by the split photons. Since, in general, these electrons contribute little to the dose in the patient, it is not practical to simulate the many interactions required for each electron. Using Russian Roulette, the number of electrons can be reduced back down to that without splitting. This is carried out through comparison of a uniform random number, generated for each particle, to a survival threshold and terminating each particle above this threshold. To statistically account for the termination, each surviving electron is weighted by the applied splitting factor. This technique permits to reduce the number of particles simulated and thus the time needed to simulate their transport. Further improvement to the bremsstrahlung splitting technique was achieved using DBS [92]. Using DBS, multiple bremsstrahlung photons are sampled at each bremsstrahlung interaction site as before. Resulting photons that are aimed into the field of interest (defined by the user) are kept. All photons aimed outside of the field undergo Russian Roulette. To reduce the number of charged particles in the defined field, all photons about to undergo pair production, incoherent, or photo-electric events

are forced to take part in Russian Roulette. DBS was found to increase efficiency by approximately 20 times over uniform bremsstrahlung splitting. However, DBS must be used appropriately as it will result in only a few charged particles exiting the accelerator model outside of the defined field.

3.3.3.4 Photon Forcing

Photon forcing is the process by which photons are forced to interact in specific regions of the accelerator model where relatively few interactions occur statistically. A copy of the photon is created and is forced to undergo an interaction. The weight of the scattered photon is changed by the interaction cross section. The original photon continues on its path "unscattered" but scaled by a weight of 1 minus the interaction cross section. Photon forcing is commonly used to determine the electron contamination from particular regions of the accelerator model (such as in the air within the accelerator). Using this technique the variance of a simulation investigating particle scatter can be reduced when photon interactions are sparse.

3.3.3.5 Further techniques

The aforementioned techniques were implemented in EGSnrc code, but there are other efficient approaches that could be used. Simultaneous Transport Of Particle Sets (STOPS) can improve total calculation time by grouping particles with the same energy and transporting them simultaneously. This permits material independent quantities to be calculated just once whereas material dependent properties are sampled separately. This VRT is implemented in VMC++ code [93].

Other VRT are Macro Monte Carlo, history repetition, boundary-crossing algorithms, precalculated interaction densities, Woodcock tracing, correlated sampling, interaction forcing, exponential transform and others. Quasi-random sequences are also considered as a strategy for increasing the efficiency in simulations.

A detailed description of these and other VRT used is provided by Sheikh-Bagheri et al [94].

3.3.4 Hardware Performance Improvements

The introduction of greater processing power can also reduce the time required for accurate simulations. To decrease the calculation time, the calculations should be performed in faster computers or implementing parallel calculation processes on multicore workstations and computing clusters. Parallel computing is a technique that can provide significant increase in power. MC simulations can be performed in a parallel mode as the simulation of one history is independent of the simulation of any other history, and there is no difficulty in splitting the tasks into smaller components. Parallel computing can be implemented in single systems or over a network of systems.

Single system parallel computing requires computers with multiple processors or cores which are typically identical. For instance, for a dual core system, a MC code could assign half the desired number of histories to each core, and then combine the results when each allocation is completed. The performance in this case would increase near-linearly with the number of processors or cores available.

Multiple system parallel computing, which is more often referred to as distributed computing, is another possibility in which multiple systems are networked and one system (a server) manages the tasks and allocates the tasks to the remaining systems (nodes). This is a much more complex implementation as the resources have to be shared over a network and the nodes may not offer identical performance (and the jobs shouldn't be split evenly). This distributed computing method has become more popular for scientific computation, as it is a cost-effective method for providing high performance.

Most of the simulations performed during this project were done in Centro de Física Nuclear of Universidade de Lisboa, on the high performance computing cluster ALFC, that contained 100 processing cores of 2.2 GHz AMD Opteron processors. The EGSnrc package *exb* was configured to use the available batch submission software, allowing parallel job submission to be performed.

3.4 Simulation of radiation transport with EGSnrc

The MC methods briefly described in the previous section have been applied to many of the known interactions a particle may undergo with matter. Using these

methods the ability to transform distributions of random numbers to model individual particle interactions is realized. However, in order to model the passage of a particle through, for example, a slab of lead, a particle detector, or even the human body, the ability to link the outcomes of successive interactions and particle trajectories forming the particle shower is required. The EGS (Electron-Gamma-Shower) code [83], developed at the Stanford Linear Accelerator Center, represents an mixture of particle interactions for the coupled simulation of electrons and photons in an arbitrary material geometry from a few keV up to several hundred GeV. Using EGS, quantities of interest can be calculated by averaging over a given set of MC particle cases or histories.

Further refinements of the physics within EGS to improve its use in the modeling of radiotherapy were implemented by the Omega group in the mid 1990's within the National Research Council of Canada (NRC). The named EGSnrc contained enhancements specifically to the electron transport algorithm, variance reduction techniques (bremsstrahlung splitting, Russian roulette, range rejection) and several of the physics models (bremsstrahlung angular sampling, photoelectric/Compton electron relaxations). A detailed account of the physics instituted in EGSnrc can be found in NRC Technical Report PIRS-701 [93].

The EGSnrc code is written in a programming language called MORTRAN. This code relies on two user codes that simplify the simulation process:

- a. **The BEAMnrc code** [91] is a Monte Carlo simulation tool for the modeling of radiation beams from any radiotherapy units, including orthovoltage units, 60Co units and linear accelerators.
- b. **The DOSXYZnrc code** [95] is an EGSnrc-based code dedicated to the calculation of dose distributions within phantoms consisting of rectilinear volume elements (voxels) which contain a specific physical density and material. Voxel dimensions are independently variable in all 3 directions (x, y and z). The code allows to select between different source types, including monoenergetic diverging or parallel beams, phase-space data generated by BEAMnrc simulations, or a model-based beam reconstruction produced by the BEAMDP software.

Patau et al [79] were among the first to simulate a complete photon beam linac using MC techniques and and McCall et al [78] attempted to use EGS3 code [96], focused on the optimization of the target and flattening filter composition which

affects the depth of the dose maximum in water and the average energy of the photon spectrum exiting the linac for 10-25 MV photon beams. Bielajew et al [97] implemented bremsstrahlung angular sampling in EGS4, leading to a significant difference in the degree of the target absorption. Cross sections accuracy for bremsstrahlung production still remains a matter of study.

This code simulates the following particles:

- photons,
- electrons, and
- positrons.

It also provides other tools such as particle tagging according to interaction types and sites. Lovelock [98] modeled the radius of a uniform primary electron beam hitting the target and achieved good results.

Information on the particles crossing a plane can be stored in a called, phase-space file. The simulations are done in stages and the phase-space information from one plane can be used as an input source for a subsequent stage.

3.4.1 Photon interaction cross-sections within EGSnrc

The interaction of photons with matter occurs via four basic processes [93]:

1. (i) Coherent (Rayleigh) scattering with atoms or molecules in the medium (figure 3.2.d);
2. (ii) Photoelectric absorption (figure 3.2.b);
3. (iii) Incoherent (Compton) scattering with atomic electrons (figure 3.2.a); and
4. (iv) Materialization into an electron/positron pair in the presence of the electromagnetic field of an atomic nuclei and surrounding electrons (pair production) (figure 3.2.c).

With the exception of coherent scattering, each process transfers energy from the incoming photons to electrons of the media. The interaction probabilities are dependent on the media in which the processes occur and on the energy of

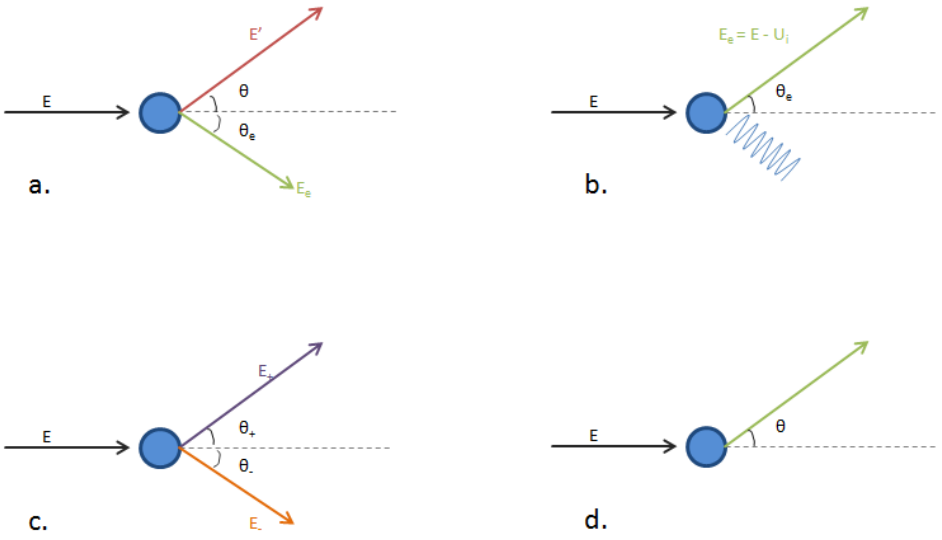

FIGURE 3.2: Diagram of the main photon interactions: a. Compton scattering; b. photoelectric effect; c. pair production; d. Rayleigh scattering. E - energy of the incident particle; E_e - electron energy; E' - energy of the resulting photon; U_i - lost energy; E_- - electron pair; E_+ - positron pair.

the photons.The interaction probabilities in water below 100 MeV for the above processes are shown in figure 3.3. It is evident that the pair production process dominates at higher energies (above 5 - 10 MeV), Compton scattering dominates at intermediate energies (from 0.5 to 5 MeV), and at lower energies (below 0.5 MeV), photo-electric absorption occur more often.

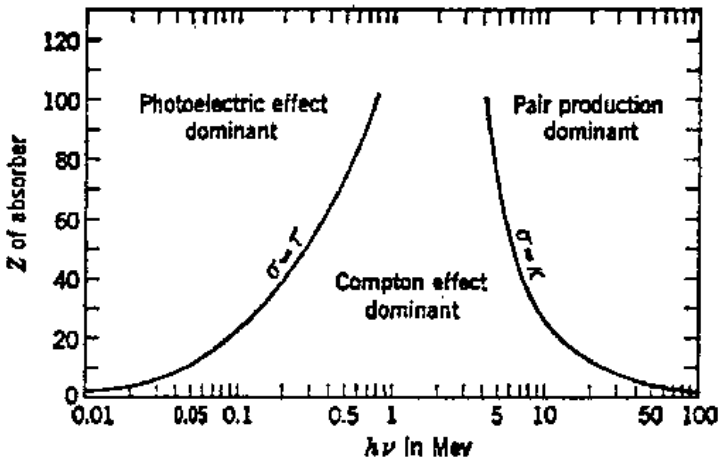

FIGURE 3.3: Photon interaction probabilities in water depending on the medium and energy of the photons [99].

A thorough description of the cross-sections adopted within EGSnrc is available in NRC Technical Report PIRS-701 [93]. A summary is compiled in table 3.1.

TABLE 3.1: Summary of interaction cross-sections implemented in EGSnrc

Interaction	Cross-Section
Coherent	Storm and Israel [100] (atomic form factors [101]) or XCOM [102]
Photoelectric	Storm and Israel [100] (Sauter distribution for photon-electron direction [103]) or XCOM [102]
Incoherent	Klein-Nishina (binding effects and Doppler broadening [104])
Pair /Triplet	Relativistic first Born approximation [105] (Coulomb corrected $\geq$ 50 MeV)

The cross-section databases for photon and electron interactions are provided in look-up tables for the materials found in the simulation geometries. These tables are generated with PEGS4 program, the cross section data preprocessor for EGSnrc. It generates energy dependent photon attenuation coefficients and electron stopping powers based on experimental data and theoretical cross section calculations. By specifying elemental composition, density and energy range, data tables are generated for use in the EGS simulation.

3.4.2 Electron interactions and transport within EGSnrc

An electron traveling through matter loses energy in two ways [93]:
(i) Inelastic collisions with atomic electrons
(ii) Radiative energy loss
Radiative energy losses (ii) occur in the form of bremsstrahlung and annihilation events with positrons. Inelastic collisions (i) dominate at lower energies. Bremsstrahlung production dominates at high energies. In addition, electrons undergo a large number of elastic collisions with atomic nuclei leading to frequent changes in direction.

Electron Transport: PRESTA II

The modeling of charged particle transport is inherently difficult. Cross-sections for electron interaction become infinite as the kinetic energy approaches zero. The cross-sections are, in fact, finite but the exact values are not well known [83]. However, low momentum transfer events do not significantly affect the shower results and so multiple steps can be lumped together in some cases without significant loss of simulation accuracy and approximated using a continuous slowing down type approximation (CSDA). Lumping electron scattering events is known as a condensed history (CH) technique, introduced by Berger [106]. A major difficulty with this technique arises in the region of material boundaries where the approach breaks down because one cannot account for the ensemble of paths occurring in

the adjacent medium. Solving this problem required the development of new multiple scattering theories and more complex algorithms for transporting electrons, including reverting to modeling single scattering events near material boundaries. EGSnrc makes use of an algorithm PRESTA II [107] (acronym for Parameter Reduced Electron-Step Transport Algorithm) that automatically selects the optimum step-size saving time to the user, permitting the use of fewer and larger electron steps without compromising the simulation accuracy. The size of the condensed history step is regulated by the parameter ESTEPE which limits the fractional loss of energy for the continuous process. With the PRESTA-II algorithm, the typical ESTEPE value is set to 25% to ensure the convergence for the correct spatial distribution.

It has been shown, however, that PRESTA is not adequate for simulating the dose deposited in a small air cavity or in the neighborhood of high-Z interfaces. This led to the introduction of a new algorithm, EXACT, which allows the user to revert to a single scattering model in the close neighborhood of boundaries, thereby reducing the minimum path length to very small values. This appears to solve the problem in these circumstances.

3.5 Monte Carlo modeling of Radiotherapy linacs

One of the most frequent and important applications of MC modeling in external beam RT is the creation of a virtual model of the radiation source.

By modeling it is meant the necessary fit of some parameters of the CM and incident electron beam on a trial-error basis until a good match between the simulations and the experimental data is attained.

One approach, extensively adopted in the last years, to characterize clinical photon beams, has been to perform a full MC simulation through the linac head. The implementation of a complete model of a linac head is not a trivial task due to its complexity and need of detailed modeling to obtain accurate dose calculations. However, the task is worth the effort because once the MC model is validated, it will provide the most accurate dose predictions, particularly in irregular geometries and inhomogeneous media. Additionally, MC simulations permit attain angular and energy distributions or other quantities difficult to obtain experimentally.

A potentially limiting factor in the MC dose calculation process remains the ability to accurately represent the radiation field emerging from the accelerator head.

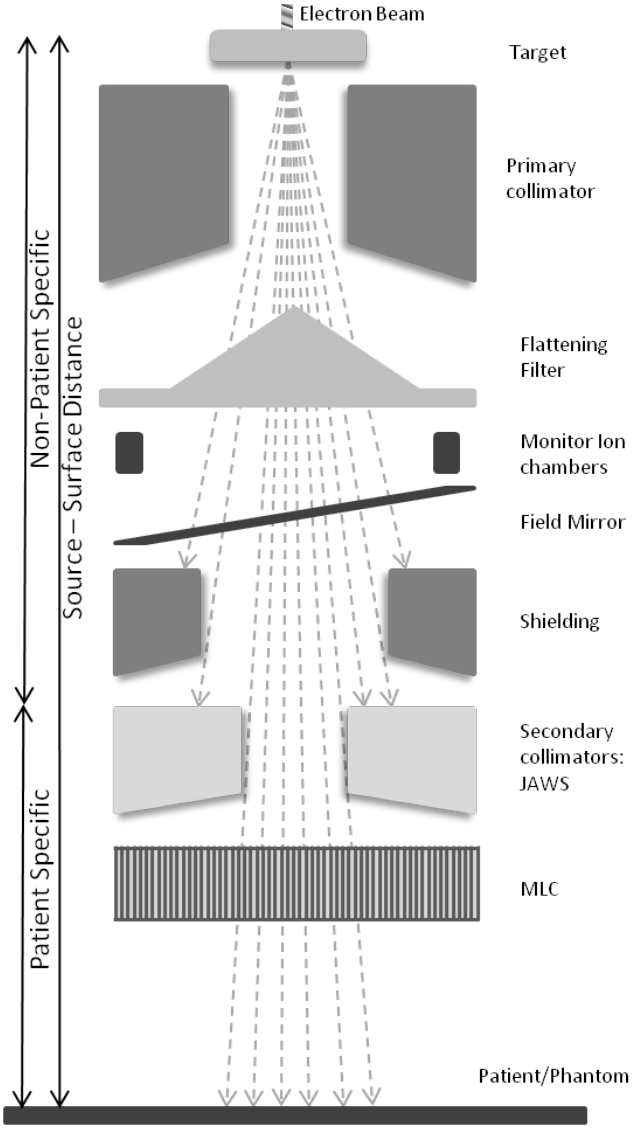

FIGURE 3.4: Schematic representation of the components that integrate a Trilogy VARIAN head linac.

The subject has been extensively researched with proposed solutions coming from a variety of modifications such as to the physical densities of components (target, flattening filter) in the accelerator head model [108], modifications to geometric components of the model (flattening filter, primary collimator, lead shielding, etc.) [108], variations in incident electron beam spectrum [109, 110], modifications to the EGSnrc interaction models.

Several MC models for the major three linac manufacturers (Elekta, Siemens and Varian) were carried out by different groups [58, 110–116]. Some studies were dedicated to investigate the sensitivity of MC simulations to the characteristics of the initial electron beam incident on the target, with particular focus on its

energy and radius, as well as other treatment head components, such as the flattening filter and the primary collimator [110, 116]. Other work was devoted to the characterization of the produced beam, in terms of their spectral distributions for different beam energies [58, 114, 117].

Despite all the works carried out so far, each linac has its own specificity and characteristics. Therefore it is necessary to model this accelerator for its calibration and curves. In a first attempt, M. D. Anderson Cancer Center provided the PSF before the jaws to avoid a detailed modeling of this part of the linac, as at the time, I still did not have the data with the detailed linac geometry from Varian. However, discrepancies were found between the simulations and the measurements and the data was not used (results not presented). The necessity for modeling is due to the need to finely tune the initial energy and radius of the primary electron beam. An accurate beam model of the linac is essential to guarantee accurate dose calculations in the patient, in the subsequent work. All the presented results are from original simulations.

3.6 Simulation of radiation transport within the accelerator head: BEAMnrc

EGSnrc is a tool to accurately model a particle shower using MC methods within a defined geometry. The software package BEAMnrc [54], represents a specialized user code of EGSnrc for the simulation of radiation beams from RT units including high-energy electron and photon beams, Cobalt-60 (Co60) beams and orthovoltage machines.

Geometries of the accelerator's components are defined through the use of component modules (CM) which consist of a wide choice of building blocks of a variety of geometrical shapes such as disks, cones, trapezoids, parallelepipeds and others, that can be assembled to build the RT unit. The CMs are re-usable, independent and can even be tested separately. They can not overlap in the beam direction. Typical CM used in linac modeling are FLATFILT for flattening filters, SLABS for the X-ray target, CONESTAK for the primary collimator, JAWS for the jaws, and so on.

The ability to score particle characteristics in a phase space file (PSF) is an integral part of the BEAMnrc code, allowing the stopping/restarting of simulations, analysis of particle characteristics, modification of particle characteristics, etc. The

characteristics recorded in the PSF include each particle's energy, position, direction cosines, weight, LATCH history, and optionally, the Z coordinate of the last interaction.

All future simulations can be started from this plane using a PSF as a particle source, effectively eliminating the need to remodel many of the unchanging linac components for each simulation. A second PSF is commonly created to record the final output of the BEAMnrc simulation and acts as the source for particle transport into a patient model or phantom.

As addressed by Sempau et al [118], the use of phase space techniques in MC simulation introduces a baseline level of statistical variance that cannot be suppressed through the use of particle recycling[1] techniques. To obtain low uncertainty results from two-step MC simulation, the size of the PSF must be rather large. To further reduce statistical uncertainty in the MC simulation, one can either increase the size of the intermediate PSF (increase particle density) or recycle the particles that have already been recorded. When a particle is recycled, the PSF record for the particle is reused. The recycled history differs from the original history only by the random number chosen to restart the particle's transport through the remainder of the accelerator model.

These PSF are accompanied with summaries containing fluence results, phase space outputs, processing time and energy deposition.

BEAMDP (BEAM Data Processor) [119] is a utility that permits beam data processing and ultimately display fluence, energy distribution and angular distribution data extracted from the PSF.

3.7 Components of a MC model of a linac in photon beam mode

The first requisite of utmost importance is to have an accurate geometric and materials description of the components that integrate the linac head, usually provided by the manufacturers, including the position, dimensions and shape of the several components; their motion and limits; the composition of materials and alloys and their mass densities. After implementation, MC linac models need to

[1]Particle recycling or history repetition: particles' complete history are precalculated with all their histories and saved for reuse

be validated against a set of dose measurements, such as depth and lateral profiles and output factors in water using different setups.

The most important linac components to consider in a photon linac model are the target, flattening filter (FF) and secondary collimators, namely the jaws and the multileaf collimator (MLC).

After the accelerated primary electron beam exits the flight tube, it possesses a narrow-energy, angular and spatial distribution. The electron beam impinges on the target, consisting of a high atomic number (Z) metal in which the electrons produce bremsstrahlung photons. These photons are then collimated initially by the primary collimator and the photon fluence is differentially attenuated by the FF to produce a reasonably flat dose distribution in water at a certain depth. The target and FF are the most important source of contaminant electrons. The monitor unit chambers and the field mirror may also be simulated but both present small attenuation to a photon beam, being therefore often omitted from MC models [120], [121]. The photon beam is finally shaped and modulated by secondary collimators and beam modifiers such as jaws, blocks, MLC and/or wedges, as represented in figure 3.4.

3.7.1 Monte Carlo simulation parameters

MC simulations were made using the BEAMnrc [54] and DOSXYZnrc [122] MC code system, based on the underlying EGSnrc [93] particle transport code. The following MC transport parameters were used in all simulations:

- $AP = PCUT = 0.010 MeV$
- $AE = ECUT = 0.700 MeV$ (including rest mass)

, where AP and AE are the low-energy thresholds for the production of secondary bremsstrahlung photons and knock-on electrons, respectively, while PCUT and ECUT define the global cutoff energy for photon and electron transport, respectively.

Range rejection was employed by setting ESAVE to 1.0 MeV for all linac components modeled except the target, where it was set to 0.7 MeV, to guarantee the production of lower energy photons.

Directional bremsstrahlung splitting (DBS) was used with a splitting factor NBRSPL=20, to increase the number of photons created in the target. Russian roulette was turned on whereas the photon forcing option was not.

The accelerator model, a Varian Trilogy 2300CD (Varian Medical Systems, Palo Alto, California) linac, was defined exactly by specifications provided by the 2008 Varian Oncology Systems Monte Carlo Project package.

3.7.2 Measurements

Measured data for depth dose and lateral profile comparisons were obtained from departmental quality assurance measurements. Ionometric measurements were performed using a PTW 31010 (volume of 0.125 cc) ionization chamber, a PinPoint chamber, in a PTW water phantom or a solid water phantom. Some measurements were also performed with EBT2 Gafchromic films, afterwards processed in a Epson 10000XL flatbed scanner. More specific details are provided throughout the thesis on the measurements performed.

3.7.3 Primary electron beam distribution and photon target

The photons produced in the target are mostly derived from a relatively thin layer on the upstream side, due to the high energy degradation of the electron energy in a high-Z material, the dependence of the bremsstrahlung cross section on the electron kinetic energy for high energies, and electron scattering in the target. At high electron energies, the average bremsstrahlung photon emission angle is approximately given by m_0c^2/E_0, where the numerator is the electron's rest energy and the denominator, its total energy, yielding a strongly forward-peaked angular distribution. Targets must be thick enough to completely stop the primary electrons.

In some accelerators, some years ago, a gold target was used to generate bremsstrahlung photon beams. However, this target material implied having a complex water cooling system directly in the path of the beam. In order to simplify the circuitry, this material has been replaced by a bi-layer target of W and Cu with the purpose of generating a photon beam (through W) and being able to self-cool (function performed by Cu). There are, however, some slight differences in the spectral distributions on the central axis of each beam that do not affect the dosimetric

characteristics of the beam, as can be seen figure 3.5. In fact, there are no significant differences in the depth and lateral dose profiles for the different targets of Au, W and W-Cu.

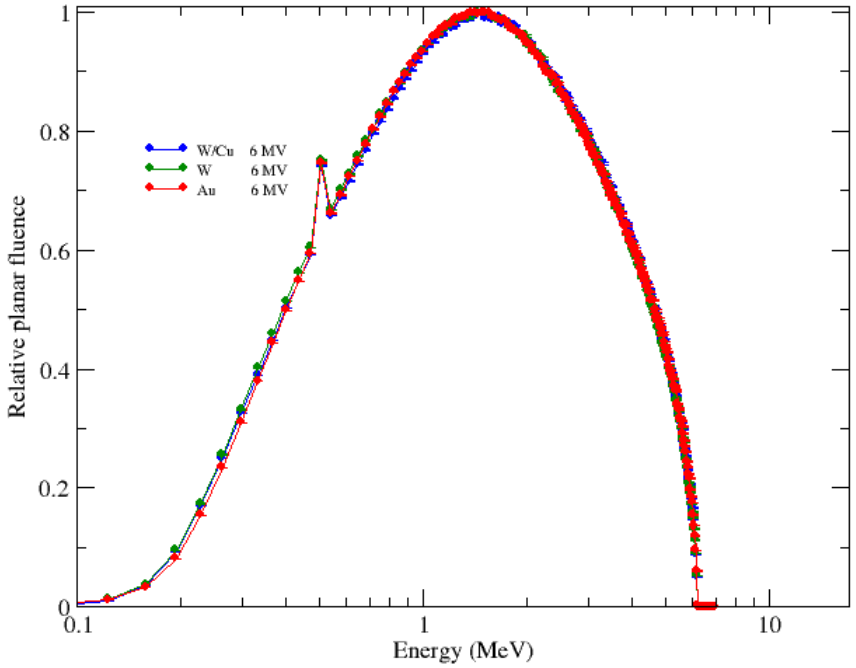

FIGURE 3.5: Photon energy spectra scored below the jaws, for Au, W and W-Cu used in the final target design.

For the 6 MV beam, the differences observed between the different target materials are not significant. However, for higher photon beam energies, there are considerable differences [123].

The photon angular distribution is spread out due to electron multiple scattering, resulting in a strongly anisotropic photon fluence and an isotropic photon spectrum, not possible to obtain with analytical methods.

The focal spot size of the photon beam and the primary electron beam affects the calculated dose and fluence distributions. Jaffray et al [124] found that the x-ray source has an elliptical shape with full width half maximum (FWHM). A fine tuning to the initial electron beam energy and FWHM was performed. However, differences are observed when measuring with different chambers, as can be observed in figure 3.6. The Pinpoint chamber presents a better agreement (about 2%) in the build-up region than the 0.125 cm^3 chamber (inferior to 5%); however,

the agreement after d_{max} (depth of maximum dose) is better for the 0.125 cm^3 chamber (about 2%).

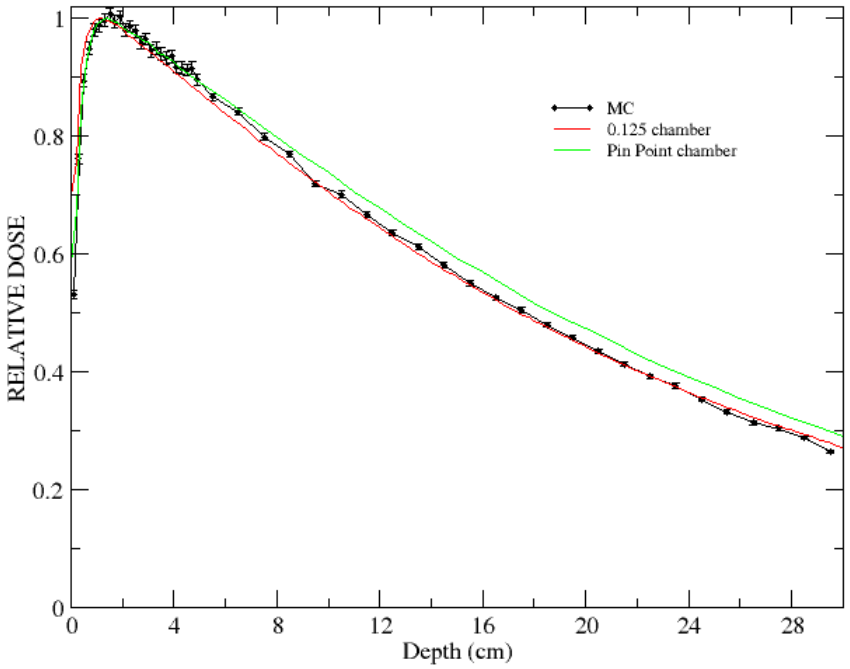

FIGURE 3.6: Depth dose curves for the 6 MV beam for the square 30 × 30 cm^2 field. The black curve represents the simulation result whereas the green and red curves are the measurements performed with the PinPoint and 0.125 cc ionization chamber, respectively.

3.7.3.1 Pre-target electron beam parameters

The sensitivity of megavoltage MC simulations to the pre-target electron beam parameters in medical linear accelerator MC models has been thoroughly investigated. A comprehensive review of past research in this area is presented by Verhaegen and Seuntjens [82] and more recently by AAPM TG report No. 105 [59]. The intensity distribution of the pre-target electron beam is among the most sensitive parameters of a medical linac model [108, 110]. It is well known that off-axis dose profiles are particularly sensitive to the pre-target electron intensity distribution [108–110, 125, 126]. A Gaussian pre-target electron beam intensity distribution has been consistently implemented in MC simulation of Varian accelerators with variations of energy and FWHM of the beam intensity.

The assumption of a Gaussian electron intensity distribution is, in part, based on an educated guess by the physicist (derived from beam line optics/accelerator physics), approximate recommendations by accelerator manufacturers, and in part implied from focal spot measurements sparsely published thus far in the literature [124, 127–130].

Using a technique similar to that of Loewenthal et al [129], Jaffray et al [124] used a CT reconstruction technique to make quantitative measurements of the size and shape of the focal spot from a total of 9 accelerators. Jaffray et al determined a range for the Clinac 2100C focal spot intensity FWHM of 1.2 - 1.4 mm for the 6 MV beam. Huang et al [130] have published measurements of the focal spots of electron beam's for the Clinac 21EX using the beam spot camera technique of Lutz et al [127]. The work is also useful in the determination of pre-target electron intensities for photon beam models. The measurements of Huang et al [130] were the first and only measurements made to date for the purpose of MC simulation. They concluded varying elliptical eccentricities of the focal spot (up to 21%) for electron energies from 6 to 16 MeV with FWHM in the range of 1.69 mm to 2.24 mm. Lateral shifts in the focal spot were also observed with reported displacements of as much as 7.79 mm. Some of the first published focal spot measurements were produced by Lutz et al [127] who performed measurements of the emerging radiation field from the target using a beam spot camera technique. Based on the above measurements performed thus far in the literature it is clear that the electron focal spot intensities deviate from the ideal Gaussian shape assumed in MC simulation. So far, no measurements of pre-target electron beam intensity distributions specifically for use in megavoltage MC photon therapy simulations have been published.

A common method for the determination of the pre-target electron beam parameters for a particular MC simulation (as outlined by Sheikh-Bagheri and Rogers [110]) is to begin with a best guess of the electron beam energy and FWHM and subsequently perform iterative trial-error adjustments of these parameters until acceptable agreement with measured the dose distribution is achieved. Typically, the energy is determined first by varying the electron energy until optimal agreement with measured depth dose profiles is obtained. Adjustments of the FWHM of the Gaussian intensity distribution are then applied until acceptable agreement with lateral (off-axis) profiles is met. It has been shown that the correlation between FWHM and central axis depth dose profile shape is minimal beyond the depth of maximum dose deposition [108, 109, 114]. However, further fine-tuning of the electron beam parameters may be required if the initial guess of FWHM

was sufficiently inaccurate during the energy tuning stages. For the remainder of this chapter, the above method will be referred to as trial-error commissioning method. It was noticed that calculated depth dose profiles in water are relatively insensitive to the primary electron energy but the horns of the lateral dose profiles are a good indicator of the primary electron beam energy, introducing a tuning procedure to estimate its energy (usually not known).

Using this method, the commissioning of a MC model can be laborious, as the time required for the high-statistics simulation of each parameter adjustment is generally large and achieving the optimal combination of electron parameters using a so-called blind search of the solution space is not guaranteed. The process/results from using the conventional method to commission MC linacs are presented by several groups [108, 110, 125].

Another error-trial type method for determining both the pre-target electron energy and FWHM for commissioning a MC model is through comparison of MC calculated lateral profiles in air with measurement. Tonkopi et al [126] have investigated the influence of ion chamber response on the MC-based measurement of in-air off-axis ratio profiles for megavoltage photon beams. Their work confirmed the conclusions of Sheikh-Bagheri and Rogers that in-air off-axis ratio profiles can be useful in the MC beam commissioning process. The use of off-axis ratio profiles could potentially reduce the time required to commission a MC beam by reducing the number of in-water simulations.

The sensitivity of the MC model to the incident energy has also been thoroughly investigated [81, 109, 114, 125, 131]. It has been shown that while the simulation is highly sensitive to the mean electron energy, the energy distribution has little effect on the resulting beam [109, 110].

The method began with the determination of a pre-target electron energy range to be optimized by observing the agreement of MC calculated depth-dose curves with measurement. Because of the relatively weak dependence of depth-dose curves with modification of the incident electron intensity distribution [108, 110], those energies producing unacceptable depth-dose curve agreement ($\geq 2\%$) beyond the build-up region were not used in the optimization. The range of incident electron energies examined was chosen in accordance with energies examined by Keall et al [108] for the Clinac 21EX and based on experience from previous commissioning efforts by the authors.

For modeling the linac, the energy and FWHM were adjusted on a trial-error basis and the best fit, when comparing with the measurements. The results are presented in [132]. The best fit was obtained for an incident electron energy of 5.8 MeV and a Gaussian intensity profile with a FWHM of 0.12 cm.

3.7.4 Flattening Filter

The flattening filter (FF) is a component with major influence on the beam, generating flat dose distributions at a certain depth in water. McCall et al [78] were among the first to perform simulations of different FF materials recommending these should be made of medium-Z materials such as steel or copper. Mohan et al [81] developed a BEAMnrc CM for easier implementation of the FF for MC simulation purposes and proved that the FF causes significant spectral hardening both on and off the beam axis.

The influence of the FF was investigated in this work. The figure 3.7 displays the result of the simulations performed with and without the FF. When the FF is present, curve in black, the lateral profiles are more flat within the jaws aperture; when it is absent, the profile presents a maximum dose in the central axis and decreases with the jaws opening.

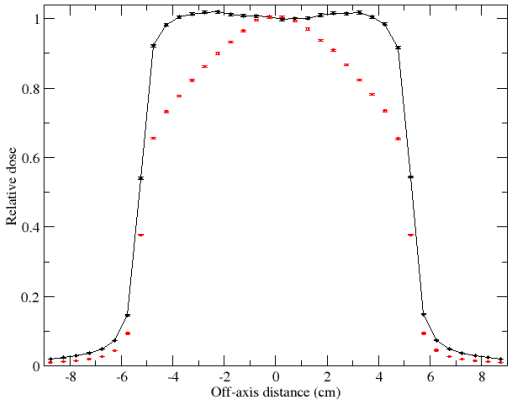

FIGURE 3.7: MC linac lateral profiles simulated with and without flattening filter, in black and red, respectively.

Further investigation was also performed on the material density of the FF and the results are presented in figure 3.8.

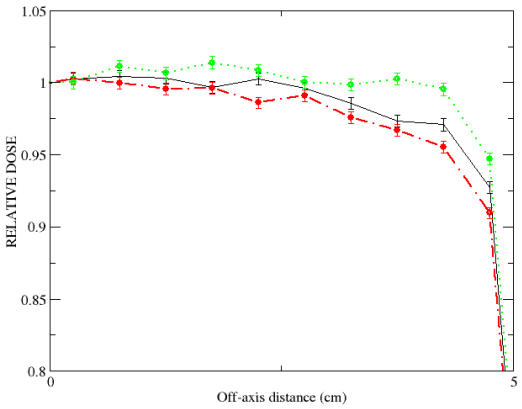

FIGURE 3.8: Lateral profiles calculated at a 5 cm depth in a water phantom for a 10 x 10 cm^2 field, for different densities of a copper flattening filter, for the 6 MV beam: 7.0 g/cm^3, in red; 8.933 g/cm^3, in black; and 11.0 g/cm^3, in green.

The density of the FF material does influence the lateral profiles. The density used was 8.933 g/cm^3 for being the data provided by the manufacturer, Varian Medical Systems. No significant differences were observed in the depth dose curves.

3.7.5 Modeling the multileaf collimator (MLC)

For a given treatment, the MLC may be static, such as in conformal radiotherapy and aperture based IMRT, or dynamic, such as in dynamic IMRT and volumetric modulated arc therapies. Transport through the MLC has been documented in the following ways [59]:

1. Explicit transport of each history through a detailed model of the MLC [91, 115, 133];
2. Explicit-approximate transport in which the MLC is explicitly modeled but approximations are employed in the Monte Carlo photon/electron tracking scheme to improve simulation efficiency [61, 134, 135];
3. Pseudo-explicit transport where an MLC characterization model or "toy-model" is used to describe the modulation effects [57].

Examples of explicit transport (1.) include the BEAMnrc CM:

- MLC, MLCQ, VARMLC [91] and DYNVMLC [133] for the Varian Millenium MLC, and

- MLCE [115] for the Elekta MLC.

Explicit transport is inherently the most accurate method of modeling the MLC since a particle shower is transported through a detailed MLC geometry. However, it is also the most computationally demanding. In the case of modeling a dynamic MLC, where only a small area of the field may be exposed throughout the leaf motion, the explicit transport method can result in a large number of particles terminating within the MLC [61].

Examples of explicit-approximate transport (2.) methods include the work of Liu et al [134], Siebers et al [61] and Tyagi et al [135]. The approximations introduced include simplifications to the MLC geometry [134], modeling only a single Compton scattering event for each photon passing through the MLC [61] or modeling only primary electrons created within the MLC [135].

An example of pseudo-explicit transport (3.) is presented by Chetty et al [57] in which a virtual source model is developed for simulating arbitrary, external beam, intensity distributions. The pseudo-explicit transport method is expected to be the least computer intensive method of modeling the MLC.

For the body of research presented in this dissertation, the explicit-approximate method of Siebers et al [61] further developed by Heath et al [133] was chosen and adapted for modeling of the MLC. This method was selected to optimize the balance of accuracy and simulation efficiency.

The most important components to achieve beam conformation are the jaws and the multileaf collimator. The first are usually two movable block pairs made of tungsten. Their opening dimensions are defined depending on the tumor dimensions through square or rectangular opened fields.

The first part of the linac modeling consisted in benchmarking the linac simulations up to the jaws. [2]

To achieve higher conformation, two banks of tungsten leaves are installed in the linac head. For Varian linacs, the MLC are usually placed below the jaws and are among the most challenging geometrical structures to model in a linac due to the complex design of the leaves. Furthermore, these leaves can move during beam delivery in step-and-shoot and dynamic treatments (such as IMRT). The MLC collimation can be considered either by a direct MC simulation of particle

[2] These results without the MLC were presented on the Second European Workshop Monte Carlo Treatment Planning (MCTP), held in Cardiff, in October 2009.

transport and interaction in the MLC leaf geometry or by ray tracing through the MLC leaf geometry to determine whether the particles can go through the MLC opening.

BEAMnrc contains pre-prepared CMs for several types of MLCs. However, the HD120 MLC had never been previously modeled and no simulations were ever performed before. Therefore it was necessary to model and validated it with further measurements. This was a complex work and the modeling was based on the Millenium MLC CM, DYNVMLC, developed by Heath et al [133]. The details of this work and the creation of a new CM, HDMLC, are presented in section 3.9.

3.8 Simulating radiation transport into the phantom/patient: DOSXYZnrc

For the commissioning of the linac, the MC simulations performed in DOSXYZnrc, were done in a homogeneous water voxelized phantom.

For the patient simulations, a 3D voxelized phantom converted from the patient/phantom CT scan was used for dose calculation. The density and material for each voxel were converted based on the CT number.

3.8.1 CTCreate

A phantom is constructed using a 3-D matrix of voxels (volume elements) for which each voxel contains a physical density and material assignment. There are two ways by which this matrix is most commonly created. The first way is by simply defining a set of x, y, and z boundaries and assigning densities and material types to these voxels using an (.egsinp) input file. The second way, used commonly for simulations on patient geometries, is to create the phantom from a set of CT images taken of the patient. From this set of images, the CT densities in Hounsfield units (HU) are interpolated onto a 3-D matrix of voxels and converted into equivalent physical densities

Typically, the CT-numbers range between -1000 HU (air) to +1000 HU (bone). The conversion function for any individual CT scanner is unique and obtained based on the CT calibration with a standard phantom. The material type (composition) and mass density data within each voxel are derived from the Hounsfield

number exported from the CT using a CT conversion curve, included in table 3.2. More details on the HU and calculation considerations can be found in 4.2.2.1.

TABLE 3.2: CT numbers and density range for the four materials used in the ramp for converting CT numbers to material parameters (composition and density).

	Air	Lung	Tissue	Bone
CT number range	0 - 50	50 - 300	300 - 1125	1125 - 3000
Density range	0.001 - 0.044	0.044 - 0.302	0.302 - 1.101	1.101 - 2.088

The conversion from CT densities to physical densities is achieved through interpolation of optical-to-physical density relations forming a CT ramp. The matrix of physical densities is then written to a file (.egsphant). Also included in this file is a list of media present in the patient model, as well as a map of individual voxels to material type. It should be noted that, in general, not every material type is defined in this file. Instead, only the most common material types may be included.

The BEAMnrc software package includes CTCreate, a tool for creating phantom models, as part of the distribution. The DICOM (Digital Image and Communications in Medicine) image format provides a standard format by which the CT scanner data can be exported. The image resolution is not fixed, although 512 $\times$ 512 pixels is commonly used. The spacing of the pixels is determined by the size of the area that was imaged and is uniform along each axis. The number of CT images or slices is generally determined by the volume of the prescribed region to be imaged and the slice spacing specified by the oncologist.

3.8.2 DOSXYZnrc

DOSXYZnrc [122] is another user code for the EGSnrc system dedicated to the calculation of dose distributions within phantoms that can be defined either by voxels or extracted from CT data.

Once particle transport through the accelerator head has been simulated with BEAMnrc, the output can be transported into the constructed patient phantom using the DOSXYZnrc user code (included in the BEAMnrc distribution). There are several ways in which the particles emerging from the accelerator head may be passed on to DOSXYZnrc. First, through the use of a phase space file generated in BEAMnrc. Second, by characterizing the particles from BEAMnrc into a series of histograms and sampling from the derived particle source model. Lastly, by incorporating the BEAMnrc simulation as a shared library in DOSXYZnrc such

that each particle requested by DOSXYZnrc is transported through the BEAMnrc simulation on-the-fly.

DOSXYZnrc is specifically written for obtaining the dose (and accompanying uncertainty) in a cartesian geometry. In DOSXYZnrc, a spherical coordinate system is defined to describe the beam incidence on the phantom with an origin set to the isocenter, as defined by (x_{iso},y_{iso},z_{iso}) the x, y, and z distances from the defined (0, 0, 0) origin of the phantom. The incident beam angle is specified by θ, ϕ, and ϕ_{col} (see figure 2.7 from DOSXYZnrc manual). In practical use of the accelerator, the incident beam angle is more commonly defined by specifying a gantry angle, couch rotation angle, and collimator rotation. A coordinate transformation is then required. The absorbed dose is recorded or scored in a 3-D array of voxels with boundaries as defined in the CT phantom. The user can choose to omit specific voxels from the scoring array. By default, the dose, uncertainties, and voxel boundaries are all written in American Standard Code for Information Interchange (ASCII) format to a (.3ddose) file.

When PSF are used as input of the DOSXYZnrc, there is a strategy to increase the number of particles simulated in a run that consists in re-using the PSF. The number of times the PSF is used/recycled is defined through the NRCYCL input parameter. Along with this particle recycling strategy, ISMOOTH is used to redistribute the recycled particles about the central axis of the linac beam. Recycling can, nonetheless have a significant effect on the final statistical uncertainty of the dose , possibly creating correlations between particles in the PSF. This effect is much more considerable for electron than for photon beams [95]. In this work, a maximum of 20 recycling factors was used in the dose calculations except for the closed fields, for the adjustment of the MLC parameters.

The results of MC simulations are not immediately comparable to absolute dose calculations and in the commissioning process, relative (normalized) curves are generally used. However, for the calculation of dose distributions, absolute dose is important and depends on the MU necessary to administer the patient in predetermined conditions. In the case of the linac used, 1 UM corresponds to 1 cGy at an SSD of 100 cm, at 10 cm in depth, for a 10 x 10 cm^2 field. It is not possible to simulate all the particles that are present in a single MU (6.23×10^{10} keV per cm^3, of water). The number of source particles are restricted to the smallest value capable of producing the desired statistical accuracy, in order to minimize the calculation time. A calibration process is required to obtain the desired absolute dose values.

3.9 Simulation and validation of the High Definition MLC using Monte Carlo

This section presents the MC simulations performed for the modeling and validation of the Trilogy linac equipped with a HD120 MLC, never previously modeled and simulated. These results were published in Medical Physics journal [132].

Monte Carlo modeling and simulations of the High Definition (HD120) micro MLC and validation against measurements for a 6 MV beam

C. Borges[a)]
MedicalConsult SA, Campo Grande n°56 8A 1700-093 Lisboa, Portugal

M. Zarza-Moreno
Faculdade de Ciências e Tecnologia da Universidade Nova de Lisboa, 2829-516 Caparica, Portugal

E. Heath
Department of Physics, Ryerson University, 150 Victoria Street. Toronto, Ontario M5B 2K3, Canada

N. Teixeira
Escola Superior de Tecnologias da Saúde, Av. D. João II, Lote 4.69.01 1990 - 096 Lisboa, Portugal

P. Vaz
Instituto Tecnológico e Nuclear, Estrada Nacional 10, 2686-953 Sacavém, Portugal

(Received 23 August 2011; revised 23 November 2011; accepted for publication 1 December 2011; published 27 December 2011)

Purpose: The most recent Varian® micro multileaf collimator (MLC), the *High Definition* (HD120) MLC, was modeled using the BEAMNRC Monte Carlo code. This model was incorporated into a Varian medical linear accelerator, for a 6 MV beam, in static and dynamic mode. The model was validated by comparing simulated profiles with measurements.
Methods: The Varian® Trilogy® (2300C/D) accelerator model was accurately implemented using the state-of-the-art Monte Carlo simulation program BEAMNRC and validated against off-axis and depth dose profiles measured using ionization chambers, by adjusting the energy and the full width at half maximum (FWHM) of the initial electron beam. The HD120 MLC was modeled by developing a new BEAMNRC component module (CM), designated HDMLC, adapting the available DYNVMLC CM and incorporating the specific characteristics of this new micro MLC. The leaf dimensions were provided by the manufacturer. The geometry was visualized by tracing particles through the CM and recording their position when a leaf boundary is crossed. The leaf material density and abutting air gap between leaves were adjusted in order to obtain a good agreement between the simulated leakage profiles and EBT2 film measurements performed in a solid water phantom. To validate the HDMLC implementation, additional MLC static patterns were also simulated and compared to additional measurements. Furthermore, the ability to simulate dynamic MLC fields was implemented in the HDMLC CM. The simulation results of these fields were compared with EBT2 film measurements performed in a solid water phantom.
Results: Overall, the discrepancies, with and without MLC, between the opened field simulations and the measurements using ionization chambers in a water phantom, for the off-axis profiles are below 2% and in depth-dose profiles are below 2% after the maximum dose depth and below 4% in the build-up region. On the conditions of these simulations, this tungsten-based MLC has a density of 18.7 g cm^{-3} and an overall leakage of about $1.1 \pm 0.03\%$. The discrepancies between the film measured and simulated closed and blocked fields are below 2% and 8%, respectively. Other measurements were performed for alternated leaf patterns and the agreement is satisfactory (to within 4%). The dynamic mode for this MLC was implemented and the discrepancies between film measurements and simulations are within 4%.
Conclusions: The Varian® Trilogy® (2300 C/D) linear accelerator including the HD120 MLC was successfully modeled and simulated using the Monte Carlo BEAMNRC code by developing an independent CM, the HDMLC CM, either in static and dynamic modes. © *2012 American Association of Physicists in Medicine*. [DOI: 10.1118/1.3671935]

Key words: Monte Carlo, linear accelerator, radiotherapy, micro multileaf collimator, dosimetry

I. INTRODUCTION

Micromultileaf collimators are widely used in the treatment of lesions, in techniques such as stereotactic radiotherapy and radiosurgery,[1] mainly applied to brain cancers, nonmalignant brain lesions,[2,3] and small-cell lung tumors.[4] Typically, these are small lesions which require high doses, being extremely important to minimize the exposure to radiation of the surrounding healthy tissue. Therefore, highly conformed fields are required. The HD120 multileaf collimator (MLC) is the most recent Varian (Varian Oncology Systems, Palo Alto, CA) MLC which fulfills this requirement, possessing 64 inner

and 56 outer leaves whose width projects to 2.5 and 5.0 mm, at the linac isocenter, respectively.

Multileaf collimators consist of banks of tungsten leaves[5] that allow shaping of conformal or intensity modulated fields. Due to the complex design of these devices, they are among the most challenging geometrical structures to implement in a linac model to perform Monte Carlo (MC) simulations. The leaf openings can be individually user-defined to set irregular shapes to conform to nonsymmetric volumes. Furthermore, the leaves have complex geometries and can even move during beam delivery (dynamic MLC). Modeling the details of the MLC using MC methods is considered of primordial importance to fully account for the loss of electronic equilibrium and for the effects of the MLC tongue and groove,[6] leaf transmission, leaf side and end transmissions, and abutting leaf leakage, which have a significant impact on the penumbra and ultimately on patient dose calculations.[7]

BEAMNRC (Ref. 8) is a tool used worldwide to model and simulate the behavior of linear accelerators used in radiotherapy. There are several multileaf collimators available in the market from different manufacturers. Their characteristics change according to the linac specifications. Several papers have been published on BEAMNRC simulations of different MLCs: Elekta,[9] BRAINLAB M3,[10] Millennium 120.[11]

In BEAMNRC, there was no component module (CM) that could directly be adapted to adequately model the Varian HD120 MLC as its design is unique, so far. The BEAMNRC CM VARMLC,[12] one of the first CM developed for MLC, does not fully account for some physical properties of Varian MLCs such as the leaf tips, driving screw holes, and supporting rail grooves. However, some studies prove that this CM can be used, with modifications and approximations to simulate MLCs.[10,13]

The most commonly MLC implemented in radiotherapy facilities, using Varian® accelerators, is the Millennium MLC, which has three types of leaves: full, half target and half isocenter with projected widths at 100 cm of 10 mm, 5 mm, and 5 mm, respectively. This collimator was modeled in an independent CM, DYNVMLC, by Heath and Seuntjens.[11] The strategy to fully model the MLC consists in dividing the leaves into geometrical regions. The leaves are composed by several individual simple regions that attenuate the particles as they traverse the entire MLC.[14] Nevertheless, due to its specificities the HD120 MLC cannot be modeled using the DYNVMLC CM.

The main purpose of this work was to develop a Monte Carlo model of this particular micro MLC and to incorporate it into the 6 MV photon mode of the 2300C/D Varian accelerator model either in static and dynamic modes.

II. MATERIALS AND METHODS

In this section, the methods and materials used for the simulations on BEAMNRC and the measurements, necessary for the validation of the linac without and with the HD120 MLC, are presented.

II.A. Monte Carlo simulations

A model of the Varian® Trilogy® (2300C/D) treatment head was implemented using the Monte Carlo software BEAMNRC (Refs. 15 and 16) (version 4-2-2-3). The detailed geometry of the linac head was kindly provided by Varian® and the specificities of each module in BEAMNRC were set according to the technical documentation provided. The accelerator model includes the target, the primary collimator, the flattening filter, the shield, the secondary collimator, the backup jaws, and the micro HD120 MLC. As the attenuation of the photon beam by the monitor ion chambers and the field mirror is negligible, these were not considered in the simulations.[17]

The code implementation for this accelerator was performed using BEAMNRC/EGSNRC (Refs. 15 and 16) and DOSXYZNRC (Ref. 18) was used for dose calculation in the phantom. Each simulation was run using four parallel jobs in a cluster of 2.2 GHz AMD Opteron processors at the Nuclear Physics Centre of the University of Lisbon.

In order to improve the efficiency and to decrease treatment head simulation times, some variance reduction techniques were used, such as range rejection, which terminates a charged particle's history and depositing all its energy in the current region, by setting ESAVE to 1.0 MeV except for the target, where it was set to 0.7 MeV, to guarantee lower energy photon production; uniform bremsstrahlung splitting was set to 20 to increase the number of photons created in the target; russian roulette was turned on and the photon forcing option, whereby photons are forced to interact in specified CMs, was not used. For both BEAMNRC and DOSXYZNRC simulations, the following transport parameters were defined[19]: PCUT = AP = 10 keV and ECUT = AE = 700 keV, where PCUT and ECUT define the global cutoff energy for photon and electron transport, respectively, and AP and AE are the low-energy thresholds for the production of secondary bremsstrahlung photons and knock-on electrons, respectively.

For the linac simulations, the phase space files containing the details of the position, direction and energy of the particles (photons, electrons, and positrons) at the exit of the treatment head, were generated for different sized-fields. After the phase space data were obtained, it was used as an input for DOSXYZNRC to calculate off-axis (inplane and crossplane) profiles at the source-to-surface distance (SSD) of 100 cm and percentage depth dose (PDD) profiles in the central axis.

The particle transport validation through the accelerator was performed in two steps: primarily only up to the jaws, to validate the model of the accelerator without the MLC, and afterward including the HD120 MLC.

II.A.1 Accelerator up to the jaws

The schematic representation of the Varian® Trilogy® linac head modeled and simulated and the components considered are displayed in Fig. 1.

Among the physical components of the linac head operating in photon mode, the modeling of the target is of

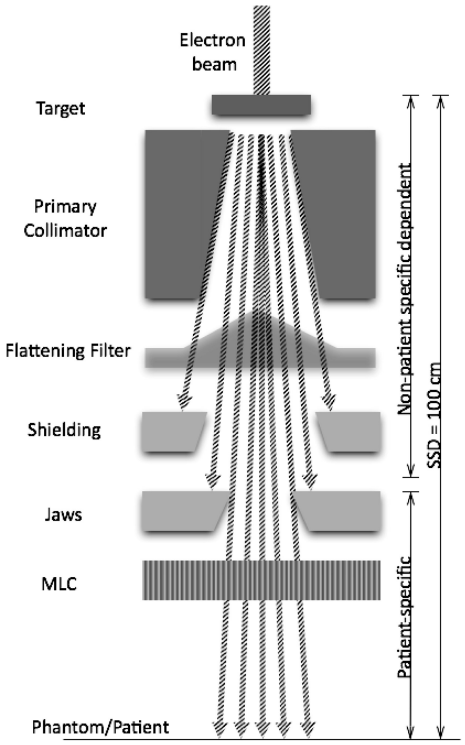

FIG. 1. Schematic overview of the simulated Varian® Trilogy® linac head. The different components considered in the model are displayed. The HD120 MLC may be present (if not retracted) after the jaws to conform to the volume to be irradiated.

paramount importance as it is the component where the beam main particles are produced.[20] The primary electron beam hits the high density target originating, mainly by bremsstrahlung interactions, photons. For the 6 MV beam, the target is made of two layers of different materials, tungsten and copper.[21] The manufacturer provided precise dimensions of the flattening filter which is meant to flatten a beam at a specific depth. The flattening filters' composition and density strongly influence the average energy of the beam.[22,23]

The jaws are the first collimators controlled by the user by changing their aperture to set the shape to the volume to irradiate. There are two pairs of tungsten jaws, one pair in the crossplane and the other pair in the inplane.

The initial electron beam energy was modeled as a parallel beam, with a Gaussian intensity distribution and a monoenergetic spectra, as also described in previous studies.[24,25] There are different methods to determine the parameters of the electron beam incident on the target, as these may vary within linacs of the same model.[26–28] The method applied in this study was an iterative approach, described by Sheikh-Bagheri and Rogers.[22] According to this work, combinations of energies and radius [full width at half maximum (FWHM) of the 2D Gaussian distribution in the X-direction] of the initial electron beam that impinges on the target were simulated in order to achieve a satisfactory match between the simulations and the experimental measurements.[29,30] The beam energy was tuned to match the PDD curves and the size of the initial electron beam was varied to match lateral dose profiles for a 30×30 cm^2 field. The energy of the incident electron beam was varied from 5.6 to 6.8 MeV in steps of 0.2 MeV. Three values for the radius of the initial electron beam were investigated: 0.8, 1.0, and 1.2 mm.

The simulations of the accelerator were run in two parts: first, the linac was simulated only with its fixed components (before the jaws, see Fig. 1); this output phase space file was then used to simulate the patient-specific part of the accelerator which consists on the jaws and, if present, the MLC configurations under investigation. The phase space files were scored at a distance of 100 cm from the front face of the target. These phase space files were then provided as input to the DOSXYZNRC to calculate the dose distributions in a water phantom. The calculated lateral and PDD profiles of squared fields of 3, 5, 10, 15, and 30 cm^2 were compared to the corresponding experimental measurements.

About 5×10^8 electrons were run in BEAMNRC for simulating the fixed part of the accelerator. This phase space file, containing mainly photons but also electrons and positrons, was then used for the simulation of jaw-defined fields: for smaller than 5×5 cm^2, about 1.5×10^9 particles (mainly photons) were used whereas for the larger fields (larger than 10×10 cm^2), 10^9 particles scored in the phase space file were simulated. In DOSXYZNRC, about 10^9 photons were simulated in the water phantom for the smaller fields and about 2×10^9 particles for the larger opened fields, in order to obtain a maximum uncertainty of 2% (2 SD) and to avoid excessive incident particle recycling. Recycling particles affects the statistics by increasing the dose uncertainties; however, these effects are less dramatic for photons along the central axis.[31]

II.A.2. Accelerator including the HD120 MLC

The micro HD120 MLC consists of two banks with 60 leaves pairs each, driven by independent motors, computer controlled from a remote location. This specific MLC has two different types of tungsten leaves: 32 central leaves of 2.5 mm in width (quarter leaves) and the 28 outer leaves of 5.0 mm width (half leaves). All reported dimensions are projected at the linac isocenter. Furthermore, these two types of leaves are arranged in an alternated way in which isocenter leaves (thicker end of the leaf is toward the isocenter) and target leaves (thicker end of the leaf is toward the target) are intercalated. The material of the leaves is a tungsten alloy whose density may vary, depending on the alloy composition and leaf manufacturing. The geometry and constituent materials of the HD120 MLC were implemented according to the manufacturers' data. The tungsten-based MLC alloy used in the simulations was composed by 90% ^{74}W, 6% ^{28}Ni, 2.5% ^{29}Cu, and 1.5% ^{26}Fe, as it is the same material as for the Millennium MLC.[11] The upper edge of the MLC, Z_{min}, was specified to be 47 cm below the target; the interleaf gap was set to 0.0047 cm. The leaf ends are rounded with a radius of

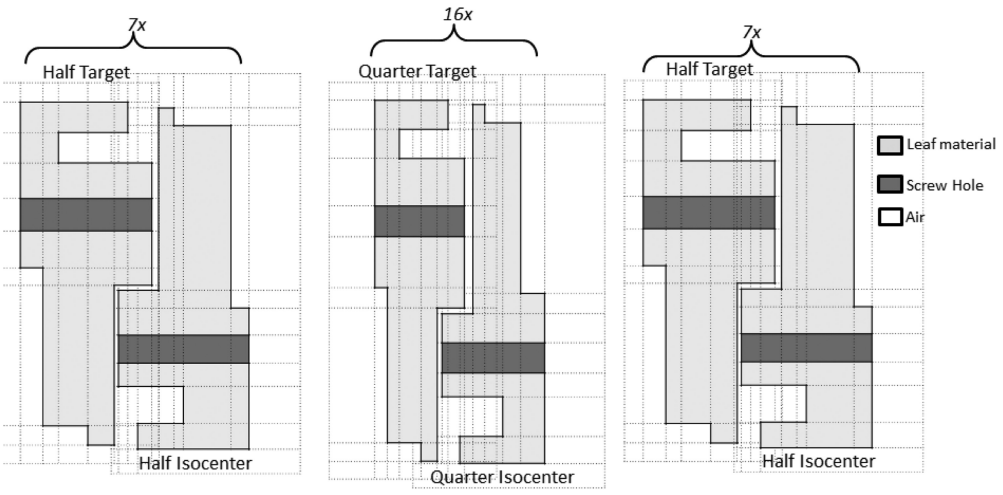

FIG. 2. Schematic representation of the HD120 MLC geometry. This MLC has half and quarter tungsten-based alloy leaves. Both types of leaves have target and isocenter leaves. Drawings not to scale.

curvature of 16 cm and the leaves are 6.9 cm thick. A schematic drawing of the MLC is shown in Fig. 2.

A new BEAMNRC CM, designated HDMLC CM was developed to include the specific characteristics of this MLC by making modifications to the original DYNVMLC CM to include half target and half isocenter leaves as outer leaves and quarter target and quarter isocenter leaves as inner leaves. Their geometries were changed in the DYNVMLC_macros.mortran and DYNVMLC_cm.mortran files of BEAMNRC and these files were called HDMLC_macros.mortran and HDMLC_cm.mortran, respectively. In the input file, the details of the leaves such as the dimensions of the tongue, groove, screw holes and rails were specified at Z_{min}.

The maximum opening dimensions of this MLC, projected at the isocenter are 22 cm by 40 cm, in the inplane (y) and in the crossplane (x), respectively, with the collimator at 0°. The leaves of this MLC can be set moving along the x direction, to different shapes and to guarantee conformity to the volumes to treat.

The MLC model in the DYNVMLC component module divides the MLC leaves into several geometrical regions which together represent, as realistically as possible, the MLC geometry. The relevant simulation parameters, namely, the abutting leaf gap, the MLC density, and Z_{min}, were adjusted in order to minimize the discrepancies between the simulation results and the measurements performed. In order to avoid damages that would result from physical collisions between the leaves, there is a small air gap between opposing leaves. Due to this feature, and the fact that the leaf ends are rounded, simulations of the leakage between opposing leaf pairs had to be further investigated. Therefore, simulations of a closed field (MLC closed at the center $x = 0$ and the jaws set to 10×10 cm^2) were done to determine the abutting leaf gap.[11] An open 10×10 cm^2 field with the MLC retracted and the same field with the MLC leaves closing beyond the jaws (blocked field), varying the MLC material density, were simulated in order to estimate the transmission properties of the HD120 MLC. Z_{min} was adjusted by comparing simulated and measured alternated leaf pattern fields. The blocked and closed fields were measured using film dosimetry in a solid water phantom and the alternated fields using a diode in a water phantom, at the SSD of 100 cm, at 5 cm depth. For the closed and blocked fields, 16×10^9 particles were simulated in BEAMNRC. For the closed field about 4×10^7 particles reached the water phantom surface; whereas for the blocked field, the number of particles at this level was approximately of 2.4×10^7 particles. These particles were used in the DOSXYZNRC for simulating 1.0×10^9 particles in the phantom. The voxel size used was 1×1 mm^2 for both the inplane and the crossplane and 2 mm in depth. On these simulations, incident photons were recycled about 20 times for the closed field and approximately 40 times for the blocked field, to guarantee a 3% (1 SD) statistical uncertainty.

To perform the validation of the MLC, taking into consideration the rounded edge leaves implemented in the model, opened MLC-defined fields of different sizes were simulated. The computational conditions were similar to the opened fields only defined by the jaws, as previously defined.

Other fields with irregularly shaped patterns were also simulated, in order to validate the model of tongue and groove design implemented with the HDMLC CM.

Accurate dose calculations for segmental MLC or dynamic MLC (dMLC) is even more challenging and Monte Carlo simulations are recognized as the most accurate methodology for patient dose assessment. For simulating complex types of treatments in radiotherapy such as IMRT (Intensity Modulated Radiation Therapy), all the characteristics of the MLC leaves have to be taken into account.[11,14,32] The method for implementing the dynamic mode was the same used by Heath and Seuntjens.[11] An MLC sequence file generated by the planning system or the user with the different MLC projections at 100 cm as a function of the fractional monitor units of the total beam delivery was used in the

input file for transporting the particles through the MLC. The particles that traverse the MLC are written to a phase space file that is used as input for MC calculations in the water phantom.[14]

II.B. Measurements

In order to validate the simulations, measurements were performed in a Trilogy® Varian® linac using a 0.125 cm^3 PTW®, model 31001, ionization chamber in a water phantom PTW FREIBURG®, model 41006. The phantom was connected to the PTW® software MEPHYSTO MCC to automatically control the phantom for data acquisition of dose distribution and analysis of radiation profiles. A p-type silicon PTW® diode, model 60016, was used for measuring fields smaller than 5×5 cm^2 and to measure the alternated MLC field. The uncertainties associated with the ionization chamber system acquisition are estimated to be about 2%, according to the IAEA TRS 398 protocol.[33]

For the validation of the HDMLC, measurements were also performed using GAFCHROMIC® EBT2 films placed into a solid water phantom. Measurements were performed at the SSD of 100 cm, at 5 cm depth in the phantom, to match the conditions defined in the simulations. The films were processed in an *Epson 10000XL* flatbed scanner and analyzed in the software FILMQA™. The EBT2 film uncertainty is considered to be about 3% according to recent work.[34]

An independent perpendicular film calibration was performed, to convert optical density into dose for each profile, by exposing different parts of the film to different monitor units (MU), ranging from 0 cGy to 230 cGy, at 5 cm in a solid water phantom.

For the blocked field, the film was irradiated with 10 000 MU and the closed field was irradiated with 800 MU. An opened field of 10×10 cm^2 was irradiated with 200 MU to assess the transmission characteristics of the MLC. To verify irregular shaped-fields, a repeated pattern consisting of one leaf closed and two leaves opened was measured using a photon diode in a water phantom. The dose distributions of the dynamic fields were measured using film dosimetry.

III. RESULTS AND DISCUSSION

The validation of the implemented computational model for the Varian® Trilogy® linear accelerator for the 6 MV beam was done by comparison of the measurements performed without and with the HD120 MLC incorporated.

III.A. Accelerator up to the jaws

The best agreement between the Monte Carlo simulation results and the measurements performed was obtained for an incident electron energy of 5.8 MeV and a Gaussian intensity profile with a FWHM of 0.12 cm. The comparison between the calculated PDD and off-axis profiles and the measurements performed using ionometric dosimetry are displayed in Fig. 3, for several square fields.

Analyzing the phase space files, in all the opened fields, more than 5×10^7 particles were scored after the jaws, from which 99.7% were photons whilst the remaining were electrons and positrons.

For the beam profiles, the MC statistical uncertainty is below 2% (2 SD), for all fields. Differences of about 2% were obtained for the flat region of all the fields when comparing the experimental results with the simulations.

When comparing the simulated PDD curves with the corresponding measured curves, the results in the build-up region present discrepancies lower than 4% and 2% before and after the build-up region, respectively.

III.B. Including the HD120 MLC

The geometry and constituent materials of the HD120 MLC were implemented according to the manufacturers'

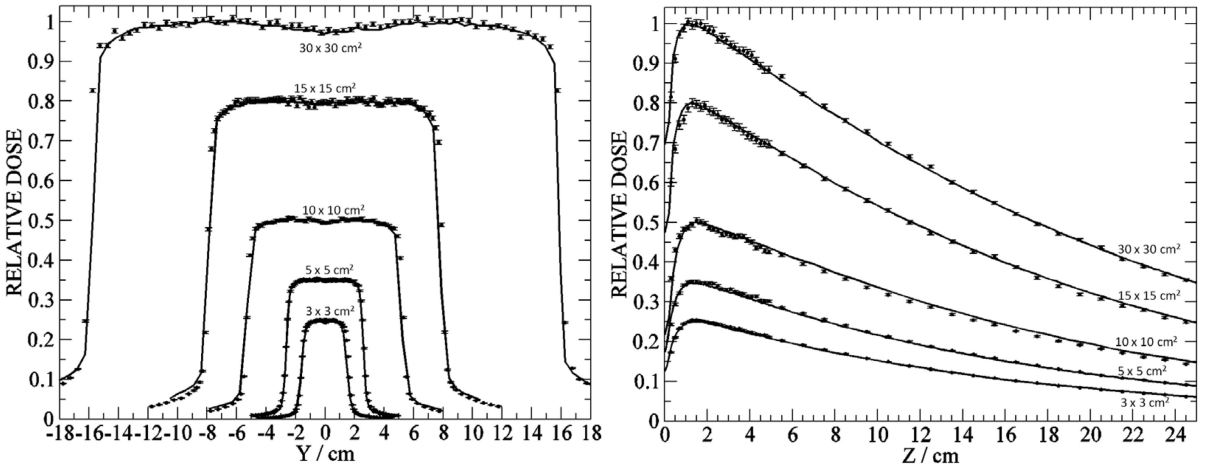

FIG. 3. Validation of the simulations of the Trilogy accelerator up to the jaws using ionometric dosimetry: on the left, lateral profiles, of the squared fields 30, 15, 10, 5, and 3 cm^2, at 5cm depth; on the right, depth dose profiles of the squared fields 3, 5, 10, 15, and 30 cm^2. The maximum dose values of the profiles of 30, 15, 10, 5, and 3 cm^2 fields were normalized to 1, 0.8, 0.5, 0.35, and 0.25, respectively. The continuous lines correspond to the film measurement whereas the full dots correspond to the MC simulation.

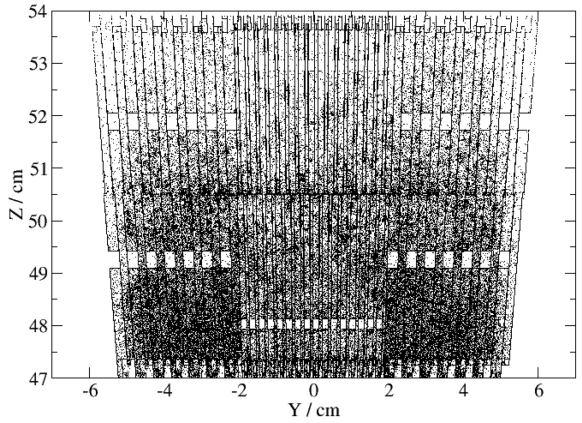

FIG. 4. Ray tracing of the HD120 MLC. The leaf geometry (XZ plane) was visualized by tracing particles through the CM and recording their position when a leaf boundary is crossed.

data. The relevant simulation parameters, namely the abutting leaf gap, the MLC density and Z_{min}, were adjusted in order to minimize the discrepancies between the simulation results and the measurements performed. The abutting leaf gap was assessed by simulating a closed MLC field; the MLC material density was determined with a blocked field in which the MLC closed beyond the jaws opening and Z_{min} was adjusted using alternated leaf pattern fields. The blocked and closed fields were measured using film dosimetry in a solid water phantom and the alternated fields using a diode in a water phantom, at the SSD of 100 cm, at 5 cm depth.

III.B.1. Ray tracing

After the HD120 MLC was implemented, its geometry was visualized by tracing particles produced through the CM and recording their position when a leaf boundary is crossed. These positions were then plotted in 2D projections, as shown in Fig. 4.

On Fig. 4, from the left to right, there are the 14 half, 32 quarter, and 14 half leaves, respectively, in each bank; target leaves are intercalated with isocenter leaves. It is possible to visualize the details of the leaves such as the driving screw holes, as air gaps, in the widest part of the leaves, and top and end details of the leaves.

III.B.2. Tuning of the MLC: assessment of the density of the leaves and of the abutting gap

The MLC leakage radiation, obtained by Monte Carlo simulations varying the MLC material density was compared with film measurement in a direction perpendicular to the leaf motion. Simulations were performed with densities ranging from 17.0 to 19.0 g cm^{-3} and it was observed that the material density is one of the properties that affect the radiation profile that traverses the MLC. For the densities of 17.0, 17.5, 18.0, 18.5, 18.7, and 19.0 g cm^{-3}, the following average interleaf leakage values obtained were 1.55%, 1.44%, 1.26%, 1.15%, 1.10%, and 1.03%, respectively. The MC simulation uncertainties are about 2% (1 SD). The best agreement between simulation results and measurements is displayed in the left plot of Fig. 5 and was obtained for a density value of 18.7 g cm^{-3}. With this result it is possible to estimate an average interleaf leakage of about 1.10% ± 0.03%, in the central part of the MLC. The profiles presented in Fig. 5 are normalized to the open 10×10 cm^2 field. The maximum discrepancy between the dose peaks and troughs comparing film dosimetry with the simulations is of 15%. The average discrepancies between the simulation and measurement are about 8%. These discrepancies were accepted as the film is only exposed to low doses and its response in this range of doses is sensitive making these measurements very challenging, even using radiochromic EBT2 films.[35]

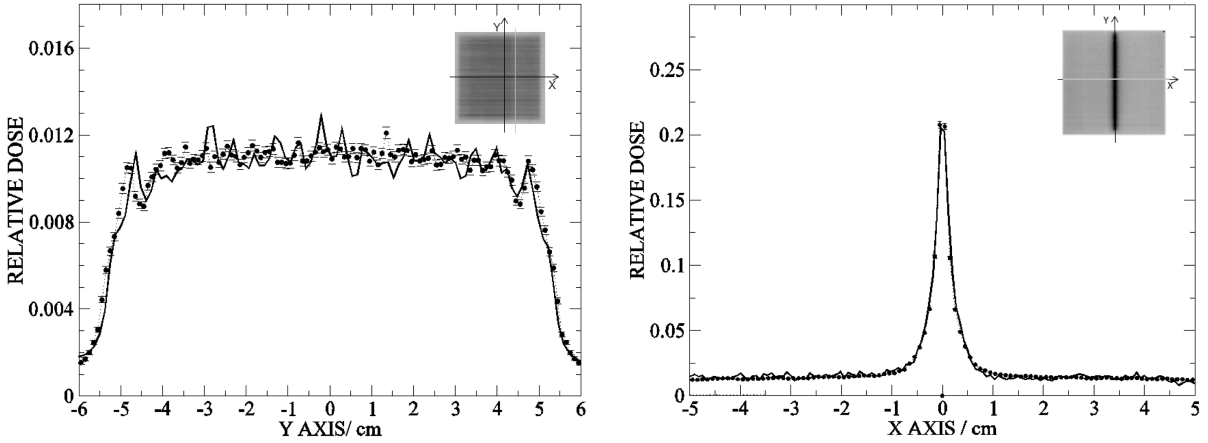

FIG. 5. Comparison of 6 MV MLC leakage profiles at the positions indicated by the lighter lines on the figures located inside the graphs, on their top right corners. On the left, determination of the leaf density using a MLC-blocked field, profile taken at 1 cm offset from the central axis, with a density of 18.7 g cm^{-3}. On the right, assessment of the abutting gap between leaves of 0.03 cm, in the central axis. The continuous line corresponds to the film measurement whereas the full dots correspond to the MC simulation. The results were normalized to the opened 10×10 cm^2 field.

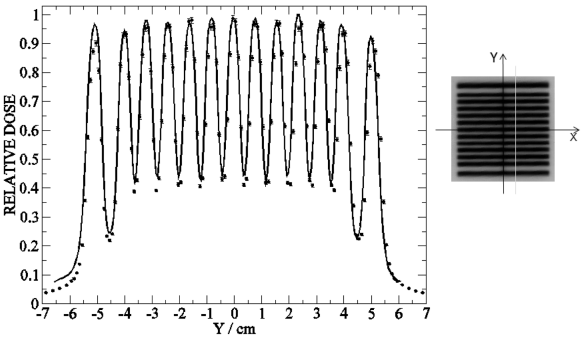

FIG. 6. Comparison of 6 MV off-axis profiles, at +1 cm off-axis from the central axis for a static MLC pattern with two leaves opened and one closed alternately, as represented by the film image placed in the right side of the figure. The results are normalized to 1, for the maximum dose; the continuous line represents the measurements, whereas the dots correspond to the simulation result using the HDMLC CM.

The abutting gap was determined by simulating a closed field in the central axis, with the collimator set to 0°. Several simulations were performed in these conditions, with abutting gaps ranging from 0.002 to 0.04 cm (in 0.002 cm steps up to 0.01 and 0.01 cm steps from 0.01 to 0.04 cm). The simulation result that best reproduces the measurements is displayed in Fig. 5 (right) and corresponds to an abutting gap of 0.03 cm. The leakage between abutting leaves is estimated to be $20.5 \pm 1\%$. The MC relative uncertainties are about 2% (1 SD) and the discrepancies between measurements and simulations are within 2%.

III.B.3. Irregular MLC pattern

A MLC static pattern was performed in order to evaluate how accurately the tongue and groove effect is handled by this new CM. This field is defined by a repeated pattern of one leaf closed and two leaves opened beyond the backup jaws which were set to 10×10 cm^2. The measurements were performed with the p-diode in a water phantom, at 5 cm depth, at the SSD of 100 cm. The profiles were taken in the inplane direction, at an offset of +1 cm from the central axis, as shown in the right side of Fig. 6. The relative dose distribution as function of the position is displayed in the graph of Fig. 6. Both the MC profile and the measurements were normalized to 1 as maximum relative dose. The MC relative uncertainties are about 2% (1 SD). A good agreement is visible, with discrepancies between the simulation results and the measurements below 4%.

III.B.4. Ionometric measurements

With all the details of the MLC defined, the opened fields of 2×2, 3×3, 5×5, 10×10, 15×15, and 30×22 cm^2 with the jaws set to 4×4, 5×5, 7×7, 12×12, 17×17, and 32×22 cm^2, respectively, were simulated. The obtained results were compared against the ionometric measurements performed using a water phantom with a 0.125 cm^3 ionization chamber for fields larger than 5×5 cm^2 and a photon diode for smaller fields. The off-axis profiles along the central axis, at 5 cm in depth and depth dose distribuitions are displayed in Fig. 7.

For the relative dose profiles, on the left, a good agreement between the computational results and the measurements is evident, as for most points, the simulated profiles agree with the measurements to within 2%; as for the PDD profiles, the discrepancies between the calculated and the measured profiles are at the level of 2% after the build-up region and within 4% in the build-up region, for all fields.

III.B.5. Dynamic mode

As the HD120 MLC has been designed to perform IMRT treatments, its dynamic mode of operation was implemented in BEAMNRC. The implementation method used was similar to the one existing for the DYNVMLC CM. The comparison

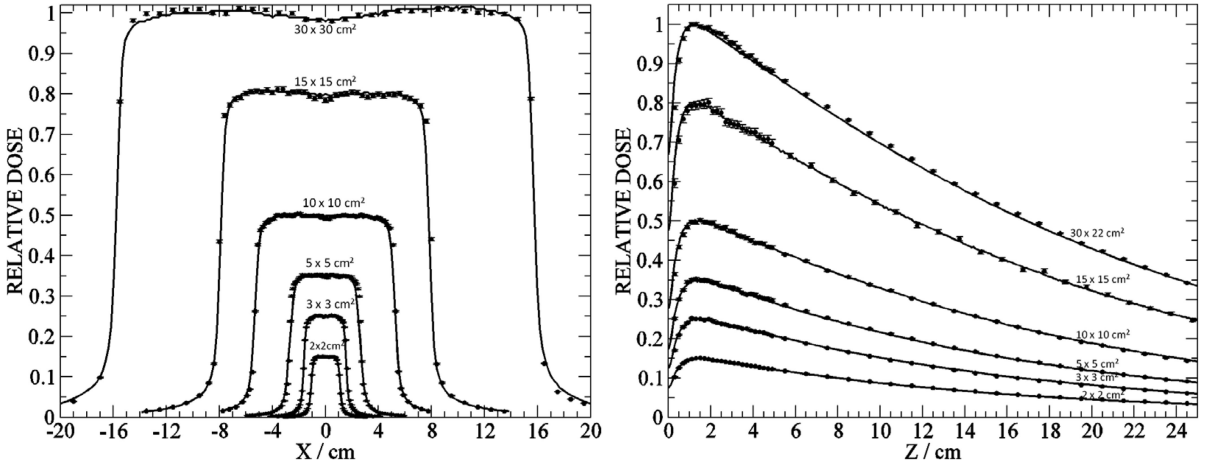

FIG. 7. Comparison of off-axis (on the left) and PDD (on the right) profiles of the opened MLC-defined fields of 2×2, 3×3, 5×5, 10×10, 15×15, and 30×22 cm^2, normalized to the 0.15, 0.25, 0.35, 0.5, 0.8, and 1.0 the maximum dose, respectively, at 5 cm in depth. The dots correspond to the MC simulation results whereas the continuous lines correspond to the measurements.

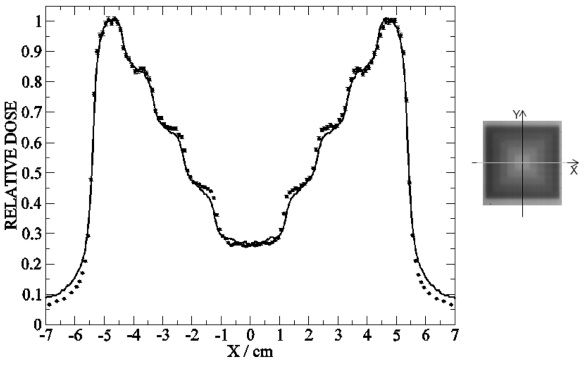

FIG. 8. Dynamic MLC field of an inverse pyramid: the continuous line corresponds to the film measurement; the full dots represent the Monte Carlo simulation result. The results were normalized to the maximum dose.

between the obtained simulated result and the film measurement performed is displayed in Fig. 8.

The MC uncertainties are at the level of 2% (2 SD). The discrepancies between the simulated results and the measurements are below 5% with exception of the penumbrae region, presumably due to the poor response of EBT2 films to low dose. It is also possible to notice that the higher discrepancies occur at the field edges presumably due to inadequate resolution of the film calibration curve at low dose levels and the film energy dependence response to low dose scattered photons.[36]

IV. CONCLUSIONS

The Varian® Trilogy® (2300 C/D) linear accelerator including the HD120 MLC was successfully modeled and simulated using the Monte Carlo BEAMNRC code and the newly developed CM, HDMLC CM.

In a first step, the linac was modeled in the absence of MLC; the nominal value of the mean energy and the parameters characterizing the spatial distribution of the primary electron beam used in the MC simulations were determined as those values which minimize the discrepancies between the Monte Carlo simulation results and the measurements performed, for the depth dose distributions and off-axis profiles in a water phantom.

Overall, a good agreement between the MC simulations and the measurements performed using ionometric and film dosimetry was obtained; for the off-axis profiles the discrepancies between the simulation results and the measurements are smaller than 2%, whilst for the PDD distributions the discrepancies are smaller than 2% after the build-up region and below 3% in the build-up.

In a second step, the HDMLC CM, was implemented in BEAMNRC in order to model the specific characteristics of the new *High Definition* multileaf collimator (HD120 MLC) equipping the aforementioned Varian® linac. The HDMLC CM was developed adapting the DYNVMLC CM created by Heath and Seuntjens.[11] With the HDMLC CM it is possible to simulate the micro HD120 MLC using either static or dynamic fields and taking into account the transmission, effect of tongue and groove design of the leaves.

The specific characteristics of the HD120 MLC were assessed using film dosimetry (GafChromic EBT2). The agreement achieved for the closed and blocked fields was about 2% and 8%, respectively, considered satisfactory due to the nature of the measurement involving low doses. The validation of the implemented computational model against measurements was also performed for other irregular static MLC patterns. The discrepancies between MC simulation results and measurements for an alternated pattern are about 4%. Measurements on off-axis and PDD profiles using ionization chambers were compared to the correspondent simulations for opened MLC-defined fields. The discrepancies were found to be about 2% for the off-axis profiles and below 5% in the build-up region and about 2% after the point of maximum dose for the PDD profiles. The dynamic mode of the MLC was implemented in BEAMNRC and a reasonable agreement was obtained, with discrepancies within 4% between simulated results and measurements using film.

The newly developed HDMLC CM fully models the details of the four different types of leaves taking into account the contribution of leaf leakage scatter and tongue and groove effects. This is of paramount importance when patient dose distributions are considered. The new *High Definition* MLC is now modeled by an independent BEAMNRC CM, HDMLC, to accurately simulate radiotherapy treatments, using Monte Carlo techniques, either in static and dynamic modes.

ACKNOWLEDGMENTS

Varian Medical Systems (Palo Alto, CA) are sincerely acknowledged for having provided all the specifications needed for the linac simulations. The authors express their thanks to Quadrantes, Centro Oncológico Dra Natália Chaves (Portugal) for providing the logistic resources.

[a]Author to whom correspondence should be addressed. Electronic mail: cissa9@gmail.com

[1]A. Dhabaan *et al.*, "Dosimetric performance of the new high-definition multileaf collimator for intracranial stereotactic radiosurgery," J. Appl. Clin. Med. Phys. **11**(3), 197–211 (2010).

[2]Q. Wu *et al.*, "Impact of collimator leaf width and treatment technique on stereotactic radiosurgery and radiotherapy plans for intra- and extracranial lesions," Radiat. Oncol. **4**, 3 (2009).

[3]M. Ding, F. Newman, C. Chen, K. Stuhr, and L. Gaspar, "Dosimetric comparison between 3DCRT and IMRT using different multileaf collimators in the treatment of brain tumours," Med. Dosim. **34**, 1–8 (2009).

[4]J. Tanyi *et al.*, "Implications of high-definition multileaf collimator (HD-MLC) on treatment planning techniques for stereotactic body radiation therapy (SBRT): A planning study," Radiat Oncol. **4** (2009).

[5]A. Boyer *et al.*, "Basic applications of multileaf collimators," Report of Task Group No 50 Radiation Therapy Committee, AAPM Report No. 72 (Medical Physics Publishing, Madison, WI, 2001).

[6]J. Deng *et al.*, "The MLC tongue-and-groove effect on IMRT dose distributions," Phys. Med. Biol. **46**, 1039–1060 (2001).

[7]S. Y. Jang, O. N. Vassiliev, H. H. Liu, R. Mohan, and J. Siebers, "Development and commissioning of a multileaf collimator model in Monte Carlo dose calculations for intensity-modulated radiation therapy," Med. Phys. **33**, 770–781 (2006).

[8]D. W. O. Rogers, B. A. Faddegon, G. X. Ding, C.-M. Ma, and J. We, "BEAM: A Monte Carlo code to simulate radiotherapy treatment units," Med. Phys. **22**, 503–524 (1995).

[9]J. Van de Walle, C. Martens, N. Reynaert, H. Palmans, and M. Coghe, "Monte Carlo model of the Elekta SLiplus accelerator: Validation of a new MLC component module in BEAM for a 6 MV beam," Phys. Med. Biol. **48**, 371–785 (2003).
[10]J. Belec, H. Patrocinio, and F. Verhaegen, "Development of a Monte Carlo model for the Brainlab microMLC," Phys. Med. Biol. **50**, 787–799 (2005).
[11]E. Heath and J. Seuntjens, "Development and validation of a BEAMnrc component for accurate Monte Carlo modelling of the Varian dynamic Millenium multileaf collimator," Phys. Med. Biol. **48**, 4045–4063 (2003).
[12]A. Kapur, C.-M. Ma, and A. L. Boyer, "Monte Carlo simulations for multileaf-collimator leaves: Design and dosimetry," *World Congress on Medical Physics and Biomedical Engineering*, Chicago, Illinois (2000), Vol. 27.
[13]T. Kairn *et al.*, "Technical Note: Modeling a complex micro-multileaf collimator using the standard BEAMnrc distribution," Med. Phys. **37**, 1761–1767 (2010).
[14]J. V. Siebers, P. J. Keall, J. O. Kim, and R. Mohan, "A method for photon beam Monte Carlo multileaf collimator particle transport," Phys. Med. Biol. **47**, 3225 (2002).
[15]D. W. O. Rogers, B. Walters, and I. Kawrakow, "BEAMNRC Users Manual," NRCC Report No. PIRS-0509(A) rev.K (2009).
[16]I. Kawrakow, E. Mainegra-Hing, D. W. O. Rogers, F. Tessier, and B. R. B. Walters, "The EGSnrc code system: Monte Carlo simulation of electron and photon transport," NRCC Report No. PIRS-701 (2010).
[17]J. V. Siebers, P. J. Keall, B. Libby, and R. Mohan, "Comparison of EGS4 and MCNP4b Monte Carlo codes for generation of photon phase space distributions for a Varian 2100C," Phys. Med. Biol. **44**, 3009–3026 (1999).
[18]B. Walters, I. Kawrakow, and D. W. O. Rogers, "DOSXYZNRC Users Manual," NRCC Report No. PIRS-794revB (2009).
[19]D. Sheikh-Bagheri and D. W. O. Rogers, "Comparison of measured and Monte Carlo calculated dose distributions from the NRC linac," Med. Phys., 2256–2266 (2000).
[20]A. Faddegon, C. Ross, J. Sempau, J. Tinslay, and F. Salvat, "Benchmarking of Monte Carlo simulation of bremsstrahlung from thick targets at radiotherapy energies," Med. Phys. **35**, 4308–4317 (2008).
[21]B. Faddegon, B. Egley, and T. Steinverg, "Comparison of beam characteristics of a gold x-ray target and a tungsten replacement target," Med. Phys. **31**, 91–97 (2004).
[22]D. Sheikh-Bagheri and D. W. O. Rogers, "Sensitivity of megavoltage photon beam Monte Carlo simulations to electron beam and other parameters," Med. Phys. **29**, 379–390 (2002).
[23]A. Meshabi, "Dosimetric characteristics of unflattened 6MV photon beams of a clinical linear accelerator: A Monte Carlo study," Appl. Radiat. Isot. **65**, 1029–1036 (2007).
[24]D. A. Jaffray, J. J. Battista, P. Munro, and A. Fenster, "X-ray sources of medical linear accelerators: Focal and extrafocal radiation," Med. Phys. **20**, 1417–1427 (1993).
[25]A. Tzedakis, J. E. Damilakis, H. Varveris, and N. Gourtsoyiannis, "Influence of initial electron beam parameters on Monte Carlo calculated absorbed dose distributions for radiotherapy photon beams," Med. Phys. **31**, 907–913 (2004).
[26]K. Aljarrah, G. C. Sharp, T. Neicu, and S. B. Jiang, "Determination of the initial beam parameters in Monte Carlo linac simulation," Med. Phys. **33**, 850–858 (2006).
[27]J. Pena, M. Castaño, F. Gómez, F. S. Doblado, and G. H. Hartmann, "Automatic determination of primary electron beam parameters in Monte Carlo simulation," Med. Phys. **34**, 1076–1084 (2007).
[28]C.-M. Ma, B. A. Faddegon, D. W. O. Rogers, and X. Ding, "Accurate characterization of Monte Carlo calculated electron beams for radiotherapy," Med. Phys. **24**, 401–416 (1997).
[29]J. A. Antolak, M. R. Bieda, and K. R. Hogstrom, "Monte Carlo methods to commission electron beams: A feasibility study," Med. Phys. **29**, 771–786 (2002).
[30]M. R. Bieda, J. A. Antolak, and K. R. Hogstrom, "The effect of scattering foil parameters on electron-beam Monte Carlo calculations," Med. Phys. **28**, 2527–2534 (2001).
[31]B. Walters, I. Kawrakow, and D. Rogers, "History by history statistical estimators in the BEAM code system," National Research Council of Canada (NRCC), Ottawa, NRCC Report No. PIRS-0791 (2002).
[32]R. F. Aaronson, J. J. DeMarco, I. J. Chetty, and T. D. Solberg, "A Monte Carlo based phase space model for quality assurance of intensity modulated radiotehrapy incorporating leaf specific characteristics," Med. Phys. **27**, 2952–2958 (2002).
[33]International Atomic Energy Agency, "Absorbed dose determination in external beam radiotherapy," Technical Report Series No.398 (IAEA, Vienna, 1998).
[34]T. Aland, T. Kairn, and J. Kenny, "Evaluation of a Gafchromic EBT2 film dosimetry system for radiotherapy quality assurance," Australas. Phys. Eng. Sci. Med. **34**, 251–260 (2011).
[35]B. Hartmann, "Technical note: Homogeneity of Gafchromic EBT2 film," Med. Phys. **37**, 1753–1757 (2010).
[36]B. Arjomandy *et al.*, "Energy dependence and dose response of Gafchromic EBT2 film over a wide range of photon, electron, and proton beam energies," Med. Phys. **37**, 1942–1947 (2010).

Chapter 4

Breast treatment Radiotherapy techniques

Is the delivered dose, the real dose prescribed by the radiation oncologist?

There are three important and distinct concepts to the dosimetrists and physicists realities: what we want; what we see; what is real but we can not see.

In this chapter, the breast treatment techniques are presented along with the treatment plan calculation algorithms used throughout this work. The evaluation criteria for each of the techniques and algorithms are also provided.

4.1 RT to the breast

Breast cancer is a challenging site to treat due to its particular shape: the breasts are prominent concave structures, typically of homogeneous tissue, that are on top of the ribs (bone), right after the lungs and the heart (in the case of left breast) which are critical and essential organs. These are also highly heterogeneous media. Furthermore, with the lungs right underneath and the necessity of women to breath, there is also movement of the thoracic cavity. The skin is also an important tissue as radiogenic issues should be avoided.

The treatment plan in RT contains all the irradiation parameters of the treatment that will be administered to the patient. These included: the number of beams, their position, orientation, fluence distribution as well as the MU. These dose distributions are calculated by algorithms, given the prescribed dose and the

constraints. In a treatment plan, the dose distribution should be uniform on the target volume and the critical OAR should receive a dose inferior to the tolerance levels, specified by the institution protocol or the radiation oncologist. In the breast, it is difficult to obtain homogeneous dose distributions, due to the shape of the breast and the different densities of the types of tissues. Therefore, for some treatment plans of breast cancer, the dose distributions may be heterogeneous, with regions receiving doses superior to the prescription, leading to an increase in toxicity in the normal tissues and poor cosmetic results, or with under-dose regions which may result in the failure of tumor control and ultimately the goal of the treatment.

In particular for breast cancer, one of the main concerns is the occurrence of acute and late secondary effects, induced by radiation, once there are many patients being treated to this pathology and the survival rate is high, when compared to other pathologies. The acute symptoms induced by radiation can occur up to 6 months after RT, changing then to a chronic fibrous state. The complications due to breast RT can be classified into:

- Acute secondary effects (occur between the 2^{nd} and the 3^{rd} week after the RT start): radiodermitis, skin erythema, desquamation of the inframammary fold or the axillar fold (specially in large breasts), pruritis, fatigue and aching breast.

- Late secondary effects (occur 3 to 6 months after the RT conclusion): breast fibrosis, arm lymphedema, brachial plex dysfunction, reduction and/or breast hardening, pain and breast sensibility, shoulder tension, arm paralysis, rib fracture, pulmonary toxicity (such as radiogenic pneumonitis or apical pulmonar fibrosis) or cardiac toxicity (such as cardiac ischaemia symptomatic cardiac lesion, accelerated atherosclerosis or pericarditis). Some patients may even develop secondary tumors, related to the radiation exposition.

Moreover, the RT treatment after breast conserving surgery may be related to the increase of acute and late secondary effects, due to the unwanted exposure of healthy tissues to radiation, affecting the life quality of the patients and their survival possibilities. Thereby, the effects in the OAR are significant and constitute a real clinical problem, in breast cancer, in which the secondary effects may reduce the survival results aimed with RT. The awareness of the potential effects induced by radiation has been contributing to an extra effort to reduce the dose in the

healthy tissues, through new RT schemes, the re-definition of the target volume and new dose constraints.

However, it is not possible to completely avoid the exposure of the healthy tissues to the radiation. For left breast cancer patients, where the heart is unavoidably involved in the treatment radiation fields, there is scientific evidence [136, 137] in the increase of complications, especially on what the cardiovascular disease and mortality are concerned, when compared to right breast cancer patients. In this particular case, the cardiac mortality may decrease the survival rate of the breast patients and it is therefore important to analyze the risk of complications when planning the treatment.

Understanding the risk of late toxicity in the dose-volume relationships is clinically more relevant with the active investigation of new treatment techniques. However, the aim of increasing the cure has to be balanced with dose given to the normal tissues and their response to radiation. Any change in the treatment regimen, such as the use of advanced techniques, dose escalation, introduction of chemotherapy or other biologic agents, will change the therapeutic ratio. The challenge of the radiation oncologist is to guarantee that any change will improve this ratio and that a dose increase won't lead to secondary effects.

Current breast irradiation schemes in RT are whole breast irradiation or partial breast irradiation, as presented in the following.

4.1.1 Whole breast irradiation (WBI)

The principle of WBI is based on irradiating microscopic foci of mammary carcinoma in the mammary gland and in node-positive patients also loco-regional lymph nodes with doses of 50 Gy in 25 fractions delivered as daily treatment 5 days per week for 5 weeks. Large trials demonstrated this is a safe procedure with local failure rates of 0.5 –1% per year of follow-up and acceptable side effects and cosmetics [27]. The Early Breast Cancer Trialists' Collaborative Group (EBCTCG) systematic review [138] confirmed a 75% reduction in local recurrence risk after RT.

Over recent years, different techniques have been established for irradiating the breast. The techniques explored in this work for WBI are presented in section 4.4.

4.1.2 Accelerated Partial Breast Irradiation (APBI)

The local recurrence rate after breast conserving strategy has decreased steadily over the last decade due to improved surgery techniques, more effective chemotherapy and hormonal therapy, CT-based RT and also the criteria for offering the patients adjuvant therapy have decreased so that fewer patients are now classified low risk. The incidence of early breast cancer has peaked in the USA, and since 2002 also in Europe, and adjuvant breast RT is a heavy burden in the RT facilities [139].

The rationale for APBI is derived from studies reporting that the majority of first local relapses are in or close to the surgical cavity; on the assumption that radiotherapy does not prevent the development of new primary tumors developing elsewhere in the breast and on the wish to spare the patient late radiation morbidity. The reduction on treatment volume and increasing fraction dose, this form of treatment can be completed in a single week (significantly reducing the duration of the treatment when compared to WBI), allowing more patients to benefit from BCT. ASTRO Society recently published the first guidelines for APBI [140].

Many centers are now investigating partial breast irradiation in phase I and II trials. Large randomized phase III trials are running at the present time in North America (NBSABP/RTOG), Canada (OCOG\RAPID), Europe (GEC–ESTRO, IMPORT–LOW), Milan and UK (Targit) [141, 142].

The eligibility for BCT is assessed by clinical examination, imaging studies, pathology, individual preference, and expected cosmetic outcome (best with small tumor to large breast size). Considering a cost-effectiveness perspective [143] if a patient is randomized to APBI it can be performed using:

- RT delivered as 3D-CRT;
- intraoperative radiotherapy (IORT);
- interstitial brachytherapy: 34 Gy/10 fractions, with 2 fractions daily (5 days) using HDR (High Dose Rate); and
- MammoSite device

APBI and hypo-fractionated WBI are treatment approaches that promise both reduced overall treatment times and the potential for increased use of breast-conservation therapy [144, 145].

4.2 Breast cancer patient in the RT department for EBRT

4.2.1 Medical decision

The patient is indicated to the RT department after a multidisciplinary medical decision meeting. It is essential that the medical community identify the risk factors involved in the probable complication caused by radiation. The patient then goes to a first consultation with the radiation oncologist where she/he is informed of the benefits and risks when undergoing RT treatment. The patient is told about the treatment and how to minimize the probable radiation late effects. In some cases, the late damage effects are unavoidable when the cure is aimed. After all the indications, the patient decides whether to perform the treatment (or not) and in case of agreement, she/he signs an informed consent declaration.

4.2.2 Imaging

After the medical consensus that the patient gathers all the necessary conditions to perform RT, the patient undergoes a CT scan that is required for treatment planning.

4.2.2.1 CT considerations

For the purpose of this study, the slice thickness used was 3 mm and the images were acquired with the Siemens Biograph 64R, CT scanner that can be seen in figure 4.1.

The CT scanner is composed by two main systems:

- acquisition;
- signal treatment.

The acquisition system is made of a X-ray source and a detector. It provides the necessary information for the image reconstruction. The treatment signal system reconstructs the 2D or 3D image according to the scanner characteristics and the applied reconstruction methods. The CT slices provide 3D information on the tissue density distribution. The slices are then transferred to the TPS, so that:

FIGURE 4.1: CT scanner used for scanning the phantoms and the patients.

1. the radiation oncologist contours the target volumes and the OAR for planning the treatment; and,

2. the patient treatment dose calculations take into account the density variations of the different tissues involved.

4.2.2.2 Heterogeneities and electronic densities

The CT represents a precise geometry model of the patient, providing electronic density data necessary for the 3D dose calculations, taking into account the heterogeneities in the different tissues.

In practice, the patient is viewed as a volume divided into small elements, or voxels. To each voxel, it is associated a Hounsfield number (HU). The HU value of each voxel permits, through a calibration curve, to determine the electronic density of the tissue within the voxel and to characterize the x-ray interactions within that volume.

The HU are defined by:

$$HU = \left(\frac{\mu}{\mu_{water}} - 1 \right) \times 1000 \tag{4.1}$$

, where μ is the linear attenuation coefficient at the pixel position, which are dependent on the x-rays spectra of the CT-machine. In general, the CT numbers range between +1000 HU and -1000 HU from bone to air, respectively, while, by definition, the water has a CT number of 0 HU.

4.2.2.3 Breast patient CT scan

The patient is laid down in an immobilization device, the breast board (see figure 4.2), in supine position, with the ipsilateral arm lifted up, for arm comfort and to ensure a stable and reproducible position that will be repeated during the treatment course.

FIGURE 4.2: Breast board immobilization device.

Before the scan, the technician imprints marks at the patients' skin along the midline and the external border of the breast, for guidance while planning the treatment fields. A radiopaque wire is placed to mark the tangential field borders, which will remain marked during, at least, all the treatment sessions. The superior and inferior field borders are placed at about 2 cm beyond clinically palpable breast tissue. The medial border is set in the midline of the sternum, and the lateral border along the midaxillary line. A radiopaque wire may also be used to cover the surgical scar.

A representation of the imprinted marks is given in figure 4.3.

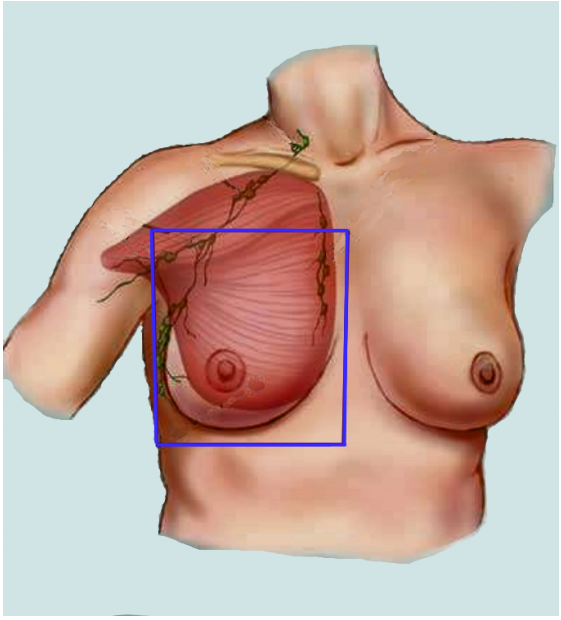

FIGURE 4.3: Schematic representation of the marks placed on the breast patient skin for helping contouring and positioning.

Then, the scan is acquired from the midneck (just below the mandible) to several centimeters caudal to the breasts, ensuring that the entire breast and the markers at the skin near the ipsilateral and contralateral lower axilla are included in the scan volume.

The CT planning is clearly superior to the previous 2D calculations based on orthovoltage orthogonal images, permitting to easily and precisely evaluate, the tumoral bed, the mammary gland and the adjacent structures like the heart, lung or contralateral breast exposed during the RT treatments, in terms of volume included in the beams and the dose they are exposed to. These conformal fields lead to using more beams, which are adjusted with the aid of the BEV (Beam's Eye View), to provide conformation confined to the target volume.

The 3D planning techniques demand rigorous quality control measurements, reproducibility of the patient positioning, using imaging acquisition so that the patient receives the planned dose and treatment. Conformal RT has reduced significantly the incidence of late adverse effects and improved the life quality of the patients, by reducing the healthy tissues volume irradiation.

4.2.3 OAR volumes involved in breast RT

Before planning, it is necessary that all the target volumes and OAR are contoured. The main OAR involved in breast RT treatment are:

- the lungs - mainly the ipsilateral one;
- the heart - particularly in left breast cancer;
- the medulla;
- the contralateral breast; and
- the esophagus.

Other considered structures may be the muscles and the ribs. The dose that reach these structures can be quantified visually by analyzing the dose distribution and graphically through dose-volume histograms. The dose tolerances are defined by the radiation oncologist and despite the goal to adequately irradiate the PTV, the dosimetrist plan aims at respecting these constraints.

The OAR can be located at a significant distance, in the vicinities or inside the PTV, and should be considered when planning the treatment. It may happen that the total dose may be limited by the dose to the OAR, in order not to exceed the limits. A careful assessment of the risks in the normal tissues, with the possible consequences of loss of tumor control needs to be done by the radiation oncologist. Not prescribing enough dose to the PTV may be more dangerous than exceeding the dose constraints in the OAR due to the increased risk of primary tumor recurrence. Therefore it is essential to consider the severity of the effects, the possible consequences of the local recurrence and the way the patient will tolerate RT [37].

4.2.4 To treat or not treat the axilla?

Depending on the ganglia analysis results, the medical team will decide whether the ganglia (region identified in figure 1.3) will be also treated with radiation therapy. In case this region is included in the treatment fields, the strategy for treating these volumes is adapted.

4.2.4.1 Breast irradiation without axillary involvement

For this type of treatment, the beam isocenter is, at first, chosen to be, approximately, in the center of the breast parenchyma. Depending on the irradiation technique chosen, the procedure may vary. Specific details for each technique are provided in section 4.4. The aim is, nonetheless, to cover the all PTV with at least the 95% isodose and without high hot spots, avoiding the OAR.

4.2.4.2 Breast irradiation with axillary involvement

When axillary irradiation is prescribed, the match line is set at the level of the caudal edge of the sternoclavicular junction [146]. To prevent divergence of the tangential into the axillary fields, the isocenter of both sets of fields is chosen to be the same, at the transition between the superior border of the tangents and the inferior border of the axillary fields. The isocenter is found with the aid of an anterior and a lateral fields to determine the center of the volume in these projections. The tangential fields are defined according to the criteria referred above. In the past, in 2D planning, the axillary nodes used to be irradiated with an anterior supraclavicular field (rotated 15° in the opposite direction of the medulla), with the MLC protecting the arm and the umerus, and a posterior field (low weighted field with a maximum height up to the top of the umerus) defined with the appropriate MLC protection to the lung, umerus and clavicula.

Nowadays, with a precise contour of the ganglia on the CT images, other fields with different beam incidences should be chosen to avoid hot spots and high dose on the lung apices, on the umerus and on healthy tissues [147]. There is a study proving that the location of the nodes varies according to the patients anatomy being therefore more precise to draw the nodes involved and conforming the irradiation fields to the volume delineated [148]. In the case of this study, breast without axillary irradiation was investigated because with ganglia involved, the treatment

involves a hemi-field technique which is difficult to accomplish in this linac because of its small maximum field size of $22 \times 40 cm^2$.

4.2.5 Contouring and dose prescription

The images acquired in the CT scanner are imported to the TPS. The first task consists in creating a 3D image where the delineation of the volumes will be made. The structures typically created for breast treatment are the external contour (usually called *Body*, which is compulsory to perform calculations), lungs, bones, medulla, heart, contralateral breast and the volumes to irradiate, CTV, GTV and PTV. These structures are delineated by the radiotherapy oncologist. Typically, the PTV is defined 3 mm subdermally, in the radial direction.

The contouring is considered a subjective task as the identification of these volumes may vary significantly depending on the person and their background education [149, 150]. The radiation oncologist is also responsible for the dose prescription to the target volumes, at this time.

An example of a breast cancer patient CT image 3-dimensionally contoured is presented in figure 4.4.

4.2.6 Planning the treatment

After the physicians' contouring and prescription, the dosimetrists' first procedure is to define the CT isocenter to register it in the TPS in order to establish the link between the image and the patient.

The next step is to define the beam isocenter. Its choice depends on whether axillary nodes irradiation is required. For WBI without axillary involvement, the isocenter is defined at the center of the PTV whereas for breast irradiation with axillary involvement, the beam isocenter is set at the transition between the breast and the axillary ganglia involved.

Actual standards in RT establish a dose of 50 Gy to the tangential fields in standard fractionation of 1.8–2.0 Gy/fraction using photons of 6 MV or mixed-beam energies of 6 MV and 15/16 MV. To achieve an optimal treatment, it is necessary to accurately correlate the target volume and the OAR with the positions and orientations of the beams used for planning and subsequent treatment.

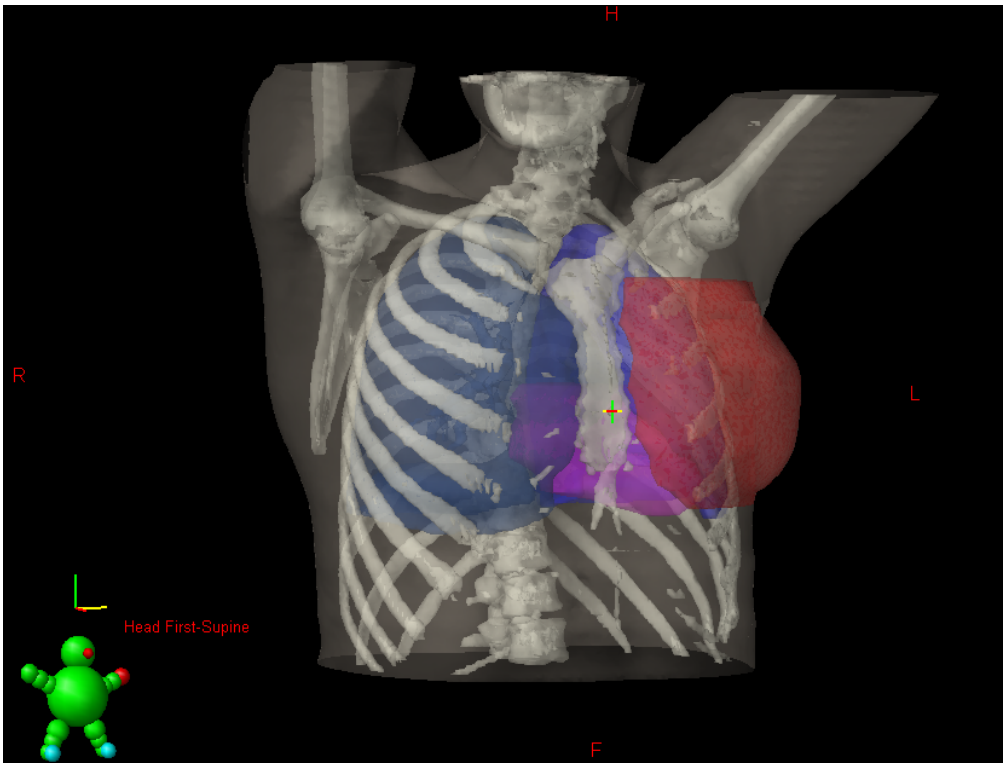

FIGURE 4.4: Example of a cancer patient for breast treatment with the contouring prepared by the radiation oncologist: in red, the PTV; in pink, the heart, in blue, the lungs.

A boost[1] to the tumor bed can be used according to the physician criteria, usually varying from 10 Gy to 20 Gy, using either photons or electrons depending on its location to decrease the risk of tumor relapse in the tumor bed [151, 152]. Large trials demonstrated this is a safe procedure with local failure rates of 0.5 - 1% per year of follow-up and acceptable side effects and cosmetics [27]. Significantly fewer local failures were seen among young patients (<50 years) who received an additional boost of 16 Gy in 8 fractions to the tumor bed [153].

The clinical validation of the treatment plan(s) consists in analyzing the dose distribution in the 3D image of the patient. The validated plan by the radiation oncologist and the medical physicist should verify two goals:

- the calculated dose contains the tumoral lesion with a good coverage;
- and respect the dose constraints for the OAR.

The TPS creates digitally reconstructed radiographs (DRR) for anterior-posterior (AP), lateral setup beams and tangential treatment fields, to verify the correct positioning of the patient before the treatment.

[1]Boost: extra dose to the surgical loca.

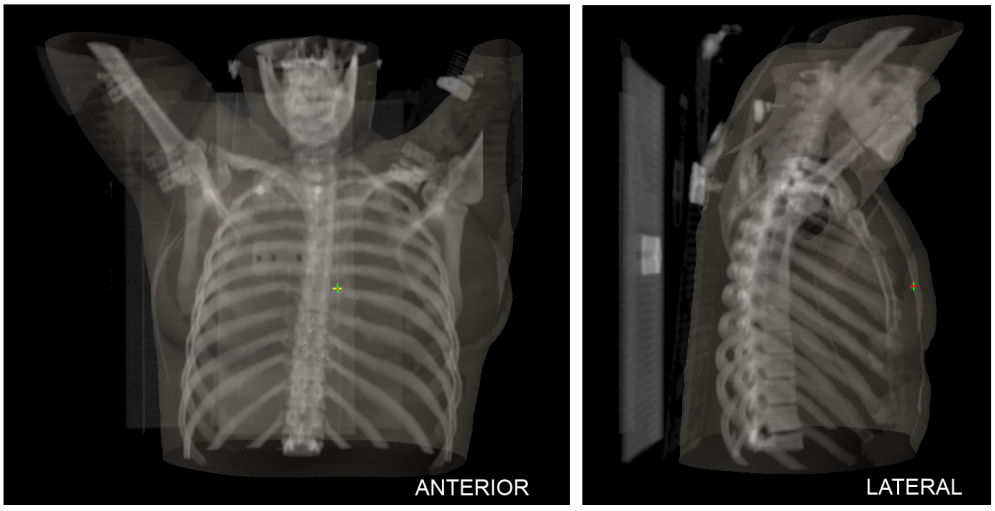

FIGURE 4.5: Anterior and lateral DRR, on the left and right, respectively

4.2.7 Initial treatment setup

On the first day of treatment, the patient is placed in the same position in the custom-made board that was used at the time of the CT scan. The patient is then aligned according to the marks and the AP and lateral SSD (source to skin distance) are verified. Once it has been determined that the SSD are correct, AP and lateral port films are acquired and compared to the AP and lateral isocenter DRR, respectively. If the physician considers the setup satisfactory, the medial tangential field is set and a port film is obtained and compared to the medial tangential field DRR. Once approved, one proceeds to the lateral tangent field for which it is also obtained a port film. After this lateral tangent field port field has been approved by the physician, its dose delivery is initiated.

4.3 Dose calculation: TPS algorithms

The calculated dose entails different types of uncertainties associated to the TPS and its calculation algorithm. The *slightly unadapted* doses can reduce the treatments' efficacy or increase the complication risk in the healthy tissues. A dose variation of 5% may lead to 20%-30% variation in the risk of complications in the healthy tissues [62]. It is expected that reducing the dose uncertainties leads to more predictable and reproducible results to the prescribed dose, given the personal variability reactions of the patients. In practice, the radiation oncologist

validates the dose calculated by an algorithm, if it is within a theoretical acceptable range. Therefore, the dose calculation method should be the most accurate to decrease the uncertainty in the dose calculation associated to the treatment.

4.3.1 Commercial RT systems using MC dose calculation

Modern cancer treatment techniques, such as IMRT and stereotactic body radiation techniques have increased the demand for more accurate dose calculation tools, along with more precise target and OAR volume delineation and precise delivery. One of the actual opportunities of RT departments is to use fast and accurate MC dose calculations within the TPS [59, 154].

Several challenges have historically impeded the clinical implementation of MC dose calculation algorithms. The most significant reason was insufficient computation available for dose calculations to be performed within a reasonable time frame. Along with consistent advances in computer science, many variance reduction techniques have been implemented in today's MC simulation codes in an effort to improve efficiency [84, 91, 113, 122, 155–158]. Although still requiring significantly more computation than conventional dose calculation techniques, MC dose calculation times were reduced, in some TPS, to the point of clinical acceptability. PEREGRINE (North American Scientific: Nomos Division) was the first TPS with MC dose calculation for EBRT approved by Food and Drug Administration (FDA). PEREGRINE, developed at the Lawrence Livermore National Laboratory, implemented a modified version of the EGS4 library with a new condensed history electron transport algorithm. VMC codes are also making their way into many of the latest commercial TPS (CMS Monaco, Elekta PrecisePlan, BrainLAB iPlan, Nucletron MasterPlan and Varian Eclipse).

Initial implementations were focused on MC dose calculations for electron beam therapy planning as the performance of analytical electron beam dose deposition calculations have shown significant inaccuracies (as much as 5-10%) [56, 159–161] and the modeling of a clinical electron beam can be inherently faster than a photon beam. In the initial stages, MC was used as a research tool for dosimetry calculations, and is now being used as the primary dose calculation engine in commercial TPS. This is possible due to the development of special-purpose MC codes optimized for fast and accurate radiation transport in the MV energy range. The transport mechanics and boundary crossing implementations are more efficient, resulting in faster convergence, requiring fewer condensed history steps for the same

precision relative to general-purpose codes such as MCNPX or EGSnrc [56, 77, 82]. In particular, BEAM code system served as a major breakthrough in the development of methods for MC in clinical settings due to the detailed simulations performed in the linac head and associated beam devices, such as the MLC [162] and enabled the detailed study of particle interactions within each component of the treatment head.

Currently, MC dose calculations are available in the clinic for conventional RT and IMRT for photon beams [163, 164] and for treatments with electron beams [160, 165]. Some of the MC dose engines used in commercial TPS are:

- PEREGRINE [159, 165, 166] used in CORVUS inverse TPS (NOMOS, Pittsburgh, PA);
- VMC++ [155] in ONCENTRA TPS [167] (Nucletron B.V., Veenendaal, The Netherlands);
- macro MC [168] in Eclipse TPS [169, 170] (Varian Medical Systems, Palo Alto, CA);
- modified version of DPM [171] in Pinnacle TPS [172] (Philips Radiation Oncology Systems, Madison, WI);
- PENELOPE [173] MC user code PENFAST in ISOgray TPS (DOSIsoft, Cachan, France);
- XVMC [93, 174] in iPlan (BrainLAB AG, Feldkirchen, Germany), XiO and Monaco (CMS Inc, St Louis, MO) and PrecisePLAN (Elekta Inc., Norcross, GA) TPS.

4.3.2 XVMC photon beam dose calculation algorithm

The BrainLAB iPlan MC dose algorithm is based on the x-ray Voxel Monte Carlo (XVMC) dose algorithm developed by Kawrakow and Fippel [93, 155, 174–178]. Electron transport within XVMC is based on VMC originally proposed for electron beams [155]. Later, VMC was modified to incorporate photon transport (XVMC) developed by Fippel [174].

The iPlan MC dose calculation algorithm consists of the following three components:

i. a virtual (multi-source) energy fluence model of interactions within patient-independent structures of the treatment head, such as the target, flattening filter, primary collimator, and so on [178];
ii. full MC simulation of interactions within the collimation system (jaws and MLC) [175];
iii. the MC dose computation engine [174].

4.3.2.1 iPlan MC virtual source model

The virtual energy fluence (VEF) [178] is used to characterize the radiation interactions within the linac head, in the components that are independent of the patient specific treatment plan. The primary and scatter sources are modeled by Gaussian-shaped photon sources. The primary photon source accounts for the primary bremsstrahlung photons produced in the target, while the scatter sources account for Compton-scattered photons originating from the primary collimator and flattening filter. The Gaussian source function parameters are iteratively adjusted to produce the best agreement between analytical calculations of the energy fluence and measured profiles in air [178].

4.3.2.2 Beam modeling of the patient-specific collimation

Fippel developed a method for tracking particles through the patient-specific jaws and MLC [175]. The MLC leaf geometry was modeled and photon interactions are simulated for physical processes including Compton scattering, photoelectric effect and pair production by sampling from relevant cross -section data pre-calculated for tungsten alloy and air. An approximation used is that particles are not transported through the jaws, improving the calculation efficiency [179]. Other groups proposed other approaches for the particle transport in the jaws and MLC:

- to perform transport of the first Compton scattered photons only [61, 180]; or
- deposition of the electron energies locally [61, 135, 180], achieving significant speed up in calculation time, with minimal impact on accuracy.

4.3.2.3 Patient dose calculation

The XVMC photon dose algorithm is used for MC transport of particles in the patient. It is a condensed history algorithm [93, 155, 177] with an implementation where large electron energy transfer collisions are treated in an analog manner, while small energy loss collisions are modeled using the continuous slow down approximation [155]. Improvements in calculation efficiency were obtained using several variance reductions and approximate efficiency enhancing techniques, such as electron history repetition, photon forcing and Russian roulette [93].

The cross-sections for photon interactions and electron radiative and collision stopping powers are calculated from parametrization of the interaction cross-sections in a given material with respect to that of the water, as a function of the material density [155], requiring a calibration of the CT scanner Hounsfield units (HU) using materials of known densities through a pre-established HU-to-density relation.

4.3.3 iPlan MC dose calculation features

The following four options can be changed by the user in the MC dose display settings window:

- spatial resolution (in mm),
- dose result type (dose-to-water or dose-to-medium),
- mean variance (in mm), and
- MLC model (Precise or Fast).

The spatial resolution parameter defines the size of the MC dose computation grid. The default resolution size is 5 mm. For small target volumes it is recommended to use smaller grid sizes (2-3 mm).
The mean variance parameter is related to the statistical uncertainty of the MC calculation. The mean variance estimates the number of histories required to achieve this variance per beam in percentage of the maximum dose of that beam (normalized to that beam). Therefore, the variance in overlapping regions is less than the specified mean variance. The default setting is 2%.
For the dose result type there are two options: dose to medium (D_m) or dose to

water (D_w). The MC dose calculation does inherently compute (D_m) - energy deposited per unit mass in the tissue of interest. The conversion to (D_w) is performed by invoking Bragg-Gray cavity theory:

$$D_w = D_m \left(\frac{S}{\rho}\right)_m^w \tag{4.2}$$

, where $\left(\frac{S}{\rho}\right)_m^w$ is the unrestricted water-to-medium electron mass collision stopping power averaged over the energy spectrum of the primary electrons.
The MLC model can be set to Precise or Fast modes. In the first mode, all the features of the MLC geometry, such as the gap between leaves, rounded tip leaves, leaf thickness, etc., are taken into account whereas with the Fast mode the calculation times decrease, but does not take into account some details of the MLC specifications.

Pencil-beam and collapsed-cone algorithms are different implementations of the superposition/convolution technique. They are based on several approximations and simplifications such as:

- the linac head is modeled by simple sources, i.e., point sources or parallel sources;
- the electron transport is modeled on straight lines;
- neglect or simplify modeling the lateral density scaling (slab approximation), in the case of pencil-beam algorithms;
- discretization of the point-spread function (energy kernel), in the case of collapsed-cone algorithms;
- neglect or approximate representation of the energy kernel tilt angle to reduce computation time;
- neglect or estimation of effects such as depth hardening and off-axis softening.

Usually these techniques provide results within seconds but the dose calculation can be incorrect especially in the head and neck and thorax regions due to the approximations used.

Several groups have already developed MC models in independent MC codes to verify TPS algorithms, specially for more complex techniques such as IMRT [135].

There are evidences pointing to PBC overestimating the doses in air regions such as lung and head and neck localizations, up to 10% when compared to MC calculations [181].

Other studies involving verification of TPS (convolution/superposition algorithm: Collapsed Cone approximation algorithm) with MC (BEAM EGS4-based MC code) used monitor units calculation comparison particularly for narrow and irregular segments was performed by Francescon et al [182]. Maximum differences of 8% were found for such segments where there is electronic disequilibrium and inhomogeneities which become of paramount importance.

Carrasco et al [183] also performed MC simulations using PENELOPE code and performed comparisons with several TPS correction-based and superposition/-convolution algorithms for percentage depth doses (PDD) measured with TLD, metal-oxide semiconductor field-effect transistors (MOSFETs), plane parallel and cylindrical IC, and beam profiles with films. The superposition convolution algorithm had a better performance than the corrected-based algorithms especially in the build up region.

In the case of this study, the calculation algorithms the TPS has, are the Pencil Beam Convolution (PBC) and the commercial Monte Carlo (iMC). The required data was measured and introduced in iPlan BrainLAB TPS and the data was afterwards validated according to the BrainLAB requirements and specifications. This TPS has a license to perform calculation in arc gantry mode which was adopted for Dynamic Conformal Arc RT (DCART). However, it does not allow the use of wedges. The modulation was accomplished by using field in field technique and smaller segments, whenever necessary, to achieve the beam irradiation goals.

Comparison of iPlan algorithms: PBC and iMC

iMC was verified by Künzler et al [184] using gamma analysis performed measurements and compared the results with the calculations. They concluded that, even in heterogeneous media, the iMC algorithm leads to accurate dosimetric results. Fragoso et al [185] also performed a dosimetric and clinical evaluation of iMC and achieved good agreement in homogeneous and heterogeneous media.

Ali et al [186] performed a comparison between PBC and iMC for several pathologies (brain, prostate, lung, head and neck and paraspinal tumors). Dose volume histogram analysis showed that agreement within 5% for all cases except in lung

tumors where discrepancies can be up to 30% with MC not covering the lung tumor against PBC prediction.

Petoukhova et al [187] explored further the heterogeneous pathologies such as lung and head and neck by performing IC and film measurements and achieved excellent agreement in homogeneous media for several static shaped and IMRT fields between iMC and the measurements. In the presence of heterogeneities, iMC accurately predicts the dose and it accurately takes into account the lateral electron transport. The sample of patients chosen had breast sizes varying from 350 to 1750 cm^3; no correlation between the breast size and the irradiation doses was in the scope of this study. Das et al [188], in fact, claim there is a relationship between the breast volume and the CLB doses; however, Zurl et al [189] studies did not find a relationship between these parameters, after analyzing the anatomic and field specific parameters.

4.4 External beam delivery techniques

Traditional external beam photon radiotherapy (EBRT) delivery is defined as the application of uniform or non-uniform intensity beams, without gantry rotation during beam-on, to irradiate the tumor volume and spare the healthy tissues surrounding. The techniques explored in this work for WBI are the following:

- 3D-CRT
- IMRT
- DCART

Specifically for the breast, all these techniques aim at reaching a balance between an adequate irradiation of the breast with the sparing of the OAR involved.

4.4.1 3D Conformal Radiotherapy

For many decades, improvements in RT were limited due to the lack of scientific methods to precisely know the location of the tumors. In the past, external marks such as contrast materials (liquid or surgical clips), skin-topography or bony landmarks related to the tumor location were used to roughly define their shape.

With the development of CT-scanners, RT was boosted: the treatment fields changed from apertures defined to the edges of the tumor to conformal shaped fields; linac machines were developed to replace the ^{60}Co equipments; more complex beam modulation was introduced. In this type of therapy, the photon beams are of uniform intensity across the field. The conformation to the clinical treatment volume is achieved through the use of a heavy alloy shielding placed in the beam path, or more recently, using the MLC to create conformal radiation fields. The use of wedges (physical or dynamic) and/or field compensators are optional. However, using uniform beams, it is expected that tumors with concave surfaces shall be over-dosed in the non-tumor volume in the concavities.

Conformal breast RT is delivered to the whole ipsilateral breast through tangential fields with the use of 6 MV photons.

Lateral tangential fields are created to encompass the entire breast following standard techniques. Due to image segmentation, which allows to take into consideration the critical anatomical structures through volume rendering in the 3D beam's-eye-view (BEV) display, it is possible to shape the collimators such that the critical organs are avoided as far as possible, while ensuring adequate coverage of the breast.

Gantry angles are adjusted to make the deep tangential borders coplanar to eliminate divergence into the lung, so that the posterior and anterior borders of the PTV projections coincide guaranteeing that the medial tangent does not pass through the CLB. The deep edges of the tangential beams pass through the medial and lateral borders set at simulation. Additional adjustments in gantry and collimator rotations may be necessary to limit the volume of lung, heart and contralateral breast in the field. Field collimation is adjusted to follow the slope of the chest wall, as shown in figure 4.6. The jaws are defined so that the upper and lower jaws (y_1 and y_2, when the collimator is at 0 °) cover the all PTV volume and the anterior/posterior jaws (x_1 and x_2) include the PTV and the anterior jaw has at least a 2 cm fall-off to consider breast movement due to breathing. The MLC is defined so that it protects the ipsilateral lung (and heart in case of left breast irradiation). With this technique, it is very often necessary to use pair wedged modifiers to irradiate adequately the PTV volume. Due to proved increase in scattered doses using physical standards wedges some strategies to perform enhanced dynamic wedges (EDW) using the jaws to modify the beam while irradiating were developed and investigated [190–192]. There are cases in which this strategy may

fail due to high involvement of the OAR. Other options have been studied using static fields, such as a three-field technique [193–195].

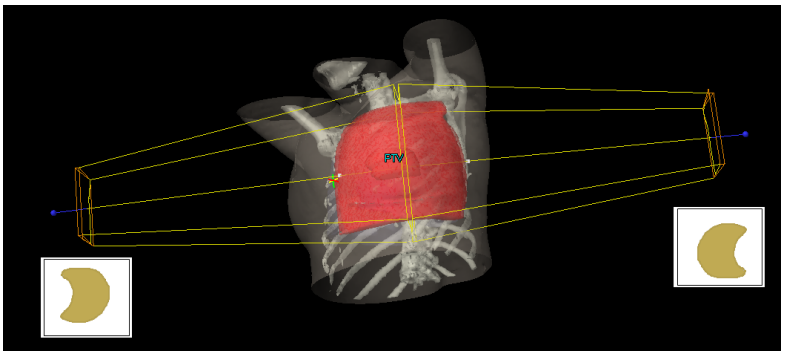

FIGURE 4.6: Representation of WBI using static tangential fields, 3D CRT technique.

4.4.2 Intensity Modulated Radiotherapy (IMRT)

The basic idea behind IMRT is the possibility to obtain non-uniform spatial intensity distributions using non-uniform beams. Several beams from different directions of incidence can be used to ultimately achieve the desired dose distribution in the tumor with the adequate sparing of the surrounding critical structures. By the mid-1990's, advances in technology and software allowing the calculation and delivery of non-uniform fluence maps on 3D patient volumes, together with the development of the modern MLC, enabled the clinical implementation of a class of delivery techniques known as intensity modulated radiation therapy (IMRT). Some investigators claim IMRT represents one of the most important technical advances in RT since the advent of the medical linac [196].

The modulation aimed with IMRT may be achieved through direct or inverse processes implemented in the TPS. Direct planning consists in using several uniform beams, defined by the user, on a trial-error basis. In inverse treatment planning, computer algorithms are used to convert a (clinically established) desired dose distribution into beam intensity maps. The number of fields and gantry angles are defined by the user and each (open field) beam is divided into a number of segments (beamlets). A search of beamlet weights is performed by the algorithm to determine the optimal beamlet weights (fluence map) such that the sum of weighted beamlet dose distributions is in optimal agreement with the objective dose distribution, for the given number of fields and gantry angles [197–199]. This

technique is commonly referred as fluence based optimization. For dynamic treatments, the fluence is executed by the MLC. Its leaf sequence must be derived from the ideal fluence map [200–202].

Some conclusions reported by the National Cancer Institute (NCI) about IMRT [196] were the following:

- Reduce normal tissue radiation exposure
- Decrease treatment efficiency by delivering less dose per MU
- Increase the total-body dose received by the patient during delivery
- Increase stress on the linac from increased heating and movement of the MLC

The difference between 3D-CRT and IMRT is illustrated in figure 4.7. In the particular case of breast RT, the same scheme of beams can be applied both for 3D-CRT and IMRT.

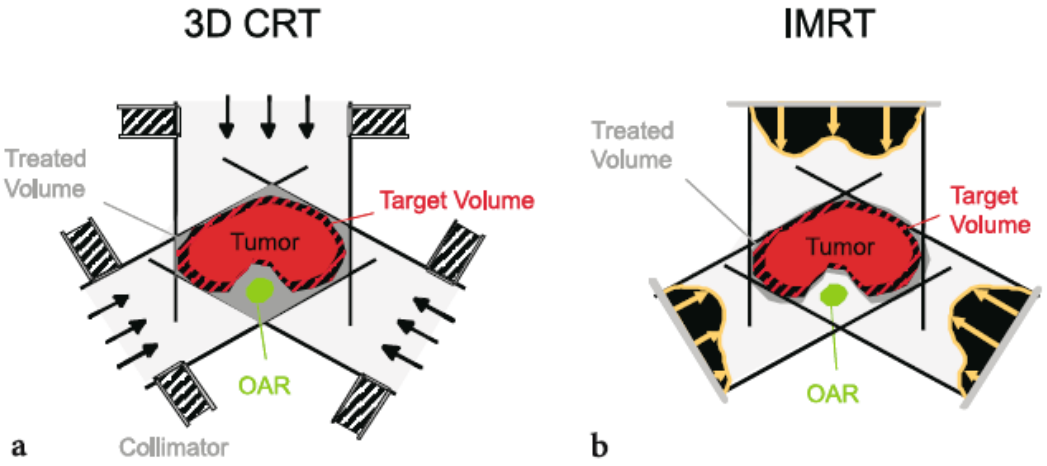

FIGURE 4.7: Comparison of the principles of a. 3D-CRT and b. IMRT. The first makes use of uniform fields, whereas the second involves non-uniform fields. Image taken from [203].

Intensity Modulated Radiotherapy (IMRT) is a treatment technique driven by computer-optimized planning that envisages optimized field fluence distributions to obtain highly conformal dose delivery [204], as represented in figure 4.8. IMRT is explored as a technique to improve breast dose homogeneity by decreasing hot spots and decrease dose to normal tissues, OAR and acute side effects compared with conventional RT [140, 192, 205–213]. The first technique developed was to add sub-fields to the open beams with identical gantry angles, using *field-in-field* technique [214–220]. This technique is known as forward-planning IMRT (f-IMRT). It evolved to varying the gantry angles and the number of fields.

There are two techniques described in the literature for inverse-IMRT, to modulate the photon intensity, using the MLC, to ultimately deliver a highly sculpted dose of radiation:

- *step-and-shoot technique* [221–223], and
- *sliding window technique* [224, 225].

With the first technique, a specific MLC is static during irradiation and field-in-field segments are used to compensate dose in parts of the tissue to irradiate [220, 226–230]. In the second method, the irradiation beamlets are defined and optimized making use a dynamic MLC which change the position of the leafs while the beam is on[211]. Intensity modulated beams were proven to be able to create homogeneous concave distributions [197].

According to the literature, there are mainly three groups of irradiation for breast IMRT using: two tangential beams; 4 to 6 fields covering an 180° sector avoiding portals from the contralateral side [231]; 9 or more fields evenly spaced in a 180° sector angle [232].

Implementation in clinical practice of IMRT requires additional resources compared to conventional breast treatment because IMRT treatment planning, delivery and verification is more time consuming and complex [233–235].

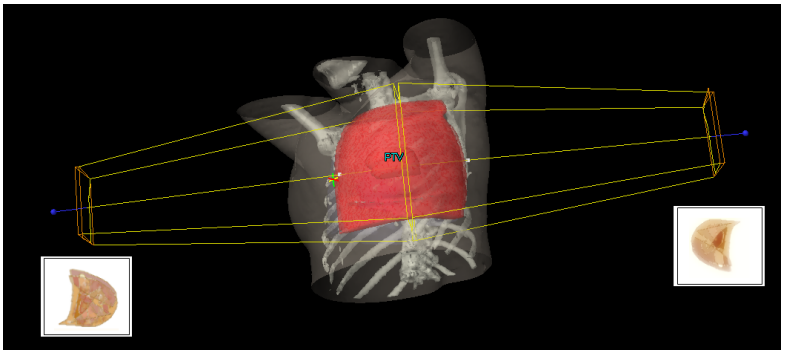

FIGURE 4.8: Representation of WBI using tangential fields, with dynamic MLC during irradiation, generating fluences and non-homogeneous dose distributions within the PTV.

4.4.3 Dynamic Conformal Arc RT (DCART)

Arc beam therapy solutions have also been developed in the past few years, to deliver the prescribed dose while the gantry rotates. This radiation therapy technique can also be forwardly or inversely planned, and the MLC dynamically conforms to the planning target volume projection while the gantry rotates, being therefore considered an intensity modulated technique. This technique was first proposed by Yu in 1995 [236]. However, this technique is demanding in what the dose calculation is related as the intensity solution space is non-convex and further developments were only made when Shepard et al [237] improved the optimization process for the TPS. Multiple arcs may be required to deliver the prescribed dose distribution.

Varian's RapidArc delivery system is capable of delivering the entire treatment with a single rotation of the gantry, being therefore potentially faster in treating but extremely demanding in quality control tests. This technique presents several advantages compared to the static IMRT techniques:

- decrease in the number of monitor units delivered;
- faster treatment times;
- reduce patient exposure to scattered radiation;
- consequent decrease in patient movement.

An equivalent solution is offered by Elekta (Elekta AB, Stockholm, Sweden), known as VMAT (Volumetric Modulated Arc Therapy). Several early studies compare the effectiveness of RapidArc with other arc treatment modalities [238–242].

The system used in this work for arc therapy is a previous version to RapidArc implemented in the Trilogy linac (Varian Medical Systems, Palo Alto, CA). This linac permits treating in arc mode and the TPS solution used is a forward planning strategy in which the MLC assumes a different configuration in a pre-defined gantry rotation interval. This technique may be used in modern linacs, permitting gantry rotation while the beam is on. In the case of a treatment delivered by arctherapy, the target dose is delivered by a series of arcs, all isocentric and corresponding to a fixed couch position, as represented in figure 4.9. The amplitude of the arcs is generally inferior to 180° avoiding coplanar beams (opposing

and parallel within the same plan), susceptible of generating high dose gradients outside the target volume. In DCART, the size and the shape of the irradiation beams adapt to the target volume projection in a plan perpendicular to the beam axis which vary with the gantry rotation.

This technique is conformal and the total fluence of the beams is modulated with the ultimate goal of improving the target volume irradiation and sparing the healthy tissues. The most simple technique of intensity modulation consists in manually adapting the parameters of the multileaf collimator (MLC) to obtain conformational fields (forward planning).

In the case of sequential modulated irradiation, the field is divided into several beamlets corresponding to a static position of the linac head. The MLC movement is not continuous, programmed for the different gantry positions. The total fluence is the sum of the several segments of irradiation. In the dynamic configuration, the gantry continuously rotates while irradiates with individual movements of each leaf at a differential speed to define the shape of the field.

More complex treatments (such as RapidArc) have evolved to inverse planning, that instead of looking for the best dose distribution by direct adjustment of the beam parameters, the goals are set and the aim is to satisfy the pre-defined criteria. This strategy increases the efficacy of the treatment as the clinical criteria are set a priori instead of trying to satisfy them *a posteriori*. As there are multiple solutions, it is necessary to solve an inverse problem preferable to the iterative optimization method. These techniques require extra quality control.

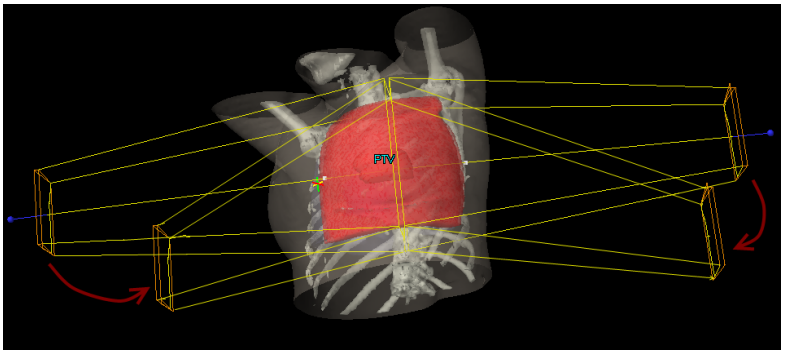

FIGURE 4.9: Representation of DCART technique using partial arcs used for breast irradiation.

For WBI, the techniques investigated were:

1. f-IMRT - forward-intensity modulated RT, using 2 tangential broader fields and whenever necessary smaller fields, with the same beam incidence as the tangential fields, to obtain better homogeneity inside the target volume.

2. IMRT2 - inverse planning technique using 2 modulated tangential fields. For modulation, the MLC assumes different positions during irradiation (sliding window technique).

3. IMRT5 - inverse planning technique using 5 modulated fields with different beam incidents within the tangential fields. The sliding window technique was also used for beam modulation.

4. DCART - forward planning technique using several arc beams, modulated with conformal MLC adjusted every 10° (gantry angle).

4.5 Parameters investigated

For assessing the quality of the beam irradiation plan, during optimization, cumulative dose-volume frequency distribution, in the form of histograms, usually known as dose-volume histograms (DVH) can be plotted by the TPS. It graphically summarizes the simulated radiation distribution within a volume of interest of a patient which would result from a proposed radiation treatment plan. These DVH permit comparing rival treatment plans for a specific patient by clearly quantifying the uniformity of the dose in the target volume and hot spots in adjacent normal tissues or organs. However, because of loss of positional information in the volume(s) under consideration, it should not be the sole criterion for plan evaluation.

From the DVH it is also possible to evaluate several dosimetric parameters, in order to quantitatively analyze the dose distributions, in what the coverage and homogeneity inside the target volume and OAR are concerned. The dose values were extracted from the DVH, analyzing each structure, according to the volume that receives a certain dose, or the dose that reaches at a percentage of volume, relating *a posteriori* with the tolerance estimated dose.

4.5.1 Evaluation of the PTV doses

For the PTV, the following parameters were analyzed:

- $V_{95\%}$ - PTV volume that receives, at least 95% of the prescribed dose;
- $V_{107\%}$ - PTV volume that receives, more than 107% of the prescribed dose;
- D_{max} - maximum dose the PTV receives;
- HI - homogeneity index;
- CI - conformity index;
- CN - conformation number.

Coverage of the target volume by the 95% isodose curve, $V_{95\%}$

For all the patients and techniques, the PTV percentage volume, that was covered by the 95% isodose was analyzed, according to ICRU [34, 35] recommendations. The ultimate goal is that the 95% isodose encompasses the total PTV, which is difficult to achieve in WBI due to the shape of the breast.

Evaluation of higher doses in the dose distribution

High doses or hot spots, are doses above 107% of the prescribed dose, often obtained in breast dose distributions. D_{max}, the point of maximum dose in the distribution is also determined. One of the goals of the dosimetrist is to decrease these doses as much as possible, being sometimes not possible to have no doses higher than 107%, as recommended by ICRU50. Having such high doses also means the dose distribution is not homogeneous.

Heterogeneity and Conformity Indexes

To evaluate the quality of the dose distribution within the PTV, the following indexes were assessed:

Heterogeneity Index, HI It is a measure of the degree of heterogeneity of the prescribed dose (95% isodose) of the plan, defined as the ratio between the minimum dose in the hottest 5% and 95% of the total PTV volume:

$$HI = \frac{V_{5\%}}{V_{95\%}} \tag{4.3}$$

The closer to unity, the more homogeneous, the dose distribution is.

Conformity Index The conformity index (CI) is a measure of how the prescribed dose fits the contoured PTV: the closest to 1, the most conformal the dose distribution is. It is determined as the ratio between the V_{RI} (volume covered by the reference isodose) and the target volume (TV).

$$CI = \frac{V_{RI}}{TV} \tag{4.4}$$

This conformity index does not take into account whether the V_{RI} is surrounding the PTV and its efficacy is therefore limited.

Conformation Number Due to the limitations of the CI, another conformity index was calculated according to the definition provided by van't Riet et al [243]:

$$CN = \frac{TV_{RI}}{TV}\frac{TV_{RI}}{V_{RI}} \tag{4.5}$$

, where TV_{RI} is the target volume covered by the reference (95%) isodose. The closest to 1, the most conformal is the dose distribution.

4.5.2 Evaluation of the OAR doses

In all the patients, the contour of both lungs, heart and CLB were performed and were used to assess the doses that reach these specific OAR. The following dose parameters in the OAR were analyzed:

Ipsilateral lung

The lung right beneath the irradiated breast is a volume that can easily receive high doses, due to the breast shape and its localization. The following doses were extracted from the DVH:

- D_{mean}, the mean dose in the lung;
- $V_{10\%}$, the lung volume that receives at least 5 Gy (10% of the prescribed dose);
- $V_{20\%}$, the lung volume that receives more than 10 Gy (20% of the prescribed dose);

- $V_{40\%}$, the lung volume that receives at least 20 Gy (40% of the prescribed dose);
- $V_{80\%}$, the lung volume that receives more than 40 Gy (80% of the prescribed dose).

Contralateral lung

The right lung, contralateral to the PTV being treated is expected to only receive residual dose. The following parameters were assessed:

- D_{mean}, the mean dose in the right lung;
- $D_{5\%}$, the maximum dose that is in 5% of the lung;
- $V_{5\%}$, the lung volume that receives at least 2.5 Gy (5% of the prescribed dose).

Heart

The heart is a sensitive organ and high doses should be avoided. The following parameters were investigated:

- D_{mean}, the mean dose in the heart;
- $V_{20\%}$, the heart volume that receives more than 10 Gy (20% of the prescribed dose);
- $V_{50\%}$, the heart volume that receives more than 25 Gy (50% of the prescribed dose).

Contralateral breast

The contralateral breast is often in the beam path of medial tangential fields and it is required that these receive as low dose as possible to avoid second breast cancer in the other breast. The parameters assessed for the CLB were:

- D_{mean}, the mean dose in the CLB;

- $V_{10\%}$, the CLB volume that receives more than 5 Gy (10% of the prescribed dose);
- $V_{4\%}$, the CLB volume that receives more than 2 Gy (4% of the prescribed dose).

Body without PTV

The external contour of the body was considered and the PTV was subtracted. The goal is that this (Body-PTV) volume receives as low dose as possible, meaning that the dose should be confined to the PTV. The parameters assessed for this volume were:

- D_{mean}, the mean dose in the Body-PTV;
- $V_{80\%}$, the Body-PTV volume that receives more than 40 Gy (80% of the prescribed dose);
- $V_{40\%}$, the Body-PTV volume that receives more than 20 Gy (40% of the prescribed dose);
- $V_{4\%}$, the Body-PTV volume that receives more than 2 Gy (4% of the prescribed dose).

4.6 Statistical analysis

The statistical tests aim at verifying if the observed differences are significant. For statistical analysis purposes, there are two types of tests:

- the parametric, and
- the non-parametric.

The parametric tests are used to compare parameters that describe the distributions, such as the mean, percentage, variance and differences, with normal distribution. The non-parametric tests do not require the dependent variable to have a known distribution.

Two situations to be considered for statistical analysis are for the comparison tests to know whether the series of measurements are independent or paired.

- Independent series: for comparison of two distinct series considering the same variable;
- Paired series: comparison of two series considering the same variable observed in the same individuals.

The decision of the statistical tests to perform was made considering that the test to be applied are non-parametric and the samples are paired, provided that the sample of this study are the 7 patients (the same individuals along all this investigation) or the calculation algorithms. The choice was made based on the diagram depicted in figure 4.10.

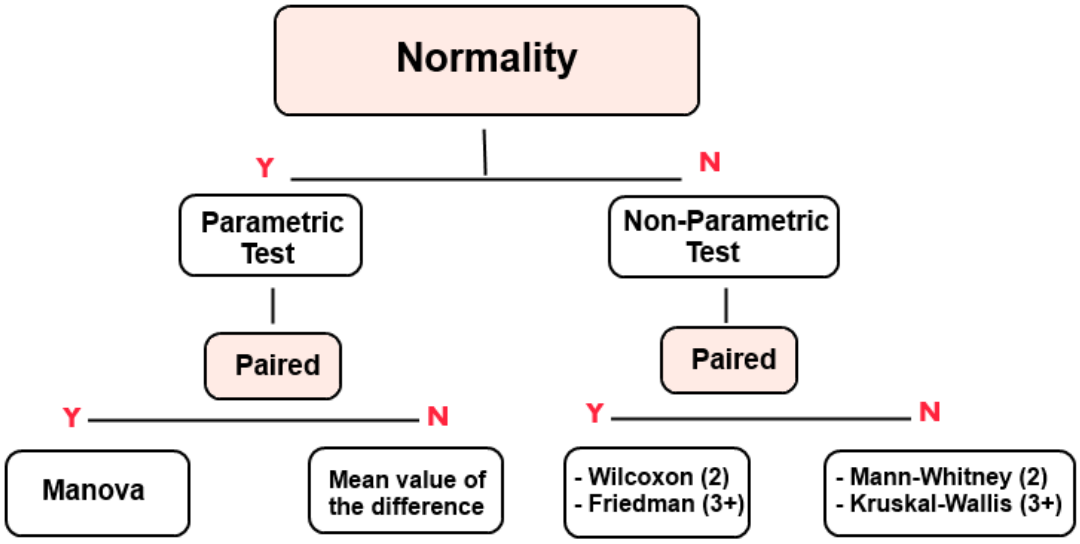

FIGURE 4.10: Diagram on the statistical tests to be used given the type of samples. (2) stands for 2 samples; (3 or more) means 3 or more samples.

The reported values for each irradiation technique were compared using SPSS version 20 applying related-samples Friedman's two-way analysis of variance test and performing a pairwise comparison between the variables that reject the null hypothesis (p-value ≤ 0.05, i.e. it is considered that there are significant statistical differences between the variables under investigation when p-value is inferior to 0.05), for both calculation algorithms, individually. For more details on this test, please refer to Appendix A (data from http://psych.unl.edu/psycrs/handcomp/).

The Friedman test is a non-parametric test appropriate to compare 2 or more populations, for paired samples. In this case, the samples are considered paired because the same parameters are being investigated for the same individual, despite being for different techniques.

To compare the algorithms, the Wilcoxon test was used (p-value ≤ 0.05), for the variables under investigation. The samples are also paired, for the same reason presented before and this test is the most adequate for small samples. Further details on the application of Wilcoxon test can be looked up at Appendix A (data from http://psych.unl.edu/psycrs/handcomp/).

4.7 Comparison of different breast planning techniques and algorithms for radiation therapy treatment

This section contains the article published in Physica Medica, in 2014. This article compares the 4 breast irradiation techniques under investigation, f-IMRT, IMRT2, IMRT5 and DCART, using two calculation algorithms from the commercial iPlan BrainLAB TPS. It contains all the relevant results and conclusions regarding WBI irradiation using the aforementioned techniques and the differences between the calculation algorithms referred.

ARTICLE IN PRESS

Physica Medica xxx (2013) 1–11

Contents lists available at SciVerse ScienceDirect

Physica Medica

journal homepage: http://www.physicamedica.com

Original paper

Comparison of different breast planning techniques and algorithms for radiation therapy treatment

C. Borges [a,*], G. Cunha [b], I. Monteiro-Grillo [c], P. Vaz [d], N. Teixeira [b]

[a] *Medicalconsult SA, Campo Grande, n° 56 – 8° A, 1700-093 Lisboa, Portugal*
[b] *Escola Superior de Tecnologias da Saúde, Avenida Dom João II, 1900-096 Lisboa, Portugal*
[c] *Departamento de Radioterapia, Hospital de Santa Maria, Centro Hospitalar Lisboa, Norte, EPE, Avenida Professor Egas Moniz, 1649-035 Lisboa, Portugal*
[d] *Instituto Superior Técnico, Campus Tecnológico e Nuclear, Unidade de Protecção e Segurança Radiológica, Estrada Nacional 10 (ao km 139,7), 2695-066 Bobadela LRS, Portugal*

ARTICLE INFO

Article history:
Received 8 November 2012
Received in revised form
23 April 2013
Accepted 30 April 2013
Available online xxx

Keywords:
Breast radiotherapy
Irradiation techniques
Calculation
Algorithms

ABSTRACT

This work aims at investigating the impact of treating breast cancer using different radiation therapy (RT) techniques – forwardly-planned intensity-modulated, f-IMRT, inversely-planned IMRT and dynamic conformal arc (DCART) RT – and their effects on the whole-breast irradiation and in the undesirable irradiation of the surrounding healthy tissues. Two algorithms of iPlan BrainLAB treatment planning system were compared: Pencil Beam Convolution (PBC) and commercial Monte Carlo (iMC).

Seven left-sided breast patients submitted to breast-conserving surgery were enrolled in the study. For each patient, four RT techniques – f-IMRT, IMRT using 2-fields and 5-fields (IMRT2 and IMRT5, respectively) and DCART – were applied. The dose distributions in the planned target volume (PTV) and the dose to the organs at risk (OAR) were compared analyzing dose–volume histograms; further statistical analysis was performed using IBM SPSS v20 software.

For PBC, all techniques provided adequate coverage of the PTV. However, statistically significant dose differences were observed between the techniques, in the PTV, OAR and also in the pattern of dose distribution spreading into normal tissues. IMRT5 and DCART spread low doses into greater volumes of normal tissue, right breast, right lung and heart than tangential techniques. However, IMRT5 plans improved distributions for the PTV, exhibiting better conformity and homogeneity in target and reduced high dose percentages in ipsilateral OAR. DCART did not present advantages over any of the techniques investigated. Differences were also found comparing the calculation algorithms: PBC estimated higher doses for the PTV, ipsilateral lung and heart than the iMC algorithm predicted.

Introduction

Breast radiotherapy (RT) is particularly challenging due to the concave anatomy of the chest wall and breast that make it a difficult localization to achieve homogeneous dose distributions. Its complex shape is located near the body–air interface. There are organs at risk (OAR) in the vicinities, such as the lungs, heart and contralateral breast (CLB) that must receive doses as low as possible to avoid long term complications. It is also important to achieve dose homogeneity in target and high doses outside the target volume should be avoided. Other concerns are the dose to the CLB which is related to induced second malignancies [1,2], the increased risk of fatal cardiac events, [3] and of pneumonitis [2] for women after undergoing RT. As long as the volume to treat has adequate dose coverage, the side effects should be minimized.

Breast conserving therapy has become a widely accepted treatment option in the management of early-stage breast cancer improving local control [4–8]. The conventional radiotherapeutic approach after lumpectomy generally consists of delivering 50 Gy to the entire breast, with conventional wedged tangential fields, optimized using a single central-axis isodose distribution and a 10–15 Gy boost to the tumor bed [9,10].

Treatment of whole breast using a photon tangential field technique is still standard within radiotherapy departments, using isocentric tangential treatment fields, geometrically nondivergent at their posterior and superior borders, using 6 MV or combined

* Corresponding author. Av. Embaixador Assis Chateaubriand, n2 2 D, 2780-196 Oeiras, Portugal. Tel.: +351 927054182.
E-mail address: cissa9@gmail.com (C. Borges).

1120-1797/$ – see front matter © 2013 Associazione Italiana di Fisica Medica. Published by Elsevier Ltd. All rights reserved.
http://dx.doi.org/10.1016/j.ejmp.2013.04.006

6 MV with 10 MV or 16 MV according to the energies available in each linac, based on the method of Casebow [11], which has been modified and adapted with the advent of 3D treatment planning systems (TPS) and the use of beam modifiers, other beam configurations, etc. (e.g. Refs. [12–14]).

ICRU [15] recommends the enclosure of the planning target volume (PTV) within 95% and 107% isodose lines. However, this may be difficult to achieve with only two standard tangential beams using wedges technique, typically called 3D-CRT (3D-conformal RT). More complex treatment planning strategies have been developed to improve dose homogeneity, namely intensity modulated RT (IMRT) techniques varying in complexity, ranging from manual division of beam fields into several segments – forward-IMRT, f-IMRT – [16–23] to more complex techniques using inverse planning algorithms to treat using several individual beamlets [24].

Woo et al. [25] and Bhatnagar et al. [26], in separate experimental studies concluded that tangential-wedged 3D-CRT increases scattered dose into the normal tissues.

Several studies claim that IMRT has the potential to improve dose homogeneity and conformity in breast radiotherapy improving cosmetic results [27–31], reducing pulmonary and cardiac complications and CLB doses [23,32,33].

f-IMRT, using open fields and segments, is claimed to be dosimetrically superior to 3D-CRT using wedges and reported to have similar PTV coverage, better dose homogeneity and lower doses in the OAR [23,25,34–37].

When comparing 3D-CRT with IMRT (inverse planning), the implications on the irradiation of the healthy tissues surrounding are not as conclusive: some studies reported lower doses using IMRT on the CLB [16,26,33,38], on the heart [39–41], and on the ipsilateral lung [33,38,41,42] whilst other studies verified lower doses on the CLB [43] and on the normal tissues [44] using 3D-CRT. Jagsi et al. [45], comparing different IMRT techniques concluded tangential beamlet IMRT technique reduced exposure to normal tissues and maintained reasonable tissue coverage.

It is well-established that 3D-CRT with wedges increases scattered doses [16,23,25,26,34,35]. Therefore in this study f-IMRT with multiple static fields was used and compared to other techniques without wedges.

Treatment plans are, in general, evaluated on the basis of dose calculations. Some comparisons between calculation algorithms may be found in the literature on breast irradiation, for Pencil Beam Convolution (PBC) [46] and Analytical Anisotropic Algorithm (AAA) [47–49]. The calculations using the PBC algorithm are known to be inaccurate in regions of electronic non-equilibrium, such as in air cavities or in build-up regions, and inhomogeneity corrections due to the lung media [50] or irregular body contour, which are major issues in breast RT [48,51]. Monte Carlo (MC) simulation methods and techniques are widely reported for their dose calculation accuracy. Applying MC techniques to dose calculations in RT has therefore the potential to decrease the uncertainties when compared to analytical/conventional treatment planning algorithms, regardless the beam geometry and target composition [52].

The main focus of the present study is to evaluate and compare the irradiation plans of four radiotherapy techniques (f-IMRT, IMRT using 2 and 5 fields – IMRT2 and IMRT5, respectively – and dynamic conformal arc RT – DCART), relevant for entire breast irradiation, considering only the 50 Gy plan as the boost plan is more patient-dependent due to tumor bed localization and prognostic factors for dose prescription. This study also aims at comparing two different algorithms, Pencil Beam Convolution, PBC, and commercial Monte Carlo, iMC, from iPlan (BrainLAB AG, Feldkirchen, Germany) treatment planning system (TPS) [53,54] for the techniques under investigation for breast cancer treatment.

Patients, materials and methods

Patient selection and simulation

7 Patients with left-sided stage I or II breast cancer that were referred to adjuvant RT after breast conserving surgery (BCS) were investigated. All the selected patients were randomly chosen among the 394 patients treated between 2010 and 2011 to left breast cancer using 3D-CRT. The breast volume of the elected patients varied from 350 cc to 1750 cc and was not a selection criterion in order to achieve general conclusions on the irradiation techniques despite the breast size.

CT scanning for treatment planning

The patients were positioned in a standard breast immobilization device on the scanner table, in the treatment position with bilateral arm abduction above the head. Radiopaque wires were placed around the patients' breast and marked the superior–inferior (2 cm above and below the breast tissue) and the midline lateral borders. CT images of the thorax were acquired, with a Siemens®, Biograph 64R, CT scanner. The slice thickness was 3 mm, with coverage from above the mandible to several centimeters below the inframammary fold, to include the entire breasts, complete left and right lungs and heart. The CT data was then transferred to the iPlan® BrainLAB treatment planning system (TPS).

Delineation of target and OAR

All contours were performed in the axial CT slices. For whole breast RT after BCS, the remaining mammary glandular tissue was considered clinical target volume (CTV). The heart, ipsilateral lung, contralateral lung and CLB were considered OAR. Auto contouring of the body and both lungs was used. For consistency, the delineation of the CTV, planning target volume (PTV), heart and CLB was performed by the same radiation oncologist. The PTV was defined by adding a 5 mm margin to the CTV. All structures were confined to 3 mm from the external surface of the patient. An additional structure specified as Body-PTV was also created to evaluate the doses on the body excluding the PTV.

Treatment planning

The treatment plans were generated using iPlan® v. 4.1, the BrainLAB TPS. Four plans to deliver 50 Gy to the PTV in 25 fractions were developed for each patient: two plans used forward planned techniques (f-IMRT, and DCART); whereas for the other two plans (IMRT2 and IMRT5), inverse optimization was applied. The treatment sessions were planned for a Trilogy linear accelerator (Varian Medical Systems, Palo Alto, CA) equipped with the High Definition (HD) micromultileaf collimator (MLC) with 120 leaves. The plans were normalized to a point in the isocenter axial plane inside the PTV. For all plans, the isocenter was placed in the center of the PTV volume and the couch rotation was set to 0°; the collimator rotation was left free to minimize the opening of the main jaws, but normally was set to 0°.

For treating the PTV, specific objectives were established to treat 95% of the PTV with ideally 47.5 Gy but at least 45 Gy, and maximum hotspots should not exceed 110%. Other goals were to keep the dose to the OAR as low as possible by setting higher priority upon avoidance of the contralateral breast, lungs and heart, without compromising the PTV dose coverage considering

Please cite this article in press as: Borges C, et al., Comparison of different breast planning techniques and algorithms for radiation therapy treatment, Physica Medica (2013), http://dx.doi.org/10.1016/j.ejmp.2013.04.006

adaptations from QUANTEC [55] and RTOG 1005 [56] criteria. Specifically for the OAR, the criteria used for evaluation adopted were: the ipsilateral lung V_{20Gy} should be lower than 20%, V_{10Gy} should be inferior to 35%, V_{5Gy} should be inferior to 50%; 5% of contralateral breast should receive less than 5 Gy; for the heart, V_{25Gy} was expected to be inferior to 10% and V_{10Gy} not superior to 30%; 10% of the contralateral lung should not receive more than 5 Gy.

The PBC algorithm was used to calculate dose at each step of the plan optimization process, for all plans. After optimization, the plans were recalculated using a dose-to-medium calculation MC algorithm with $3.0 \times 3.0 \times 3.0$ mm^3 spatial resolution and 3.0% mean variance. In iPlan, for IMRT techniques, for iMC, the user can define 4 levels of priorities, by assigning structures to the following "importance levels": 1. 100%; 2. 66%; 3. 33%; 4. 0%. Initially, the priorities were defined as 100% to the PTV and 33% to the OAR. These priority levels were continuously adjusted during optimization to adequately irradiate the PTV. In case, the objectives were not met, the input parameters such as the beam gantry and collimator angles were also adjusted. The optimal parameters were chosen with beams-eye view display support. For the inverse-planning techniques, the technique used for intensity modulation of dose was sliding-window.

f-IMRT

Two tangential 6 MV conformal fields, without wedges – due to the increased scatter extensively reported in other studies [16,25,26,41] – were positioned to cover the PTV. Forward planning field-in-field MLC compensation was required to fulfill the dose constraints either to block regions of high doses or to minimize the irradiated lung and heart volumes without compromising the PTV coverage. The beam weights, MLC shaping and gantry angles were varied to ensure the plan met the requirements. Lateral beams ranged from 120° to 135°; medial gantry angles varied between 300° and 310°.

IMRT2

This technique used two intensity modulated photon beams similar to those commonly used in 3D-CRT. For the inverse planning technique, the gantry angle of the beams was defined and submitted to inverse calculation with an optimization engine, the DPL2i (version 4.1) to determine the MLC shaping, monitor units at each gantry angle and the speed of leaf motion for each field. The cost (objective) function was based on dose–volume constraints individually specified for the target PTV and OAR. For IMRT2, two 6 MV opposing tangential conformal fields were defined with specific and adjustable constraints to adequately irradiate the PTV and spare the OAR. The lateral and medial gantry angles ranged from 120° to 135° and 300° to 310°, respectively.

IMRT5

Five beams with different gantry angles were defined and optimized to meet the requirements established for irradiating the PTV and sparing the OAR. For IMRT5, inverse optimization was also used. The lateral and medial gantry angles were the same used for IMRT2; the other 3 fields were placed between these fields for gantry angles between 80° and 120°; 25° and 55°; 340° and 350°.

DCART

For the dynamic conformal arc technique, two beam arcs were chosen in medial (gantry angles from 300° to 350°) and lateral (gantry angles from 100° to 150°) positions, to avoid direct incidences towards the heart and lungs, by closing the MLC in some arc positions to protect these OAR. In some plans, additional partial arcs were added if necessary to improve sparing of normal tissues while providing adequate target coverage. These plans were created using a forward-planned technique, in which the linac delivers the dose while the gantry rotates, by changing the MLC conformation, every 10°.

Statistical analysis/evaluation tools

f-IMRT, IMRT2, IMRT5 and DCART plans were optimized for seven patients, using the PBC algorithm, taking into account the goals and constraints previously mentioned. After optimization, the plans were recalculated using iMC algorithm. Dose volume histograms (DVH) were calculated and different metrics were selected to compare the techniques.

For the PTV, the parameters $V_{47.5Gy}$ and $V_{53.5Gy}$ were used to assess maximum doses. The heterogeneity index (HI) of the plans was defined as the ratio between the minimum dose in the hottest 5% and 95% of the total PTV volume. [57] The conformity index (CI) was determined as the ratio between V_{RI} (volume covered by the 95% isodose) and TV (target volume). Furthermore, the degree of conformity [58] was also calculated, as the conformation number, CN, defined by van't Riet et al. [59], which simultaneously takes into account irradiation of the target volume and irradiation of the healthy tissues:

$$CN = \frac{TV_{RI}}{TV} \times \frac{TV_{RI}}{V_{RI}},$$

where TV_{RI} is the target volume covered by the reference (95%) isodose.

For all treatment plans, DVH of the OAR (lungs, heart and CLB) and normal tissue sparing (Body-PTV) were calculated and compared.

The reported values for each technique were compared using SPSS v20 [60,61] applying related-samples Friedman's two-way analysis of variance test and performing a pairwise comparison between the variables that reject the null hypothesis (p-value ≤ 0.05, i.e. it is considered that there are significant statistical differences between the variables under investigation when p-value is below 0.05), for both calculation algorithms, individually.

To compare the algorithms, the Wilcoxon test was used (p-value ≤ 0.05), for the variables under investigation.

Results

Pencil beam algorithm

Figure 1 shows the dose distributions, for the 4 techniques, for PBC algorithm, just for one of the patients, for simplicity matters.

Considering the results presented in Fig. 1, PTV coverage by the 95% isodose was expected to be better for IMRT5 as this curve fits best to the concave shape of the PTV comparatively to the other techniques. Moreover, it is possible to infer that with IMRT5 and DCART there was a wider spread of low doses into the body and into the heart, lung and contralateral OAR.

A comparison of the DVHs of the patients enrolled in this study is presented in Fig. 2.

A detailed statistical analysis for the PTV and the OAR was performed and the results are presented in Table 1. For the PTV, all the techniques had the expected shape for its adequate irradiation (Fig. 2(I)). Regarding D_{max} criterion, with f-IMRT, in only 57% of the cases was the goal achieved; for IMRT5, one patient of the 7 studied cases did not respect this criterion having high hotspots in a small percentage of PTV volume. There were no significant statistical differences between the techniques. As expected from Fig. 1, IMRT5 presented the best mean $V_{47.5Gy}$ values, with 86% of f-IMRT and

Please cite this article in press as: Borges C, et al., Comparison of different breast planning techniques and algorithms for radiation therapy treatment, Physica Medica (2013), http://dx.doi.org/10.1016/j.ejmp.2013.04.006

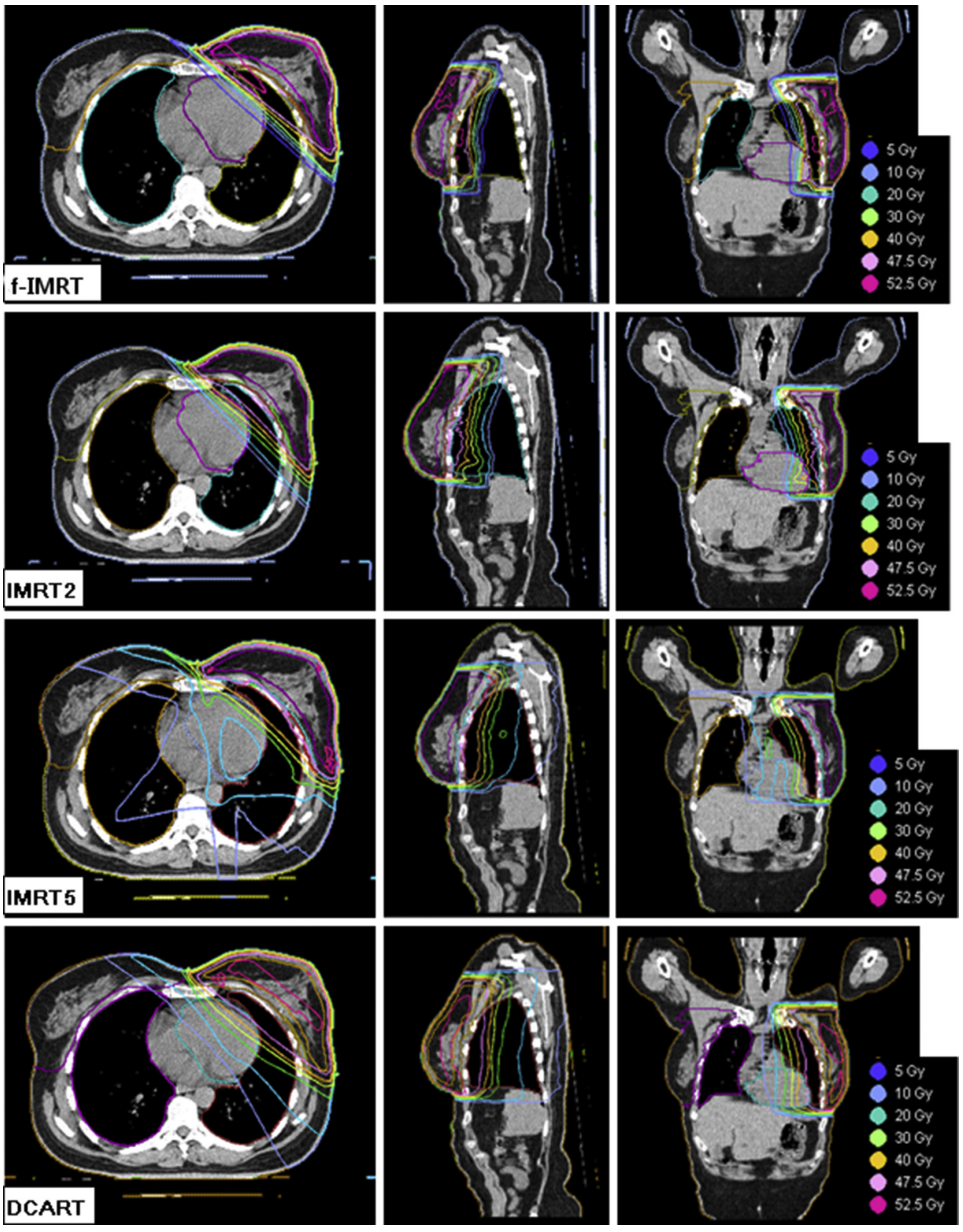

Figure 1. TPS results for the 4 techniques, f-IMRT, IMRT2, IMRT5 and DCART from top to bottom, in axial, sagittal and coronal views, from left to right, respectively, for one of the patients enrolled in this study, using the PBC algorithm.

IMRT5 and 71% of IMRT2 and DCART plans meeting the goal of $V_{47.5Gy}$ to be superior to 90%. Significant statistical differences were not found between the techniques. DCART had the lowest $V_{47.5Gy}$ average with 3 out of 7 plans not reaching, the 90% of PTV coverage; had higher $V_{53.5Gy}$ average values and was the technique with the highest percentage of PTV volume with high doses (see Fig. 2(I)). Therefore DCART was considered the technique with worst PTV coverage. f-IMRT had a better performance on this parameter compared to DCART but the IMRT techniques achieved the best results. Concerning the heterogeneity and conformity indexes calculated, IMRT5 was the technique with the most conformed and homogeneous (average values closer to unity) dose distributions. f-IMRT had the worst performance for CI. Significant statistical differences were observed between the techniques for HI, CI and CN.

Considering the results for the OAR presented in Table 1, on the left lung, f-IMRT did respect all the constraints imposed and had lower D_{mean} values; IMRT2 verified all the constraints imposed, with exception of one case of IMRT2, that did not verify V_{20Gy}; IMRT5 did not achieve the objectives for V_{5Gy}, in 6 out of 7 cases, and V_{10Gy}, in 4 out of 7 cases, but verified V_{20Gy} for 5 out of 7 patients; DCART did not respect V_{5Gy} in 43% of the cases, V_{10Gy} and V_{20Gy}, in 6 out of 7 patients. Nonetheless, IMRT5 exhibited lower V_{40Gy} compared to the other techniques, see Fig. 2(IV). On the right lung (Fig. 2(V)), IMRT5 was the technique with higher doses and

Please cite this article in press as: Borges C, et al., Comparison of different breast planning techniques and algorithms for radiation therapy treatment, Physica Medica (2013), http://dx.doi.org/10.1016/j.ejmp.2013.04.006

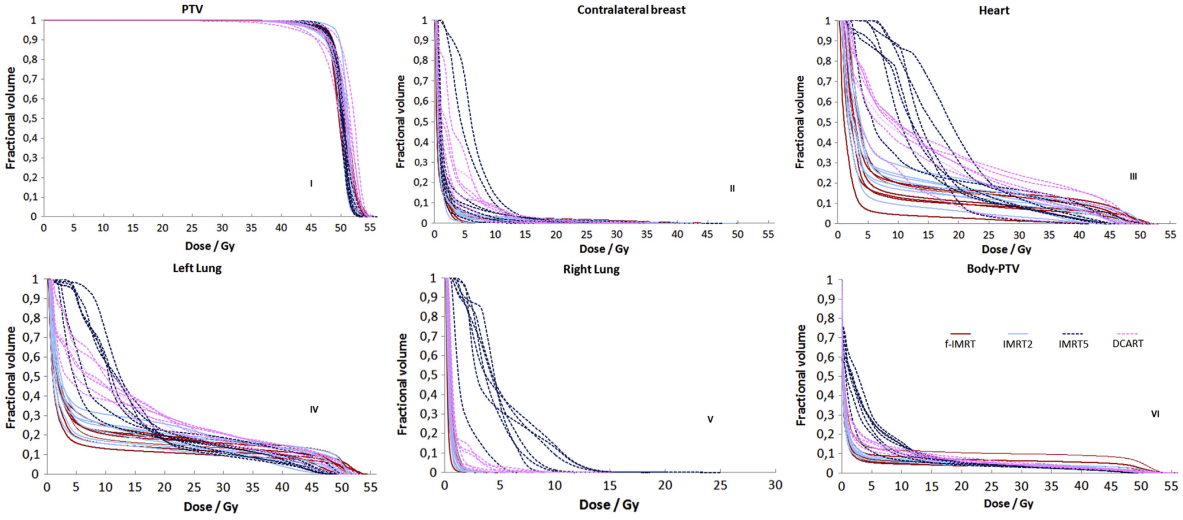

Figure 2. DVH comparison between the 4 irradiation techniques f-IMRT in red, IMRT2 in light blue, IMRT5 in dark blue and DCART in pink, for the (I) PTV, (II) contralateral breast, (III) heart, (IV) left and (V) right lungs and (VI) Body-PTV. (For interpretation of the references to color in this figure legend, the reader is referred to the web version of this article.)

Table 1
PTV and OAR parameters evaluated for f-IMRT, IMRT2, IMRT5 and DCART irradiations, for PBC algorithm. The displayed values are the mean with their respective standard deviations and *p*-values calculated using the Friedman test. The values in bold are the variables with significant statistical differences (p-value ≤ 0.05). ALARA: As Low As Reasonably Achievable. PMC: percentage of patients meeting the criteria.

	Plans	Criteria	f-IMRT	PMC	IMRT2	PMC	IMRT5	PMC	DCART	PMC	*p*-Value
PTV	D_{max} (%)	<110%	109.87 ± 0.67	57%	109.01 ± 1.46	71%	111.31 ± 4.29	86%	109.57 ± 1.01	71%	0.510
	$V_{53.5Gy}$ (%)	ALARA	2.97 ± 0.69	–	0.19 ± 0.05	–	0.64 ± 0.33	–	5.17 ± 1.47	–	**0.008**
	$V_{47.5Gy}$ (%)	≥90%	93.41 ± 0.77	86%	92.84 ± 1.04	71%	93.89 ± 0.58	86%	89.87 ± 1.92	71%	0.093
	HI	Ideally 1	1.14 ± 0.01	–	1.12 ± 0.01	–	1.11 ± 0.01	–	1.17 ± 0.02	–	**0.001**
	CI	Ideally 1	1.47 ± 0.10	–	1.34 ± 0.09	–	1.09 ± 0.04	–	1.24 ± 0.04	–	**0.002**
	CN	Ideally 1	0.61 ± 0.11	–	0.66 ± 0.09	–	0.82 ± 0.07	–	0.66 ± 0.06	–	**0.001**
Left lung	D_{mean} (%)	ALARA	17.94 ± 1.16	–	18.93 ± 1.53	–	28.40 ± 1.25	–	28.70 ± 1.02	–	**0.001**
	V_{5Gy} (%)	≤50%	23.54 ± 4.34	100%	27.57 ± 6.03	100%	82.09 ± 6.03	14%	57.50 ± 8.55	43%	**0.000**
	V_{10Gy} (%)	≤35%	18.92 ± 1.36	100%	23.08 ± 2.07	100%	52.04 ± 6.16	43%	44.94 ± 2.02	14%	**0.000**
	V_{20Gy} (%)	≤20%	16.34 ± 1.24	100%	18.61 ± 1.69	86%	19.50 ± 0.81	71%	27.73 ± 1.06	14%	**0.001**
	V_{40Gy} (%)	ALARA	11.43 ± 0.86	–	10.21 ± 1.49	–	7.79 ± 0.98	–	11.83 ± 1.03	–	**0.013**
Right lung	D_{mean} (%)	ALARA	3.73 ± 2.55	–	1.10 ± 0.09	–	8.61 ± 0.88	–	1.61 ± 0.15	–	**0.002**
	$D_{5\%}$ (%)	≤5 Gy	2.21 ± 0.40	100%	2.41 ± 0.15	100%	17.96 ± 2.03	43%	4.70 ± 0.83	100%	**0.000**
	V_{5Gy} (%)	≤10%	0.00	100%	0.00	100%	35.82 ± 4.49	29%	0.99 ± 1.13	100%	**0.000**
CLB	D_{mean} (%)	ALARA	2.99 ± 0.30	–	2.90 ± 0.29	–	6.21 ± 1.70	–	5.49 ± 0.75	–	**0.001**
	V_{5Gy} (%)	≤5%	2.90 ± 0.67	86%	3.39 ± 0.59	86%	21.53 ± 9.66	14%	16.76 ± 3.64	0%	**0.001**
	V_{2Gy} (%)	ALARA	14.30 ± 1.25	–	13.11 ± 1.58	–	38.89 ± 14.31	–	40.47 ± 5.92	–	**0.003**
Heart	D_{mean} (%)	ALARA	14.82 ± 1.92	–	16.86 ± 1.70	–	30.79 ± 2.24	–	26.20 ± 2.77	–	**0.000**
	V_{10Gy} (%)	≤30%	14.69 ± 5.65	100%	20.44 ± 6.25	100%	68.76 ± 20.51	0%	43.63 ± 8.23	14%	**0.000**
	V_{25Gy} (%)	≤10%	10.62 ± 4.72	57%	13.24 ± 4.63	14%	13.58 ± 6.12	14%	20.26 ± 7.88	14%	**0.001**
Body-PTV	D_{mean} (%)	ALARA	6.13 ± 0.92	–	5.41 ± 0.26	–	8.94 ± 0.57	–	7.33 ± 0.32	–	**0.004**
	V_{40Gy} (%)	ALARA	3.23 ± 0.24	–	2.67 ± 0.24	–	2.05 ± 0.10	–	2.59 ± 0.11	–	**0.001**
	V_{20Gy} (%)	ALARA	4.49 ± 0.25	–	4.94 ± 0.22	–	5.16 ± 0.23	–	6.41 ± 0.40	–	**0.001**
	V_{2Gy} (%)	ALARA	11.81 ± 0.73	–	12.07 ± 0.67	–	43.53 ± 3.64	–	20.74 ± 1.12	–	**0.000**
PTV	D_{max} (%)	<110%	110.44 ± 1.10	71%	110.31 ± 2.23	43%	112.61 ± 4.29	43%	110.86 ± 1.83	29%	0.864
	$V_{53.5Gy}$ (%)	ALARA	0.40 ± 0.12	–	0.73 ± 0.58	–	0.30 ± 0.20	–	1.14 ± 0.28	–	0.128
	$V_{47.5Gy}$ (%)	≥90%	73.54 ± 2.52	0%	78.23 ± 2.26	14%	81.67 ± 1.75	0%	74.99 ± 3.59	0%	0.054
	HI	Ideally 1	1.20 ± 0.02	–	1.18 ± 0.01	–	1.15 ± 0.01	–	1.23 ± 0.02	–	**0.001**
	CI	Ideally 1	1.02 ± 0.10	–	0.98 ± 0.07	–	0.86 ± 0.03	–	0.93 ± 0.06	–	0.134
	CN	Ideally 1	0.56 ± 0.17	–	0.63 ± 0.05	–	0.77 ± 0.04	–	0.61 ± 0.06	–	**0.003**

lung involvement (higher D_{mean}); in fact, V_{5Gy} to be inferior to 10% was not achieved by 5 out 7 cases and $D_{5\%}$ to be less than 5% was only achieved in 3 out of 7 plans, for IMRT5. On the contrary, IMRT2 presented the lowest D_{mean}.

Analyzing the CLB results, IMRT5 and DCART were the options with higher doses for all reported variables (see Fig. 2(II)), meeting the criteria V_{5Gy} to be inferior to 5% in none and 1 out of 7 plans, respectively. For the tangential techniques 6 out of 7 cases met V_{5Gy}.

Regarding the heart, f-IMRT and IMRT2 were the techniques with the best results: V_{10Gy} was achieved for all cases; V_{25Gy} was only achieved in 57% of the f-IMRT and 14% of IMRT2 plans; for IMRT5 and DCART, V_{10Gy} was achieved for none and 1 out of 7 cases,

Table 2
PTV and OAR mean and standard deviations for f-IMRT, IMRT2, IMRT5 and DCART plans, for iMC algorithm. The displayed values are the mean, standard deviation and *p*-value using Friedman's test. The values in bold are the variables with significant statistical differences (p-value ≤ 0.05). ALARA: As Low as Reasonably Achievable. PMC: percentage of patients meeting the criteria.

	Plans	Criteria	f-IMRT	PMC	IMRT2	PMC	IMRT5	PMC	DCART	PMC	*p*-Value
PTV	D_{max} (%)	<110%	110.44 ± 1.10	71%	110.31 ± 2.23	43%	112.61 ± 4.29	43%	110.86 ± 1.83	29%	0.864
	$V_{53.5Gy}$ (%)	ALARA	0.40 ± 0.12	–	0.73 ± 0.58	–	0.30 ± 0.20	–	1.14 ± 0.28	–	0.128
	$V_{47.5Gy}$ (%)	≥90%	73.54 ± 2.52	0%	78.23 ± 2.26	14%	81.67 ± 1.75	0%	74.99 ± 3.59	0%	0.054
	HI	Ideally 1	1.20 ± 0.02	–	1.18 ± 0.01	–	1.15 ± 0.01	–	1.23 ± 0.02	–	**0.001**
	CI	Ideally 1	1.02 ± 0.10	–	0.98 ± 0.07	–	0.86 ± 0.03	–	0.93 ± 0.06	–	0.134
	CN	Ideally 1	0.56 ± 0.17	–	0.63 ± 0.05	–	0.77 ± 0.04	–	0.61 ± 0.06	–	**0.003**
Left lung	D_{mean} (%)	ALARA	27.32 ± 0.96	–	28.00 ± 1.15	–	18.43 ± 1.40	–	16.86 ± 1.06	–	0.000
	V_{5Gy} (%)	≤50%	26.46 ± 5.44	100%	30.71 ± 6.30	100%	81.83 ± 19.02	14%	57.43 ± 8.67	29%	0.000
	V_{10Gy} (%)	≤35%	20.99 ± 1.35	100%	24.10 ± 1.88	100%	51.44 ± 5.76	29%	43.19 ± 1.97	14%	0.000
	V_{20Gy} (%)	≤20%	16.30 ± 1.22	100%	18.69 ± 1.67	71%	20.59 ± 0.76	71%	26.96 ± 1.04	14%	0.001
	V_{40Gy} (%)	ALARA	9.27 ± 0.74	–	8.37 ± 1.39	–	5.49 ± 1.29	–	10.71 ± 1.04	–	0.008
Right lung	D_{mean} (%)	ALARA	7.75 ± 0.76	–	8.03 ± 0.86	–	33.87 ± 4.94	–	17.99 ± 3.52	–	0.001
	$D_{5\%}$ (%)	≤5 Gy	1.20 ± 0.22	100%	1.25 ± 0.14	100%	16.06 ± 1.70	14%	3.58 ± 0.81	86%	0.000
	V_{5Gy} (%)	≤10%	0.00	100%	0.00	100%	31.93 ± 5.10	29%	0.81 ± 1.0	100%	0.000
CLB	D_{mean} (%)	ALARA	2.84 ± 0.30	–	2.60 ± 0.31	–	6.23 ± 1.64	–	4.57 ± 0.74	–	0.007
	V_{5Gy} (%)	≤5%	3.70 ± 0.68	71%	3.91 ± 0.62	86%	21.58 ± 9.31	14%	13.49 ± 2.88	0%	0.002
	V_{2Gy} (%)	ALARA	14.63 ± 1.42	–	13.89 ± 1.93	–	40.59 ± 13.75	–	30.56 ± 5.90	–	0.006
Heart	D_{mean} (%)	ALARA	13.56 ± 1.43	–	16.10 ± 2.19	–	30.30 ± 2.19	–	26.36 ± 2.50	–	0.007
	V_{10Gy} (%)	≤30%	16.14 ± 6.85	100%	23.40 ± 7.33	100%	81.21 ± 22.82	0%	48.90 ± 12.06	14%	0.000
	V_{25Gy} (%)	≤10%	10.06 ± 4.50	71%	13.19 ± 4.59	14%	13.71 ± 5.90	14%	19.99 ± 8.11	14%	0.003
Body-PTV	D_{mean} (%)	ALARA	5.79 ± 0.52	–	4.75 ± 0.39	–	8.73 ± 0.56	–	6.87 ± 0.32	–	0.002
	V_{40Gy} (%)	ALARA	2.88 ± 0.21	–	2.33 ± 0.23	–	1.76 ± 0.11	–	2.37 ± 0.12	–	0.001
	V_{20Gy} (%)	ALARA	4.51 ± 0.24	–	4.94 ± 0.22	–	5.16 ± 0.23	–	6.26 ± 0.37	–	0.001
	V_{2Gy} (%)	ALARA	11.54 ± 0.62	–	10.99 ± 1.75	–	43.51 ± 3.79	–	19.30 ± 1.12	–	0.000

Please cite this article in press as: Borges C, et al., Comparison of different breast planning techniques and algorithms for radiation therapy treatment, Physica Medica (2013), http://dx.doi.org/10.1016/j.ejmp.2013.04.006

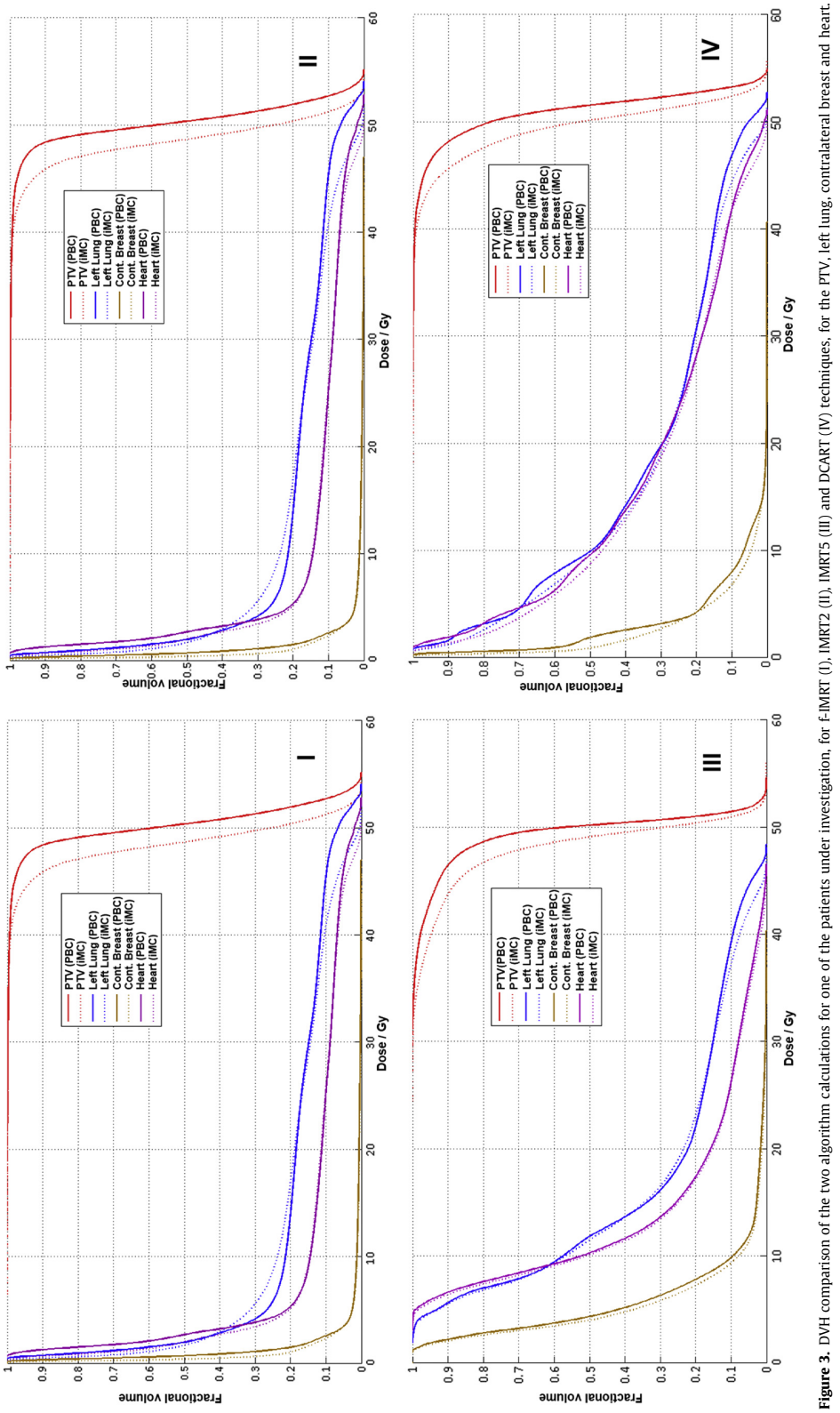

Figure 3. DVH comparison of the two algorithm calculations for one of the patients under investigation, for f-IMRT (I), IMRT2 (II), IMRT5 (III) and DCART (IV) techniques, for the PTV, left lung, contralateral breast and heart.

Please cite this article in press as: Borges C, et al., Comparison of different breast planning techniques and algorithms for radiation therapy treatment, Physica Medica (2013), http://dx.doi.org/10.1016/j.ejmp.2013.04.006

respectively; for V_{25Gy}, only in 1 plan out of 7 was the goal achieved, for both techniques. D_{mean} was lower for f-IMRT and IMRT2, as expected analyzing Fig. 2(III).

On the Body-PTV, D_{mean} was higher for IMRT5 and DCART; IMRT5 was the technique with lower V_{40Gy} but that most spread, mainly low doses (verified by V_{2Gy} in Table 1 and for doses up to 15 Gy in Fig. 2(VI)) into the body whereas f-IMRT and IMRT2 had the lowest values for V_{2Gy} and V_{20Gy}.

For the OAR involved in breast cancer treatment, the 4 techniques under investigation had statistical significant differences (p-value ≤ 0.05) for all the variables studied and presented in Table 1.

Monte Carlo algorithm

The final optimized PBC plans were recalculated using iMC algorithm and a detailed analysis was performed. The results are presented in Table 2.

With the recalculation of the optimized plans using iMC, the mean values for $V_{47.5Gy}$ criteria did not reach the 90% PTV coverage for any of the techniques (except one case of IMRT2) and mean D_{max} results were higher than the limit established (110%) for 71% of f-IMRT, 43% of IMRT2 and IMRT5 and 29% of DCART cases.

Among these results, IMRT5 was the technique with better $V_{47.5Gy}$, lower $V_{53.5Gy}$, best HI and CN; f-IMRT was the technique with the worst $V_{47.5Gy}$. IMRT techniques have the closest HI to unity, presenting therefore the most homogeneous dose distributions. Considering the conformity indexes, the tangential techniques had CI closer to unity; however for CN, the best results were achieved by IMRT5 which means that with the tangential techniques there is a higher percentage of non-PTV volume being irradiated with 95% of the prescribed dose because of the limitation of the tangential fields to confine to the PTV due to the concave shape of the breast PTV.

For the iMC, no significant statistical differences were observed for the PTV parameters, except for HI and CN.

On the left lung, all plans of f-IMRT respected all the criteria; IMRT2 did not achieve V_{20Gy} for 2 out of the 7 patients, respecting V_{5Gy} and V_{10Gy}; for IMRT5 only 1 case verified V_{5Gy}, 2 respected V_{10Gy} and only 2 did not meet V_{20Gy}; for DCART only 2 cases respected V_{5Gy} and no more than 1 case verified V_{10Gy} and V_{20Gy}. With these results, it is evident that with IMRT5 and DCART higher percentages of lung received low doses (expressed by V_{5Gy} and V_{10Gy}) particularly when compared to f-IMRT and IMRT2. However with IMRT5 the percentage of lung that received doses above 40 Gy was significantly lower when compared to the other techniques. On the right lung, all the variables were significantly higher for IMRT5, with only 1 and 2 cases out of respecting $D_{5\%}$ and V_{5Gy}, respectively; DCART (with only one case not verifying $D_{5\%}$ criteria) had lower percentage of volume involved compared to IMRT5 (with only one and two cases verifying $D_{5\%}$ and V_{5Gy} criteria, respectively) but still had significantly higher values when compared to the tangential techniques. On the CLB, similar results were achieved with IMRT5 and DCART spreading lower doses into this OAR, with 1 and 0 cases out of 7 respecting the criterion established, respectively. 5 and 6 cases out of 7 had V_{5Gy} inferior to 5% for f-IMRT and IMRT2, respectively. On the heart, f-IMRT was the technique with lower mean doses for all cases verifying V_{10Gy} inferior to 30% and 5 out of 7 meeting the criterion V_{25Gy} to be less than 10%; IMRT2 had higher doses on these parameters and only 1 case respected V_{25Gy}; IMRT5 had the highest heart volume involvement for doses up to 10 Gy, with at most one case respecting the criteria; but DCART was the technique with higher volume involvement for 25 Gy, with only one case respecting the criteria. Regarding the Body-PTV, IMRT5 presented the highest mean values for D_{mean} and V_{2Gy} and the lowest V_{40Gy}; DCART exhibited the highest V_{20Gy}. IMRT2 presented the lowest D_{mean} and V_{2Gy}. There were significant statistical differences for all the OAR variables investigated for iMC, which should be carefully taken into account.

Comparison between PBC and iMC algorithms

A comparison between the two algorithms was performed and the results are presented in Fig. 3, where it is possible to visualize the dose–volume differences between the two calculations for the PTV, left lung, CLB and heart, for f-IMRT (I), IMRT2 (II), IMRT5 (III) and DCART (IV).

Considering the results in Fig. 3, the major differences between the two calculation algorithms were for the PTV, for doses above 40 Gy, for f-IMRT (I), IMRT2 (II) and DCART (IV) and above 30 Gy for IMRT5 (III), with PBC predicting higher doses than iMC. The maximum dose differences observed were of 4 Gy. In the left lung, iMC also estimated lower doses, mainly for doses above 35 Gy.

The variables with significant statistical differences were further investigated performing a pairwise comparison between techniques and the results are presented in Table 3.

PBC presented significant statistical differences for $V_{53.5Gy}$, HI, CI and CN, whereas for iMC differences were observed for HI and CN.

For the PBC algorithm, for $V_{53.5Gy}$, the significant statistical differences were observed between DCART and the inverse IMRT techniques. For HI, significant statistical differences were found between f-IMRT and IMRT5, DCART and the inverse IMRT techniques. CI presented significant statistical differences between IMRT5 and the tangential techniques; CN exhibited differences between f-IMRT and IMRT5.

For the iMC algorithm, the statistical significant differences, found were for HI, between f-IMRT and IMRT5, DCART and the inverse IMRT techniques; for the CN between f-IMRT and IMRT5.

The results of the comparison performed for the OAR, for the variables with significant statistical differences (p-value ≤ 0.05), for PBC and iMC, are presented in Table 4.

The results of a statistical analysis to compare PBC and iMC algorithms using Wilcoxon test are presented in Table 5.

Significant statistical differences (p-value ≤ 0.05) were found for most of the PTV variables investigated (the exceptions were for D_{max} and CN for f-IMRT, IMRT2 and IMRT5; $V_{53.5Gy}$ for IMRT2 and

Table 3
Pairwise comparison using the Friedman's test between the techniques for the PTV variables that exhibit significant statistical differences (p-value ≤ 0.05). The cells in white background are related to the PBC algorithm whereas the cells in light gray background correspond to the iMC results. The values in bold are the variables with significant statistical differences (p-value ≤ 0.05).

			f-IMRT	IMRT2	IMRT5	DCART
PTV	$V_{53.5Gy}$	f-IMRT		0.078	0.214	0.178
		IMRT2	NS		0.605	**0.002**
		IMRT5	NS	NS		**0.010**
		DCART	NS	NS	NS	
	HI	f-IMRT		0.098	**0.030**	0.178
		IMRT2	0.214		0.605	**0.003**
		IMRT5	**0.023**	0.301		**0.000**
		DCART	0.147	**0.007**	**0.000**	
	CI	f-IMRT		0.408	**0.000**	0.098
		IMRT2	NS		**0.004**	0.408
		IMRT5	NS	NS		**0.038**
		DCART	NS	NS	NS	
	CN	f-IMRT		0.586	**0.001**	0.884
		IMRT2	0.471		0.137	1.000
		IMRT5	**0.003**	0.471		0.078
		DCART	1.000	1.000	0.058	

NS – no significant statistical differences.

Please cite this article in press as: Borges C, et al., Comparison of different breast planning techniques and algorithms for radiation therapy treatment, Physica Medica (2013), http://dx.doi.org/10.1016/j.ejmp.2013.04.006

Table 4
Pairwise comparison using the Friedman's test between the techniques for the OAR variables that exhibit significant statistical differences. The cells in white background are related to the PBC algorithm whereas the cells in light gray background correspond to the iMC results. The values in bold are the variables with significant statistical differences (p-value ≤ 0.05).

			f-IMRT	IMRT2	IMRT5	DCART
Contralateral Breast	D_{mean}	f-IMRT		0.535	**0.017**	**0.017**
		IMRT2	0.918		**0.003**	**0.003**
		IMRT5	**0.007**	**0.005**		1.000
		DCART	**0.049**	**0.038**	0.469	
	V_{5Gy}	f-IMRT		0.535	**0.002**	**0.001**
		IMRT2	0.679		**0.013**	**0.007**
		IMRT5	**0.004**	**0.013**		0.836
		DCART	**0.004**	**0.013**	1.000	
	V_{2Gy}	f-IMRT		0.535	0.098	**0.007**
		IMRT2	0.836		**0.023**	**0.001**
		IMRT5	**0.013**	**0.023**		0.301
		DCART	**0.007**	**0.013**	0.836	
Heart	D_{mean}	f-IMRT		0.301	**0.000**	**0.002**
		IMRT2	0.408		**0.007**	**0.038**
		IMRT5	**0.000**	**0.005**		0.535
		DCART	**0.003**	**0.030**	0.535	
	V_{10Gy}	f-IMRT		0.844	**0.000**	**0.011**
		IMRT2	0.884		**0.043**	0.586
		IMRT5	**0.000**	**0.043**		1.000
		DCART	**0.011**	0.586	1.000	
	V_{25Gy}	f-IMRT		0.062	**0.004**	**0.000**
		IMRT2	0.062		0.301	**0.038**
		IMRT5	**0.004**	0.301		0.301
		DCART	**0.000**	**0.038**	0.301	
BodyPTV	D_{mean}	f-IMRT		0.836	**0.004**	0.062
		IMRT2	0.469		**0.002**	**0.038**
		IMRT5	**0.005**	**0.000**		0.301
		DCART	0.214	**0.049**	0.121	
	V_{40Gy}	f-IMRT		0.062	**0.000**	**0.038**
		IMRT2	**0.030**		**0.038**	0.836
		IMRT5	**0.000**	0.078		0.062
		DCART	**0.030**	1.000	0.078	
	V_{20Gy}	f-IMRT		0.098	**0.038**	**0.000**
		IMRT2	0.098		0.679	**0.013**
		IMRT5	**0.038**	0.679		**0.038**
		DCART	**0.000**	**0.013**	**0.038**	
	V_{2Gy}	f-IMRT		0.535	**0.000**	**0.013**
		IMRT2	0.301		**0.001**	0.062
		IMRT5	**0.000**	**0.002**		0.147
		DCART	**0.007**	0.098	0.147	

			f-IMRT	IMRT2	IMRT5	DCART
LeftLung	D_{mean}	f-IMRT		0.214	**0.001**	**0.001**
		IMRT2	0.535		**0.038**	**0.038**
		IMRT5	**0.038**	**0.007**		1.000
		DCART	**0.002**	**0.000**	0.301	
	V_{5Gy}	f-IMRT		0.884	**0.000**	**0.011**
		IMRT2	0.884		**0.043**	0.586
		IMRT5	**0.000**	**0.043**		1.000
		DCART	**0.011**	0.586	1.000	
	V_{10Gy}	f-IMRT		0.147	**0.000**	**0.001**
		IMRT2	0.301		**0.013**	0.062
		IMRT5	**0.000**	**0.007**		0.535
		DCART	**0.002**	**0.038**	0.535	
	V_{20Gy}	f-IMRT		0.062	0.062	**0.000**
		IMRT2	0.098		1.000	**0.023**
		IMRT5	0.078	0.918		**0.023**
		DCART	**0.000**	**0.017**	**0.023**	
	V_{40Gy}	f-IMRT		0.214	**0.007**	0.836
		IMRT2	1.000		0.147	0.147
		IMRT5	**0.023**	**0.023**		**0.004**
		DCART	0.301	0.301	**0.001**	
RightLung	D_{mean}	f-IMRT		0.408	**0.007**	0.301
		IMRT2	0.679		**0.000**	0.062
		IMRT5	**0.000**	**0.001**		0.098
		DCART	**0.038**	0.098	0.098	
	$D_{5\%}$	f-IMRT		0.756	**0.001**	0.062
		IMRT2	0.679		**0.000**	**0.030**
		IMRT5	**0.000**	**0.001**		0.121
		DCART	**0.017**	**0.049**	0.147	
	V_{5Gy}	f-IMRT		1.000	**0.003**	0.375
		IMRT2	1.000		**0.003**	0.375
		IMRT5	**0.003**	**0.003**		0.586
		DCART	0.375	0.375	0.586	

IMRT5 that did not exhibit significant statistical differences). For the left lung, there were significant statistical differences between PBC and iMC for D_{mean} and V_{40Gy}, for all techniques, for V_{10Gy}, for f-IMRT and DCART; for V_{5Gy}, for IMRT2; and V_{20Gy} for IMRT5 and DCART. On the right lung, the differences were observed for D_{mean} and $D_{5\%}$ for all the techniques. On the CLB, differences with statistical significance were observed for all the variables for DCART and IMRT2, except V_{2Gy}, for IMRT2. On the heart, D_{mean} for IMRT2 and IMRT5 and V_{10Gy} for DCART also had statistically significant differences. On the Body-PTV, differences were verified for D_{mean} (except for f-IMRT); in all techniques for V_{40Gy} and V_{20Gy}; and for V_{2Gy}, for DCART.

Discussion

From the results of the optimized plans for f-IMRT, IMRT2, IMRT5 and DCART it is possible to infer that all techniques present possible solutions for breast irradiation even though with some drawbacks that must be taken into consideration. However, with IMRT5 was the technique with the best HI and CN indexes (see Tables 1 and 2) for both algorithms.

With IMRT5 larger percentages of healthy tissues, such as the left lung (V_{5Gy}, V_{10Gy} and V_{20Gy}), right lung ($D_{5\%}$ and V_{5Gy}), CLB (V_{5Gy} and V_{2Gy}), heart (V_{10Gy}) and Body-PTV (V_{2Gy}) received more low doses compared to the techniques that use only tangential fields (f-IMRT or IMRT2).

In this study, for PBC, significant statistical differences were found between the techniques for all the OAR parameters investigated, mainly between the tangential and the non-tangential techniques. With the use of non-tangential fields/incidences to the breast, there was a wider spread of doses into the OAR and healthy tissues surrounding the PTV. Nonetheless with IMRT5, higher doses do reach lower percentages of left lung (V_{40Gy}) and heart, sparing these organs to high doses. Especially high-dose cardiac irradiation is of particular concern according to several studies [2,3,62,63].

Please cite this article in press as: Borges C, et al., Comparison of different breast planning techniques and algorithms for radiation therapy treatment, Physica Medica (2013), http://dx.doi.org/10.1016/j.ejmp.2013.04.006

Table 5
Wilcoxon comparison of the PBC and iMC algorithms for the PTV and OAR (*p*-values). The values in bold are the variables with significant statistical differences (*p*-value ≤ 0.05).

		f-IMRT	IMRT2	IMRT5	DCART
PTV	D_{max}	0.345	0.080	0.225	**0.043**
	$V_{53.5Gy}$	**0.031**	0.922	0.125	**0.016**
	$V_{47.5Gy}$	**0.016**	**0.016**	**0.016**	**0.016**
	HI	**0.031**	**0.016**	**0.016**	**0.016**
	CI	**0.031**	**0.016**	**0.016**	**0.016**
	CN	0.176	0.310	0.128	**0.028**
Left lung	D_{mean}	0.016	0.031	0.016	0.016
	V_{5Gy}	0.080	**0.043**	0.465	0.686
	V_{10Gy}	**0.031**	0.297	0.813	**0.016**
	V_{20Gy}	0.266	0.719	**0.016**	**0.047**
	V_{40Gy}	**0.031**	**0.016**	**0.016**	**0.016**
Right lung	D_{mean}	0.297	**0.016**	**0.016**	**0.016**
	$D_{5\%}$	**0.031**	**0.016**	**0.016**	**0.031**
Contralateral breast	D_{mean}	0.266	**0.016**	1.000	**0.016**
	V_{5Gy}	0.078	**0.016**	0.438	**0.016**
	V_{2Gy}	0.813	0.234	0.313	**0.016**
Heart	D_{mean}	0.219	**0.016**	**0.031**	0.297
	V_{10Gy}	0.156	0.938	0.063	**0.016**
	V_{25Gy}	0.345	0.310	0.612	0.176
Body-PTV	D_{mean}	0.672	**0.016**	**0.016**	**0.016**
	V_{40Gy}	**0.016**	**0.016**	**0.016**	**0.016**
	V_{20Gy}	0.500	1.000	1.000	**0.031**
	V_{2Gy}	0.406	0.969	0.797	**0.016**

Our results are in agreement with previous work concluding that using non-tangential fields increase the homogeneity and conformity to the PTV, and heart and lung volumes receiving high doses decrease but more healthy tissues receive low doses [24,38,39,41,45,64].

In our study, tangential inverse-planning IMRT (IMRT2) did not verify dose homogeneity improvement or reduction of dose to the heart or left lung, compared to tangential multi-segmented f-IMRT, in contrast with previous results [20]. Nonetheless, f-IMRT and IMRT2 presented the solutions with less percentage of healthy tissues receiving low and medium doses in the OAR but had worse conformation CI and CN indexes when compared to the non-tangential techniques. It was also observed that IMRT2 did not significantly reduce the doses in the ipsilateral OAR when compared to f-IMRT, in concordance to the observations made by Zhou et al. [44]. On the other hand, these techniques presented higher doses than IMRT5 on the left lung and heart for doses above 40 Gy, due to the concave shape of the breast and the incapacity of the tangential fields to conform to the breast geometry.

No benefit in using DCART when compared to the IMRT techniques presented before on what the PTV coverage and dose in the OAR are concerned.

In general, the conclusions achieved concerning the techniques were similar for both algorithms. However, according to the data and considering Fig. 3 it can be clearly observed that there were differences between the algorithms, mainly for the PTV, with the PBC overestimating the higher doses in this structure, from 12% up to 20%. Furthermore, on the OAR, there are also relevant differences for the left lung and heart, in the high doses range (>40 Gy), with PBC also overestimating the doses in these organs.

These differences may arise from the limitations of the PBC to estimate the doses on tangential beams due to the lack of electron equilibrium in the superficial (buildup) region in the irregular curvature of the breast and the inaccurate management of heterogeneities, in particular at the interfaces between air (lung) and soft tissue as the PBC does not model the rebuild-up and does not adequately account for electron transport [48–50].

It is presumed that iMC calculations are more accurate than the PBC algorithm calculations. The major concern becomes that the most relevant irradiation goal, $V_{47.5Gy}$ to be superior to 90% is not achieved by iMC algorithm. From the past experience and the results achieved up to now, PBC was used and the clinical results are known. Increasing the dose to achieve the $V_{47.5Gy}$ goal with iMC (by increasing, for instance, the normalization value) would increase the dose to the whole breast. The consequences of such a procedure are not well known and care should be taken when changing the calculation algorithm, as it may also contribute to an increase in the dose to the OAR.

Conclusions

This study presents the results from a breast irradiation comparison between 4 different techniques: f-IMRT (without wedges), IMRT2, IMRT5 and DCART. The plans were evaluated based on criteria adapted from QUANTEC [55] and RTOG 1005 [56].

Sizable discrepancies remain concerning between the 4 techniques investigated on breast irradiation and between the two algorithms studied (PBC and iMC). The dose distributions were optimized for the PBC algorithm. The PTV was adequately covered with all the techniques (evaluated by $V_{47.5Gy}$), considering PBC. IMRT5 had advantages over the other techniques based on the dosimetric comparison performed in this study especially in the high dose region of the left lung and heart, target conformation and heterogeneity indexes; DCART was the technique with the lowest $V_{47.5Gy}$ and did not present improvement in sparing the OAR or the PTV coverage over the IMRT techniques investigated. However, the non-tangential techniques (IMRT5 and DCART) do increase the scattered dose and expose larger percentage of healthy volumes to low and medium doses.

f-IMRT is still the recommended technique for breast irradiation. Nonetheless, in case of high heart or left lung involvement, IMRT5 should be considered to breast cancer irradiation as it creates the most conformal distribution at the expense of more normal tissue receiving low dose.

These observations are valid both for PBC and iMC. However, statistical significant differences were found between PBC and iMC calculations, on the variables investigated, mainly in the higher doses regimen (>40 Gy) for the PTV, left lung and heart.

References

[1] Stovall M, Smith S, Langholz B, Boice J, Shore R, Andersson M, et al. Dose to the contralateral breast from radiotherapy and risk of second primary breast cancer in the WECARE study. Int J Radiat Oncol Biol Phys 2008;72(4):1021–30.
[2] Clarke M, Collins R, Darby S, Davies C, Elphinstone P, Evans V, et al. Effects of radiotherapy and of differences in the extent of surgery for early breast cancer on local recurrence and 15-year survival: an overview of the randomised trials. Lancet 2005;366:2087–106.
[3] Cuzick J, Stewart H, Rutqvist L, Houghton J, Edwards R, Redmond C, et al. Cause-specific mortality in long-term survivors of breast cancer who participated in trials of radiotherapy. J Clin Oncol 1994;12(3):447–53.
[4] Fisher B, Anderson S, Redmond C, Wolmark N, Wickerham L, Cronin W. Reanalysis and results after 12 years of follow-up in a randomized clinical trial comparing total mastectomy with lumpectomy with or without irradiation in the treatment of breast cancer. N Engl J Med 1995;333:1456–61.
[5] Veronesi U, Marubini E, Mariani L, Galimberti V, Luini A, Veronesi P, et al. Radiotherapy after breast-conserving surgery in small breast carcinoma: long-term results of a randomized trial. Ann Oncol 2001;12:997–1003.
[6] Poortmans P. Evidence based radiation oncology: breast cancer. Radiother Oncol 2007;84:84–101.
[7] Veronesi U, Luini A, Vecchio M, Greco M, Galimberti V, Merson M, et al. Radiotherapy after breast-preserving surgery in women with localized cancer of the breast. N Engl J Med 1993;328(22):1587–91.
[8] Overgaard M, Hansen P, Overgaard J, Rose C, Andersson M, Bach F, et al. Post-operative radiotherapy in high-risk premenopausal women with breast cancer who receive adjuvant chemotherapy. N Engl J Med 1997;337(14):949–55.
[9] Bartelink H, Horiot JC, Poortmans P, Struikmans H, Van den Bogaert W, Fourquet A, et al. Impact of a higher radiation dose on local control and

Please cite this article in press as: Borges C, et al., Comparison of different breast planning techniques and algorithms for radiation therapy treatment, Physica Medica (2013), http://dx.doi.org/10.1016/j.ejmp.2013.04.006

survival in breast-conserving therapy of early breast cancer: 10-year results of the randomized boost versus no boost EORTC 22881-10882 trial. J Clin Oncol 2007;25(22):3259–65.
[10] Romestaing P, Lehingue Y, Carrie C, Coquard R, Montbarbon X, Ardiet J, et al. Role of a 10-Gy boost in the conservative treatment of early breast cancer: results of a randomized clinical trial in Lyon, France. J Clin Oncol 1997;15(3):963–8.
[11] Casebow M. Matching of adjacent radiation beams for isocentric radiotherapy. Br J Radiol 1984;57:735–40.
[12] van Asselen B, Raaijmakers C, Hofman P, Lagendijk J. An improved breast irradiation technique using three-dimensional geometrical information and intensity modulation. Radiother Oncol 2001;58:341–7.
[13] Lu X, Sullivan S, Eggleston T, Holupka E, Bellerive M, Abner A, et al. A three-field breast treatment technique with precise geometric matching using multileaf collimator-equipped linear accelerators. Int J Radiat Oncol Biol Phys 2003;55(5):1420–31.
[14] Romeo N. A new isocentric technique for exact geometric matching in the radiotherapy of the breast and ipsilateral supraclavicular fossa using dual asymmetric jaws. Phys Med 2012;28:281–7.
[15] International Commission of Radiation Units and Measurements. Dose specification for reporting external beam therapy with photons and electrons: report 50. Bethesda, MD: ICRU; 1992.
[16] Chang S, Deschesne K, Cullip T, Parker S, Earnhart J. A comparison of different intensity modulation treatment techniques for tangential breast irradiation. Int J Radiat Oncol Biol Phys 1999;45(5):1305–14.
[17] Kestin L, Sharpe M, Frazier R, Vicini F, Yan D, Matter R, et al. Intensity modulation to improve dose uniformity with tangential breast radiotherapy: initial clinical experience. Int J Radiat Oncol Biol Phys 2000;48(5):1559–68.
[18] Donovan E, Johnson U, Shentall G, Evans P, Neal A, Yarnold J. Evaluation of compensation in breast radiotherapy: a planning study using multiple static fields. Int J Radiat Oncol Biol Phys 2000;46(3):671–9.
[19] Evans P, Donovan E, Partridge M, Childs P, Convery D, Eagle S, et al. The delivery of intensity modulated radiotherapy to the breast using multiple static fields. Radiother Oncol 2000;57:79–89.
[20] Lo YC, Yasuda G, Fitzgerald T, Urie M. Intensity modulation for breast treatment using statis multi-leaf collimators. Int J Radiat Oncol Biol Phys 2000;46(1):187–94.
[21] Vicini F, Sharpe M, Kestin L, Martinez A, Mitchell C, Wallace M, et al. Optimizing breast cancer treatment efficacy with intensity-modulated radiotherapy. Int J Radiat Oncol Biol Phys 2002;54(5):1336–44.
[22] Richmond N, Turner R, Dawes P, Lambert G, Lawrence G. Evaluation of the dosimetric consequences of adding a single asymmetric or MLC shaped field to a tangential breast radiotherapy technique. Radiother Oncol 2003;67(2):165–70.
[23] Ahmed R, De Los Santos J, Fiveash J, Keene K, Popple R. An imrt technique to increase therapeutic ratio of breast irradiation in patients with early-stage left breast cancer: limiting second malignancies. Med Dosim 2008;33(1):71–7.
[24] Mayo C, Urie M, Fitzgerald T. Hybrid IMRT plans – concurrently treating conventional and IMRT beams for improved breast irradiation and reduced planning time. Int J Radiat Oncol Biol Phys 2005;61(3):922–32.
[25] Woo T, Pignol J, Rakovitch E, Vu T, Hicks D, O'Brien P, et al. Body radiation exposure in breast cancer radiotherapy: impact of breast IMRT and virtual wedge compensation techniques. Int J Radiat Oncol Biol Phys 2006;65(1):52–8.
[26] Bhatnagar A, Brandner E, Sonnik D, Wu A, Kalnicki S, Deutsch M, et al. Intensity modulated radiation therapy (IMRT) reduces the dose to the contralateral breast when compared to conventional tangential fields for primary breast irradiation. Breast Cancer Res Treat 2006;96:41–6.
[27] Pignol J, Olivotto R, Rakovitch E, Gardner S, Sixel K, Beckham W, et al. A multicenter randomized trial of breast intensity-modulated radiation therapy to reduce acute radiation dermatitis. J Clin Oncol 2008;26(13):2085–92.
[28] Freedman G, Anderson P, Li J, Eisenberg D, Hanlon A, Nicolaou N. Intensity modulated radiation therapy (IMRT) decreases acute skin toxicity for women receiving radiation for breast cancer. Am J Clin Oncol 2006;29(1):66–70.
[29] McDonald M, Godette K, Butker E, David L, Johnstone P. Long-term outcomes of IMRT for breast cancer: a single-institution cohort analysis. Int J Radiat Oncol Biol Phys 2008;72(4):1031–40.
[30] Harsolia A, Kestin L, Grills I, Wallace M, Jolly S, Jones C, et al. Intensity-modulated radiotherapy results in significant decrease in clinical toxicities compared with conventional wedge-based breast radiotherapy. Int J Radiat Oncol Biol Phys 2007;68(5):1375–80.
[31] Freedman G, Li T, Nicolaou N, Chen Y, Ma C, Anderson P. Breast intensity-modulated radiation therapy reduces time spent with acute dermatitis for women of all breast sizes during radiation. Int J Radiat Oncol Biol Phys 2009;74(3):689–94.
[32] Selvaraj R, Beriwal S, Pourarian R, Lalonde R, Chen A, Mehta K, et al. Clinical implementation of tangential field intensity modulated radiation therapy (IMRT) using sliding window technique and dosimetric comparison with 3D conformal therapy (3DCRT) in breast cancer. Med Dosim 2007;32(4):299–304.
[33] Hong L, Hunt M, Chui C, Spirou S, Forster K, Lee H, et al. Intensity-modulated tangential beam irradiation of the intact breast. Int J Radiat Oncol Biol Phys 1999;44(5):1155–64.
[34] Huang X, Jiang G, Chen J, Cjen L, Hu W. Dosimetric evaluation of intensity-modulated tangential beam versus conventional tangential irradiation for breast cancer. Ai Zheng 2006;25(7):855–60.
[35] Smith W, Menon G, Wolfe N, Ploquin N, Trotter T, Pudney D. IMRT for the breast: a comparison of tangential planning techniques. Phys Med Biol 2010;55:1231–41.
[36] Lohr F, El-Haddad M, Dobler B, Grau R, Wertz H, Kraus-Tiffenbacher U, et al. Potential effect of robust and simple IMRT approach for left-sided breast cancer on cardiac mortality. Int J Radiat Oncol Biol Phys 2009;74(1):73–80.
[37] Li J, Freedman G, Price R, Wang L, Anderson P, Chen L, et al. Clinical implementation of intensity-modulated tangential beam irradiation for breast cancer [Abstract]. Med Phys 2004;31(5):1023–31.
[38] Jurkovic I, Bice W, Sadeghi A, Sims M, Prestidge B. The dosimetric superiority of inverse planned IMRT compared to 3D whole breast irradiation techniques [Abstract]. Int J Radiat Oncol Biol Phys 2007;69(Suppl. 3):S226.
[39] Landau D, Adams E, Webb S, Ross G. Cardiac avoidance in breast radiotherapy: a comparison of simple shielding techniques with intensity-modulated radiotherapy. Radiother Oncol 2001;60:247–55.
[40] Hurkmans C, Cho B, Damen E, Zipj L, Mijnheer B. Reduction of cardiac and lung complication probabilities after breast irradiation using conformal radiotherapy with or without intensity modulation. Radiother Oncol 2002;62:163–71.
[41] Beckham W, Popescu C, Patenaude V, Wai E, Olivotto I. Is multibeam IMRT better than standard treatment for patients with left-sided breast cancer? Int J Radiat Oncol Biol Phys 2007;69(3):918–24.
[42] Johansen S, Cozzi L, Olsen D. A planning comparison of dose patterns in organs at risk and predicted risk for radiation induced malignancy in the contralateral breast following radiation therapy of primary breast using conventional, IMRT and volumetric modulated arc treatment technique. Acta Oncol 2009;48:495–503.
[43] Saur S, Fjellsboe L, Lindmo T, Frengen J. Contralateral breast doses measured using film dosimetry: tangential techniques and an optimized IMRT technique. Phys Med Biol 2009;54:4743–58.
[44] Zhou G, Xu S, Day X, Ju Z, Gong H, Xie C, et al. Clinical dosimetric study of three radiotherapy techniques for postoperative breast cancer: helical tomotherapy, IMRT, and 3D-CRT. Technol Cancer Res Treat 2011;10(1):15–23.
[45] Jagsi R, Moran J, Marsh R, Masi K, Griffith K, Pierce L. Evaluation of four techniques using intensity-modulated radiation therapy for comprehensive locoregional irradiation of breast cancer. Int J Radiat Oncol Biol Phys 2010;78:1594–603.
[46] Ahnesjö A, Saxner M, Trepp A. A pencil beam model for photon dose calculation. Med Phys 1992;19(2):263–73.
[47] Yoo S, Wu Q, O'Daniel J, Horton J, Yin F. Comparison of 3D conformal breast radiation treatment plans using the anisotropic analytical algorithm and pencil beam convolution algorithm. Radiother Oncol 2012;103:172–7.
[48] Panettieri V, Barsoum P, Westermark M, Brualla L, Lax I. AAA and PBC calculation accuracy in the surface build-up region in tangential beam treatments. Phantom and breast case study using the Monte Carlo code PENELOPE. Radiother Oncol 2009;93:94–101.
[49] Chakarova R, Gustafsson M, Bäck A, Grugge N, Palm A, Lindberg A, et al. Superficial dose distribution in breast for tangential radiation treatment, Monte Carlo evaluation of eclipse algorithms in case of phantom and patient geometries. Radiother Oncol 2012;102:102–7.
[50] Knöos T, Ahnesjö A, Nilsson P, Weber P. Limitations of a pencil beam approach to photon dose calculations in lung tissue. Phys Med Biol 1995;40:1411–20.
[51] Almberg S, Lindmo T, Frengen J. Superficial doses in breast cancer radiotherapy using conventional and IMRT techniques: a film-based phantom study. Radiother Oncol 2011;100:259–64.
[52] Reynaert N, van der Marck S, Schaar D, Van der Zee W, Van Vliet-Vroegindeweij C, Tomsej M, et al. Monte Carlo treatment planning for photon and electron beams. Radiat Phys Chem 2007;76:643–86.
[53] Fippel M. Fast Monte Carlo dose calculation for photon beams based on the VMC electron algorithm. Med Phys 1999;26:1466–75.
[54] Fippel M. Efficient particle transport simulation through beam modulating deviced for Monte Carlo treatment planning. Med Phys 2004;31:1235–42.
[55] Marks L, Yorke E, Jackson A, Ten Haken R, Constine L, Eisbruch A, et al. Use of normal tissue complication probability models in the clinic. Int J Radiat Oncol Biol Phys 2010;76(3):810–9.
[56] Protocol from RTOG. www.rtog.org/ClinicalTrials/ProtocolTable/StudyDetails.aspx?action=openFile&;FileID=9366. [Online].
[57] Wang X, Zhang X, Dong L, Liu H, Gillin M, Ahamad A, et al. Effectiveness of noncoplanar IMRT planning using a parallelized multiresolution beam angle optimization method for paranasal sinus carcinoma. Int J Radiat Oncol Biol Phys 2005;63(2):594–601.
[58] Feuvret L, Noël G, Mazeron J, Bey P. Conformity index: a review. Int J Radiat Oncol Biol Phys 2006;64(2):333–42.
[59] van't Riet A, Mak A, Moerland M, Elders L, van der Zee W. A conformation number to quantify the degree of conformality in brachytherapy and external beam irradiation: application to the prostate. Int J Radiat Oncol Biol Phys 1997;37(3):731–6.
[60] Marôco J. Análise estatística com o SPSS statistics. Report Number. 5th ed. 2011.
[61] Jar J. Biostatistical analysis. 5th ed. Prentice Hall; 2010.
[62] Darby S, Ewertz M, McGale P, Bennet A, Blom-Goldman U, Bronnum D, et al. Risk of ischemic heart disease in women after radiotherapy for breast cancer. N Engl J Med 2013;368(11):987–98.
[63] Gagliardi G, Lax I, Söderström S, Gyenes G, Rutqvist L. Prediction of excess risk of long-term cardiac mortality after radiotherapy of stage I breast cancer. Radiother Oncol 1998;46:63–71.
[64] Moon S, Kim Y, Kim S, Lee M, Keum H, Kim S, et al. A dosimetric analysis of IMRT and multistatic fields techniques for left breast radiotherapy. Med Dosim 2011;36(3):276–83.

Please cite this article in press as: Borges C, et al., Comparison of different breast planning techniques and algorithms for radiation therapy treatment, Physica Medica (2013), http://dx.doi.org/10.1016/j.ejmp.2013.04.006

Chapter 5

Monte Carlo validation and simulations of the breast cancer treatment plans

The main goal of this chapter is to compare the different external beam irradiation techniques used for breast cancer (BC) treatment, using conventional Pencil Beam Convolution (PBC) and Monte Carlo (MC) dose calculation methods. Two independent MC methods were used: iMC, the commercial Monte Carlo algorithm from iPlan BrainLAB treatment planning system (TPS) and an independent model validated with the state-of-the-art software EGSnrc/BEAMnrc. The irradiation techniques investigated were:

- forward intensity modulated RT (f-IMRT) using tangential fields,
- intensity modulated RT (IMRT) using 2 fields (IMRT2), and
- IMRT using 5 fields (IMRT5).

Note: DCART was not included as no EGSnrc MC calculations were done due to the gantry rotation feature of this technique, not yet implemented or validated in this EGSnrc MC work.

In this study, in order to assess and quantify the accuracy of the absorbed dose calculations determined by an analytical algorithm, the comparison between such calculations and those obtained using an independent MC algorithm were performed and the discrepancies were analyzed. An independent model of the VARIAN® Trilogy® linear accelerator was used to simulate breast cancer treatments in

EGSnrc [54, 244]. The High Definition micro multileaf collimator (HDMLC), previously modeled and validated in water-based phantoms [132], was included in the model. The accelerator model was benchmarked with measurements using ionization chambers and film dosimetry. A comparison between the PBC, iMC and EGSnrc MC calculations is presented. Measurements were performed in homogeneous phantoms to verify absolute and relative dose differences between the PBC and the MC calculations. Gamma analysis was also used to perform comparisons between the different calculations. Seven clinical cases were investigated. Dose volume histograms (DVH) and gamma evaluation were used for the analysis. No significant differences were found between the MC calculations performed using the iPlan BrainLAB TPS and the EGSnrc code; however differences were found both for the homogeneous and patient calculations between PBC and MC. These differences were more relevant in the build up region and in regions containing heterogeneities.

5.1 Motivation and goals

In RT, the accurate calculation of absorbed dose is of utmost importance. Therefore accurate dose calculation methodologies have been developed for EBRT. To achieve the total desirable accuracy of 3% in dose delivery to a point or volume [62], it is estimated that the accuracy of computed dose distributions should be between 1% and 2% [62]. There is a notable effort to develop TPS with increasingly complex algorithms to achieve this goal. The simplest algorithms are point dose estimates. These methods are reported to be limited in accuracy and fail to model specific geometries. Deterministic dose calculation methods could have been developed based on the photon transport equation and using the well-known interaction cross sections. However, these were not developed for photon beams as they could not be general enough to deal with the complex geometries involved in RT and would only work if few events were involved in the particle's energy absorption [41].

Given the current use of RT for treating breast cancer using linear accelerator technology, the influence of the dose algorithms is relevant to accurately determine the dose in the target volume and estimate the risks in the OAR for assessing normal tissue toxicity or the risk of secondary cancer. The influence of the choice of the dose algorithm for breast RT is an important challenge due to its complex

concave geometry and localization near the rib bones, lung and its proximity to the interface body-air.

The analytical algorithms are known [52, 245] not to accurately determine the absorbed doses, especially the algorithms primarily based on equivalent path length (EPL) for inhomogeneity corrections. The absorbed dose depends on beam spectrum, field size, incidence and contaminating electrons. With these algorithms, electrons derived from primary photon interactions and parts of the linac head and the air volume downstream to the patient are not taken into consideration [246]. Convolution-superposition models such as the analytical anisotropic algorithm (AAA) were developed to deal with inhomogeneities through the scaling of photon and electron scatter kernels anisotropically, depending on the medium [50]. A family of semianalytical dose calculation algorithms based on energy deposition kernels has been developed, namely convolution and superposition algorithms . These algorithms have a better performance than correction based algorithms as they account for penumbra broadening effect in low density media (eg. lung) [72, 247].

In this work, iPlan TPS was used with two algorithms: PBC and iMC, previously described in chapter 4. The PBC algorithm is used in clinical routine. The Monte Carlo independent model details were provided in chapter 3. It was mainly used to compare the two clinical TPS algorithms.

5.2 Materials and Methods

5.2.1 Phantoms and patients

In order to account for the concave surface of the chest wall and of the breast of a patient, two phantoms were used in this work. The first phantom, named BELEM, was built for the specific purpose of this work, to reproduce the breast shape. It was made using a vegetal fat that was melt and put into a plaster mold made from a Rando-Alderson female torso. The phantom was cooled in the fridge and was later removed from the mold and kept in the fridge for conservation. This phantom is homogeneous and has an approximate density (not assessed) to the water density. It was placed on top of a set of water-equivalent slabs as presented in figure 5.1. To perform the dose measurements, a 0.125 cm^3 PTW® model 31010 ionization chamber was placed in a cavity in the phantom specially drilled for the

FIGURE 5.1: The Belem phantom. On the left, the breasts made of vegetal fat; on the right, the breasts are placed on top of a set of water-equivalent slabs to perform the measurements.

FIGURE 5.2: The NAOMI phantom. Left homogeneous breast and right breast with a hole placed on top of a set of water-equivalent slabs to perform the measurements by placing an EBT2 film within two slices of the phantom.

purpose. CT scans of the phantom were acquired at a Siemens®, Biograph 64R PET-CT scanner, with a resolution of $0.0977 \times 0.0977 \times 0.3\ cm^3$.

The second phantom, NAOMI, was kindly lent by the Department of Fisiología Médica y Biofísica, Facultad de Medicina, Universidad de Sevilla. Its complete description can be found in Fernández, B. PhD thesis [248]. It was placed on top of a set of water-equivalent slabs as depicted in figure 5.2. GAFCHROMIC® EBT2 films were placed in the coronal plane between the slabs of the NAOMI phantom.

The NAOMI phantom underwent a computed tomography (CT) scan on the same conditions as the BELEM phantom. The images were imported to the TPS. Seven left breast cancer patients (stage I or II), referred to adjuvant RT after breast conserving surgery, were randomly chosen among a population of 394 breast

patients treated between 2010 and 2011 and their CT images were imported to the iPlan TPS.

5.2.2 EGSnrc calculations

The Varian 2300C/D Trilogy linac equipped with a HDMLC was accurately modeled for a 6 MV photon beam using the EGSnrc [244] user code with BEAMnrc [54] and DOSXYZnrc [122] for MC dose calculations. The detailed geometry and dimensions of all the linac head components were set based on the manufacturer's specifications. The simulation results were fully modeled and accurately commissioned against experimental data [132]. The MC simulations were performed in three stages as illustrated in chapter 3, figure 3.4. The patient-independent part involved the fixed component modules of the Varian 2300 C/D linac, resulting in a phase space file scored above the jaws. The first part of the simulation was run once with 5×10^8 incident particles on the target. The resulting particle coordinates (particle type, energy, location and direction) were scored in a phase space file for subsequent use in the next step of the simulation. This patient-independent phase space file was then used as a source to the patient-dependent part, to simulate the radiation interactions in the including the jaws and the MLC.

In the second stage, depending on the details exported from the TPS for each field, output phase space files for the different field sizes and MLC configurations are obtained, below the MLC. For this patient-dependent part, four independent runs (with different random number seeds) using the total number of particles scored in the previous stage (about 4.7×10^8) were simulated. he final number of particles collected in the second phase space file for each beam did largely depend on the field size beam, on the MLC beam arrangement and on the weight the field had on planning. The larger main tangential beams had between 5×10^7 to 8×10^7 particles in the second stage phase space file. The time each simulation took did also depend on the field size and on the MLC arrangement. The larger tangential fields simulation took in average 37.2 hours to be simulated (considered the tangential fields in f-IMRT, IMRT2; for IMRT5, as there were more beams, in general, the weight was divided among the 5 fields, taking in average less time - in average, 22.7 hours for complete simulation). The following transport parameters were set for the BEAMnrc simulations:

- $ECUT = AP = 700keV$,
- $PCUT = AP = 10keV$

, where AP and AE are the low-energy thresholds for the production of secondary bremsstrahlung and knock-on electrons, respectively; while ECUT and PCUT define the global cutoff energy for electron and photon transport, respectively. In order to improve the calculation efficiency, and decrease the head simulation times, various variance reduction techniques were employed:

- i. uniform bremsstrahlung splitting with a photon splitting factor of 20, to increase the number of photons created in the target;
- ii. russian roulette; and
- iii. the range rejection technique with ESAVE of 0.7 MeV in the bremsstrahlung target and 1.0 MeV for the other accelerator components.

These outputs were then used as input for the DOSXYZnrc code for dose calculation in the phantom/patient geometry derived from the CT data. The resulting phase space files were then combined in a final phase space file using BEAMDP [119]. To calculate dose in the patient, at the third and last stage of the simulation process, the final scored phase space files of each individual beam were used as input for the DOSXYZnrc code [122], to independently simulate in the **CT-based phantom**. The planning CT images were manipulated using a DICOM RT toolbox in MATLAB [249] to create a phantom-based image, with same resolution used for TPS calculations, $3.0 \times 3.0 \times 3.0\ mm^3$. The particles in the patient-dependent phase space files were recycled several times (less than 20) in the DOSXYZnrc calculations. MC dose calculations in the CT images were carried out for:

- $ECUT = 0.521 MeV$, and
- $PCUT = 0.01 MeV$.

The value of the parameter ESTEPE (maximum fractional energy a charged particle can lose per step) was set to its default value of 25%. The conventional CTCREATE/DOSXYZnrc conversion ramp using four materials (air, lung, tissue and bone with the adequate mass density) was considered for the calculations. Using this program, a CT data set can be converted into the appropriate voxel geometry for DOSXYZnrc calculations. The material type (composition) and mass density data within each voxel are derived from the Hounsfield number exported from the patient CT using a CT conversion ramp. The default ramp for converting CT to material and density in CTCREATE is shown in figure 5.3. The ICRU

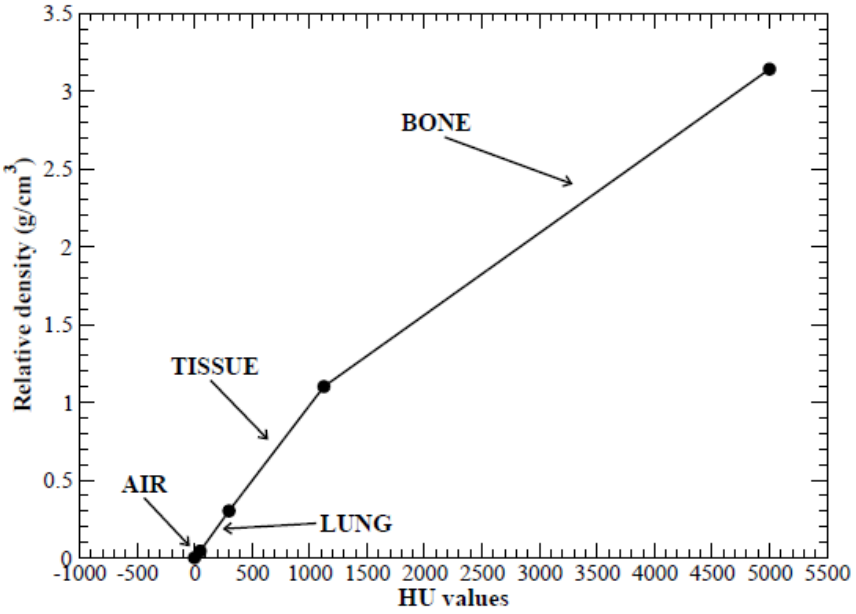

FIGURE 5.3: The DOSXYZnrc default ramp for converting CT-number to material density [95]. Indicated in the figure are the ICRU standardized points for "Air", "Lung", "Tissue" and "Bone". Note that the CT numbers considered for the DOSXYZnrc presents an offset of 1000 with respect to the standard definition of Hounsfield number ([-1000, 1000]).

standardized materials used to characterize this ramp are "Air", "Lung", "Tissue" and "Bone" where material densities between the fixed points are linearly interpolated. Note that the CT numbers presents a shift of 1000 with respect to the standard definition of the Hounsfield number.

The final dose distribution for each phase was the summation of the dose distributions from all individual beam arrangements. The individual uncertainty for the final distribution was less than 2%. For each phantom and patient data, the plan information data, jaw positions, gantry and collimator angles, MLC configuration and patient isocenter position were exported from iPlan TPS and introduced in the correspondent input files of the BEAMnrc and DOSXYZnrc codes. The calculations were performed in a cluster of 2.2 GHz AMD Opteron processors at the Nuclear Physics Center of the University of Lisbon.

5.2.3 Measurements

Two phantoms were used to validate the treatment plans. The BELEM phantom permitted placing an ionization chamber to perform absolute point dose measurements, referred from now on as *absolute dosimetry* or *absolute dose measurements*. The NAOMI phantom was used to place films inside, as shown in figure 5.2. The

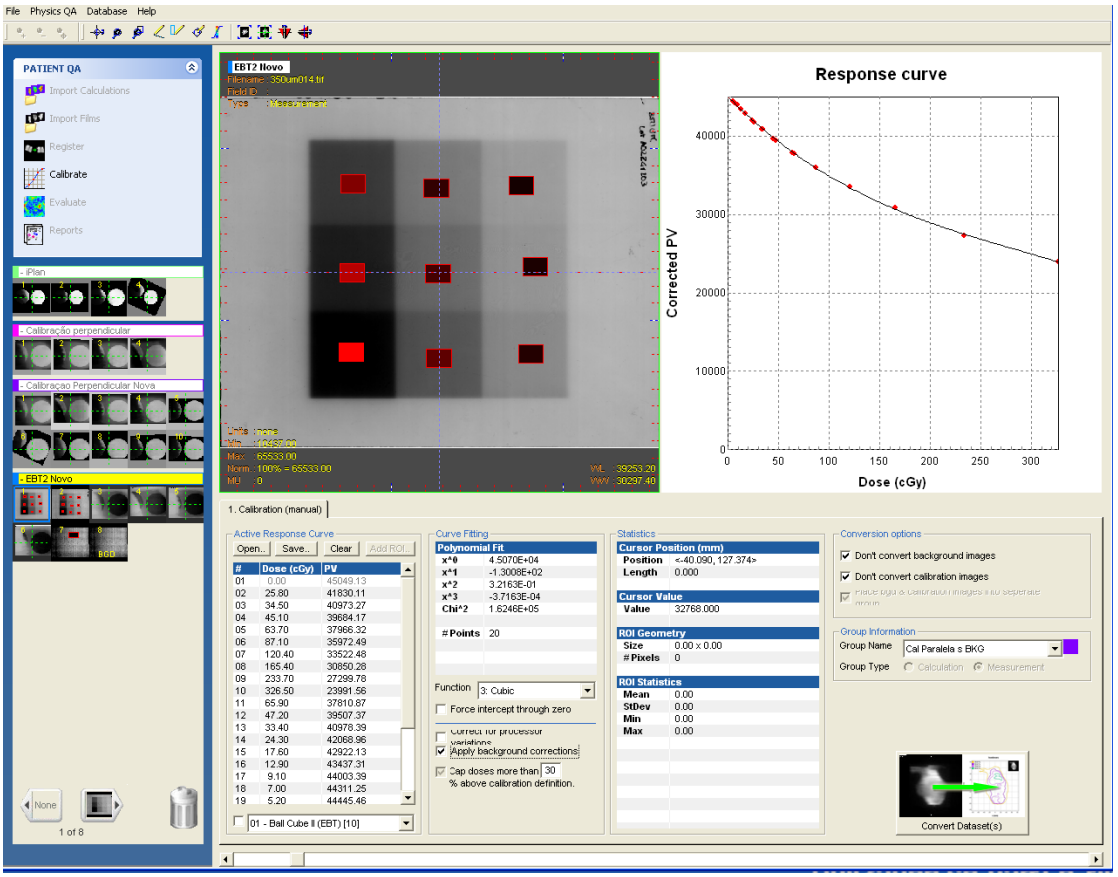

FIGURE 5.4: Film analysis. Calibration curve of the EBT2 films using FilmQA^{TM} software. A film was irradiate with different doses, creating a pattern to establish a correlation between the OD (optical density) measured in the film and the dose imprinted in the film.

dose film measurements are considered relative as they depend on a calibration curve also established at the time the validation plans were irradiated, as depicted in figure 5.4. This will be from now on referred as *relative dosimetry*.

5.2.3.1 Absolute dosimetry using the BELEM phantom

Dose measurements were performed using a 0.125 cm^3 31010 PTW® ionization chamber that was placed in the cavity specially drilled in the BELEM phantom, connected to a UNIDOS E PTW electrometer, with ambient conditions corrections . All the optimized treatment plans for f-IMRT, IMRT2 and IMRT5 of the seven patients were irradiated and measurements were performed. The results were compared with the dose determined in the TPS for PBC and iMC and that calculated with the independent MC calculations. Furthermore, to quantitatively compare the PBC with the MC simulation plans, the 3D gamma index was calculated in CERR® [250] (further details in section 5.2.5.2).

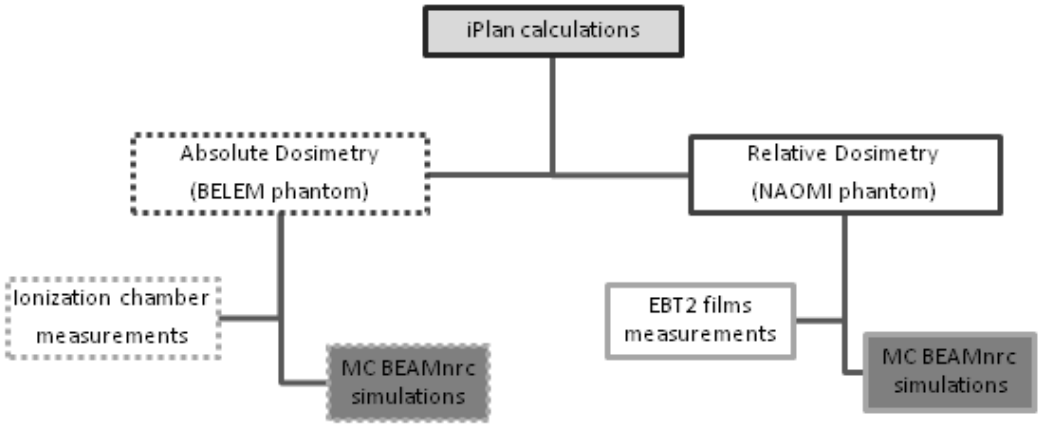

FIGURE 5.5: Validation scheme. iPlan calculations were performed for absolute and relative verifications. For absolute dose validation, measurements were performed using the BELEM phantom and ionization chambers for comparison with iPlan calculations. Moreover, MC calculations were performed and compared to the measurements. For relative dosimetry, the NAOMI phantom was used with EBT2 films for comparison with the iPlan plans; EGSnrc MC simulations were also compared with iPlan.

5.2.3.2 Relative dosimetry using the NAOMI phantom

An EBT2 GAFCHROMIC film was placed between two slices of the NAOMI phantom and dose measurements were performed. These measurements were done for one of the patients, for the three techniques (f-IMRT, IMRT2 and IMRT5) due to limited resources. After irradiation of the treatment plans, the films were processed in an Epson 10000XL flatbed scanner and analyzed in the software FilmQA^{TM} [75]. An optical density versus dose, calibration curve was applied for film measurements (see figure 5.4) and the data was normalized to the maximum dose on the central axis.

For these plans, calculations were performed on the CT image of the NAOMI using iMC and the independent MC calculations. The TPS plans were compared with the corresponding films, using FilmQA^{TM} gamma analysis. Furthermore, the MC results were compared with the TPS calculations, using the 3D gamma evaluation function in CERR®.

In figure 5.5, a scheme of the work performed for validation purposes is presented.

5.2.4 Patient dose calculations

EGSnrc MC simulations of the optimized treatment plans on the patients original CT images were performed for the 3 techniques under investigation. The

results were compared to the iPlan results for PBC and iMC, using dose volume histograms (DVH) and 3D gamma analysis in CERR [250].

5.2.5 Evaluation tools

5.2.5.1 CERR

CERR® [1] is a software developed in MATLAB© for radiotherapy research. It was used to import the 3D dose files created in EGSnrc and iPlan and is able to display DICOM-RT format [251]. When the DICOM dataset is imported into CERR® the whole plan archive is stored in a MATLAB© binary format. Subsequently, CERR provides a variety of possibilities such as DVH and treatment planning comparisons, including gamma evaluation [250].

5.2.5.2 Gamma Map Algorithm

The gamma index was introduced by Low et al [252] and Depuydt et al [253] to compare and evaluate the dose distribution in 2D and 3D. The gamma-volume cumulative histograms were developed by Spezi and Lewiset [254] to evaluate the IMRT treatment plans. Like the DVH, the gamma-volume histograms are represented in function of a cumulative volume. This permits to quantitatively compare measured and calculated absorbed dose distribution values.

Fundamentals Modern RT techniques such as 3D-CRT and IMRT often give rise to complex dose distributions with several low and high dose gradient regions. A simple comparison with superimposition of two dose maps can quantify the differences between these maps. However, in the region of high dose gradient, a small difference in spatial position can result in a large difference in the dose value. To solve this problem, Low et al [252] proposed a method called the Gamma Map Algorithm. This method takes into account both the dose difference and the spatial displacement between the corresponding points on the two dose maps. The gamma index is based on the comparison of two dose distributions: one considered the reference dose distribution (D_r) and another is the dose distribution to compare (D_c).
For a reference point with position p_r, receiving a dose D_r, and a dose point to

[1] CERR: http://www.cerr.info/about.php)

compare p_c, receiving a dose D_c, the distance between the two points p_r and p_c is $d(p_r, p_c)$ and the dose difference is $\Delta D(p_r, p_c)$. The tolerance criteria are defined by a maximum distance difference (Δd_M) and a maximum dose difference ΔD_M, represented by an ellipsoid envelope, centered in the reference dose point and defined by the following relationship:

$$1 = \sqrt{\left(\frac{d(p_r, p_c)}{\Delta d_M}\right)^2 + \left(\frac{\Delta D(p_r, p_c)}{\Delta D_M}\right)^2} \tag{5.1}$$

For 2D comparison between reference and compared dose distributions, the acceptance criteria for the Gamma analysis can be depicted as represented as the ellipsoid in figure 5.6. The size of this ellipsoid is defined by ΔD_M and Δd_M.

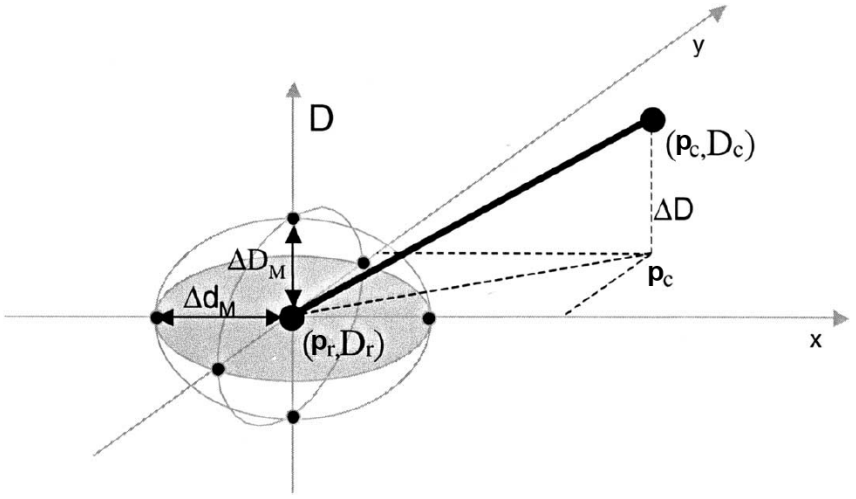

FIGURE 5.6: Schematic representation of the theoretical concept of the gamma evaluation method. The reference and compared dose distributions are denoted by ($\mathbf{p}_r$, D_r) and ($\mathbf{p}_c$, D_c), respectively. The criteria defining the ellipsoid of acceptance are denoted by the dose difference tolerance ΔD_M and the maximal distance to agreement Δd_M. Image from [253].

The calculation of the gamma index, γ, requires two user-defined criteria:

- ΔD_M in % - represents the maximum acceptable dose difference, in percentage;
- Δd_M or DTA (dose-to-agreement) - represents the maximum accepted tolerance for the misalignment of the corresponding dose maps due to positioning uncertainty in the to-compare dose map, in order words, is the spatial distance between calculated and measured data points that receives the same absorbed dose.

The clinically accepted values of ΔD_M and Δd_M are generally 3% and 3 mm, respectively.

The gamma index is calculated for every to-compare dose point and according to Low et al [252] algorithm, the investigated dose is said to have passed if the Gamma index is less than or equal to one, mathematically expressed by:

$$\Gamma(p_r, p_c) = \sqrt{\left(\frac{d(p_r, p_c)}{\Delta d_M}\right)^2 + \left(\frac{\Delta D(p_r, p_c)}{\Delta D_M}\right)^2} \leq 1 \tag{5.2}$$

From equation 5.1, it can be seen that the smaller the values of ΔD_M and Δd_M, the harder it is to pass the gamma comparison.

The coordinate system in figure 5.6 is made up of x, y and D axis. The combination of x and y axis are represented by the position vector $\vec{p}$ (x, y) which describes the direction and the distance between the reference point relative to the to-compare point, which is the origin in this coordinate system. This distance is defined as follows:

$$p(x, y) = \sqrt{x^2 + y^2} \tag{5.3}$$

The D axis describes the reference and the to-compare dose difference. The passed and failed values correspond to the compared points that are inside and outside the ellipsoid, respectively.

Further developments of the gamma algorithm are reported in the literature. In 2002, Depuydt et al [253] introduced a refined gamma algorithm that provided a faster solution for comparing complex dose distributions. The key difference in this algorithm is that the gamma indices are either 0 or 1 for failed and passed, respectively, in the comparison. The quality of the comparison is determined by how small are a user defined ΔD and Δd acceptance criteria. Its advantage is that it provides a simple result which is useful for making quick decisions on whether the two data sets (measured and calculated dose maps) agree within the acceptable tolerance. However, this algorithm provides no indication on how good the agreements between the measured and calculated points are. Bakai et al [255] also reported another improvement of the Gamma algorithm, extending Low's et al algorithm for 3D dose distributions. The algorithm also allows the distance to agreement criterion to be set for three spatial directions to account for positioning errors that are not uniform in the anterior/posterior, lateral and

superior/inferior directions. The flexibility of setting the distance to agreement to criterion for all three spatial direction in this method was claimed to improve the gamma calculation time in comparison to Low [252] method.

5.2.5.3 FilmQA

$FilmQA^{TM}$ was used to compare the film measurements with the iPlan calculated plans, either PBC or iMC. The quantitative evaluation tools available in the $FilmQA^{TM}$ software for comparison of dose distributions are the distance-to-agreement (DTA) method, the dose deviation method and the gamma analysis method.

The absorbed dose deviation method compares the absorbed dose in the data points in the reference plan with the corresponding data points that are to be evaluated. In the $FilmQA^{TM}$ evaluation software the criteria for the maximum acceptable absorbed dose deviation are set regarding to the global absorbed dose. The $FilmQA^{TM}$ software creates an isodose surface by interpolating between the data points in the reference plan. This isodose surface is compared with measured data points. A criterion for maximum acceptable DTA can be chosen manually by the user. The distance between the measured and reference data points with the same absorbed dose must not exceed the chosen maximum DTA to pass the evaluation.

The gamma evaluation method described by Low et al [252] applies two comparison tools, a direct comparison of the absorbed dose deviation and comparison of the DTA between calculated and measured absorbed dose distributions and provides a numerical index as a measure of agreement of the two dose distributions. The gamma evaluation method sets the criteria for both absorbed dose deviation and the distance to the closest data point in the reference plan.

For 2D absorbed dose distributions the two criteria, the absorbed dose deviation and the DTA, includes an ellipsoid with the surface representing the acceptance criterion (figure 5.6).

5.2.5.4 CERR

The dose distributions from the TPS and the EGSnrc MC calculations were compared using the gamma analysis as built into CERR® software. The acceptance

criterion was set to 3% dose difference and 3 mm for DTA, in compliance with Low et al [252] and Korreman et al [256]. The objective with the chosen acceptance criterion was to reflect a routine clinical condition. CERR displays the gamma index distribution.

5.3 Results

5.3.1 Comparison using the BELEM phantom

The optimized f-IMRT, IMRT2 and IMRT5 calculation plans were applied to the BELEM phantom using iPlan Phantom Mapping, both for the PBC and iMC algorithms. The calculated isodose distributions in the BELEM phantom are displayed in figure 5.7, for one of the patients enrolled in the study.

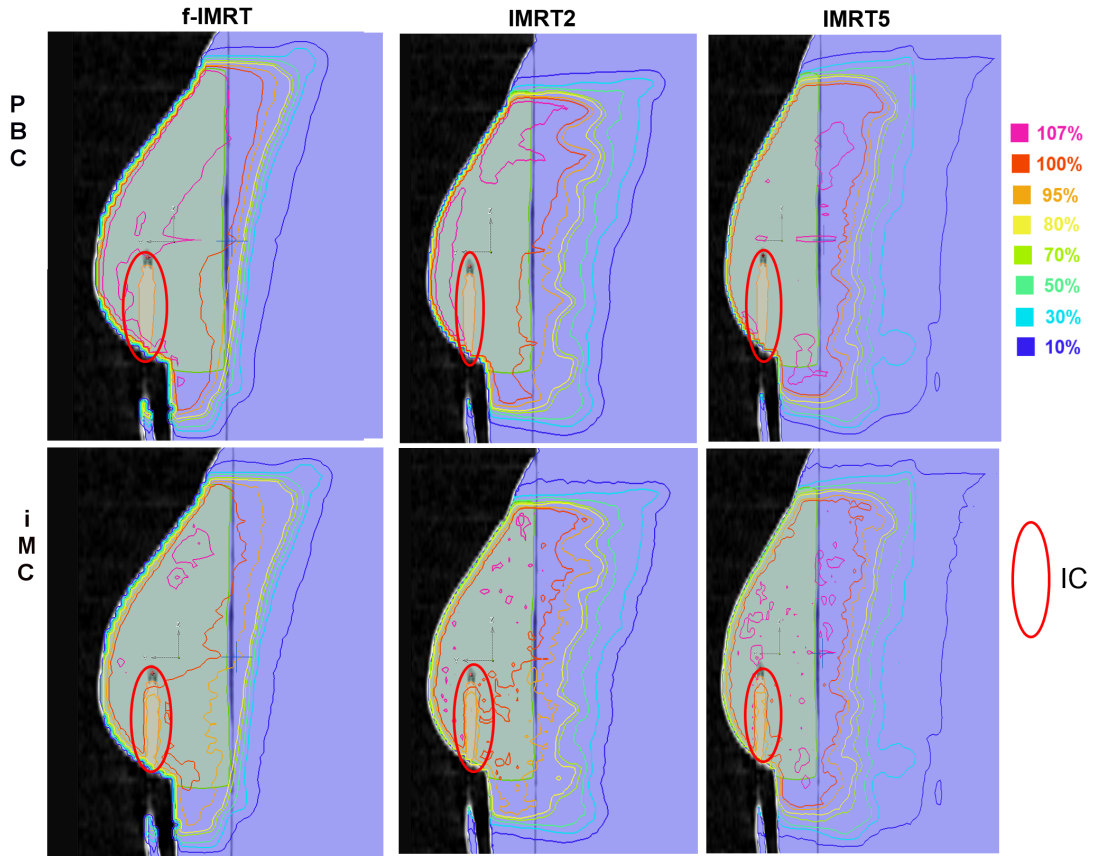

FIGURE 5.7: PBC and iMC calculation of the optimized plans in BELEM phantom, for f-IMRT, IMRT2 and IMRT5 techniques. In orange, it is represented the IC inserted in the phantom

It is possible to visually infer that, in general, PBC predicts higher breast doses compared to iMC, for all the techniques. The DOSXYZnrc/EGSnrc MC calculations were performed using the BELEM CT images with the same calculation grid used in iPlan.

5.3.1.1 Ionization chamber measurements

Dose measurements with the 0.125 cm^3 IC were also performed in the phantom insert for the positioning of the IC as previously explained. The relative dose differences between the calculations and the measurements performed with the IC are shown in figure 5.8.

In general, the PBC estimated higher doses (with an average of 2.9%) than the measured doses and presented higher discrepancies with the measurements that the iMC or EGSnrc MC calculations. Considering that the uncertainty of the IC measurements is on the order of 2-2.5% [183] and is 1-2% for the MC simulations, the MC results are in good agreement with the measurements, both for iMC and EGSnrc MC.

5.3.1.2 Gamma analysis of the calculated plans

The comparison on the calculated plans for the Belem phantom are now presented. For analysis, it is considered that for the 3%/3 mm criteria, the results are satisfactory if, at least, 95.0% of the points pass gamma evaluation for the criteria 3%/3 mm; shrinking the criteria to 2% / 2 mm, the percentage of points that is considered acceptable is reduced to 90.0%.

Using the 3D gamma analysis function from the CERR software, a comparison between PBC and MC calculations was performed. The results are presented in figure 5.9. For PBC vs EGSnrc MC, all the plans had more than 93.0% and 88.0% of the points respecting $\gamma < 1.0$ for 3%/3 mm and 2%/2 mm criteria, respectively; whereas for iMC vs EGSnrc MC, the gamma comparison was superior to 97.0% for the criteria 3%/3 mm and superior to 94.0% for 2%/2 mm, for all plans. On average, f-IMRT plans had poorer agreement compared to IMRT2 and IMRT5 plans.

Figure 5.10 shows the 3D gamma analysis for one patient. It can be observed that the differences between PBC and MC are more significant at the air-body

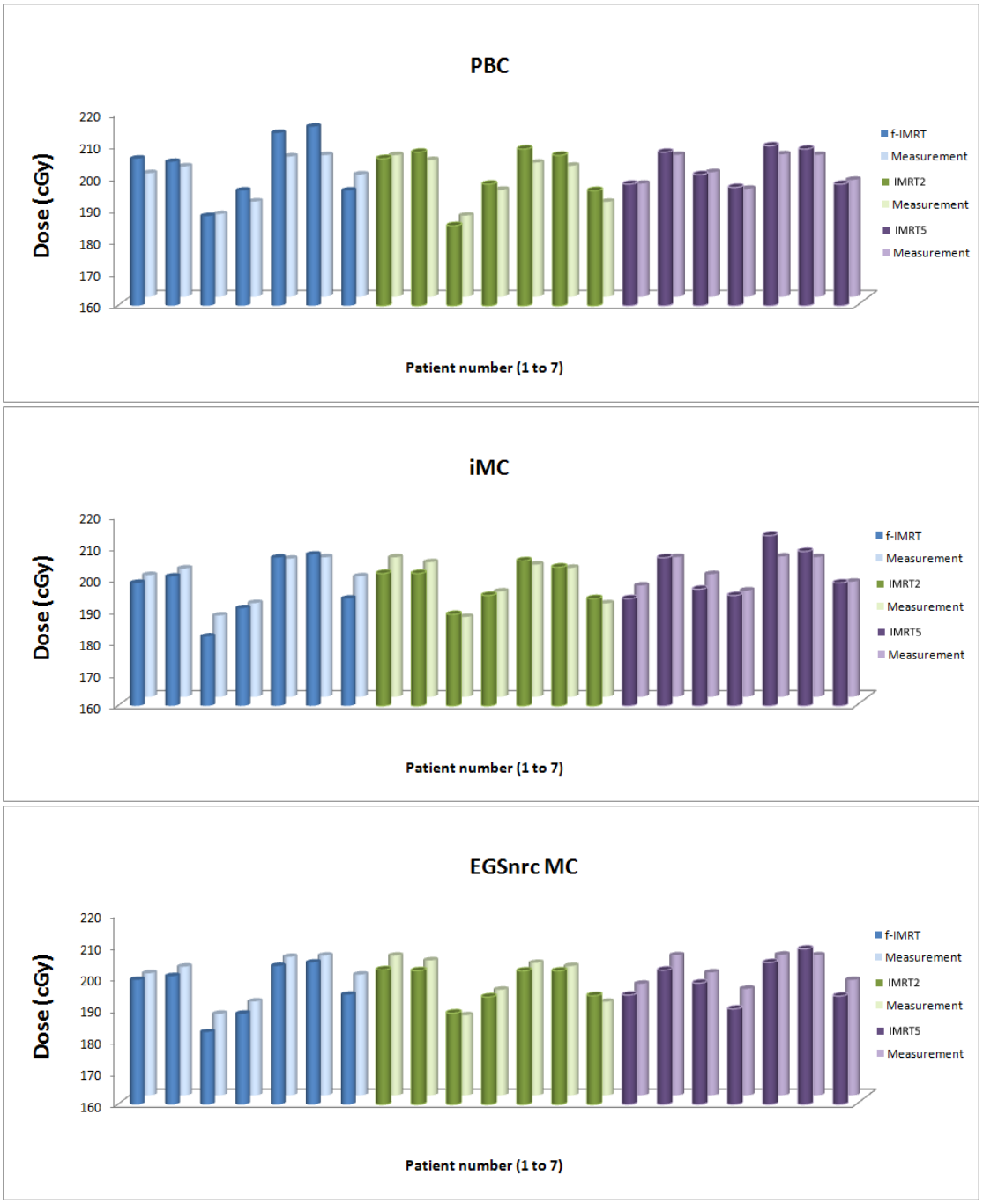

FIGURE 5.8: Absorbed dose (in cGy) calculated in the IC for the PBC (in blue), iMC (in green) and EGSnrc MC (in purple) and measurement with the 0.125 cm^3 IC (in lighter colors).

interface of the breast and inside the ionization chamber volume. Maximum dose differences of up to 1.0 Gy in the build-up region, and less than 0.2 Gy in the homogeneous region can be seen.

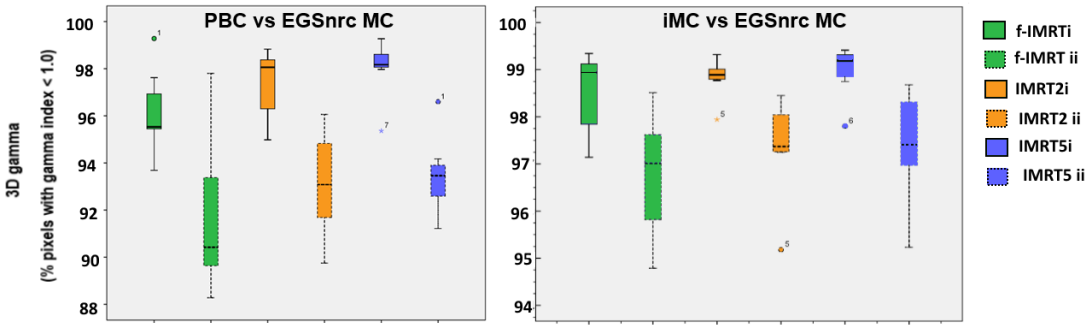

FIGURE 5.9: Representation of the 3D gamma results for the 7 patients, for f-IMRT, IMRT2 and IMRT5 (in green, orange and blue, respectively) for the criteria i. 3%/3 mm and ii. 2%/2 mm, in continuous and dashed lines, respectively; on the left for the comparison between PBC and EGSnrc MC and on the right graph for iMC and EGSnrc MC.

5.3.2 Comparison in the NAOMI phantom

Film measurements were performed in the NAOMI phantom for only one of the patients enrolled in this study. PBC, iMC and EGSnrc MC calculations were compared using 3D-gamma evaluation in CERR software [250].

5.3.2.1 Comparison between TPS and film measurements

Using $FilmQA^{TM}$ software, a 2D gamma analysis was performed between the calculated plans and the film measurements, for the following criteria: 3%/3 mm and 2%/2 mm. The results are presented in figure 5.11 and summarized in table 5.1. A comparison between iMC and the film measurements was also performed and is presented in figure 5.12 and the results are summarized in table 5.2.

PBC algorithm	3% / 3 mm	2% / 2 mm
f-IMRT	94.8%	89.5%
IMRT2	95.3%	85.1%
IMRT5	90.8%	83.7%

TABLE 5.1: 2D gamma analysis of PBC and film measurement in the NAOMI phantom, using the following criteria: 3%/3 mm and 2%/2 mm.

For f-IMRT, the results with PBC are acceptable, for both criteria, being on the limit to acceptance (95% for the criterion 3%/3 mm; 90% for 2%/2 mm). For IMRT2, for both algorithms and 3%/3 mm criteria, the results are satisfactory; however, for 2%/2 mm, the 90% goal is not reached. For IMRT5, the results were

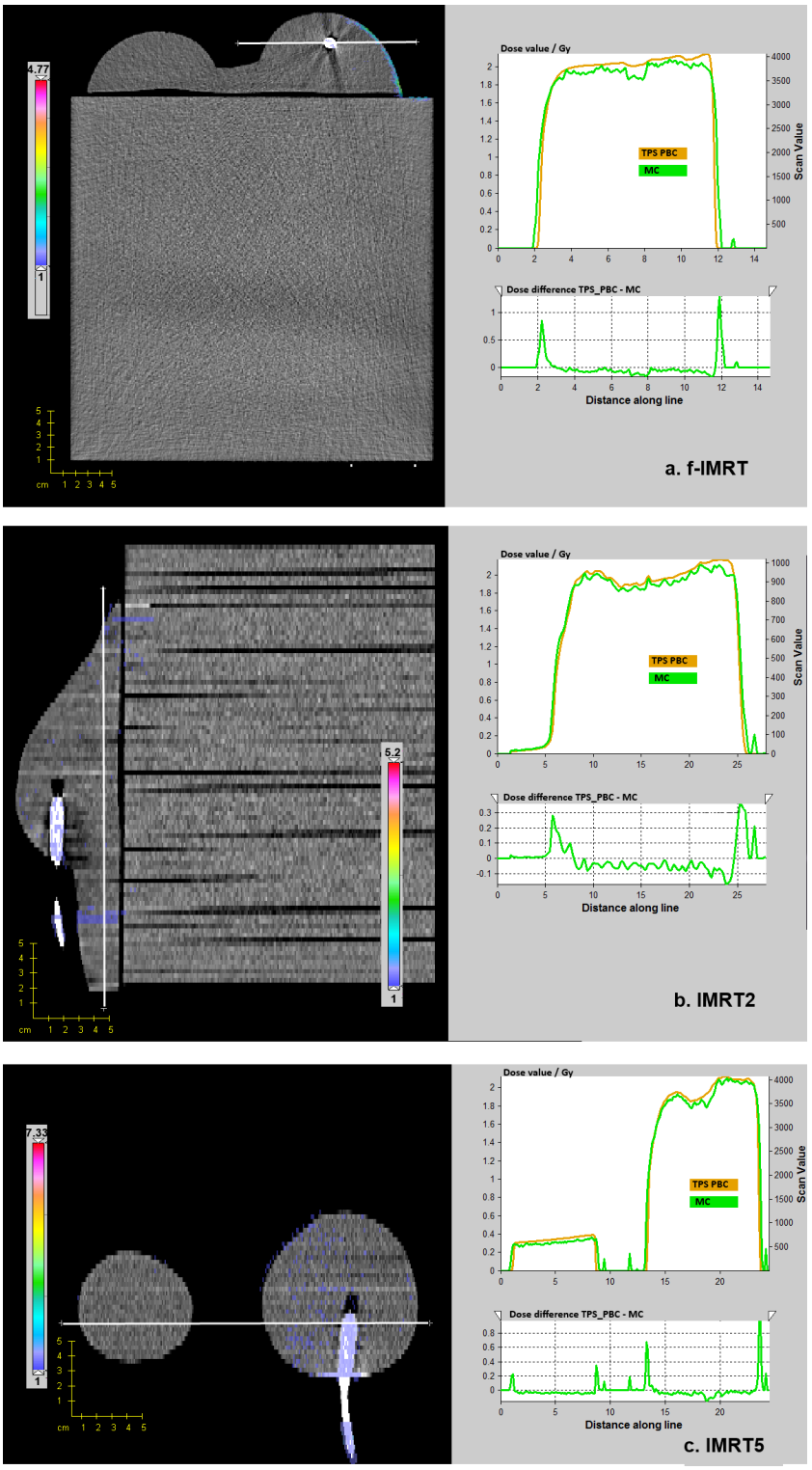

FIGURE 5.10: 3D-gamma analysis comparing PBC and EGSnrc MC calculated for (a.) f-IMRT, (b.) IMRT2 and (c.) IMRT5 for one of the patients, using the BELEM phantom, are presented, on a transversal, sagital and coronal planes, respectively. On the left images, the 3D gamma analysis is plotted. The white line represents the profile presented in the graph, on the right upper side, with PBC (orange line) and EGSnrc MC (green line) curves. The differences between the profiles of both calculations are presented in the bottom graphs, on the right.

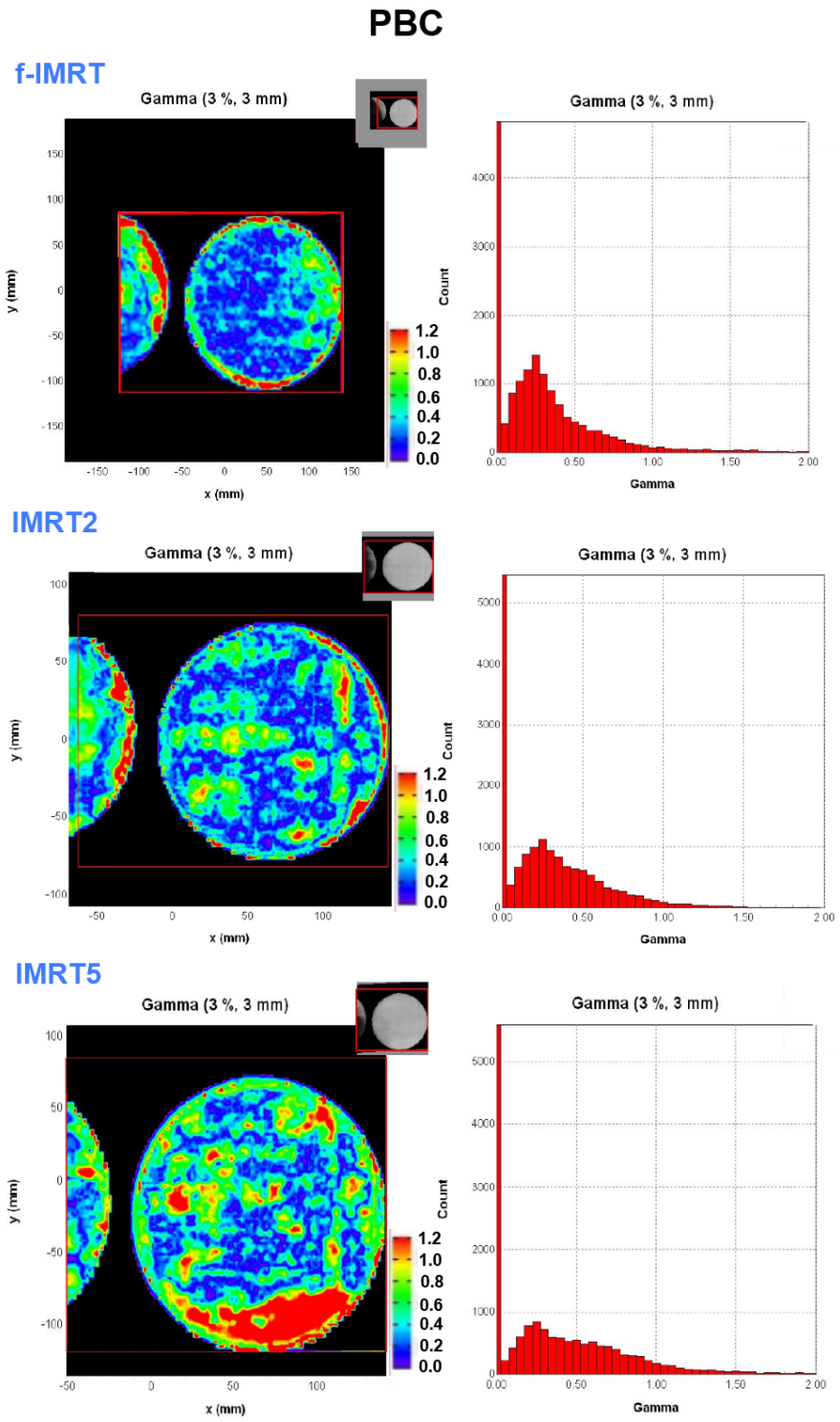

FIGURE 5.11: 2D gamma analysis between PBC and film measurements in $FilmQA^{TM}$ software in the coronal plane where the film was placed in the NAOMI phantom. On the left, the gamma evaluation representation; on the right side, the gamma analysis histogram.

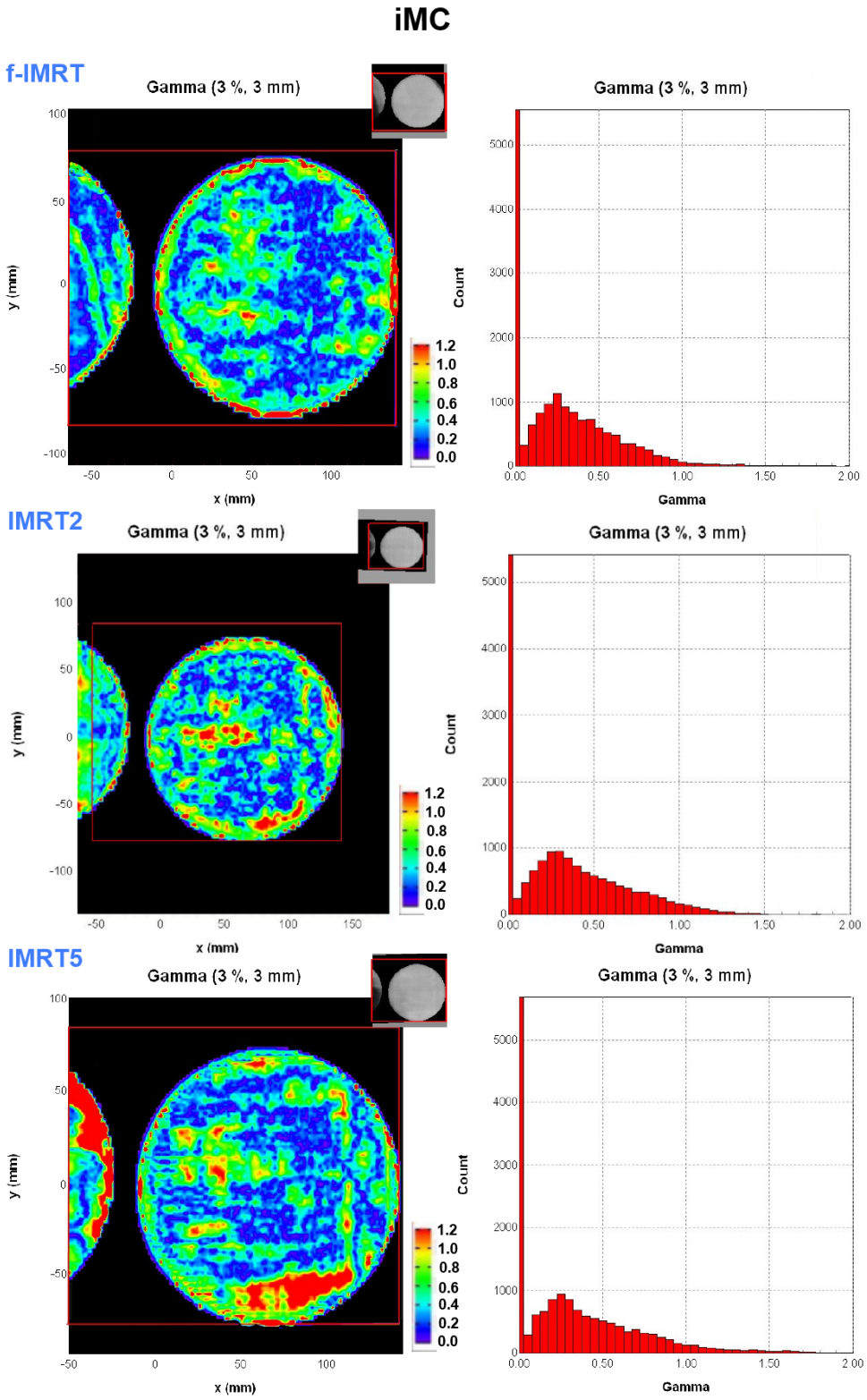

FIGURE 5.12: 2D gamma analysis of iMC and film measurements in $FilmQA^{TM}$ in the coronal plane where the film was placed in the NAOMI phantom. On the left, the gamma evaluation representation; on the right side, the gamma analysis histogram.

iMC algorithm	3% / 3 mm	2% / 2 mm
f-IMRT	97.1%	91.2%
IMRT2	96.2%	89.4%
IMRT5	92.7%	84.0%

TABLE 5.2: 2D gamma analysis of iMC and film measurement in the NAOMI phantom using the following criteria: 3%/3 mm and 2%/2 mm.

not satisfactory, with less than 95% or the points not verifying $\gamma < 1\%$, for none of the algorithms, for 3%/3 mm; for the criterion 2%/2 mm this 90% goal is not achieved either. However, the results are significantly better for the iMC than for the PBC algorithm.

5.3.2.2 Comparison between PBC and iMC using 3D-gamma evaluation

The results of the film dosimetry are not ideal, they are acceptable. Therefore, the EGSnrc MC simulations were performed and compared to the TPS results. A 3D gamma comparison, using CERR®, between the plans calculated using PBC and iMC was performed for the NAOMI phantom. The results are presented in figure 5.13.

Techniques	3% / 3 mm	2% / 2 mm
f-IMRT	98.71%	95.18%
IMRT2	99.18%	97.72%
IMRT5	99.39%	98.06%

TABLE 5.3: Average 3D-gamma results between PBC and iMC, with 3%/3 mm and 2%/2 mm criteria, for the NAOMI phantom.

According to the results presented in table 5.3, the agreement between PBC and iMC was higher than 92.0% all plans for the 3 techniques. The highest differences in the calculations were at the body-air interface in all the plans, as can be observed in figure 5.13.

5.3.2.3 Comparison between the TPS algorithms (PBC and iMC) and the EGSnrc MC using gamma evaluation

The comparison between the TPS calculations (PBC and iMC) and the EGSnrc MC calculation for the NAOMI phantom was performed using CERR® and the

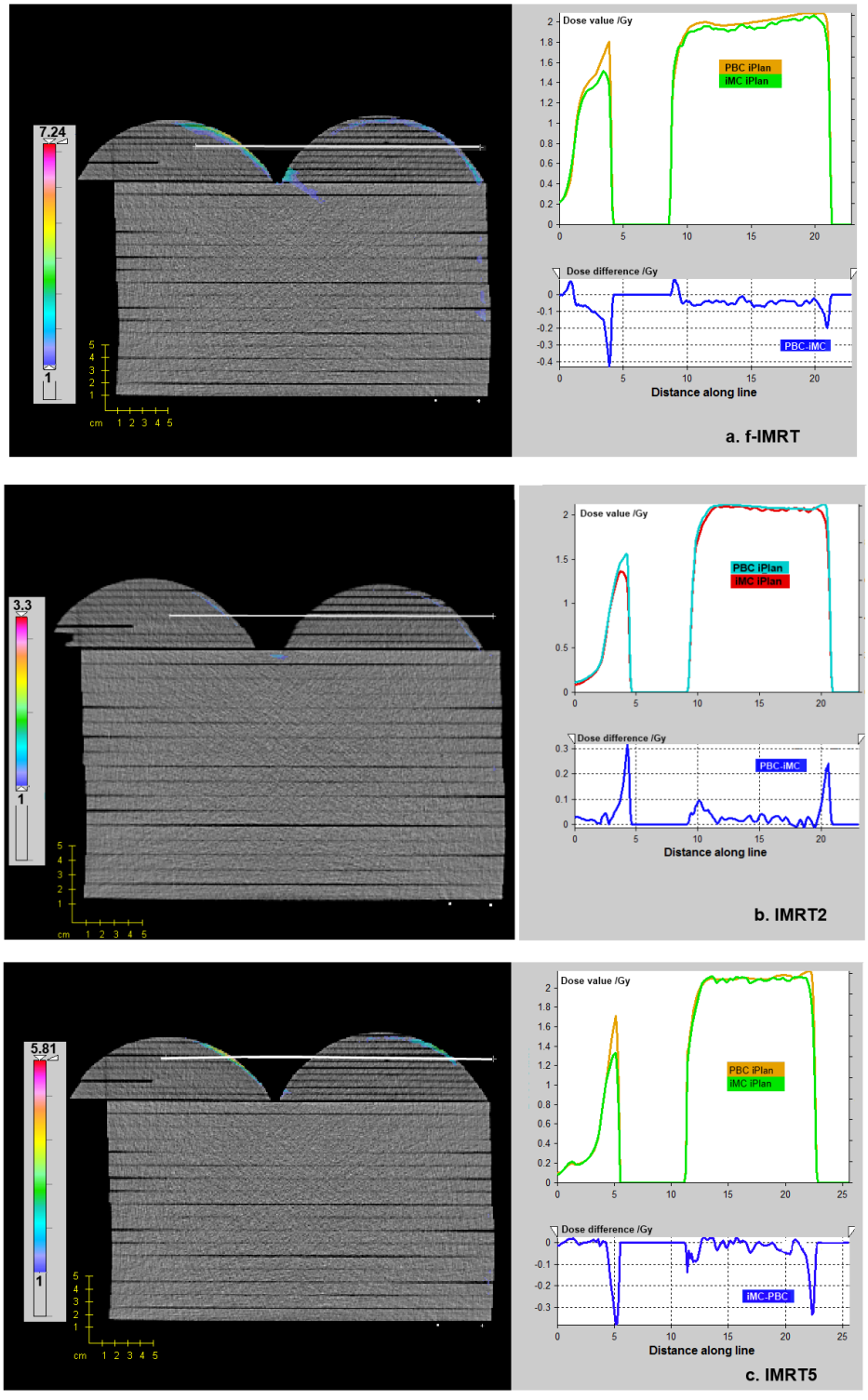

FIGURE 5.13: 3D gamma calculations for the NAOMI phantom comparing PBC and iMC algorithms from iPlan for a. f-IMRT, b. IMRT2 and c. IMRT5. On the left, image of the 3D gamma evaluation; the top graphs on the right side correspond to the dose profiles marked by the white line traced on the left image determined for the PBC and iMC dose calculations; the graph below corresponds to the dose difference between the two calculation algorithms in this line.

results are presented in figure 5.14 for f-IMRT and summarized in table 5.4, for the 3 irradiation techniques.

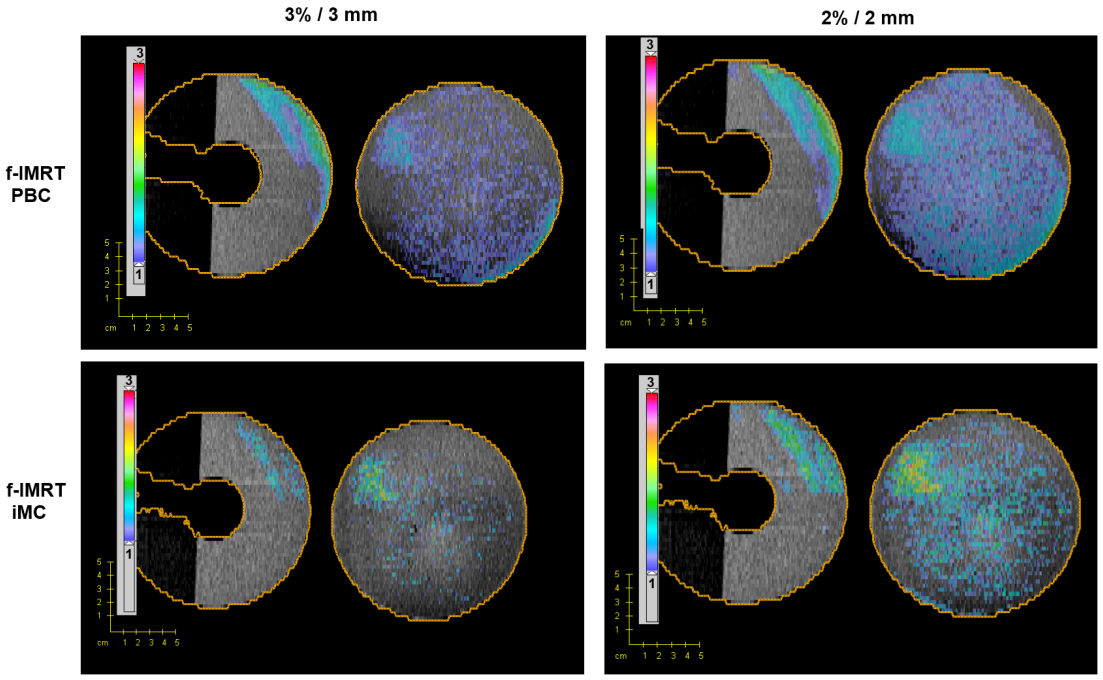

FIGURE 5.14: 2D gamma analysis for the NAOMI phantom, at the film coronal plane, comparison PBC (in the upper line) and iMC (in the lower line) with the EGSnrc MC calculations, respectively for 3%/3 mm criteria, on the left column and 2%/2 mm criteria, on the right column, for f-IMRT.

	3 %/3 mm		2 %/2 mm	
	PBC vs EGSnrc	iMC vs EGSnrc	PBC vs EGSnrc	iMC vs EGSnrc
f-IMRT	95.31%	97.66%	90.06%	93.69%
IMRT2	95.51%	95.75%	90.75%	90.82%
IMRT5	97.88%	97.92%	93.99%	94.28%

TABLE 5.4: 3D gamma evaluation between the TPS algorithms (PBC and iMC) and the EGSnrc calculations for NAOMI phantom.

According to the results presented in figure 5.14, PBC exhibits higher differences relative to the EGSnrc MC calculations than the iMC algorithm. The differences between the PBC and the EGSnrc MC are more evident at the body-air interface. The gamma results present, on average, $\gamma < 1.0$ for 95% of the points (3% / 3 mm criteria) and all the plans had gamma superior to 90%, for the 2% / 2 mm criteria.

5.3.3 Patient CT-based calculations

MC simulations were performed for the 7 clinical cases under investigation, for f-IMRT, IMRT2 and IMRT5. To compare the calculations performed using the 3 algorithms, DVH were plotted for the contoured structures. The results are presented in figure 5.15. iMC and EGSnrc MC estimate lower doses for the PTV than PBC, for all the 7 cases. The maximum differences observed between the PBC and the MC calculations can reach 5 Gy. In the structure 'Body excluding the PTV', the differences between the algorithms are more pronounced for doses higher than 40 Gy. Considering the ipsilateral lung, there are large discrepancies between the PBC and the MC algorithms particularly for doses higher than 30 Gy. For the contralateral breast, there are no visually significant differences between the DVH generated for the different algorithms. In the heart, the most significant differences between the PBC and MC calculations are for doses below 10 Gy and for doses higher than 40 Gy.

In order to further analyze the differences between the dose distributions, a 3D gamma analysis was performed, in CERR, for 3%/3 mm and 2%/2 mm criteria between the PBC and the EGSnrc MC and subsequently between the iMC and the EGSnrc MC. The results are presented in tables 5.5 and 5.6, respectively.

	Patient 1		Patient 2		Patient 3		Patient 4		Patient 5		Patient 6		Patient 7		Average	
	3% / 3 mm	2% / 2 mm	3% / 3 mm	2% / 2 mm	3% / 3 mm	2% / 2 mm	3% / 3 mm	2% / 2 mm	3% / 3 mm	2% / 2 mm	3% / 3 mm	2% / 2 mm	3% / 3 mm	2% / 2 mm	3% / 3 mm	2% / 2 mm
f-IMRT	99,28%	97,80%	95,45%	89,90%	96,24%	90,42%	95,44%	92,38%	95,53%	89,38%	93,69%	88,28%	97,62%	94,38%	96,18%	91,79%
IMRT2	98,57%	96,06%	94,98%	89,75%	98,06%	93,08%	96,66%	93,08%	95,94%	90,29%	98,83%	94,85%	98,19%	94,81%	97,32%	93,13%
IMRT5	99,27%	96,60%	97,97%	92,96%	98,52%	93,46%	98,17%	94,17%	98,16%	93,64%	98,70%	92,23%	95,36%	91,22%	98,02%	93,47%

TABLE 5.5: 3D-gamma analysis between PBC and EGSnrc MC calculations, for the 7 patients enrolled in the study, using 3%/3 mm and 2%/2 mm criteria.

	Patient 1		Patient 2		Patient 3		Patient 4		Patient 5		Patient 6		Patient 7		Average	
	3% / 3 mm	2% / 2 mm	3% / 3 mm	2% / 2 mm	3% / 3 mm	2% / 2 mm	3% / 3 mm	2% / 2 mm	3% / 3 mm	2% / 2 mm	3% / 3 mm	2% / 2 mm	3% / 3 mm	2% / 2 mm	3% / 3 mm	2% / 2 mm
f-IMRT	99,46%	98,11%	99,15%	96,86%	99,02%	95,97%	97,74%	95,18%	99,23%	96,92%	97,00%	93,12%	99,35%	97,07%	98,71%	96,18%
IMRT2	99,50%	98,03%	98,90%	96,27%	98,84%	95,56%	98,78%	96,13%	98,40%	94,76%	99,06%	96,73%	99,37%	96,82%	98,98%	96,33%
IMRT5	99,58%	97,97%	98,77%	96,13%	99,12%	95,62%	98,84%	95,68%	98,29%	93,51%	98,72%	93,43%	95,82%	92,05%	98,45%	94,91%

TABLE 5.6: 3D-gamma analysis between the iMC and the EGSnrc MC calculations using 3%/3 mm and 2%/2 mm criteria.

There is better agreement between the MC techniques than between the PBC and the EGSnrc MC. The 3%/3 mm criterion is higher than 93.0% between the PBC and the MC and higher than 97.0% between the iMC and the MC, for all plans; shrinking the tolerance to 2% and 2 mm, the gamma index is significantly lower and some plans (3 and 1 out of 7 for f-IMRT and IMRT2, respectively) do

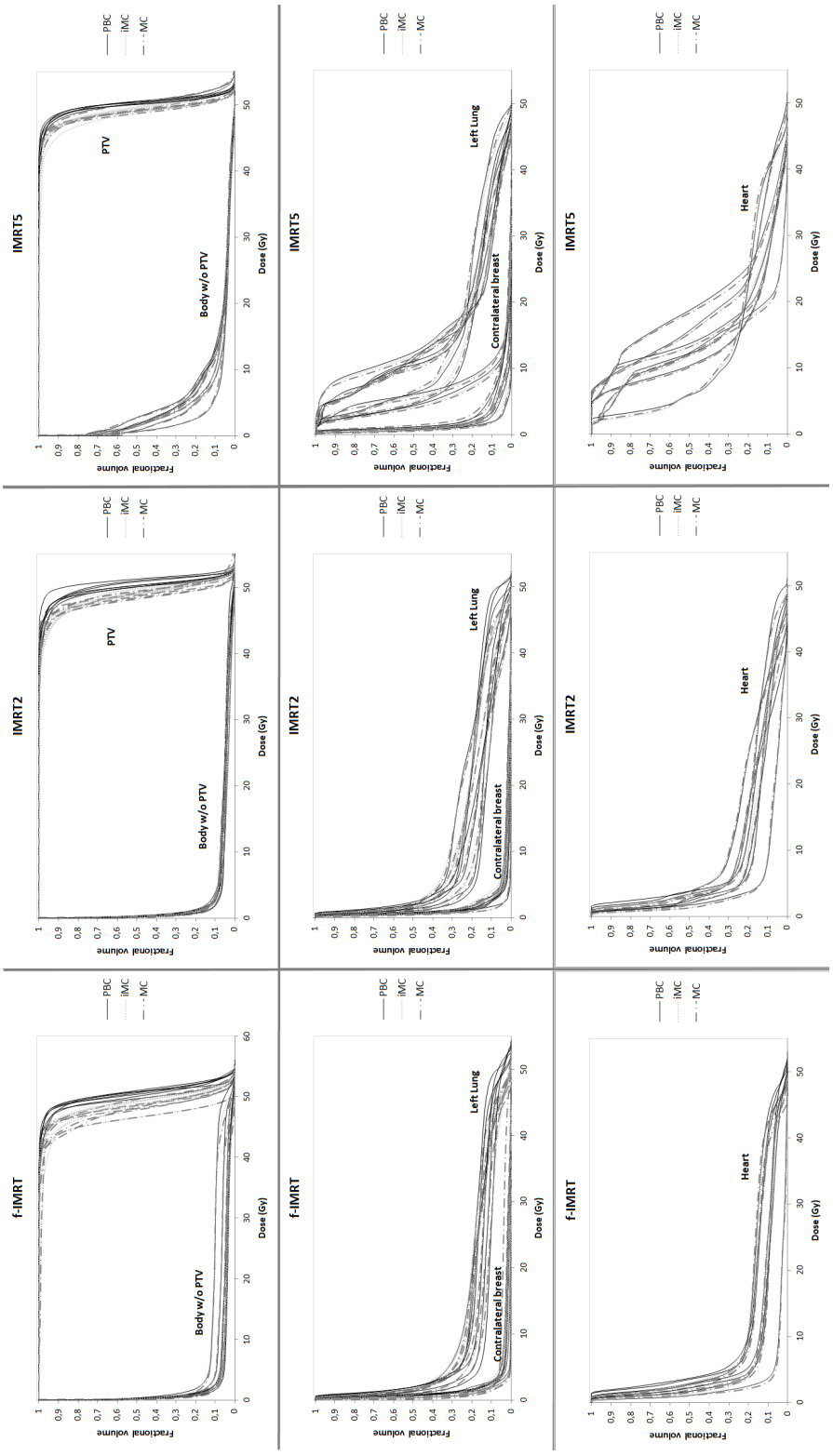

FIGURE 5.15: DVH comparison for the 3 calculation algorithms: PBC (continuous black line) iMC (light grey dots) and EGSnrc MC (dark grey point-line) for f-IMRT, IMRT2 and IMRT5, from left to right. The histograms are plotted for the PTV and Body without PTV, in the first line; left lung and contralateral breast, in the second line and in the heart, in the third line.

not achieve 90% of points within $\gamma < 1.0$, for PBC and MC but the $\gamma < 1.0$ is achieved by more than 92.0% of the points, for all plans comparing iMC and MC. There is better agreement between the MC techniques than between the PBC and the EGSnrc MC. The 3%/3 mm criterion is higher than 93.0% between the PBC and the MC and higher than 97.0% between the iMC and the MC, for all plans; shrinking the tolerance to 2% and 2 mm, the gamma index is significantly lower and some plans (3 and 1 out of 7 for f-IMRT and IMRT2, respectively) do not achieve 90% of points within $\gamma < 1.0$, for PBC and MC but the $\gamma < 1.0$ is achieved by more than 92.0% of the points, for all plans comparing iMC and MC. From the analysis of the DVH in figure 5.15, it may be inferred that the differences between the PBC and EGSnrc MC calculations are more significant in the lung, in the higher doses regions. There are also significant differences in the build-up region, in the body.

5.4 Discussion

New cancer treatment techniques such as IMRT envisage an improved control of the normal tissue complications and a more accurate absorbed dose in the target volume. Therefore, accurate dose calculations are required to generate reliable dose distributions and dose-volume information for treatment planning and plan evaluations. The choice of the dose calculation algorithm may also affect the final dose distribution.
Accurate dose calculation is dependent on the introduction of accurate measured data in the TPS beam configuration. There are limitations in obtaining such accurate data as the ionization chambers usually used for beam commissioning provide an over-response at the surface due to the perturbation caused by the electron contamination in the build-up region [59, 246]. Therefore differences between the calculated and the delivered dose to the patient in the build-up region [257] could be anticipated.

The first part of the work aimed at performing absolute dose measurements in homogeneous home-made phantoms. In general, the PBC algorithm estimated higher doses than those measured by the ionization chamber. With iMC and EGSnrc MC calculations, the computed absolute dose was closer to the measurements. Relative measurements were also performed using films in an homogeneous phantom and using 3D gamma evaluation for analysis. For the two different criteria used. With PBC, there were higher differences between the measurements

and the calculations, especially in the build-up region, as obtained in previous independent studies [72, 258, 259].

The TPS calculations were performed based on a HU-ED (Hounsfield Unit to electron density) calibration curve that was obtained with a specific calibration phantom which contained tissue-equivalent materials. For the EGSnrc MC calculations, a default CT conversion curve using 4 bins (air, lung, tissue and bone materials) from EGSnrc was used. Differences between iMC and EGSnrc MC can be assigned to the different HU-ED curves adopted.

The satisfactory results obtained between the iMC anc EGSnrc MC calculations further validated the HDMLC model [132] which proves to be a suitable tool to simulate breast cancer treatments. Therefore, further calculations were performed on clinical cases for the different verified techniques.

Comparing the DVH resultant from the comparison of the algorithms, the PBC over-estimates the dose in the higher dose region (for doses higher than 40 Gy) and presents higher doses in the lung and in the heart, compared to the dose values computed using the MC techniques. Further verification measurements should be performed in a heterogeneous phantom to precisely quantify the differences in the lung and bone. However, PBC is known for its limited accuracy mainly in heterogeneous media [260, 261].

The use of the commercial MC calculation iMC algorithm in iPlan would be preferable to PBC algorithm but it is still not possible in the actual clinical panorama due to the large amount of time each plan takes to calculate (the iMC calculations performed took between 30 to 40 min, and could not be therefore considered for optimization).

5.5 Conclusions

The aim of the present study was to compare the dose calculation accuracy of the Pencil Beam Convolution algorithm with a commercial MC algorithm from iPlan BrainLAB TPS and independent MC (EGSnrc-based code) calculations, in breast cancer radiotherapy calculations, using measurements with ionization chambers and radiochromic film.

The 3 calculation algorithms were compared and there are significant differences between the PBC algorithm and the MC-based calculations, in the build up region, in the lung regions.

The first clinical cases using the HDMLC in EGSnrc MC calculations model are presented and the results are validated against the iMC iPlan BrainLAB algorithm: there is a good agreement (superior to 97%) between the DVH in the PTV and OAR and between the 3D-gamma analysis performed.

Chapter 6

Assessment of contralateral breast doses in breast radiotherapy

Radiotherapy is a double-edged sword: it may heal but it also may induce late complications.

6.1 Second cancer malignancies

Deterministic effects appear at high doses (several Gy); however, stochastic effects, such as cancer induction, may occur at much lower doses. Second cancer induction from radiation therapy is becoming an important issue mainly for two reasons:

- the survival rates are increasing and therefore the risk for a subsequent cancer also increases [262];
- radiation therapy techniques are evolving envisaging highly modulated beams to achieve optimal dose conformality to the tumor volume while sparing healthy tissues [263], for higher doses but with low doses absorption not being assessed.

Second cancer risk assessment in RT is a struggling and demanding issue due to the large uncertainties of the dose-response relationship in human tissues. To better assess the dose-response relationship, Joosten et al [264] advocates that epidemiological studies on second cancer risk should not only incorporate in-field but also out-of-field dosimetry.

The TPS systems are accurate at determining in-field doses, however their accuracy in out-of-field dose calculations for peripheral doses may not be that accurate [265, 266]. Peripheral doses are typically determined using measurements in water phantoms [267, 268] or Monte Carlo methods [269–271].

6.1.1 Carcinogenic Effect of Radiation

The potentially carcinogenic effect of ionizing radiation is well known and has been extensively investigated. Early experiences in the 1900s were based on individuals accidentally exposed while working, for example, radium dial painters, uranium miners and in physics or chemistry research. Most of our understanding of radiation effects on humans, including functional dose-response relationships, is largely based on incidence and cancer mortality for solid cancers and leukemia among atomic-bomb survivors in Japan [272–274]. Those nuclear explosions caused acute radiation exposures over a very short period of time. Such exposures cause different biological damage mechanisms than those experienced by radiotherapy patients who are treated with prolonged exposures in fractionated intervals. Many research groups have directly studied second cancer incidence rates among radiotherapy patients. Epidemiological data have shown that an exposure to ionizing radiation above 50 - 100 mSv increases the risk of, for example, second prostate cancer [275] and second breast cancer in patients 30 years after the initial treatment [276]. Large studies were also done for breast cancer cases after treatment of childhood cancer with radiation [277, 278].
Criteria for classifying second cancers were originally defined by Cahan et al [279]:

- the second tumor occurs in locations irradiated by primary or secondary therapeutic beams,
- the histology of the second tumor is different from that of the original disease so a metastasis is excluded,
- the existence of a latency period, typically of several years,
- the second tumor was not present at the time of radiation treatment and
- the patient does not have a cancer-prone syndrome.

It is believed that the therapeutic dose aims at killing all tumor cells thus leaving little chance for cell mutation. For this reason, dosimetry studies of second cancers

often focused on regions that were 'outside the treatment volume'. Treatment-related second cancers are the direct consequence of treatment success to the first cancer.

6.1.2 Second malignancies after Radiotherapy

As a part of an epidemiological study on cervical cancer, Stovall et al [280] developed a systematic dosimetric method for determining tissue doses for about 20.000 patients who were treated for cancer of the uterine cervix at many institutions in the United States, Canada and Europe from 1916 to 1975. This work was among the most significant dosimetry efforts related to second cancer studies. The authors measured and calculated doses from external-beam radiation therapy involving several treatment machines, using an anthropomorphic female phantom.

6.2 Second malignancies after Primary Breast Cancer Radiotherapy

In 2004, Roychoudhuri et al [281] published a study on second cancers of the lung, colon, oesophagus and thyroid gland, malignant melanomas, myeloid leukemias and second primary breast cancers, investigating second cancers in patients who either have, or have not, received radiotherapy alongside surgery for breast cancer. It was observed an elevated relative risk for lung cancer (at 10-14 years and over 15); myeloid leukemia (at 1-5 years); second breast cancer (at 5-10 years and over 15); and oesaphageal cancer (at over 15 years). Other reviews on induction of second malignancies after using radiation, in different organs and using different techniques were done by Fowble et al [282], Xu et al [267] and Grantzau et al [283]. The EBCTCG study published in 2005 [27] observed an excess cancer incidence among women who underwent RT that mainly involved contralateral breast cancer and lung cancer, and an excess mortality from causes other than breast cancer that mainly involved heart disease and lung cancer. Based on much smaller numbers, there was also a moderately significant excess mortality from pulmonary embolism and excess incidence of oesophagus cancer, leukemia and soft tissue sarcoma (see table 6.1).

Site of cancer (ICD-9 categories)	Events	Logrank O-E	Variance of (O-E)	Ratio of rates	2p
Incidence of contralateral breast cancer:					
- by years since randomisation					
(and, for cases, mean year of randomisation)					
0-4 (1980)	673	1.3	161.1	1.01 (0.08)	0.9
5-14 (1980)	627	53.5	150.2	1.43 (0.10)	0.00001
15+ (1975)	151	2.1	33.4	1.06 (0.18)	0.7
- by age at randomisation					
<50	600	11.7	143.0	1.09 (0.09)	0.3
50+	851	45.1	201.3	1.25 (0.08)	0.002
- by use of systemic therapy					
with chemotherapy or tamoxifen	649	21.7	158.0	1.15 (0.09)	0.08
without chemotherapy or tamoxifen	802	35.1	186.4	1.21 (0.08)	0.01
Total contralateral breast cancer	**1451**	**56.9**	**344.4**	**1.18 (0.06)**	**0.002**
Incidence of other specified cancers:					
Lung cancer (162)	215	24.3	51.1	1.61 (0.18)	0.0007
Oesophagus cancer (150)	31	5.4	7.5	2.06 (0.53)	0.05
Leukaemia (204-208)	59	7.5	13.9	1.71 (0.36)	0.04
Soft-tissue sarcoma (158, 171)	26	5.4	6.4	2.34 (0.62)	0.03
Thyroid cancer (193)	26	-2.3	6.2	0.69 (0.34)	0.4
Bone cancer (170)	28	1.7	6.9	1.28 (0.43)	0.5
Other specified malignancy	966	16.4	220.7	1.08 (0.07)	0.3
Total other specified cancers	**1351**	**58.4**	**312.7**	**1.20 (0.06)**	**0.001**

TABLE 6.1: Effect of radiotherapy on incidence of second cancers before recurrence of breast cancer, and on mortality from causes other than breast cancer (23500 women in 46 trials of adding radiotherapy, and 9300 in 17 trials of radiotherapy vs more surgery). Taken from [15].

Contralateral Breast Cancer

Long-term survival after breast cancer diagnosis increased in the last years due to, in part the earlier detection but also to improved treatment options. Therefore, it is important to devote more attention to the breast cancer survivors and, in particular to secondary breast cancer.

Some studies suggest that CLB cancer rates range from 10% to 15% at 15 years after treatment and are higher for longer term survivors [284–286].

The risk of a breast cancer survivor developing a second breast cancer is much higher than the risk of a comparable healthy woman developing a first breast cancer [287].

There is a general consensus that the understanding of the etiology of second breast cancers is still very limited, but there are some factors that can be pointed as precursors of second breast cancers such as genetics, family history, lifestyle, lobular histology, multicentric disease and young age at diagnosis. Due to the lack of knowledge in these broad fields, prophylactic approaches are investigated to reduce the risks of second breast cancer for all breast cancer survivors. For

estrogen receptor-positive primary breast cancer patients, tamoxifen is pointed out to reduce the risk of a second breast cancer [285, 288, 289].

Other adopted options are regular screening, oophorectomy (surgical removal of an ovary or ovaries) [290], chemotherapy [29], prophylactic CLB mastectomy [291] or prophylactic CLB irradiation [292]. Clearly, these procedures present risk to the patient, and cause significant morbidity.

CLB cancer after breast irradiation and the possible impact of RT on the development of CLB cancer has been a matter of study in the last years [293–295]. Among the scientific community it is not consensual that the treatment of breast cancer with ionizing radiation increases the risk of CLB cancer. Many studies report no significant differences between treatment with and without radiation [296–300]. However, Harvey et al [301] found evidence that there is an increased risk of CLB cancer for women treated with radiation. Others groups reported an increased incidence of CLB cancer at 10 or more years after the treatment of primary breast cancer with radiation [302, 303] and for women under 45 years old [294, 304].

Several epidemiological studies were performed and the ones with more patients involved are the following:

- Basco et al [305] investigated 14000 breast women in British Columbia who were treated with mean CLB doses of 1.5 Gy, between 1946 and 1982; they registered 194 of contralateral breast cancer (about 1.4%);
- Boice et al [304] studied 41109 primary breast cancer women in Connecticut, between 1935 and 1982, with mean doses in the CLB of 2.8 Gy, and 655 second contralateral breast cancer were notificated (about 1.6%);
- Storm et al [306], published the results from a study in Denmark, in which 56540 women with breast cancer between 1943 and 1978; 529 of these women had a second breast cancer (about 0.9%);
- Stovall et al [307] published their results from a large study with 1399 patients, treated between 1985 and 1999. They concluded that RT did not play a significant role in the development of a second primary breast cancer; however, with young women with breast cancer had an elevated long-term risk of developing a CLB cancer.

It is necessary important to point out, at this stage, that the older studies include patients treated with a variety of RT techniques (orthovoltage X-rays or 60-Co) and dosages are obsolete nowadays.

Several studies estimate that the mean dose absorbed by the CLB in case of WBI with 50 Gy using conventional tangential beams, varies from 0.5 to 2 Gy [190, 308–314]. There is significant evidence of increased CLB cancer risk in young women (less than 40 years old at time of treatment) [284, 304, 307, 315]. Some studies highlight that the risk of CLB cancer increases with dose of radiation [304, 307, 315]. Thus, despite having a curative intention, the ionizing radiation has a carcinogenic effect on adjacent locations to the primary irradiation, and therefore the CLB dose should be minimized as long as it does not compromise the primary treatment, especially in younger women.

The transition from conventional 2-dimensional (2D) RT to 3D conformal RT (3D-CRT) involved a reduction in the volume of normal tissues receiving a high dose, with an increase in dose to the target volume that includes the tumor and a limited margin into the normal tissues [316].

Early breast cancer radiation treatment is commonly performed with a tangential technique. To achieve better dose homogeneity and dose coverage within the treated breast, hard wedges are very often used. However, it is accepted that wedged fields result in higher contralateral breast doses than the corresponding open fields [312, 314, 317]. Replacing the physical wedge by a virtual wedge [1] would reduce the dose in the CLB significantly [318].

When now changing from tangential static fields to field-in-field and IMRT techniques, which naturally may imply using more fields, there is a need to investigated the influence of these new techniques with regard to their roles as risk factors for secondary breast cancer in the CLB [263, 307, 319].

Indeed, there is not a consensual opinion on whether the IMRT techniques increase or not the doses in the CLB. On one side, there is the argument that with the higher conformation that may be achievable with these modulated techniques, the OAR are exposed to lower doses [228, 233, 310, 320, 321]; but increased machine time, increase in monitor units and consequent increase of leakage and volume exposed normal tissue including the CLB were reported by other groups [314, 322].

Different strategies have been used to assess the dosimetric distribution in the CLB, mainly using point detectors: thermoluminescent detectors (TLD) [190, 308, 309, 311, 312, 318, 323] and diodes [308, 324]. More recently, Saur et al [314] performed measurements in an anthropomorphic female phantom using GafChromic

[1] Virtual wedge: automatic programmed wedge effect produced by closing the jaws.

EBT films. The studies concluded that the dose distributions in the CLB are inhomogeneous and that there are differences between different irradiation techniques.

The aim of this study is to characterize the CLB dose using different breast irradiation techniques, and, on the basis of these results, identify the technique that provides the least dose to the CLB. This study includes dose calculations using the PBC, iMC and EGSnrc MC for comparison.

6.3 Material, Methods and Patients

This chapter results from the work presented in the previous chapters and it has particular emphasis on the CLB doses calculated on the seven left breast cancer patients.

The 7 patients that had the contouring of the CTV, planning target volume (PTV), heart and CLB were done by the same radiation oncologist for the sake of consistency. The PTV was defined by adding a 5 mm margin to the CTV. All structures were confined to 3 mm from the external surface of the patient. An additional structure specified as Body-PTV was also created to evaluate the doses on the body excluding the PTV. An example of a patient delineation can be seen in figure 6.1.

The patient dose calculations were optimized for the iPlan (BrainLAB AG, Feldkirchen, Germany) TPS v. 4.1, as previously presented in chapter 5 using the PBC calculation algorithm. All the plans were then recalculated for iMC and EGSnrc MC.
The validation of the EGSnrc MC dose calculations was performed with film dosimetry and absolute dose measurements using an ionization chamber and presented in chapter 5. The validation results presented were performed for a 2.0 Gy PTV irradiation.

According to the 3D gamma evaluation performed in chapter 5, the highest dose differences (see figure 5.13) were observed in surface doses, including the CLB region closer to the treated area, between PBC and iMC algorithms. Further comparison between film measurements and the TPS calculations reveals the significant dose differences are also detected at the skin (see figures 5.11 and 5.12) and in the CLB. The CLB, in breast RT calculations is exposed to low doses, mainly scattered radiation from the linac head and from photon interactions in

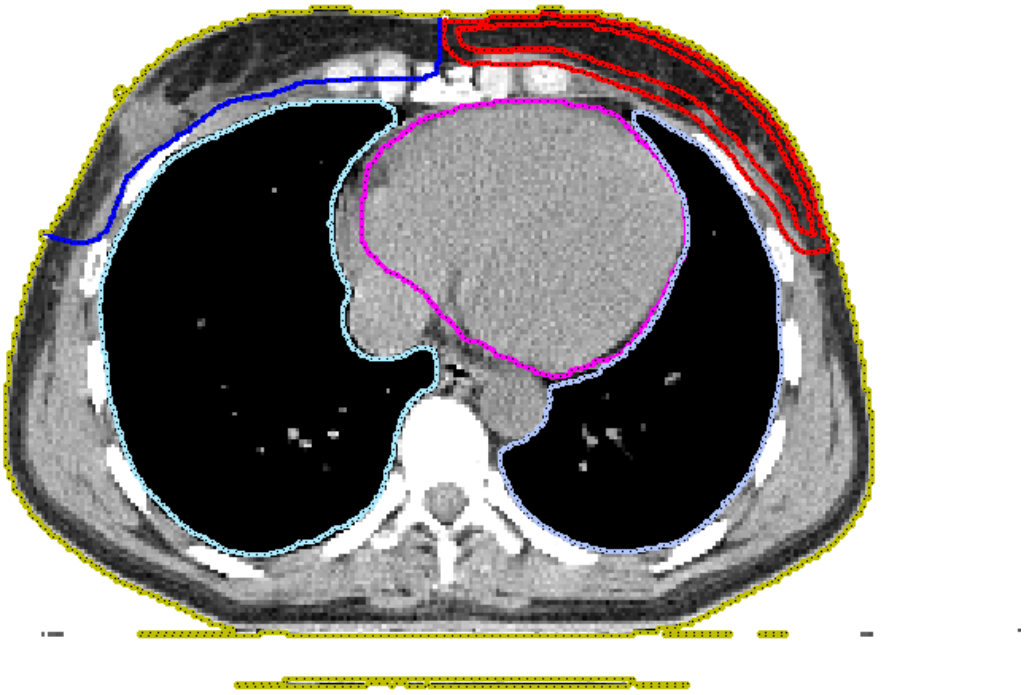

FIGURE 6.1: Contouring example in one of the patients enrolled in the study, in an axial view. In blue, it is represented the contralateral breast contour; in pink, the heart; the inner red corresponds to the CTV whereas the outer red represents the PTV.

the phantom/patient. These doses may not be accurately handled, in particular by the PBC algorithm, due to its features.

In the present work, the aim is to determine the CLB doses. Therefore, the EGSnrc MC calculations presented in chapter 5 will be used for a detailed analysis. The patient dose calculations were performed for a total prescribed dose of 50.0 Gy with the CLB receiving mean doses from 2.5% up to 7.5% of the prescribed dose (1.25 Gy and 3.75 Gy). The calculated data was introduced in SPSS version 20 (IBM software) for statistical analysis.

6.4 Results

It is particularly important to remark that the priority of the irradiation plans was set in order to adequately cover the PTV volume with the 95% isodose curve, avoiding as much as possible the OAR.

6.4.1 Breast irradiation plans

The curves obtained for the 3 calculation algorithms: PBC, iMC and EGSnrc MC, for f-IMRT, IMRT2 and IMRT5, for one of the patients are presented in figures 6.2, 6.3 and 6.4, respectively.

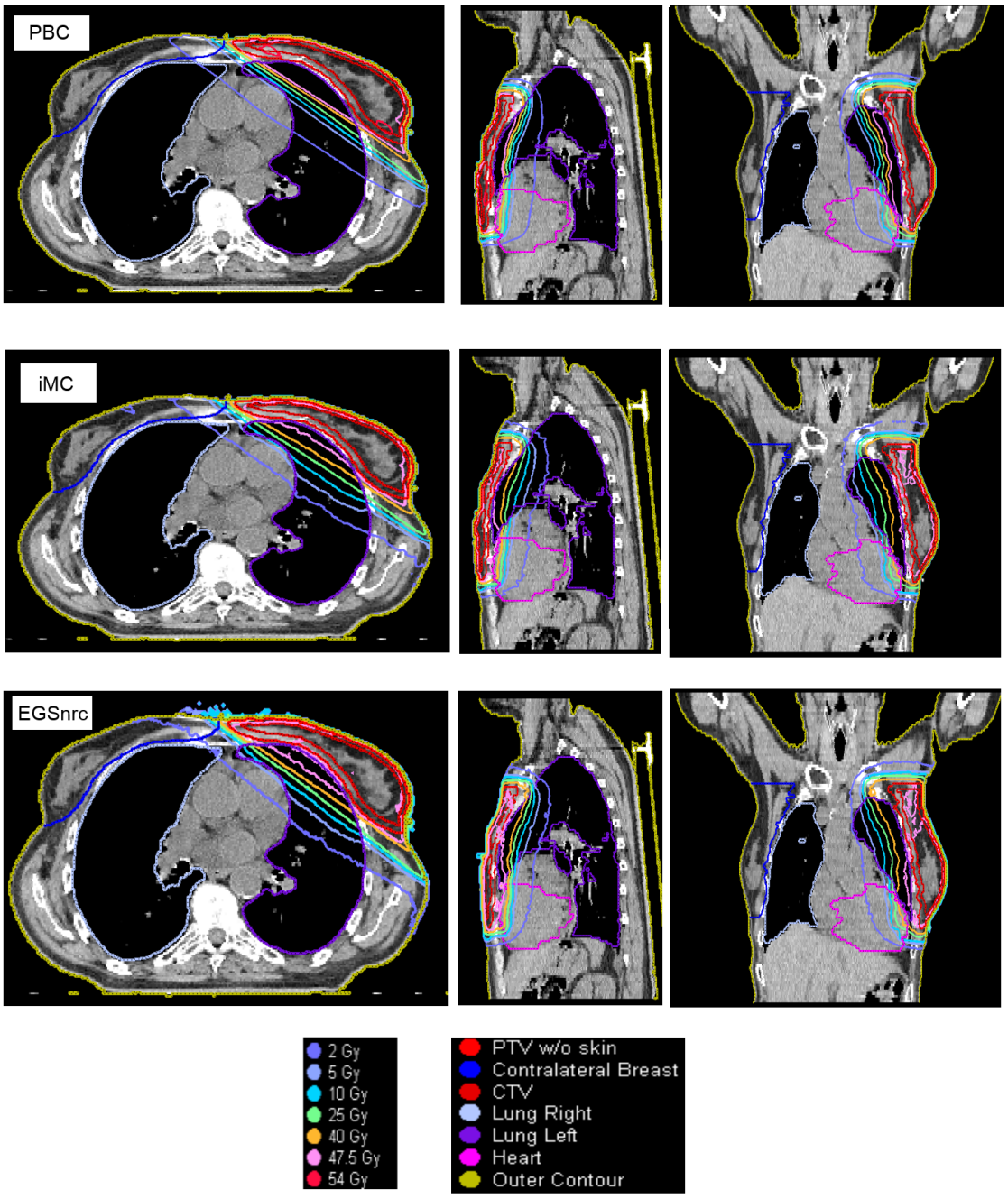

FIGURE 6.2: f-IMRT irradiation example for one of the patients, using the 3 calculation algorithms.

From the figures 6.2, 6.3 and 6.4 it is possible to observe the irradiation of the contoured structures, in axial, coronal and sagital planes, from left to right.

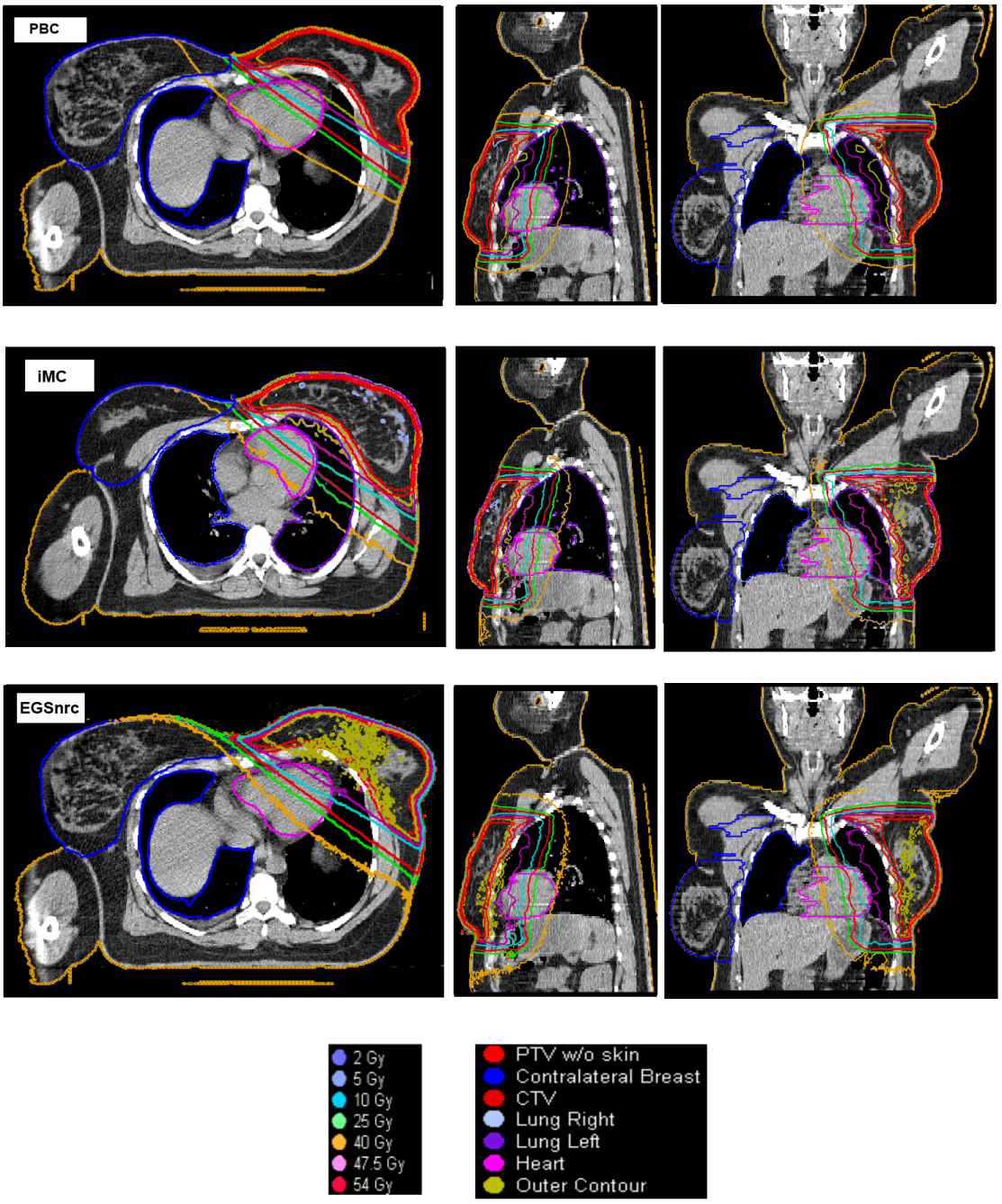

FIGURE 6.3: IMRT2 irradiation example for one of the patients, using the 3 calculation algorithms.

Comparing the irradiation techniques, it is possible to notice that with IMRT5 (figure 6.4) there is a wider spread of low doses into the body and OAR than with the tangential techniques (figures 6.2 and 6.3). However, the 47.5 Gy isodose is more conformed to the PTV volume than in the tangential options.

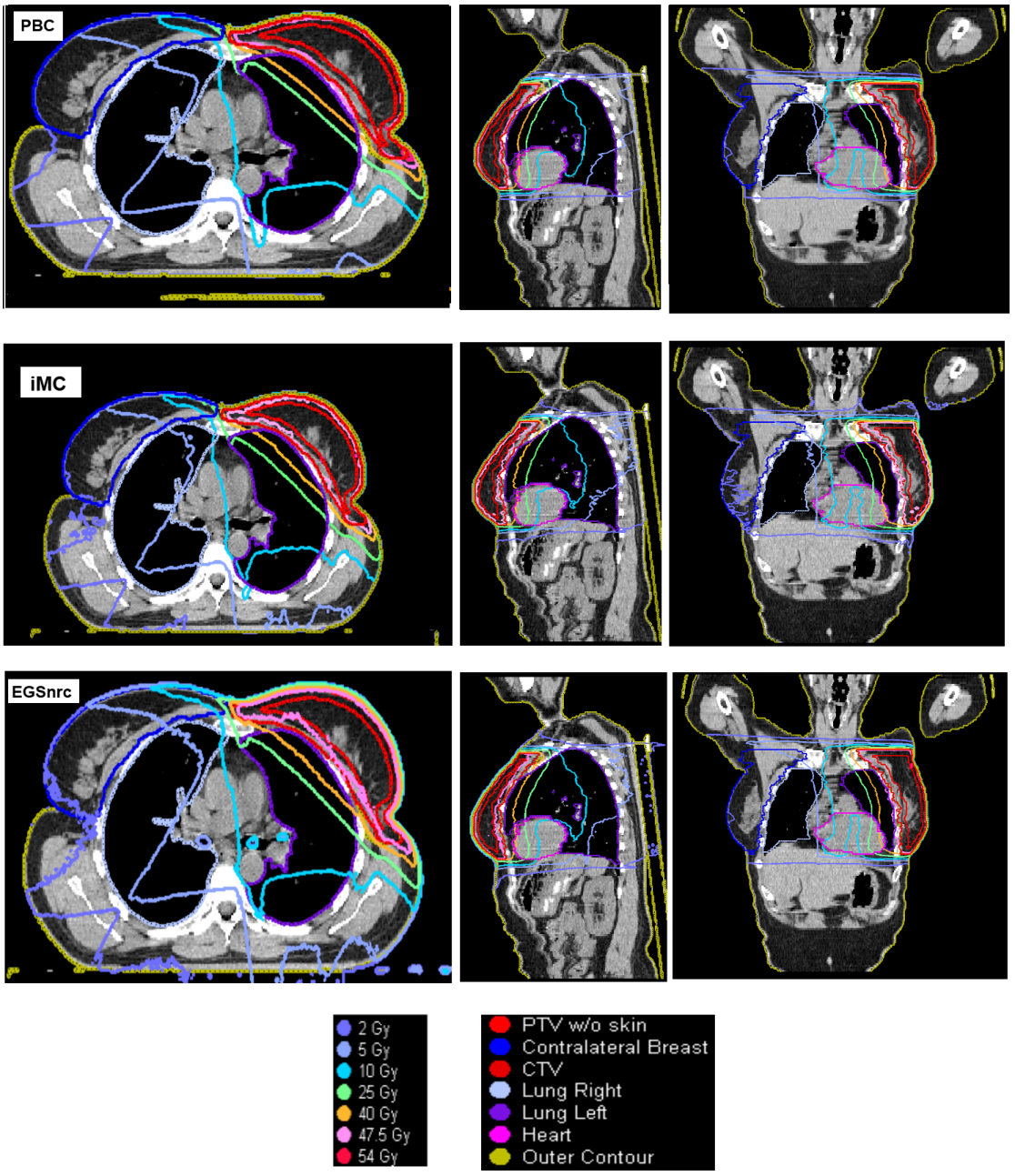

FIGURE 6.4: IMRT5 irradiation example for one of the patients, using the 3 calculation algorithms.

6.4.2 Dose Volume Histogram analysis

For a detailed analysis, the DVH of all the patients for the three irradiation techniques were determined for the CLB and the PTV and are presented in figures 6.5 and 6.6, respectively. For the CLB, the aim is to have as low dose as possible; the best DVH corresponds to low doses in this organ; for the PTV, the goal is to irradiate the all volume with the prescribed dose, avoiding higher doses ($\leq 107\%$) in and outside the PTV.

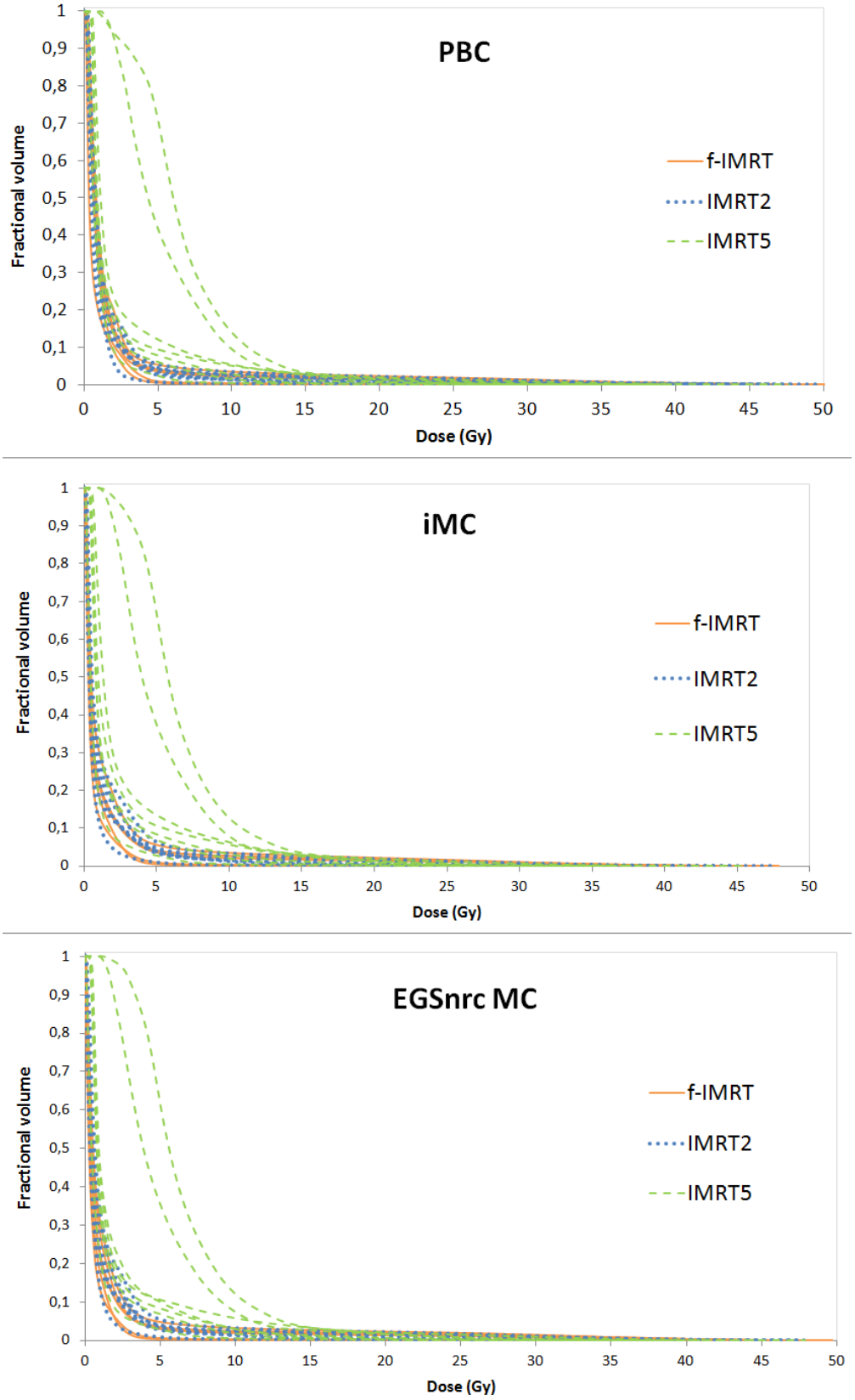

FIGURE 6.5: Dose volume histograms of the seven patients enrolled in the study, for the CLB, for the 3 calculation algorithms (PBC on top, iMC, in the middle and EGSnrc MC in the bottom) for f-IMRT, in orange; IMRT2, in blue; and IMRT5, in green. The aim is to obtain the lowest doses within this organ.

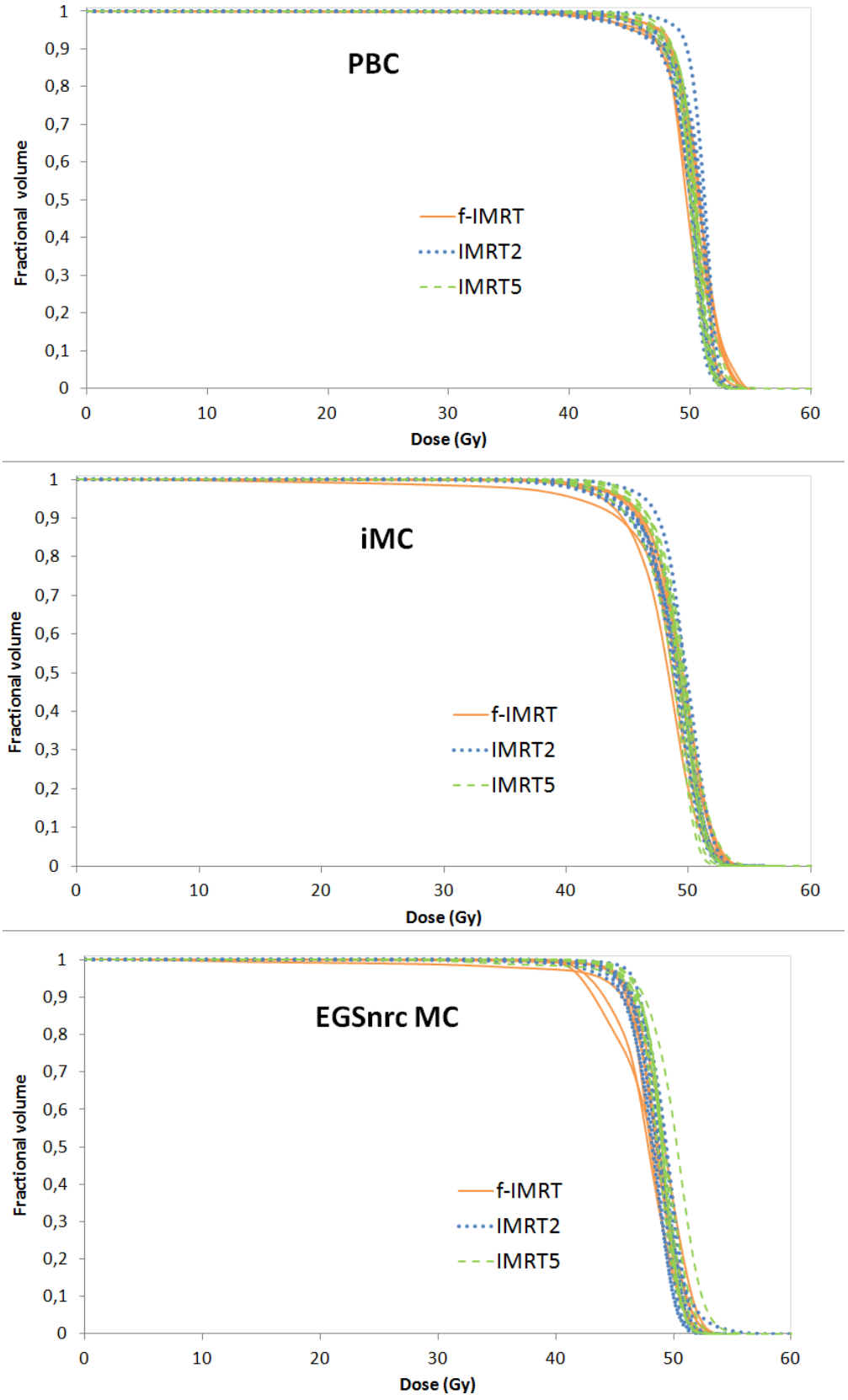

FIGURE 6.6: Dose volume histograms of the seven patients enrolled in the study, for the CLB, for the 3 calculation algorithms (PBC on top, iMC, in the middle and EGSnrc MC in the bottom) for f-IMRT, in orange; IMRT2, in blue; and IMRT5, in green. The aim is to irradiate all the PTV with the prescribed dose.

As expected from the irradiation plans, the DVH explicitly shows that for IMRT5, the CLB receives higher doses for doses up to 15 Gy, especially for 2 out of 7 patients. The DVH present higher doses independently of the calculation algorithm.

The plans were optimized for the PBC algorithm and the plans were adapted so that the 95% isodose covered the target volumes. Therefore, the PBC HDV is expected to respect this criteria. Just by simply looking at figure 6.6 it is difficult to verify that the MC algorithms satisfy this condition, despite having the expected shape for a PTV adequate irradiation.

6.4.3 Statistical analysis

For further analysis of the dose differences, a detailed evaluation of specific doses was also performed. Some parameters were extracted from the DVH and the results were introduced in SPSS for comparison. The results are plotted in figures 6.7 and 6.8.

From figure 6.7 it is possible to observe that IMRT5 has significantly higher doses in the CLB, for all parameters investigated, than the tangential (f-IMRT and IMRT2) techniques. However, for all the variables, IMRT5 presents higher CLB doses, and the values for f-IMRT and IMRT2 (the tangential techniques) do not present significant differences.

In absolute dose values, considering D_{mean}, the CLB receives 1.50 ± 0.39 Gy and 1.45 ± 0.38 Gy, for f-IMRT and IMRT2, respectively, whereas, the mean dose for an IMRT5 plan is 3.11 ± 2.25 Gy. For the MC algorithms, the results are similar, IMRT5 presenting at least twice more mean dose values than the tangential techniques. Concerning the CLB volume that receives at least 5 Gy, it increases from 2.44 ± 1.61% and 3.23 ± 1.40% for f-IMRT and IMRT2, respectively, to 19.46 ± 12.58%, for the IMRT5, as determined using the EGSnrc MC algorithm (increasing about a factor of 6). Regarding the volume of CLB that receives at least 2 Gy, the considerations are similar, with IMRT5 having more contralateral healthy breast receiving this dose (eg. for the iMC calculations: for f-IMRT and IMRT2, 14.63 ± 3.76% and 13.89 ± 5.11% of right breast receive 2 Gy, whereas, for IMRT5 the CLB percentage is 40.59 ± 36.37%).

The results between the 3 calculation algorithms present differences, in the CLB:

- D_{mean} presents similar median values for all the techniques with slightly lower values for EGSnrc MC;

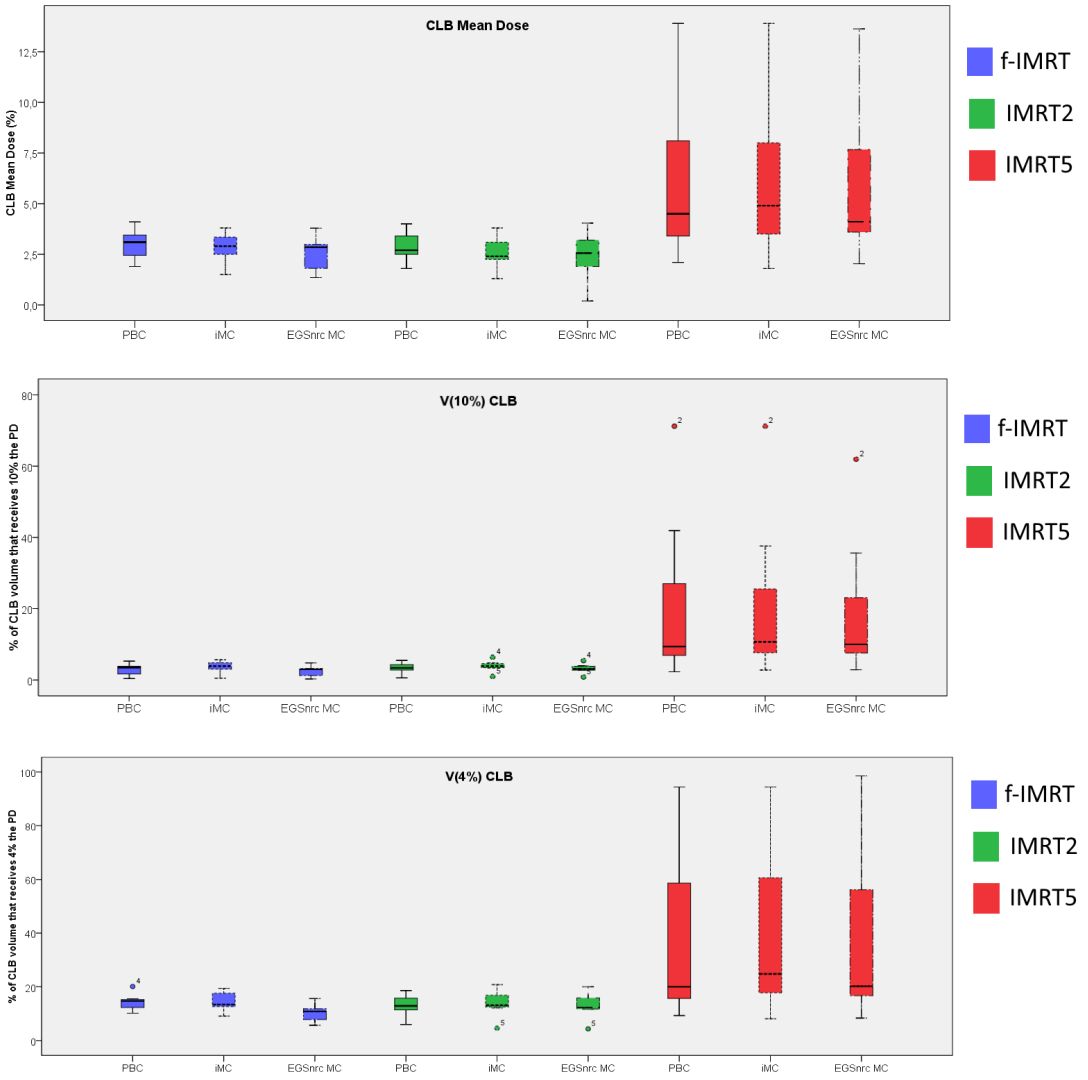

FIGURE 6.7: Diagram with mean and maximum and minimum doses in the CLB obtained for the 7 patients, for D_{mean}, V_{5Gy} and V_{2Gy}, from top to bottom, for f-IMRT (blue), IMRT2 (green) and IMRT5 (rose) and the three calculation algorithms: PBC (continuous line), iMC (dotted line) and EGSnrc MC (slash-dot-slash line).

- V_{5Gy} and V_{2Gy} median values are slightly lower for the EGSnrc MC than for the iMC.

Concerning the PTV irradiation, there are significant differences (see figure 6.8), considering the different calculation algorithms:

- for all the techniques and variables investigated, iMC and EGSnrc MC present lower PTV coverage than the PBC predicted;
- in general, the EGSnrc MC predicted lower doses than the iMC;

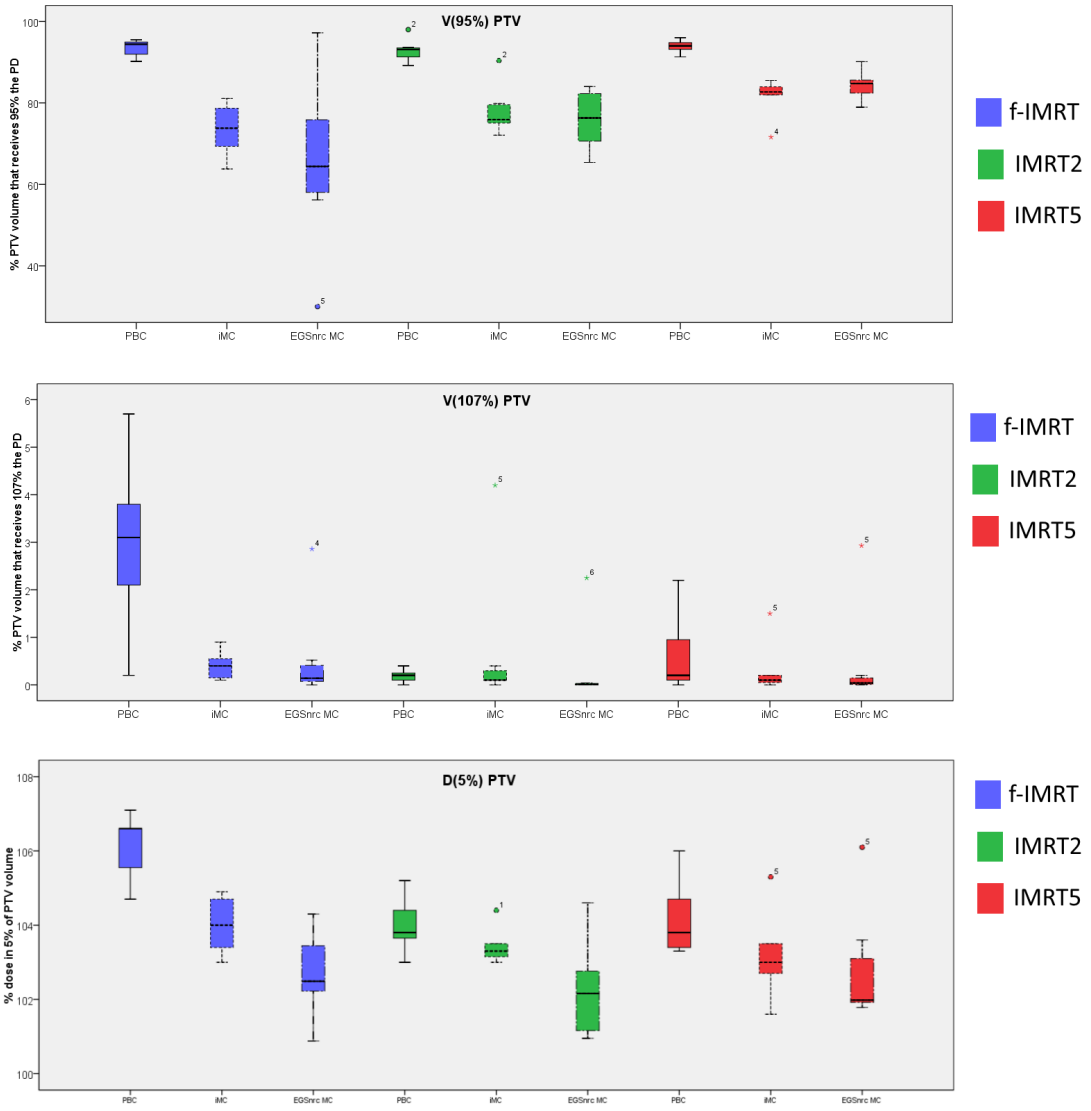

FIGURE 6.8: Diagram with mean, maximum and minimum doses in the PTV obtained for the 7 patients, for $V_{95\%}$, $V_{107\%}$ and $D_{5\%}$, from top to bottom, for f-IMRT (blue), IMRT2 (green) and IMRT5 (rose) and the three calculation algorithms: PBC (continuous line), iMC (dotted line) and EGSnrc MC (slash-dot-slash line).

- taking into consideration the $V_{95\%}$ as an irradiation quality parameter, IMRT5 is the technique with better PTV coverage, according to the MC techniques;
- considering PBC, f-IMRT is the technique with higher doses above 107% but considering the calculations with the MC algorithms, that does not seem to happen and there are no significant differences, considering this criteria;
- the EGSnrc MC and the iMC predict lower doses than the PBC for the 5% of PTV volume ($D_{5\%}$) that receive higher doses.

In summary, IMRT5 is the technique that best conforms to the PTV is also the one that causes more doses into the OAR and, in particular, to the CLB.

6.4.3.1 Comparison of the calculation algorithms

To clearly investigate the variables investigated related to the CLB (D_{mean}, $V_{10\%}$ and $V_{4\%}$), a statistical analysis was performed. Friedman's test (see details of this test in Appendix A) was applied to the variables using SPSS IBM v20 and it is assumed that there are significant statistical differences between the variables considering a p-value inferior to 0.05. The results are displayed in table 6.2.

TABLE 6.2: Friedman's statistical analysis on the CLB, comparing the calculation algorithms. The values reported are p-values; significant statistical differences are considered for p-values ≤ 0.05.

CLB	D_{mean}	$V_{10\%}$	$V_{4\%}$
f-IMRT	**0.021**	**0.002**	**0.004**
IMRT2	**0.012**	**0.004**	**0.050**
IMRT5	1.000	0.104	0.495

According to the results reported in table 6.2, for f-IMRT and IMRT2 there are significant statistical differences between the 3 calculation algorithms. So, for further investigation when significant statistical differences were found, a *pairwise comparison* between the algorithms was performed to identify where the differences come from (see table 6.3).

TABLE 6.3: Pairwise analysis of the variables with significant statistical differences on the CLB for D_{mean}, $V_{10\%}$ and $V_{4\%}$ variables, comparing the calculation algorithms. p-values are reported.

		f-IMRT		**IMRT2**	
		iMC	EGSnrc MC	iMC	EGSnrc MC
D_{mean}	PBC	**0.048**	**0.048**	**0.010**	0.855
	iMC	-	1.000	-	0.184
$V_{10\%}$	PBC	0.544	0.098	**0.048**	1.000
	iMC	-	**0.002**	-	**0.002**
$V_{4\%}$	PBC	1.000	**0.004**	0.326	1.000
	iMC	-	**0.048**	-	**0.048**

According to the analysis performed for the CLB (see table 6.2), there are only statistical significant differences (p-value ≤ 0.05) between the tangential techniques (reason why IMRT5 does not show up on table 6.3), for the 3 variables under investigation. For D_{mean}, there are significant statistical differences between the

PBC and the MC calculation algorithms; for $V_{10\%}$ the differences are between the MC techniques and also between iMC and PBC for IMRT2; for $V_{4\%}$, the differences are between the MC techniques and for f-IMRT between PBC and EGSnrc MC (see table 6.3).

A detailed statistical analysis was also performed for the PTV to better understand if the PTV coverage is affected by the irradiation technique according to the calculation algorithms predictions. The results are presented in tables 6.4 and 6.5.

TABLE 6.4: Friedman's statistical analysis on the PTV, comparing the calculation algorithms. The values reported are p-values; significant statistical differences are considered for p-values ≤ 0.05 (values in bold).

PTV	$V_{95\%}$	$V_{107\%}$	$D_{5\%}$	**HI**	**CI**	**CN**
f-IMRT	**0.021**	**0.012**	**0.001**	0.066	**0.003**	0.054
IMRT2	**0.005**	0.254	**0.016**	**0.002**	**0.004**	0.887
IMRT5	**0.002**	0.074	**0.034**	**0.002**	**0.002**	**0.042**

TABLE 6.5: Pairwise analysis of the variables with significant statistical differences on the CLB for $V_{95\%}$, $V_{107\%}$, $D_{5\%}$, HI, CI and CN variables, comparing the calculation algorithms. p-values are reported.

		f-IMRT		**IMRT2**		**IMRT5**	
		iMC	EGSnrc MC	iMC	EGSnrc MC	iMC	EGSnrc MC
$V_{95\%}$	PBC	**0.048**	**0.048**	**0.023**	**0.010**	**0.002**	0.098
	iMC	-	1.000	-	1.000	-	0.544
$V_{107\%}$	PBC	0.184	**0.010**	-	-	-	-
	iMC	-	0.855	-	-	-	-
$D_{5\%}$	PBC	0.184	**0.001**	0.326	**0.015**	0.098	0.069
	iMC	-	0.184	-	0.687	-	1.000
HI	PBC	-	-	**0.002**	0.544	**0.002**	0.544
	iMC	-	-	-	0.098	-	0.098
CI	PBC	0.184	**0.003**	**0.048**	**0.004**	**0.002**	0.098
	iMC	-	0.425	-	1.000	-	0.544
CN	PBC	-	-	-	-	0.069	0.247
	iMC	-	-	-	-	-	1.000

With exception of $V_{107\%}$ for IMRT2 and IMRT5, HI for f-IMRT and CN for IMRT2, all the variables present significant statistical differences (p-value ≤ 0.05, values in bold) (see table 6.4). With the pairwise comparison for the techniques (presented in table 6.5), all the differences with statistical significance if existent are between PBC and the MC calculation algorithms.

6.4.3.2 Comparison of the irradiation techniques

A statistical analysis focused on the irradiation techniques was also performed, considering the CLB and the PTV irradiation. The CLB results are presented in tables 6.6 and 6.7.

TABLE 6.6: Friedman's statistical analysis on the CLB, comparing the irradiation techniques. The values reported are p-values; significant statistical differences are considered for p-values ≤ 0.05, values in bold.

CLB	D_{mean}	$V_{10\%}$	$V_{4\%}$
PBC	**0.006**	**0.004**	**0.050**
iMC	**0.018**	**0.018**	**0.018**
EGSnrc MC	**0.004**	**0.002**	**0.002**

TABLE 6.7: Pairwise analysis of the variables with significant statistical differences on the CLB for D_{mean}, $V_{10\%}$ and $V_{4\%}$ variables. p-values are reported.

		PBC		**iMC**		**EGSnrc MC**	
		f-IMRT	IMRT2	f-IMRT	IMRT2	f-IMRT	IMRT2
D_{mean}	IMRT2	1.000	-	1.000	-	1.000	-
	IMRT5	0.069	**0.010**	**0.033**	0.069	**0.004**	**0.048**
$V_{10\%}$	IMRT2	1.000	-	1.000	-	1.000	-
	IMRT5	**0.004**	**0.048**	**0.023**	0.098	**0.002**	0.098
$V_{4\%}$	IMRT2	1.000	-	1.000	-	0.544	-
	IMRT5	0.326	**0.048**	**0.023**	0.098	**0.002**	0.098

According to the Friedman's analysis, there are significant statistical differences for all the investigated variables, for all the calculation algorithms. Performing a pairwise comparison, most of the significant statistical differences are found between f-IMRT and IMRT5 or between IMRT2 and IMRT5, irrespective of the calculation algorithms, as displayed in table 6.7 .

TABLE 6.8: Friedman's statistical analysis on the PTV, comparing the irradiation techniques. The values reported are p-values; significant statistical differences are considered for p-values ≤ 0.05.

PTV	$V_{95\%}$	$V_{107\%}$	$D_{5\%}$	**HI**	**CI**	**CN**
PBC	0.368	0.089	0.066	**0.028**	**0.004**	**0.002**
iMC	**0.050**	**0.042**	0.054	**0.028**	0.102	**0.012**
EGSnrc MC	**0.050**	0.317	0.565	0.066	0.651	**0.012**

On the PTV, there are significant statistical differences for the CN (all algorithms); using iMC, for $V_{95\%}$, $V_{107\%}$ and HI; using PBC, for HI and CI variables (see table 6.8).

TABLE 6.9: Pairwise analysis of the variables with significant statistical differences on the CLB for $V_{95\%}$, $V_{107\%}$, $D_{5\%}$, HI, CI and CN variables, comparing the calculation algorithms. p-values are reported.

		PBC		**iMC**		**EGSnrc MC**	
		f-IMRT	IMRT2	f-IMRT	IMRT2	f-IMRT	IMRT2
$V_{95\%}$	IMRT2	-	-	1.000	-	1.000	-
	IMRT5	-	-	**0.048**	0.326	**0.048**	0.326
$V_{107\%}$	IMRT2	0.184	-	0.247	-	-	-
	IMRT5	-	-	0.069	1.000	-	-
HI	IMRT2	0.184	-	0.544	-	-	-
	IMRT5	**0.033**	1.000	**0.023**	0.054	-	-
CI	IMRT2	1.000	-	-	-	-	-
	IMRT5	**0.004**	**0.048**	-	-	-	-
CN	IMRT2	0.544	-	0.855	-	0.855	-
	IMRT5	**0.002**	0.098	**0.010**	0.1844	**0.010**	0.184

From table 6.9, all the variables that present significant statistical differences are: between f-IMRT and IMRT5 (only CI presents differences between IMRT2 and IMRT, for the PBC algorithm). This means that the coverage of the PTV was guaranteed with all the irradiation techniques, even though differences might be found between f-IMRT and IMRT5. However, despite the adequate irradiation of the PTV, the irradiation techniques affect the dose in the CLB. Clearly, using non-tangential fields, there is a wider spread of 'low" doses into the CLB and other OAR that must be taken into consideration particularly for women with long-term survival chances, to avoid second contralateral breast cancer.

6.5 Conclusions

The doses reported are affected by the patient's anatomy but some trends might be identified:

- it is accepted and assumed that the PBC does not accurately estimate skin doses, including the CLB dose, from the results presented in chapter 5. These results are in agreement to other groups results [314];
- the PBC algorithm does clearly overestimate the dose in the PTV when compared to the MC calculation strategies, due to inaccuracies in calculation, probably due to secondary electrons as pointed out in other phantom studies [269, 308] not accounted for by the PBC algorithm. in the build-up region (skin) and in the presence of heterogeneities;

- according to the results obtained with a standard tangential technique forwardly planned IMRT, mean doses of 1.42 ± 0.41 Gy and 1.26 ± 0.45 Gy, for iMC and EGSnrc MC respectively, are administered to the CLB; an inversely calculated IMRT tangential technique results in mean doses of 1.30 ± 0.41 Gy and 1.22 ± 0.64 Gy, for iMC and EGSnrc MC respectively; whereas using non-tangential fields (IMRT5) lead to a significant increase of about 50% increase the CLB mean dose (3.12 ± 2.17 Gy and 3.02 ± 2.13 Gy, for iMC and EGSnrc MC respectively);
- concerning the PTV coverage, the best PTV coverage is obtained for IMRT5 with the prescribed 95% isodose better conformed to the target volume, sparing the OAR from high doses.

From the results presented in chapter 5, differences either due to the calculation algorithms and/or the irradiation techniques in the CLB were expected.

It is recommended that the PBC is replaced by another calculation algorithm, if not Monte Carlo, at least a superposition/convolution algorithm. With this TPS it would make sense to use iMC. However, the large calculation times make it incompatible for clinical purposes.

The use of tangential techniques is the best option to spare the CLB from low dose irradiation. According to the literature, increasing the dose in the CLB, especially for women under 45 years old may lead to higher incidence of secondary induced CLB cancer [6]. This should be taken into consideration when planning to go for new irradiation techniques with beam angles different from the standard tangential beams, such as IMRT5, DCART or VMAT.

This work could be further improved if EGSnrc MC calculations could be performed in a breast phantom with heterogeneities to assess the dose volume histograms in the phantom.

Furthermore, other dosimetry techniques - not available for this work - could be used such as point dose detectors (TLD) and in-vivo dosimetry.

Chapter 7

Conclusions

7.1 Major Conclusions

One of the main objectives of this dissertation work consisted of studying and assessing the dosimetric and clinical performance of new, emerging and complex techniques and to find out whether they can be applied to breast irradiation treatments, improving dose delivery conformation and the RT treatment outcome.

Several general questions regarding these new and emerging RT techniques were addressed, such as:

a. Do they allow a more accurate dose delivery?
b. Do they allow an adequate dose conformation to the target volumes?
c. Do they allow to achieve a reduction of the doses in the OAR and in the healthy tissues surrounding the tumor?
d. Can these techniques be used without restrictions?

Concerning the calculation algorithms,

e. How do they perform in heterogeneous media?
f. Do they effectively overcome the shortcomings and limitations from current non-MC TPS?
g. How effective are existing MC simulations and algorithms implemented in state-of-the-art TPS using MC in achieving a more accurate dose delivery to the PTV, reducing the doses in the OAR and in the surrounding healthy tissues?
h. Can they be used without restrictions?

7.1.1 MC modeling and simulation of the Trilogy Varian linac

To achieve this goal, a struggling effort was done to model and simulate the linear accelerator used, the Trilogy Varian linac. The most thrilling task was to model, simulate and validate, for the first time using Monte Carlo methods with the EGSnrc MC code, the High Definition MLC. The HDMLC component module was validated in water (in chapter 3 and further used for breast EGSnrc MC calculations (in chapter 5). Thereby, the linac Trilogy from VARIAN Medical Systems (Palo Alto, CA) was successfully modeled and validated, using measurements performed not only in water but also in breast-shaped phantoms.

7.1.2 Comparison of the dosimetric performance of TPS using MC simulations and algorithms in breast cancer RT

To perform this investigation, a deep bibliographic research was performed. Dose calculations on breast patients in clinical environment were performed regarding the topic of this research. To further complement and enhance the approximate calculations made on the treatment planning system, Monte Carlo dose calculations were done. The Monte Carlo approach was the most accurate method for dose calculation in such complex calculations as it is the radiation interaction with matter in the breast context, due to the different media involved in this treatment location.

In chapters 4 and 5, the results of breast irradiation were obtained and an intercomparison was performed for the following 4 different techniques,

- f-IMRT (without wedges),
- IMRT2,
- IMRT5, and
- DCART

, and three algorithms, namely

- PBC,
- iMC, and
- EGSnrc MC.

The plans were evaluated based on criteria adapted from QUANTEC [325] and RTOG 1005 (protocol from RTOG. www.rtog.org/ClinicalTrials/ProtocolTable/StudyDetails.aspx?action_openFile&;FileID1_9366). The comparison performed for 7 patients was performed on the TPS iPlan BrainLAB, using 2 calculation algorithms: PBC and iMC. The dose distributions were optimized for the PBC algorithm and afterwards, recalculated using iMC.
Sizable discrepancies remain concerning between the 4 techniques investigated on breast irradiation and between the two algorithms studied (PBC and iMC). The PTV was adequately covered with all the techniques (evaluated by $V_{47.5Gy}$), considering PBC. IMRT5 had advantages over the other techniques based on the dosimetric comparison performed in this study especially in the high dose region of the left lung and heart, target conformation and heterogeneity indexes; DCART was the technique with the lowest $V_{95\%}$ and did not present improvement in sparing the OAR or the PTV coverage over the IMRT techniques investigated. However, the non-tangential techniques (IMRT5 and DCART) did increase the scattered dose and expose larger percentage of healthy volumes to low and medium doses.
f-IMRT is still the recommended technique for breast irradiation. Nonetheless, in case of high heart or left lung involvement, IMRT5 should be considered to breast cancer irradiation as it creates the most conformal distribution at the expense of more normal tissue receiving low dose. These observations were valid both for PBC and iMC. However, statistical significant differences were found between PBC and iMC calculations, on the variables investigated, mainly in the higher doses regimen ($\geq$ 40 Gy) for the PTV, left lung and heart.

The EGSnrc MC implementation was further validated against iMC calculations performed using iPlan, the BrainLAB TPS, in chapter 5.
Thereby, the primary goal of comparing different irradiation techniques was also accomplished using the TPS iPlan from BrainLAB and further compared with the independently calculated EGSnrc Monte Carlo plans.

The major conclusions regarding the irradiation techniques studied, f-IMRT, IMRT and IMRT5 are the following:

- f-IMRT and IMRT2, are the tangential techniques using mainly two beam incidences, a lateral and a median. These options are adequate for PTV irradiation but are not as conformed to the target volume as dose distributions with different beam incidences; furthermore, the healthy tissues in the vicinities (such as the left lung and heart, which are right beneath the PTV)

may receive higher doses. Between the two irradiation techniques, there is no preference for any of the techniques.

- IMRT5, a technique using five different incident beams on the target volume, between the traditional tangential beams. With this technique, more homogeneous and conformal dose distributions are obtained. The heart and left lung may thereby receive a lower percentage of doses above 30 Gy, due to better conformation to the PTV, as published by Popescu et al [232]. However, the healthy tissues in the vicinities do receive significant more doses below 20 Gy, in agreement with Ayata et al [326], such as the heart, left lung and the CLB, as particularly studied in chapter 6.

In summary, IMRT5 is the technique that best conforms to the PTV is also the one that causes higher doses into the OAR and, in particular, to the CLB. In table 7.1, the main features of each technique are presented.

TABLE 7.1: Breast irradiation techniques comparison. Main characteristics, advantages and disadvantages of the techniques investigated: f-IMRT, IMRT2, IMRT5 and DCART.
* according to actual standards.

	Planning mode	**Verification complexity**	**Advantages**	**Disadvantages**
f-IMRT	Direct	Simple*	Simple planning CLB: lower doses Heart and lung: lower % with doses $\leq$ 20 Gy	PTV: low conformation Heart and lung: higher doses $\geq$ 40Gy
IMRT2	Inverse	Complex*	CLB: lower dose Heart and lung: lower % with doses $\leq$ 20 Gy	Complex planning PTV: low conformation Heart and lung: higher % with dose $\geq$ 25 Gy
IMRT5	Inverse	Complex*	PTV: better conformation Heart and lung: lower % with dose $\geq$ 30 Gy	Complex planning CLB, heart and lung: higher % with dose $\leq$ 20 Gy
DCART	Direct	Complex*	PTV: reasonable conformation	Complex planning CLB, heart and lung: higher % with dose $\leq$ 20 Gy

Besides studying the irradiation techniques, a comparison between different calculations was also performed. The calculation algorithm generally used for clinical purposes in this TPS is the Pencil Beam Convolution. Nonetheless, this analytical algorithm is, nowadays, not the most indicated for accurate dose calculations, due to the well-documented limitations referred throughout this dissertation [46, 49, 69–71]. In fact, this algorithm was inaccurate at determining doses in heterogeneous media and in build-up regions. Table 7.2 presents some considerations on the calculation algorithms used for dose calculation in this work.

TABLE 7.2: Calculation algorithms comparison. Main features of the algorithms used:PBC, iMC and EGSnrc MC.

	PBC	**iMC**	**EGSnrc MC**
Accuracy in homogeneous media	Acceptable (2% - 5%)	Good ($\leq$ 2%)	Good ($\leq$ 2%)
Accuracy in heterogeneous media	Not accurate ($\geq$ 5%)	Good ($\leq$ 2%)	Good ($\leq$ 2%)
Calculation time	Few min	30 - 60 min	hours - days

The MC algorithms presented some differences probably due to the different CT ramp used for the dose calculations. After this study, at the clinic we are doing a major effort to acquire the data for using another calculation algorithm, the AAA (Anisotropic Analytic Algorithm).
Concerning the PTV irradiation, there are significant differences (see figure 6.8), considering the different calculation algorithms:

- for all the techniques and variables investigated, iMC and EGSnrc MC present lower PTV coverage than the PBC predicted;
- in general, the EGSnrc MC predicted lower doses than the iMC;
- taking into consideration the $V_{95\%}$ as an irradiation quality parameter, IMRT5 is the technique with better PTV coverage, according to the MC techniques;
- considering PBC, f-IMRT is the technique with higher doses above 107% but considering the calculations with the MC algorithms, that does not seem to happen and there seem to exist no significant differences, considering this criteria;
- the EGSnrc MC and the iMC predict lower doses than the PBC for the 5% of PTV volume ($D_{5\%}$) that receive higher doses.

7.1.3 Dose in the CLB

In absolute dose values, considering the PBC algorithm, D_{mean}, the CLB receives 1.50 ± 0.39 Gy and 1.45 ± 0.38 Gy, for f-IMRT and IMRT2, respectively; whereas, the mean dose for the IMRT5 plans is 3.11 ± 2.25 Gy. For the MC algorithms, the results are similar, IMRT5 presenting at least twice more mean dose values than the tangential techniques. Concerning the CLB volume that receives at least 5 Gy, it increases from $2.44 \pm 1.61\%$ and $3.23 \pm 1.40\%$ for f-IMRT and IMRT2, respectively, to $19.46 \pm 21.58\%$, for the IMRT5, as determined using the EGSnrc MC algorithm (increasing about a factor of 6). Regarding the volume of CLB that receives at least 2 Gy, the considerations are similar, with IMRT5 having more contralateral healthy breast receiving this dose (eg. for the iMC calculations, for f-IMRT and IMRT2, $14.63 \pm 3.76\%$ and $13.89 \pm 5.11\%$ of right breast receive 2 Gy, whereas, for IMRT5 the CLB percentage is $40.59 \pm 36.37\%$).

Regarding the ultimate goal of this study, to conclude on CLB doses, according to the patient data results obtained for the different calculations algorithms, non-tangential techniques do increase the low doses in the OAR, mainly in the CLB 6. Special attention has to be addressed to this issue before going into more complex multi-beam incidence or arc techniques despite not being yet clear among the scientific community what the consequences of increasing the low doses in the CLB. It is therefore considered that despite better PTV homogeneity and conformity there is an increased risk of CLB cancer development, when using non-tangential techniques.

7.1.4 Usefulness of MC based TPS for breast cancer RT

Overall, the main findings reported in this thesis pinpoint the usefulness and powerful predictive power of the Monte Carlo methods in support of RT Treatment Planning Systems, allowing a more accurate dosimetric assessment therefore improving the dose delivery to the tumor volume and the efficacy and outcome of the treatments. They also seem to contribute to a better assessment of the dose in the OAR and to the healthy tissues surrounding the tumor volume therefore presumably contributing to decrease the risk of second cancer induction in those tissues and organs.

7.2 Limitations and difficulties

The topic of this work was an excuse for a much broader investigation on Monte Carlo techniques. Throughout this work, many difficulties were faced and overcome making the path to the final much more interesting. Many restrictions were made to the initial plan as it is not possible to include all the aspects in this investigation. The first decision was to investigate only breast cancer without axillary involvement due to the maximum field size of the Trilogy linac used throughout this investigation, not being wide enough to perform modulated fields larger than 22 cm in the head-feet direction. To investigate the arc rotation technique, it was necessary to use the iPlan BrainLAB TPS which does not permit the use of wedges (neither physical nor virtual ones). The path started to delineate itself with the constraints into equation.

The first real difficulty was, however, to obtain the accurate linac data to implement the linac model. However, with persistence and the fundamental help of Professor Doutor Pedro Vaz, we managed to obtain the data from Varian Medical Systems. Modeling and simulating the linac using Monte Carlo techniques is a very complex task which was accomplished with success. However, modeling and simulating the HDMLC using EGSnrc was a much more struggling and demanding, not initially planned task. However, this was the most rewarding goal accomplished due to the interest the EGSnrc responsibles have put into it. The model was already included in the last EGSnrc release; Varian also used the simulation results for their own propaganda of the MLC.

Investigating the CLB doses is also an extremely complex task due to the nature of the radiation involved: mainly low scattered doses mainly coming from linac head scatter, linac head leakage and patient scatter. Unfortunately we did not have an adequate breast phantom that gathered all the necessary aspects (breast shape, adequate for measurements, with heterogeneities) to perform all the measurements we initially aimed at. Several attempts were made to make such a phantom. We were fortunate to have a RandoAlderson breast phantom for a very short period of two weeks with which we were able to make a plaster mould and then perform the experiments mentioned in the previous chapters. The first try consisted on making a wax phantom; however, when we tried to cut the wax to put a film or a ionization chamber it broke and we did not succeed. We then tried with a suggestion from a biomaterials Professor trying to perform a bulk photopolymerization of methyl methacrylate but we did not succeed, either (probably because we did not have the

proper conditions to execute the procedure and the final product got too hard to cut). The next attempt was to make a gelatin/jelly phantom and it sort of worked until it melt just before the measurements. The vegetal fat phantom, made with V*égé*taline, was the most successful phantom we obtained. To perform a perfect straight cut was also difficult and that was when attending a conference in Seville, I heard about this phantom and Professor Antonio Leal from Universidad de Sevilla, Spain, was very kind in permitting to use it for two weeks.

7.3 Future work

There are still struggling questions to address related to breast cancer which are of major interest. Amongst them:

- The involvement of biological models seems to be most appropriate way to go to find out the influence of low doses in the CLB.
- The next challenging task is to prepare the EGSnrc MC to calculate dynamic arc conformal RT treatments and compare them with the TPS calculations.
- Another study of interest is to investigate the influence of breast implants and their influence on the calculations.
- Sensitivity and uncertainty analysis and studies of the parameters influencing the accuracy of existing MC TPS.
- Risk estimates of second cancer induction in the CLB or in other OAR, in breast cancer RT treatments.
- And others.

Appendix A

Statistical Tests

Friedman's Two-way Analysis of Variance by Ranks -- Analysis of k-Within-Group Data with a Quantitative Response Variable

Application: This statistic has two applications that can appear very different, but are really just two variations of the same statistical question. In one application the same quantitative variable is measured at two or more different times from the same sample (or from two or more samples that have been matched on one or more important variables). In the other application, two or more comparable quantitative variables are measured from the same sample (usually at the same time). In both applications, Friedman's test is used to compare the distributions of the two or more quantitative variables.

Thus, it is applied in the same data situation as an ANOVA for dependent samples except that it is used when the data are either from a too-small sample, are importantly non-normally distributed, or the measurement scale of the dependent variable is ordinal (not interval or ratio). It is important to remember the null hypothesis, and to differentiate it from the null for the dependent ANOVA.

There are two specific versions of the H0:, depending upon whether one characterizes the k conditions as representing a single population under two or more different circumstances (e.g., comparing treated vs. not treated or comparing different treatments -- some consider this a representation of two or more different populations) or as representing comparable variables measured from a single population (as in the example below). Here are versions of the H0: statement for each of these characterizations.

H0: The populations represented by the k conditions of the have the same distribution of scores.

To reject H0: is to say that the populations represented by the different conditions differ in some way, center, spread and/or shape. When the forms of the distributions from the two samples are similar (as is often the case -- check the size and symmetry of the IQR), then rejecting H0: is interpreted to mean that populations (or circumstances) tend to have some pattern of larger and smaller scores (different medians) among them.

H0: The population has the same distribution of scores on the different measures represented by the conditions.

To reject H0: is to say that the distributions of the variables are different in some way, center, spread and/or shape. When the forms of the distributions are similar (as is often the case -- check the size and symmetry of the IQR), then rejecting the H0: is interpreted to mean that the variables have some pattern of larger and smaller scores (medians) among them.

The data: In this analysis the one variable is the type of animal (fish, reptiles, or mammals), and the response variable is the number of animals on display. From our database, we use three variables **reptnum** (number of reptiles on display), **fishnum** (number of fishon display) and **mamlnum** (number of mammals on display). These scores are shown for the 12 stores below (reptnum, fishnum,).

```
12,32,34   14,41,38   15,31,45   12,38,32    7,21,12     4,13,11
10,17,22    4,22,9    14,24,20    4,11,8      5,17,19    10,20,8
```

Research Hypothesis: The data come from the Pet shop database. The researcher hypothesized that stores would tend to display more fish than other types of animals, fewer reptiles, and an intermediate number of mammals.

H0: for this analysis: Pet stores display the same number of reptiles, fish and mammals.

Step 1 Rearrange the data so that scores from each subject are in the appropriate columns, one for each condition.

reptnum	fishnum	mamlnum
12	32	34
14	41	38
15	31	45
12	38	32
7	21	12
4	13	11
10	17	22
4	22	9
14	24	20
4	11	8
5	17	19
10	20	8

Step 2 Rank order the scores SEPARATELY FOR EACH SUBJECT'S DATA with the smallest score getting a value of 1. If there are ties (within the scores for a subject) each receives the average rank they would have received.

reptnum	fishnum	mamlnum	rank reptnum	rank fishnum	rank mamlnum
12	32	34	1	2	3
14	41	38	1	3	2
15	31	45	1	2	3
12	38	32	1	3	2
7	21	12	1	3	2
4	13	11	1	3	2
10	17	22	1	2	3
4	22	9	1	3	2
14	24	20	1	3	2
4	11	8	1	3	2
5	17	19	1	2	3
10	20	8	2	3	1

Step 3 Compute the sum of the ranks for each condition.

rank reptnum	rank fishnum	rank mamlnum
1	2	3
1	3	2
1	2	3
1	3	2
1	3	2
1	3	2
1	2	3
1	3	2
1	3	2
1	3	2
1	2	3
2	3	1

$R_1 = 13$ $R_2 = 32$ $R_3 = 27$

Step 4 Determine the number of subjects.

$N = 12$

Step 5 Determine the number of conditions.

$k = 3$

Step 6 Compute Friedman's F, using the following formula (you should carry at least 3 decimals in these calculations).

$$F = \left[\frac{12}{[N * k * (k+1)]}\right] * \sum R^2 \; - \; [3 * N * (k + 1)]$$

$$= \left[\frac{12}{[12 * 3 * (3+1)]}\right] * [13^2 + 32^2 + 27^2] \; - \; [3 * 12 * (3 + 1)]$$

$$= \left[\frac{12}{144}\right] * [169 + 1024 + 729] \; - 144 \; = \; [.083*1922] - 144 \; = \; 15.526$$

For small samples (k < 6 AND N < 14):

Step 7 Determine the critical value of F by looking at the table of critical values for Friedman's test

$$F(k=3, N=12, \alpha = .05) \; = \; 8.67$$

Step 8 Compare the obtained F and the critical F values to determine whether to retain or reject the null hypothesis.

-- if the obtained F value (from Step 6) is larger than the critical value of F, then reject H0:

-- if the obtained F value is less than or equal to the critical value of F, then reject H0:

For the example data, we would decide to reject the null hypothesis, because the obtained value of F (15.526) is greater than the larger critical F value (8.67).

For large samples (k > 5 OR N > 13):

Step 9 Determine the critical value of F by looking at the table of critical values for the Chi-Square test (df = k - 1). (As an example, here is how you would apply this version of the significance test to these data.)

$$X^2 \text{ (df = 2, p=.05)} \; = \; 5.99$$

Step 10 Compare the obtained F and the critical X^2 values to determine whether to retain or reject the null hypothesis.

-- if the obtained F value (from Step 6) is less than or equal the critical value of X^2, then retain H0:

-- if the obtained F value is larger than the critical value of X^2, then reject H0:

For the example data, we would decide to reject the null hypothesis, because the obtained value of F (15.526) is greater than the larger critical X^2 value (5.99).

Step 11 IF you reject the null hypothesis, determine whether the pattern of the data completely supports, partially supports, or does not support the research hypothesis.

-- IF you reject the null hypothesis, AND if the pattern of data agrees exactly with the research hypothesis, then the research hypothesis is completely supported.

-- IF you reject the null hypothesis, AND if part of the pattern of the data agrees with the research hypothesis, BUT part of the pattern of the data does not, then the research hypothesis is partially supported.

-- IF you retain the null hypothesis, OR you reject the null BUT NO PART of the pattern of the data agrees with the research hypothesis, then the research hypothesis is not at all supported.

By the way: To properly determine whether the hypothesized pattern of differences was found, one should perform pairwise comparisons (using Friedman's test); the report of the results given below makes use of these follow-up tests (although the computations are not shown).

By the way: Usually the researcher hypothesizes that there is a difference between the conditions. Sometimes, however, the research hypothesis is that there is NO difference between the conditions. If so, the research hypothesis and H0: are the same! When this is the case, retaining H0: provides support for the research hypothesis, whereas rejecting H0: provides evidence that research hypothesis is incorrect.

For the example data, we would decide that the research hypothesis is partially supported, because the null hypothesis was rejected, and because, as hypothesized, there were fewer reptiles displayed than mammals or fish. However, there was not a significant difference between the number of fish and mammals displayed at these stores.

Step 12 Reporting the results

You will want to compute medians and IQR values to help describe the data before reporting the results of the significance test. With multiple-group designs it is often easier to present these data in a table. As for the other statistical tests, the report includes the "wordy" part and the statistical values based upon which you based your statistical decision. If you reject H0:, be sure to describe how the groups differed, rather than just reporting that there was "a difference".

Table 1 summarizes the data for the numbers of animals displayed at the stores. There was a significant difference among the distributions of the three types of animals (based on Friedman's test, $\underline{X}^2(2) = 15.526$, $\underline{p} = .0003$. Pairwise Friedman's tests ($\underline{p} < .05$) revealed that, as hypothesized, fewer reptiles were displayed than either fish or mammals. However, contrary to the research hypothesis, there was not a difference in the mean numbers of fish and mammals displayed.

Table 1
Summary of the number of animals of each type displayed in the pet stores.

	Type of Animal		
	Fish	Mammals	Reptiles
Mdn	21.50	19.50	10.00
Q1	17.00	9.50	4.25
Q3	31.75	33.50	13.50

Wilcoxin's Test -- Analysis of 2-Within-Group Data with a Quantitative Response Variable

Application: This statistic has two applications that can appear very different, but are really just two variations of the same statistical question. In one application the same quantitative variable is measured at two different times from the same sample (or from two samples that have been matched one or more important variables). In the other application, two comparable quantitative variables are measured from the same sample (usually at the same time). In both applications, Wilcoxin's test is used to compare the distributions of the two quantitative variables.

Thus, it is applied in the same data situation as a t-test or ANOVA for dependent samples except that it is used when the data are either from a too-small sample, are importantly non-normally distributed, or the measurement scale of the dependent variable is ordinal (not interval or ratio). There are two versions of the Wilcoxin test, one for small samples (i.e., N < 50, but some suggest N < 10), and one for large samples. It is important to remember the null hypothesis, and to differentiate it from the null for the dependent t-test.

There are two specific versions of the H0:, depending upon whether one characterizes the two conditions as representing a single population under two different circumstances (e.g., comparing treated vs. not treated or comparing two different treatments -- some consider this a representation of two different populations) or as representing comparable variables measured from a single population (as in the example below). Here are versions of the H0: statement for each of these characterizations.

H0: The two populations represented by the different conditions of the have the same distribution of scores.

To reject H0: is to say that the populations represented by the two conditions differ in some way, center, spread and/or shape. When the forms of the distributions from the two samples are similar (as is often the case -- check the size and symmetry of the IQR), then rejecting H0: is interpreted to mean that one population tends to have larger scores (or a larger median) than the other.

H0: The population represented by the sample has the same distribution of scores on the two different measures represented by the conditions.

To reject H0: is to say that the distributions of the variables are different in some way, center, spread and/or shape. When the forms of the distributions are similar (as is often the case -- check the size and symmetry of the IQR), then rejecting H0: is interpreted to mean that one variable tends to have larger scores (or a larger median) than the other.

The data: In this analysis "grouping" variable is the type of animal (reptiles or fishes), and the response variable is the quality rating. From our database, we use two variables **reptgood** (reptile quality rated on a 1-10 scale) and **fishgood** (fish quality rated on a 1-10 scale). These scores are shown for the 12 stores below (reptqual, fishqual).

```
2,6  8,5   9,3   7,3  4,7  7,9   4,9   4,8   5,6   9,9   7,7   2,8
```

Research Hypothesis: The researcher hypothesized that a store's fish would be of higher quality than its reptiles, because of the greater difficulty obtaining and maintaining healthy reptiles.

H0: for this analysis: The quality ratings of reptiles and fish displayed by pet stores have the same distributions.

Step 1 Rearrange the data so that scores from each subject are in the appropriate columns, one for each condition.

reptgood	fishgood
2	6
8	5
9	3
7	3
4	7
7	9
4	9
4	8
5	6
9	9
7	7
2	8

Step 2 For each pair of scores, compute the difference between the scores and then find the absolute value of this difference.

reptgood	fishgood	difference	absolute difference
2	6	-4	4
8	5	3	3
9	3	6	6
7	3	4	4
4	7	-3	3
7	9	-2	2
4	9	-5	5
4	8	-4	4
5	6	-1	1
9	9	0	0
7	7	0	0
2	8	-6	6

Step 3 Rank order the absolute differences, with the smallest absolute difference getting a value of 1. Cases with the same absolute difference each receive the average rank they would have received.

By the way: If an absolute difference has a value of 0, then the data from that subject is dropped from the analysis and the sample size is adjusted accordingly. Why? This statistical test is based upon comparisons of the number and direction of the inequalities in the data set (e.g., how many times reptgood > fishgood and how many times reptgood < fishgood), to determine if one variable has a different distribution than the other. Subjects for which reptgood = fishgood don't contribute to making this decision. What if there are several subjects with tied scores? The more subjects with tied scores (which are dropped), then it more difficult is to reject H0: -- which should make sense, since tied scores suggest that the distributions are equivalent.

reptgood	fishgood	difference	absolute difference	rank of absolute difference
2	6	-4	4	6
8	5	3	3	3.5
9	3	6	6	9.5
7	3	4	4	6
4	7	-3	3	3.5
7	9	-2	2	2
4	9	-5	5	8
4	8	-4	4	6
5	6	-1	1	1
9	9	0	0	--
7	7	0	0	--
2	8	-6	6	9.5

Step 4 Compute the signed rank absolute difference, as the rank of absolute difference (from 5th column)with the same sign as the difference (from 3rd column).

reptgood	fishgood	difference	absolute difference	rank of absolute difference	signed rank absolute difference
2	6	-4	4	6	-6
8	5	3	3	3.5	3.5
9	3	6	6	9.5	9.5
7	3	4	4	6	6
4	7	-3	3	3.5	-3.5
7	9	-2	2	2	-2
4	9	-5	5	8	-8
4	8	-4	4	6	-6
5	6	-1	1	1	-1
9	9	0	0	--	--
7	7	0	0	--	--
2	8	-6	6	9.5	-9.5

Step 5 Compute the sum of the positive signed rank absolute differences (T+) and the sum of the negative signed rank absolute differences (T-).

T+ = 3.5 + 9.5 + 6 = 19 T- = 6 + 3.5 + 2 + 8 + 6 + 1 + 9.5 = 36

Step 6 The summary statistic, called **W**, is the **SMALLER** of T+ and T-

W = 19

Step 7 Determine **N** as the number of subjects who contributed signed rank absolute difference values.

N = 10

For small samples (N < 50 -- though some suggest N < 10):

Step 8 Determine the critical values of W using the table.

With N = 10, the critical value of W (p = .05) is 8

Step 9 Compare the obtained W and the critical W values to determine whether to retain or reject the null hypothesis. **Be sure to notice that the decision rule for this statistics is "backwards" from most of the others -- smaller values of W are more likely to lead to rejecting H0: !!**

-- if the obtained W value (from Step 6) is **larger than** the critical value of W, then retain H0:

-- if the obtained W value is **less than or equal to** the critical value of W, then reject H0:

For the example data, we would decide to retain the null hypothesis, because the obtained value of W (19) is greater than the larger critical W value (10).

For large samples (one or both groups with N > 20):

Step 10 With samples this large, the value of W has approaches a normal distribution, and so the null hypothesis can be tested by a Z-test.

$$Z = \frac{W - (N*(N+1)/4)}{\sqrt{\frac{N*(N+1)*((2*N)+1)}{24}}} = \frac{19 - (10 * (10 + 1) / 4)}{\sqrt{\frac{10 * (10 + 1) * ((2*10) + 1)}{24}}}$$

$$= \frac{19 - 27.5}{\sqrt{2310 / 24}} = \frac{-8.5}{9.81} = -.87$$

Step 11 Compare the obtained Z value and the critical Z value to determine whether to retain or reject the null hypothesis.

-- if the absolute value of the obtained Z is less than 1.96, then retain H0:

-- if the absolute value of the obtained Z is greater than 1.696, then reject H0:

For the example data, we would decide to retain the null hypothesis, because the absolute value of the obtained Z (.87) is less than the critical value of 1.96.

For both small and large samples:

Step 12 IF you reject the null hypothesis, determine whether the data support or do not support the research hypothesis.

-- IF you reject the null hypothesis AND the condition that was hypothesized to have the larger scores does, then the research hypothesis is supported

-- IF you retain the null hypothesis OR you reject the null hypothesis BUT the condition that was hypothesized to have the larger scores actually has the smaller scores, then the research hypothesis is not supported.

By the way: Usually the researcher hypothesizes that there is a difference between the conditions. Sometimes, however, the research hypothesis is that there is NO difference between the conditions. If so, the research hypothesis and H0: are the same! When this is the case, retaining H0: provides support for the research hypothesis, whereas rejecting H0: provides evidence that research hypothesis is incorrect.

For the example data, we would decide that the research hypothesis is not supported, because the null hypothesis was retained.

Step 12 Reporting the results

As for the other statistical tests, the report includes the "wordy" part and the statistical values upon which the you made your statistical decision. Be sure to tell which condition tended to have the larger scores, and whether or not this agrees with the research hypothesis. You should compute sample medians and IQR values to help describe the data,

Contrary to the research hypothesis, there was no difference between the distribution of quality ratings given to fish (Mdn = 6.00, IQR = 4.00 - 7.75) and those given to reptiles (Mdn =7.00, IQR = 5.25 - 8.75) in these stores, based on Wilcoxin test, W = 19, p > .05.

Bibliography

[1] E Spezi and G Lewis. An overview of monte carlo treatment planning for radiotherapy. *Radiat Prot Dosim*, 131(1):123–9, 2008.

[2] GLOBOCAN. Estimated cancer incidence, mortality and prevalence worldwide in 2012, 2013. URL `http://globocaNiarCfr/Pages/fact_sheets_canceRaspx`. Accessed in 10 September 2013.

[3] E Farber. The multistep nature of cancer development. *Cancer Research*, 44:4417–23, 1984.

[4] JB Little. Radiation carcinogenesis. *Carcinogenesis*, 21(3):397–404, 2000.

[5] R Siegel, D Naishadham, and A Jemal. Cancer statistics, 2012. *CA: a cancer journal for clinicians*, 62:10–29, 2012.

[6] T Buchholz. Radiation therapy for early-stage breast cancer after breast-conserving surgery. *N Engl J Med*, 360(1):63–70, 2009.

[7] P Poortmans, M Aznar, and H Bartelink. Quality indicators for breast cancer: revisiting historical evidence in the context of technology changes. *Semin Radiat Oncol*, 22(1):29–39, 2012.

[8] J A Pina. *Anatomia humana dos orgaos*. LIDEL, 2004.

[9] C Haanen, C Mansfield, and J Jürgens. *Early breast cancer: its history and results of treatment*. Number voL 3 in Experimental biology and medicine. S Karger, 1976. URL `http://bookSgooglEpt/books?id=5OlPAQAAIAAJ`.

[10] B Fisher, J-H Jeong, S Anderson, J Bryant, E R Fisher, and N Wolmark. Twenty-five-year follow-up of a randomized trial comparing radical mastectomy, total mastectomy, and total mastectomy followed by irradiation. *N Engl J Med*, 347(8):567–75, 2002. doi: 10.1056/NEJMoa020128.

[11] AM Cotlar, JJ Dubose, and DM Rose. History of surgery for breast cancer: radical to the sublime. *Curr Surg*, 60(3):329, 2003.

[12] U Veronesi, N Cascinelli, L Mariani, M Greco, RO Saccozzi, A Luini, M Aguilar, and E Marubini. Twenty-year follow-up of a randomized study comparing breast-conserving surgery with radical mastectomy for early breast cancer. *N Engl J MEd*, 347(16):1227–32, 2002.

[13] B Fisher, S Anderson, J Bryant, R G Margolese, M Deutsch, E R Fisher, J-H Jeong, and N Wolmark. Twenty-year follow-up of a randomized trial comparing total mastectomy, lumpectomy, and lumpectomy plus irradiation for the treatment of invasive breast cancer. *N Engl J MEd*, 347(16):1233–41, 2002.

[14] V Vinh-Hung, C Verschraegen, and et al. Breast-conserving surgery with or without radiotherapy: pooled-analysis for risks of ipsilateral breast tumor recurrence and mortality. *J Nat Canc Inst*, 96(2):115–21, 2004.

[15] Radcliffe I CTSU. Effects of chemotherapy and hormonal therapy for early breast cancer on recurrence and 15-year survival: an overview of the randomised trials. *Lancet*, 365:1687–717, 2005.

[16] R Holland, S Veling, M Mravunac, and J Hendriks. Histologic multifocality of tis, t1-2 breast carcinomas implications for clinical trials of breast-conserving surgery. *Cancer*, 56(5):979–90, 1985.

[17] R Arriagada, MG Le, J-M Guinebretière, A Dunant, F Rochard, and T Tursz. Late local recurrences in a randomised trial comparing conservative treatment with total mastectomy in early breast cancer patients. *Annals of oncology*, 14(11):1617–22, 2003.

[18] M Poggi, D Danforth, L Sciuto, S Smith, S Steinberg, D Liewehr, C Menard, M Lippman, A Lichter, and R Altemus. Eighteen-year results in the treatment of early breast carcinoma with mastectomy versus breast conservation therapy. *Cancer*, 98(4):697–702, 2003.

[19] N Kroman, H Holtveg, J Wohlfahrt, M Jensen, H Mouridsen, M Blichert-Toft, and M Melbye. Effect of breast-conserving therapy versus radical mastectomy on prognosis for young women with breast carcinoma. *Cancer*, 100 (4):688–93, 2004.

[20] J Cuzick, H Stewart, R Peto, M Baum, B Fisher, H Host, JP Lythgoe, G Ribeiro, H Scheurlen, A Wallgren, et al. Overview of randomized trials of postoperative adjuvant radiotherapy in breast cancer. *Cancer treatment reports*, 71(1):15–29, 1987.

[21] M Horner, L Ries, M Krapcho, N Neyman, R Aminou, N Howlader, S Altekruse, E Feuer, L Huang, A Mariotto, et al. Seer cancer statistics review, 1975-2006, national cancer institute bethesda, md, 2009.

[22] K Maughan, M Lutterbie, P Ham, et al. Treatment of breast cancer. *Am Fam Physician*, 81(11):1339–46, 2010.

[23] G Lyman, A Giuliano, M Somerfield, A Benson, D Bodurka, H Burstein, A Cochran, H Cody, S Edge, S Galper, et al. American society of clinical oncology guideline recommendations for sentinel lymph node biopsy in early-stage breast cancer. *J Clin Oncol*, 23(30):7703–20, 2005.

[24] EA Strom, WA Woodward, A Katz, TA Buchholz, GH Perkins, A Jhingran, R Theriault, E Singletary, A Sahin, MD McNeese, et al. Clinical investigation: regional nodal failure patterns in breast cancer patients treated with mastectomy without radiotherapy. *Int J Radiat Oncol Biol Phys*, 63(5):1508, 2005.

[25] B Farrus, S Vidal-Sicart, M Velasco, G Zanon, PL Fernandez, M Munoz, G Santamaria, J Albanell, and A Biete. Incidence of internal mammary node metastases after a sentinel lymph node technique in breast cancer and its implication in the radiotherapy plan. *Int J Radiat Oncol Biol Phys*, 60 (3):715–721, 2004.

[26] CW Hurkmans, JH Borger, EJ Rutgers, and G van Tienhoven. Quality assurance of axillary radiotherapy in the EORTC AMAROS trial 10981/22023: the dummy run. *Radiother Oncol*, 68(3):233–40, 2003.

[27] O Abe, R Abe, and et al. Effects of radiotherapy and of differences in the extent of surgery for early breast cancer on local recurrence and 15-year survival: an overview of the randomised trials. *Lancet*, 366(9503):2087–106, 2005.

[28] G Viani, E Stefano, S Afonso, L De Fendi, F Soares, P Leon, and F Guimarães. Breast-conserving surgery with or without radiotherapy in women with ductal carcinoma in situ: a meta-analysis of randomized trials. *Radiat oncol*, 2(1):28–39, 2007.

[29] Radcliffe Infirmary CTSU. Effects of chemotherapy and hormonal therapy for early breast cancer on recurrence and 15-year survival: an overview of the randomised trials. *Lancet*, 365:1687–717, 2005.

[30] P Metcalfe, T Kron, and P Hoban. *Physics of Radiotherapy X-Rays and Electrons*. Med Phys Publishing, 2 edition, 2007.

[31] B S Teh, S Y Woo, and E B Butler. Intensity modulated radiation therapy (IMRT): a new promising technology in radiation oncology. *The Oncologist*, 4(6):433–42, 1999.

[32] L Cozzi, A Fogliata, A Bolsi, G Nicolini, and J Bernier. Three-dimensional conformal vs intensity-modulated radiotherapy in head-and-neck cancer patients: comparative analysis of dosimetric and technical parameters. *Int J Radiat Oncol Biol Phys*, 58(2):617–24, 2004.

[33] B Fraass, K Doppke, M Hunt, G Kutcher, G Starkschall, R Stern, and J Van Dyke. American association of physicists in medicine radiation therapy committee task group 53: quality assurance for clinical radiotherapy treatment planning. *Med Phys*, 25:1773–829, 1998.

[34] D Jones. ICRU report 50: Prescribing, recording and reporting photon beam therapy. *Med Phys*, 21:833, 1994.

[35] A Wambersie and T Landgerg. ICRU report 62: Prescribing, recording and reporting photon beam therapy. *ICRU Publication, Bethesda (MD)*, 1999.

[36] M Milano, L Constine, and P Okunieff. Normal tissue tolerance dose metrics for radiation therapy of major organs. *Semin Radiat Oncol*, 17:131–40, 2007.

[37] A Barret, J Dobbs, S Morris, and T Roques. *Practical Radiotherapy Planning*. Hodder Arnold, 4th edition, 2009.

[38] E Konefka and J Jassem. Complications of breast cancer radiotherapy. *Clin Oncol*, 18:229–35, 2006.

[39] L Constine, M Milano, D Friedman, M Morris, J Williams, P Rubin, and et al. *Perez and Brady's principles and practice of radiation oncology*. Wolters Kluwer Health Lippincott Williams Wilkins, 5th edition, 2008.

[40] International Atomic Energy Agency. Commissioning and quality assurance of computerized planning systems for radiation treatment of cancer. *Technical Reports Series*, 430, 2004.

[41] Anders Ahnesjö and Maria Mania Aspradakis. Dose calculations for external photon beams in radiotherapy. *Phys Med Biol*, 44(11):R99–155, 1999.

[42] J Venselaar, H Welleweerd, and B Mijnheer. Tolerances for the accuracy of photon beam dose calculations of treatment planning systems. *Radiother Oncol*, 60(2):191–201, 2001.

[43] JR Clarkson. A note on depth doses in fields of irregular shape. *British J Radiol*, 14(164):265–8, 1941.

[44] JR Cunningham. Scatter-air ratios. *Phys Med Biol*, 17(1):42–61, 1972.

[45] B Bjarngard, H Rashid, and C Obcemea. Separation of primary and scatter components of measured photon beam data. *Phys Med Biol*, 34(12):1939–45, 1989.

[46] A Boyer and E Mok. A photon dose distribution model employing convolution calculations. *Med Phys*, 12:169–77, 1985.

[47] R Mohan, C Chui, and L Lidofsky. Differential Pencil Beam dose computation model for photons. *Med Phys*, 13:64–73, 1986.

[48] A Ahnesjö. Collapsed cone convolution of radiant energy for photon dose calculation in heterogeneous media. *Med Phys*, 16:577–92, 1989.

[49] T Mackie, J Scrimger, and J Battista. A convolution method of calculating dose for 15-MV x rays. *Med Phys*, 12:188–97, 1985.

[50] W Ulmer, J Pyyry, and W Kaissl. A 3d photon superposition/convolution algorithm and its foundation on results of Monte Carlo calculations. *Phys Med Biol*, 50(8):1767–90, 2005.

[51] A Ahnesjö, P Andreo, and A Brahme. Calculation and application of point spread functions for treatment planning with high energy photon beams. *Acta Oncol*, 26(1):49–56, 1987.

[52] U Oelkfe and C Scholz. Dose calculation algorithms. *N Techn Radiat Oncol*, pages 187–96, 2006.

[53] A Mesbahi, D Thwaites, and A Reilly. Experimental and Monte Carlo evaluation of eclipse treatment planning system for lung dose calculations. *Rep Pract Oncol Radiother*, 11(3):123–33, 2006.

[54] DWO Rogers, BA Faddegon, GX Ding, C-M Ma, J We, and TR Mackie. Beam: A Monte Carlo code to simulate radiotherapy treatment units. *Med Phys*, 22:503–24, 1995.

[55] CM Ma, BA Faddegon, DWO Rogers, and TR Mackie. Accurate characterization of Monte Carlo calculated electron beams for radiotherapy. *Med Phys*, 24:401–16, 1997.

[56] C-M Ma and S B Jiang. Monte Carlo modelling of electron beams from medical accelerators. *Phys Med Biol*, 44(12):R157–89, 1999.

[57] I Chetty, JJ. DeMarco, and TD Solberg. A virtual source model for Monte Carlo modeling of arbitrary intensity distributions. *Med Phys*, 27:166–72, 2000.

[58] J Deng, S B Jiang, A Kapur, J Li, T Pawlicki, and CM Ma. Photon beam characterization and modelling for Monte Carlo treatment planning. *Phys Med Biol*, 45(2):411–27, 2000.

[59] I Chetty. Virtual source modelling in Monte Carlo-based clinical dose calculations: Methods and issues associated with their development and use. *Radiother Oncol*, 84:S38–9, 2007.

[60] S B Jiang, A L Boyer, and C-M Ma. Modeling the extrafocal radiation and monitor chamber backscatter for photon beam dose calculation. *Med Phys*, 28:55–66, 2001.

[61] JV Siebers, PJ Keall, JO Kim, and R Mohan. A method for photon beam Monte Carlo multileaf collimator particle transport. *Phys Med Biol*, 47(17): 3225–49, 2002.

[62] N Papanikolaou, J Battista, A Boyer, C Kappas, E Klein, T Mackie, M Sharpe, and J Dyk. Tissue inhomogeneity corrections for megavoltage photon beams. *American Association of Physicists in Medicine*, Report 85, 2004.

[63] A Mesbahi. The effect of electronic disequilibrium on the received dose by lung in small fields with photon beams: Measurements and Monte Carlo study. *Iran J Radiat Res*, 6(2):70–6, 2008.

[64] S Webb and R Fox. Verification by Monte Carlo methods of power law tar algorithm for inhomogeneity corrections in photon beam dose calculations. *Phys Med Biol*, 25:225–40, 1980.

[65] E El-Khatib and J Battista. Improved lung dose calculation using tissue-maximum ratios in the batho correction. *Med Phys*, 11:279–86, 1984.

[66] MR Sontag and JR Cunningham. Corrections to absorbed dose calculations for tissue inhomogeneities. *Med Phys*, 4:431–6, 1977.

[67] CM Ma, T Pawlicki, SB Jiang, JS Li, J Deng, E Mok, A Kapur, L Xing, L Ma, and AL Boyer. Monte Carlo verification of IMRT dose distributions from a commercial treatment planning optimization system. *Phys Med Biol*, 45(9):2483–95, 2000.

[68] L Wang, C-S Chui, and M Lovelock. A patient-specific Monte Carlo dose-calculation method for photon beams. *Med Phys*, 25:867–78, 1998.

[69] G Cranmer-Sargison, WA Beckham, and IA Popescu. Modelling an extreme water-lung interface using a single Pencil Beam algorithm and the Monte Carlo method. *Phys Med Biol*, 49(8):1557–67, 2004.

[70] T Knoos, Anders Ahnesjo, P Nilsson, and L Weber. Limitations of a Pencil Beam approach to photon dose calculations in lung tissue. *Phys Med Biol*, 40(9):1411–20, 1995.

[71] E Wieslander and T Knöös. A virtual linear accelerator for verification of treatment planning systems. *Phys Med Biol*, 45(10):2887–96, 2000.

[72] I Gagne and S Zavgorodni. Evaluation of the analytical anisotropic algorithm (AAA) in an extreme water-lung interface phantom using Monte Carlo dose calculations. *J Appl Clin Med Phys*, 8(1):33–46, 2007.

[73] E Sterpin, M Tomsej, B De Smedt, N Reynaert, and S Vynckier. Monte Carlo evaluation of the AAA treatment planning algorithm in a heterogeneous multilayer phantom and IMRT clinical treatments for an Elekta SL25 linear accelerator. *Med Phys*, 34:1665–77, 2007.

[74] P Andreo, M Huq, M Westermark, H Song, A Tilikidis, L DeWerd, and K Shortt. Protocols for the dosimetry of high-energy photon and electron beams: a comparison of the IAEA TRS-398 and previous international codes of practice. *Phys Med Biol*, 47(17), 2002.

[75] T Aland, T Kairn, and J Kenny. Evaluation of a gafchromic ebt2 film dosimetry system for radiotherapy quality assurance. *Austral Phys Eng Sc Med*, 34(2):251–60, 2011.

[76] IM Sobol, R Messer, J Stone, and P Fortini. *The Monte Carlo method*. University of Chicago Press, 1974.

[77] P Andreo. Monte Carlo techniques in medical radiation physics. *Phys Med Biol*, 36(7):861–920, 1991.

[78] R C McCall, R D McIntyre, and W G Turnbull. Improvement of linear accelerator depth-dose curves. *Med Phys*, 5:518–24, 1978.

[79] JP Patau, CE Vernes, M Terrissol, and M Malbert. Calcul des caracteristiques qualitatives (tel, fq, equivalent de dose) d'un faisceau de photons de freinage a usage medical, par simulation de sa creation et de son transport. In *ProC the 6th Symposium on Microdosimetry*, pages 579–88, 1978.

[80] B Nilsson and A Brahme. Contamination of high-energy photon beams by scattered photons. *Strahlenther*, 157(3):181–6, 1981.

[81] R Mohan, C Chui, and L Lidofsky. Energy and angular distributions of photons from medical linear accelerators. *Med Phys*, 12:592–7, 1985.

[82] F Verhaegen and J Seuntjens. Monte Carlo modelling of external radiotherapy photon beams. *Phys Med Biol*, 48(21):R107–64, 2003.

[83] WR Nelson, H Hirayama, D W O Rogers, and Stanford Linear Accelerator Center. *The EGS4 Code System*. Stanford Linear Accelerator Center, 1985.

[84] I Kawrakow. Accurate condensed history Monte Carlo simulation of electron transport I. EGSnrc, the new EGS4 version. *Med Phys*, 27:485–98, 2000.

[85] J Sempau, E Acosta, J Baro, JM Fernández-Varea, and F Salvat. An algorithm for Monte Carlo simulation of coupled electron-photon transport. *Nucl Inst Meth Phys Res Sect B: BEAM Interactions with Materials and Atoms*, 132(3):377–90, 1997.

[86] J F Briesmeister and et aL. MCNPTM-A general Monte Carlo N-particle transport code. *Version 4C, LA-13709-M, Los Alamos National Laboratory*, 2000.

[87] S Agostinelli, J Allison, K Amako, J Apostolakis, H Araujo, P Arce, M Asai, D Axen, S Banerjee, G Barrand, et al. GEANT4—a simulation toolkit. *Nucl Inst Methods Phys Res Sect A: Accelerators, Spectrometers, Detectors and Associated Equipment*, 506(3):250–303, 2003.

[88] G Marsaglia and W W Tsang. The ziggurat method for generating random variables. *Journal of Statistical Software*, 5(8):1–7, 2000.

[89] G EP Box and M E Muller. A note on the generation of random normal deviates. *The Annals of Mathematical Statistics*, 29(2):610–1, 1958.

[90] J Seco and F Verhaegen. *Monte Carlo Techniques in Radiation Therapy*. Imaging in Medical Diagnosis and Therapy. Taylor & Francis Group, 2013. ISBN 9781466507920.

[91] DWO Rogers, B Walters, and I Kawrakow. BEAMnrc users manual, report PIRS-0509(A) revK. Technical report, Research Council of Canada, 2005.

[92] I Kawrakow, D W O Rogers, and B R B Walters. Large efficiency improvements in BEAMnrc using directional bremsstrahlung splitting. *Med Phys*, 31(10):2883–98, 2004.

[93] I Kawrakow and M Fippel. Investigation of variance reduction techniques for Monte Carlo photon dose calculation using XVMC. *Phys Med Biol*, 45 (8):2163–83, 2000.

[94] I Sheikh-Bagheri, Dand Kawrakow, B Walters, and DWO Rogers. Monte Carlo simulations: Efficiency improvement techniques and statistical considerations. *Integrating new technologies into the clinic: Monte Carlo and image-guided radiation therapy, Proceedings of the 2006 AAPM Summer SchooL Madison, WI: Med Phys Publishing*, pages 71–91, 2006.

[95] BRB Walters, I Kawrakow, and DWO Rogers. History by history statistical estimators in the BEAM code system. *Med Phys*, 29:2745–52, 2002.

[96] R L Ford and W R Nelson. Egs code system: computer programs for the Monte Carlo simulation of electromagnetic cascade showers version 3. Technical report, Stanford Linear Accelerator Center, CA (USA), 1978.

[97] A F Bielajew, R Mohan, and C-S Chui. Improved bremsstrahlung photon angular sampling in the EGS4 code system. *Natl Res Council of Canada Report PIRS-0203*, 1989.

[98] DMJ Lovelock, CS Chui, and R Mohan. A Monte Carlo model of photon beams used in radiation therapy. *Med Phys*, 22:1387–94, 1995.

[99] FH Attix. *Gamma- and X-Ray Interactions in Matter*. A Wiley-Interscience Publication, 1986.

[100] L Storm and H I Israel. Photon cross sections from 1 kev to 100 mev for elements¡ i¿ z¡/i¿= 1 to¡ i¿ z¡/i¿= 100. *Atomic Data and Nuclear Data Tables*, 7(6):565–681, 1970.

[101] J H Hubbell and I Øverbø. Relativistic atomic form factors and photon coherent scattering cross sections. *J Phys Chem Ref Data*, 8:69–106, 1979.

[102] MJ Berger and JH Hubbell. *XCOM, Photon cross sections on a personal computer*. The Bureau, 1987.

[103] Fritz Sauter. Über den atomaren photoeffekt in der k-schale nach der relativistischen wellenmechanik diracs. *Annalen der Physik*, 403(4):454–88, 1931.

[104] R Ribberfors. Relationship of the relativistic Compton cross section to the momentum distribution of bound electron states. *Phys Rev B*, 12:2067–4, 1975.

[105] JW Motz, Haakon A Olsen, and HW Koch. Pair production by photons. *Rev Modern Phys*, 41(4):581–639, 1969.

[106] M J Berger. Monte Carlo calculation of the penetration and diffusion of fast charged particles. *Meth Comput Phys*, 1:135–215, 1963.

[107] DWO Rogers. Monte Carlo techniques in radiotherapy. *Physics in Canada*, 58(2):63–70, 2002.

[108] P J Keall, J V Siebers, B Libby, and R Mohan. Determining the incident electron fluence for Monte Carlo-based photon treatment planning using a standard measured data set. *Med Phys*, 30:574–82, 2003.

[109] B de Smedt, N Reynaert, F Flachet, M Coghe, MG Thompson, L Paelinck, G Pittomvils, C De Wagter, W De Neve, and H Thierens. Decoupling initial electron beam parameters for Monte Carlo photon beam modelling by removing beam-modifying filters from the beam path. *Phys Med Biol*, 50 (24):5935–51, 2005.

[110] D Sheikh-Bagheri and DWO Rogers. Sensitivity of megavoltage photon beam Monte Carlo simulations to electron beam and other parameters. *Med Phys*, 29:379–90, 2002.

[111] EL Chaney, TJ Cullip, and TA Gabriel. A Monte Carlo study of accelerator head scatter. *Med Phys*, 21:1383–90, 1994.

[112] J Mazurier, F Salvat, B Chauvenet, and J Barthe. Original papers-simulation of photon BEAMs from a Saturne 43 accelerator using the code PENELOPE. *Phys Med*, 15(3):101–10, 1999.

[113] CL Hartmann Siantar, RS Walling, TP Daly, B Faddegon, N Albright, P Bergstrom, AF Bielajew, C Chuang, D Garrett, RK House, and et al. Description and dosimetric verification of the PEREGRINE Monte Carlo dose calculation system for photon beams incident on a water phantom. *Med Phys*, 28:1322–37, 2001.

[114] D Sheikh-Bagheri and DWO Rogers. Monte Carlo calculation of nine megavoltage photon beam spectra using the BEAM code. *Med Phys*, 29:391–402, 2002.

[115] J Van de Walle, C Martens, N Reynaert, H Palmans, M Coghe, W De Neve, C De Wagter, and H Thierens. Monte Carlo model of the Elekta SLiplus accelerator: validation of a new MLC component module in BEAM for a 6 MV beam. *Phys Med Biol*, 48(3):371–85, 2003.

[116] J Pena, D González-Castaño, F Gómez, F Sánchez-Doblado, and G Hartmann. Automatic determination of primary electron beam parameters in Monte Carlo simulation. *Med Phys*, 34:1076–84, 2007.

[117] G X Ding. Energy spectra, angular spread, fluence profiles and dose distributions of 6 and 18 MV photon beams: results of Monte Carlo simulations for a Varian 2100EX accelerator. *Phys Med Biol*, 47(7):1025–46, 2002.

[118] J Sempau, A Sanchez-Reyes, F Salvat, H Oulad ben Tahar, SB Jiang, and JM Fernández-Varea. Monte Carlo simulation of electron beams from an accelerator head using PENELOPE. *Phys Med Biol*, 46(4):1163–86, 2001.

[119] C M Ma and D W O Rogers. BEAMdp users manual, nrcc report pirs-0509(c) reva. Technical report, Research Council of Canada, 2009.

[120] H H Liu, T R Mackie, and E C McCullough. Modeling photon output caused by backscattered radiation into the monitor chamber from collimator jaws using a Monte Carlo technique. *Med Phys*, 27:737–44, 2000.

[121] F Verhaegen, R Symonds-Tayler, H H Liu, and A E Nahum. Backscatter towards the monitor ion chamber in high-energy photon and electron BEAMs: charge integration versus Monte Carlo simulation. *Phys Med Biol*, 45(11): 3159–70, 2000.

[122] B Walters, I Kawrakow, and DWO Rogers. DOSXYZnrc users manual, report PIRS-794 revB. Technical report, Research Council of Canada, 2005.

[123] C Borges, N Teixeira, and P Vaz. Use of Monte Carlo simulations to assess contralateral breast doses in breast cancer treatments). In *ProC Second European Workshop on Monte Carlo Treatment Planning*, 2009.

[124] D A Jaffray, J J Battista, A Fenster, and P Munro. X-ray sources of medical linear accelerators: Focal and extra-focal radiation. *Med Phys*, 20:1417–27, 1993.

[125] A Tzedakis, J E Damilakis, M Mazonakis, J Stratakis, H Varveris, and N Gourtsoyiannis. Influence of initial electron beam parameters on Monte Carlo calculated absorbed dose distributions for radiotherapy photon beams. *Med Phys*, 31:907–13, 2004.

[126] E Tonkopi, MR McEwen, BRB Walters, and I Kawrakow. Influence of ion chamber response on in-air profile measurements in megavoltage photon-beams. *Med Phys*, 32:2918–27, 2005.

[127] W R Lutz, N Maleki, and B E Bjärngard. Evaluation of a beam-spot camera for megavoltage x rays. *Med Phys*, 15:614, 1988.

[128] P Munro, JA Rawlinson, and A Fenster. Therapy imaging: Source sizes of radiotherapy beams. *Med Phys*, 15:517–24, 1988.

[129] E Loewenthal, E Loewinger, E Bar-Avraham, and G Barnea. Measurement of the source size of a 6-and 18-MV radiotherapy linac. *Med Phys*, 19:687–90, 1992.

[130] V W Huang, J Seuntjens, S Devic, and F Verhaegen. Experimental determination of electron source parameters for accurate Monte Carlo calculation of large field electron therapy. *Phys Med Biol*, 50(5):779–86, 2005.

[131] BA Faddegon and I Blevis. Electron spectra derived from depth dose distributions. *Med Phys*, 27:514–26, 2000.

[132] C Borges, M Zarza-Moreno, E Heath, N Teixeira, and P Vaz. Monte Carlo modeling and simulations of the High Definition (HD120) micro MLCand validation against measurements for a 6 MV beam. *Med Phys*, 39(1):415–23, 2012.

[133] E Heath and J Seuntjens. Development and validation of a BEAMnrc component module for accurate Monte Carlo modelling of the Varian dynamic Millennium multileaf collimator. *Phys Med Biol*, 48(24):4045–63, 2003.

[134] H H Liu, F Verhaegen, and L Dong. A method of simulating dynamic multileaf collimators using Monte Carlo techniques for intensity-modulated radiation therapy. *Phys Med Biol*, 46(9):2283–98, 2001.

[135] N Tyagi, J M Moran, D W Litzenberg, A F Bielajew, B A Fraass, and I J Chetty. Experimental verification of a Monte Carlo-based MLC simulation model for IMRT dose calculation. *Med Phys*, 34:651 – Abstract, 2007.

[136] G Gagliardi, I Lax, S Söderström, G Gyenes, and LE Rutqvist. Prediction of excess risk of long-term cardiac mortality after radiotherapy of stage i breast cancer. *Radiother Oncol*, 46(1):63–71, 1998.

[137] SC Darby, M Ewertz, P McGale, AM Bennet, U Blom-Goldman, D Brønnum, C Correa, D Cutter, G Gagliardi, B Gigante, et al. Risk of ischemic heart disease in women after radiotherapy for breast cancer. *N Engl J Med*, 368(11):987–98, 2013.

[138] J Jassem. Favourable and unfavourable effects on long-term survival of radiotherapy for early breast cancer: an overview of the randomised trials early breast cancer trialists collaborative group. *Lancet*, 355(9217):1757–70, 2000.

[139] Y Belkacemi, JM Comet, Band Hannoun-Levi, S Villette, H Marsiglia, M Leblanc-Onfroy, B Delalande, D Azria, JB Dubois, and et al. [accelerated partial breast irradiation: a concept to individualize treatment in breast cancer]. *Cancer radiotherapie: journal de la Société française de radiotherapie oncologique*, 11(6-7):287, 2007.

[140] BD Smith, DW Arthur, TA Buchholz, BG Haffty, CA Hahn, PH Hardenbergh, TB Julian, LB Marks, DA Todor, FA Vicini, and et al. Accelerated partial breast irradiation consensus statement from the american society for radiat oncol (astro). *Int J Radiat Oncol Biol Phys*, 74(4):987–1001, 2009.

[141] BV Offersen, M Overgaard, N Kroman, and J Overgaard. Accelerated partial breast irradiation as part of breast conserving therapy of early breast carcinoma: a systematic review. *Radiother Oncol*, 90(1):1–13, 2009.

[142] M Mannino and J Yarnold. Accelerated partial breast irradiation trials: Diversity in rationale and design. *Radiother Oncol*, 91(1):16–22, 2009. doi: 10.1016/JradonC2008.12.011.

[143] D J Sher, E Wittenberg, A G Taghian, J R Bellon, and R S Punglia. Partial breast irradiation versus whole breast radiotherapy for early-stage breast

cancer: a decision analysis. *Int J Radiat Oncol Biol Phys*, 70(2):469–76, 2008.

[144] D W Arthur, M M Morris, and F A Vicini. Breast cancer: new radiation treatment options. *Oncol*, 18(13):1621, 2004.

[145] B D Smith, S M Bentzen, C R Correa, C A Hahn, P H Hardenbergh, and et al. Fractionation for whole breast irradiation: An american society for radiat oncol (astro) evidence-based guideline. *Int J Radiat Oncol Biol Phys*, 81(1):59–68, 2011.

[146] T Edlund and D Gannett. A single isocenter technique using ct-based planning in the treatment of breast cancer. *Med Dosim*, 24(4):239–45, 1999.

[147] W Xiaochun, T K Yu, M Salehpour, S X Zhang, T L Sun, and T A Buchholz. Breast cancer regional radiation fields for supraclavicular and axillary lymph node treatment: is a posterior axillary boost field technique optimal? *Int J Radiat Oncol Biol Phys*, 74(1), 2009.

[148] Y M Kirova, V Servois, F Campana, R Dendale, M A Bollet, F Laki, N Fournier-Bidoz, and A Fourquet. Ct-scan based localization of the internal mammary chain and supra clavicular nodes for breast cancer radiation therapy planning. *Radiother Oncol*, 79(3):310–5, 2006.

[149] C Hurkmans, J Borger, B Pieters, N Russell, E Jansen, and B Mijnheer. Variability in target volume delineation on ct scans of the breast. *Int J Radiat Oncol Biol Phys*, 50(5):1366–72, 2001.

[150] E Weiss and C F Hess. The impact of gross tumor volume (gtv) and clinical target volume (ctv) definition on the total accuracy in radiotherapy. *Strahlenther Onkol*, 179(1):21–30, 2003.

[151] P Romestaing, Y Lehingue, C Carrie, R Coquard, X Montbarbon, J Ardiet, N Mamelle, and J Gerard. Role of a 10-gy boost in the conservative treatment of early breast cancer: results of a randomized clinical trial in lyon, france. *J Clin Oncol*, 15(3):963–8, 1997.

[152] H Bartelink, J Horiot, P Poortmans, H Struikmans, W Van den Bogaert, A Fourquet, J Jager, W Hoogenraad, S Oei, C Wárlám-Rodenhuis, et al. Impact of a higher radiation dose on local control and survival in breast-conserving therapy of early breast cancer: 10-year results of the randomized boost versus no boost eortc 22881-10882 trial. *J Clin Oncol*, 25(22):3259–65, 2007.

[153] H Bartelink, JC Horiot, P Poortmans, H Struikmans, W Van den Bogaert, I Barillot, A Fourquet, J Borger, J Jager, W Hoogenraad, L Collette, M Pierart, European, Treatment, and Breast C Groups. Recurrence rates after treatment of breast cancer with standard radiotherapy with or without additional radiation. *N Engl J Med*, 345(19):1378–1387, 2001.

[154] N Reynaert, S Van Der Marck, D Schaart, W Van der Zee, C Van Vliet-Vroegindeweij, M Tomsej, J Jansen, B Heijmen, M Coghe, and C De Wagter. Monte Carlo treatment planning for photon and electron beams. *Radiat Phys Chem*, 76(4):643–86, 2007.

[155] I Kawrakow, M Fippel, and K Friedrich. 3D electron dose calculation using a voxel based Monte Carlo algorithm (VMC). *Med Phys*, 23:445–57, 1996.

[156] M Fippel, I Kawrakow, and K Friedrich. Electron BEAM dose calculations with the VMC algorithm and the verification data of the NCI working group. *Phys Med Biol*, 42(3):501–20, 1997.

[157] M Fix, P Keall, K Dawson, and J Siebers. Monte Carlo source model for photon beam radiotherapy: photon source characteristics. *Med Phys*, 31: 3106–21, 2004.

[158] N Tyagi, W Martin, J Du, AF Bielajew, and I J Chetty. A proposed alternative to phase-space recycling using the adaptive kernel density estimator method. *Med Phys*, 33:553–60, 2006.

[159] E Heath, J Seuntjens, and D Sheikh-Bagheri. Dosimetric evaluation of the clinical implementation of the first commercial IMRT Monte Carlo treatment planning system at 6MV. *Med Phys*, 31:2771–9, 2004.

[160] JE Cygler, C Lochrin, GM Daskalov, M Howard, R Zohr, B Esche, L Eapen, L Grimard, and JM Caudrelier. Clinical use of a commercial Monte Carlo treatment planning system for electron beams. *Phys Med Biol*, 50(5):1029–34, 2005.

[161] P Pemler, J Besserer, U Schneider, and H Neuenschwander. Evaluation of a commercial electron treatment planning system based on Monte Carlo techniques (eMC). *Zeitschrift für medizinische Physik*, 16(4):313–29, 2006.

[162] E Spezi, DG Lewis, and CW Smith. Monte Carlo simulation and dosimetric verification of radiotherapy beam modifiers. *Phys Med Biol*, 46(11):3007–29, 2001.

[163] D Grofsmid, M Dirkx, H Marijnissen, E Woudstra, and B Heijmen. Dosimetric validation of a commercial Monte Carlo based IMRT planning system. *Med Phys*, 37:540–9, 2010.

[164] A Leal, F Sánchez-Doblado, R Arráns, J Roselló, E Pavón, and J Lagares. Routine IMRT verification by means of an automated Monte Carlo simulation system. *Int J Radiat Oncol Biol Phys*, 56(1):58–68, 2003.

[165] C Boudreau, E Heath, J Seuntjens, O Ballivy, and W Parker. IMRT head and neck treatment planning with a commercially available Monte Carlo based planning system. *Phys Med Biol*, 50(5):879–90, 2005.

[166] CL Hartmann Siantar, RS Walling, TP Daly, B Faddegon, N Albright, Paul Bergstrom, AF Bielajew, C Chuang, D Garrett, RK House, et al. Description and dosimetric verification of the PEREGRINE Monte Carlo dose calculation system for photon beams incident on a water phantom. *Med Phys*, 28: 1322–37, 2001.

[167] JE Cygler, GM Daskalov, GH Chan, and GX Ding. Evaluation of the first commercial Monte Carlo dose calculation engine for electron BEAM treatment planning. *Med Phys*, 31:142–53, 2004.

[168] H Neuenschwander and E Born. A macro Monte Carlo method for electron beam dose calculations. *Phys Med Biol*, 37(1):107–25, 1992.

[169] G Ding, D Duggan, C Coffey, P Shokrani, and J Cygler. First macro Monte Carlo based commercial dose calculation module for electron beam treatment planning—new issues for clinical consideration. *Phys Med Biol*, 51(11):2781–99, 2006.

[170] R Popple, R Weinberg, J Antolak, S Ye, P Pareek, J Duan, S Shen, and I Brezovich. Comprehensive evaluation of a commercial macro Monte Carlo electron dose calculation implementation using a standard verification data set. *Med Phys*, 33:1540–51, 2006.

[171] J Sempau, S Wilderman, and A Bielajew. DPM, a fast, accurate Monte Carlo code optimized for photon and electron radiotherapy treatment planning dose calculations. *Phys Med Biol*, 45(8):2263–91, 2000.

[172] M Fragoso, S Pillai, T Solberg, and I Chetty. Experimental verification and clinical implementation of a commercial Monte Carlo electron beam dose calculation algorithm. *Med Phys*, 35:1028–38, 2008.

[173] F Salvat, J M Fernández-Varea, and J Sempau. PENELOPE-2006: A code system for Monte Carlo simulation of electron and photon transport. In *Workshop Proceedings*, volume 4, page 7, 2006.

[174] M Fippel. Fast Monte Carlo dose calculation for photon beams based on the VMC electron algorithm. *Med Phys*, 26:1466–75, 1999.

[175] M Fippel. Efficient particle transport simulation through beam modulating devices for Monte Carlo treatment planning. *Med Phys*, 31:1235–42, 2004.

[176] M Fippel, I Kawrakow, and K Friedrich. Electron beam dose calculations with the VMC algorithm and the verification data of the NCI working group. *Phys Med Biol*, 42(3):501–20, 1997.

[177] M Fippel, W Laub, B Huber, and F Nüsslin. Experimental investigation of a fast Monte Carlo photon BEAM dose calculation algorithm. *Phys Med Biol*, 44(12):3039–54, 1999.

[178] M Fippel, F Haryanto, O Dohm, F Nüsslin, and S Kriesen. A virtual photon energy fluence model for Monte Carlo dose calculation. *Med Phys*, 30:301–11, 2003.

[179] BrainLAB Technical Guide. Technical reference guide revision 1.0. In *BrainLAB Physics*, 2008.

[180] J Kim, J Siebers, P Keall, and R Arnfield, Mand Mohan. A Monte Carlo study of radiation transport through multileaf collimators. *Med Phys*, 28: 2497–506, 2001.

[181] L Wang, E Yorke, and C-S Chui. Monte Carlo evaluation of 6 MV intensity modulated radiotherapy plans for head and neck and lung treatments. *Med Phys*, 29:2705 – Abstract, 2002.

[182] P Francescon, S Cora, and P Chiovati. Dose verification of an IMRT treatment planning system with the BEAM EGS4-based Monte Carlo code. *Med Phys*, 30:144 – Abstract, 2003.

[183] P Carrasco, N Jornet, MA Duch, V Panettieri, L Weber, T Eudaldo, M Ginjaume, and M Ribas. Comparison of dose calculation algorithms in slab phantoms with cortical bone equivalent heterogeneities. *Med Phys*, 34:3323 – Abstract, 2007.

[184] T Künzler, I Fotina, M Stock, and D Georg. Experimental verification of a commercial Monte Carlo-based dose calculation module for high-energy photon BEAMs. *Phys Med Biol*, 54(24):7363–77, 2009.

[185] M Fragoso, N Wen, Sh Kumar, D Liu, S Ryu, B Movsas, A Munther, and IJ Chetty. Dosimetric verification and clinical evaluation of a new commercially available Monte Carlo-based dose algorithm for application in stereotactic body radiation therapy (SBRT) treatment planning. *Phys Med Biol*, 55(16):4445–64, 2010.

[186] I Ali, O Algan, S Thompson, T Herman, and S Ahmad. MO-E-204B-06: Comparative study of dose calculations using the BrainLAB Pencil BEAM and Monte Carlo dose algorithms. *Med Phys*, 37:3360 – Abstract, 2010.

[187] AL Petoukhova, K van Wingerden, RGJ Wiggenraad, PJM van de Vaart, J van Egmond, EM Franken, and JPC van Santvoort. Verification measurements and clinical evaluation of the iPlan rt Monte Carlo dose algorithm for 6 MV photon energy. *Phys Med Biol*, 55(16):4601 – Abstract, 2010.

[188] I Das, E Yangand, S Bednar, M Ewing, K Hutchins, M Cao, P Johnstone, and J Andrews. Factors affecting contralateral breast dose in radiation treatment of breast cancer. *Int J Radiat Oncol Biol Phys*, 78(3):S224, 2010.

[189] B Zurl, H Stranzl, P Winkler, and K Kapp. Quantification of contralateral breast dose and risk estimate of radiation induced contralateral breast cancer among young women using tangential fields and different modes of breathing. *Int J Radiat Oncol Biol Phys*, 85(2):500–5, 2013.

[190] W Warlick, J O'Rear, L Earley, J Moeller, D Gaffney, and D Leavitt. Dose to the contralateral breast: a comparison of two techniques using the enhanced dynamic wedge versus a standard wedge. *Med Dosim*, 22(3):185–91, 1997.

[191] B McParland. The effect of a dynamic wedge in the medial tangential field upon the contralateral breast dose. *Int J Radiat Oncol Biol Phys*, 19(6): 1515–20, 1990.

[192] T Woo, J-P Pignol, E Rakovitch, T Vu, D Hicks, P OBrien, and K Pritchard. Body radiation exposure in breast cancer radiotherapy: impact of breast IMRT and virtual wedge compensation techniques. *Int J Radiat Oncol Biol Phys*, 65(1):52–8, 2006.

[193] L Cozzi, A Fogliata, G Nicolini, T Rancati, and J Bernier. Breast irradiation with three conformal photon fields for patients with high lung involvement. *Acta Oncol*, 43(6):558–66, 2004.

[194] A Fogliata, A Bolsi, and L Cozzi. Critical appraisal of treatment techniques based on conventional photon beams, intensity modulated photon beams and proton beams for therapy of intact breast. *Radiother Oncol*, 62(2):137–145, 2002.

[195] F-M Kong, E Klein, J Bradley, D Mansur, M Taylor, C Perez, R Myerson, and W Harms. The impact of central lung distance, maximal heart distance, and radiation technique on the volumetric dose of the lung and heart for intact breast radiation. *Int J Radiat Oncol Biol Phys*, 54(3):963–71, 2002.

[196] Intensity Modulated Radiation Therapy Collaborative Working et al. Intensity-modulated radiotherapy: current status and issues of interest. *Int J Radiat Oncol Biol Phys*, 51(4):880–914, 2001.

[197] A Brahme. Optimization of stationary and moving beam radiation therapy techniques. *Radiother Oncol*, 12(2):129–40, 1988.

[198] C-S Chui and S V Spirou. Inverse planning algorithms for external beam radiation therapy. *Med Dosim*, 26(2):189–97, 2001.

[199] C Thieke, S Nill, U Oelfke, and T Bortfeld. Acceleration of intensity-modulated radiotherapy dose calculation by importance sampling of the calculation matrices. *Med Phys*, 29:676–81, 2002.

[200] D Shepard, M Earl, X Li, S Naqvi, and C Yu. Direct aperture optimization: a turnkey solution for step-and-shoot IMRT. *Med Phys*, 29:1007–18, 2002.

[201] W Que. Comparison of algorithms for multileaf collimator field segmentation. *Med Phys*, 26:2390–6, 1999.

[202] S Webb. Optimization of conformal radiotherapy dose distributions by simulated annealing: II. inclusion of scatter in the 2D technique. *Phys Med Biol*, 36(9):1227–37, 1991.

[203] R Mohan and T Bortfeld. The potential and limitations of IMRT: A physicists point of view. In *Image-Guided IMRT*, pages 11–8. Springer, 2006.

[204] H V James, C D Scrase, and A J Poynter. Practical experience with intensity-modulated radiotherapy. *Brit J Radiol*, 77(913):3–14, 2004.

[205] L L Kestin, M B Sharpe, R C Frazier, F A Vicini, D Yan, R C Matter, A A Martinez, and J W Wong. Intensity modulation to improve dose uniformity with tangential breast radiotherapy: initial clinical experience. *Int J Radiat Oncol Biol Phys*, 48(5):1559–68, 2000.

[206] B C Cho, C Hurkmans, E Damen, L J Zijp, and B J Mijnheer. Intensity modulated versus non-intensity modulated radiotherapy in the treatment of the left breast and upper internal mammary lymph node chain: a comparative planning study. *Radiother Oncol*, 62(2):127–136, 2002.

[207] C-S Chui, L Hong, M Hunt, and B McCormick. A simplified intensity modulated radiation therapy technique for the breast. *Med Phys*, 29:522–9, 2002.

[208] E Donovan, N Bleackley, P Evans, S Reise, and J Yarnold. Dose-position and dose-volume histogram analysis of standard wedged and intensity modulated treatments in breast radiotherapy. *Brit J Radiol*, 75(900):967–73, 2002.

[209] E Donovan, N Bleakley, E Denholm, P Evans, L Gothard, J Hanson, C Peckitt, S Reise, G Ross, G Sharp, and et al. Randomised trial of standard 2d radiotherapy (rt) versus intensity modulated radiotherapy (IMRT) in patients prescribed breast radiotherapy. *Radiother Oncol*, 82(3):254–64, 2007.

[210] M Oliver, J Chen, E Wong, J V Dyk, and F Perera. A treatment planning study comparing whole breast radiation therapy against conformal, IMRT and tomotherapy for accelerated partial breast irradiation. *Radiother Oncol*, 82(3):317–323, 2007.

[211] R Selvaraj, S Beriwal, R Pourarian, Rand Lalonde, A Chen, K Mehta, G Brunner, K Wagner, N Yue, S Huq, et al. Clinical implementation of tangential field intensity modulated radiation therapy (IMRT) using sliding window technique and dosimetric comparison with 3d conformal therapy (3dcrt) in breast cancer. *Med Dosim*, 32(4):299–304, 2008.

[212] J Herrick, C Neill, and P Rosser. A comprehensive clinical 3-dimensional dosimetric analysis of forward planned IMRT and conventional wedge planned techniques for intact breast radiotherapy. *Med Dosim*, 33(1):62–70, 2008.

[213] G C Barnett, J Wilkinson, A M Moody, C B Wilson, R Sharma, S Klager, A C Hoole, N Twyman, N G Burnet, and C E Coles. A randomised controlled trial of forward-planned radiotherapy (IMRT) for early breast cancer:

baseline characteristics and dosimetry results. *Radiother Oncol*, 92(1):34–41, 2009.

[214] B Cho, M Schwarz, B Mijnheer, and H Bartelink. Simplified intensity-modulated radiotherapy using pre-defined segments to reduce cardiac complications in left-sided breast cancer. *Radiother Oncol*, 70(3):231–41, 2004.

[215] C Mayo, M Urie, and T Fitzgerald. Hybrid IMRT plans—concurrently treating conventional and IMRT beams for improved breast irradiation and reduced planning time. *Int J Radiat Oncol Biol Phys*, 61(3):922–32, 2005.

[216] V Ludwig, F Schwab, M Guckenberger, T Krieger, and M Flentje. Comparison of wedge versus segmented techniques in whole breast irradiation. *Strahlenther Onkol*, 184(6):307–12, 2008.

[217] Á. Gulybán, P Kovács, Z Sebestyén, R Farkas, T Csere, G Karácsonyi, K Dérczy, K Hideghéty, and O Ésik. Multisegmented tangential breast fields: a rational way to treat breast cancer. *Strahlenther Onkol*, 184(5):262–9, 2008.

[218] N Richmond, R Turner, P Dawes, G Lambert, and G Lawrence. Evaluation of the dosimetric consequences of adding a single asymmetric or mlc shaped field to a tangential breast radiotherapy technique. *Radiother Oncol*, 67(2): 165–70, 2003.

[219] B van Asselen, C Raaijmakers, P Hofman, and J Lagendijk. An improved breast irradiation technique using three-dimensional geometrical information and intensity modulation. *Radiother Oncol*, 58(3):341–7, 2001.

[220] B Zackrisson, M Arevärn, and M Karlsson. Optimized mlc-beam arrangements for tangential breast irradiation. *Radiother Oncol*, 54(3):209–12, 2000.

[221] MA Earl, DM Shepard, S Naqvi, XA Li, and CX Yu. Inverse planning for intensity-modulated arc therapy using direct aperture optimization. *Phys Med Biol*, 48(8):1075–89, 2003.

[222] S Webb. Direct aperture optimization for a variable aperture collimator for intensity-modulated radiation therapy. *Phys Med Biol*, 49(5):N47–55, 2004.

[223] G Zhang, Z Jiang, D Shepard, B Zhang, and C Yu. Direct aperture optimization of breast IMRT and the dosimetric impact of respiration motion. *Phys Med Biol*, 51(20):N357–69, 2006.

[224] A Boyer and C Yu. Intensity-modulated radiation therapy with dynamic multileaf collimators. In *Semin Radiat Oncol*, volume 9, pages 48–59, 1999.

[225] S Webb. Intensity-modulated radiation therapy: dynamic MLC (DMLC) therapy, multisegment therapy and tomotherapy an example of QA in DMLC therapy. *Strahlenther Onkol*, 174:8–12, 1998.

[226] M L Cavey, J E Bayouth, E J Endres, J M Pena, M Colman, and S Hatch. Dosimetric comparison of conventional and forward-planned intensity-modulated techniques for comprehensive locoregional irradiation of post-mastectomy left breast cancers- abstract. *Med Dosim*, 30(2):107, 2005.

[227] F A Vicini, M Sharpe, L Kestin, A Martinez, C K Mitchell, M F Wallace, R Matter, and J Wong. Optimizing breast cancer treatment efficacy with intensity-modulated radiotherapy. *Int J Radiat Oncol Biol Phys*, 54(5):1336–44, 2002.

[228] L Hong, M Hunt, C Chui, S Spirou, K Forster, H Lee, J Yahalom, G Kutcher, B McCormick, et al. Intensity-modulated tangential beam irradiation of the intact breast. *Int J Radiat Oncol Biol Phys*, 44(5):1155–64, 1999.

[229] T Ercan, Ş. İğdem, G Alço, F Zengin, S Atilla, M Dinçer, and S Okkan. Dosimetric comparison of field in field intensity-modulated radiotherapy technique with conformal radiotherapy techniques in breast cancer. *Jap J Radiol*, 28(4):283–9, 2010.

[230] E E Ahunbay, G-P Chen, S Thatcher, P A Jursinic, J White, K Albano, and X A Li. Direct aperture optimization–based intensity-modulated radiotherapy for whole breast irradiation. *Int J Radiat Oncol Biol Phys*, 67(4): 1248–58, 2007.

[231] R Singla, S King, K Albuquerque, S Creech, and N Dogan. Simultaneous-integrated boost intensity-modulated radiation therapy (sib-IMRT) in the treatment of early-stage left-sided breast carcinoma. *Med Dosim*, 31(3):190–6, 2006.

[232] C C Popescu, I Olivotto, V Patenaude, E Wai, and W A Beckham. Inverse-planned, dynamic, multi-beam, intensity-modulated radiation therapy (IMRT): a promising technique when target volume is the left breast and internal mammary lymph nodes. *Med Dosim*, 31(4):283–91, 2007.

[233] A Fogliata, G Nicolini, M Alber, M .and Asell, B Dobler, M El-Haddad, B Hardemark, U Jelen, A Kania, M Larsson, and et al. IMRT for breast a planning study. *Radiother Oncol*, 76(3):300–10, 2005.

[234] C W Hurkmans, B C Cho, E Damen, L Zijp, and B J Mijnheer. Reduction of cardiac and lung complication probabilities after breast irradiation using conformal radiotherapy with or without intensity modulation. *Radiother Oncol*, 62(2):163–71, 2002.

[235] A Whitton, P Warde, M Sharpe, T K Oliver, K Bak, K Leszczynski, S Etheridge, K Fleming, E Gutierrez, L Favell, and et al. Organisational standards for the delivery of intensity-modulated radiation therapy in ontario. *Clin Oncol*, 21(3):192–203, 2009.

[236] C Yu. Intensity-modulated arc therapy with dynamic multileaf collimation: an alternative to tomotherapy. *Phys Med Biol*, 40(9):1435–49, 1995.

[237] D Shepard, D Cao, M Afghan, and M Earl. An arc-sequencing algorithm for intensity modulated arc therapy. *Med Phys*, 34:464–70, 2007.

[238] L Cozzi, K A Dinshaw, S K Shrivastava, U Mahantshetty, R Engineer, D D Deshpande, SV Jamema, E Vanetti, A Clivio, G Nicolini, et al. A treatment planning study comparing volumetric arc modulation with rapidarc and fixed field IMRT for cervix uteri radiotherapy. *Radiother Oncol*, 89(2):180–91, 2008.

[239] IM Gagne, W Ansbacher, S Zavgorodni, C Popescu, and WA Beckham. A Monte Carlo evaluation of rapidarc dose calculations for oropharynx radiotherapy. *Phys Med Biol*, 53(24):7167–85, 2008.

[240] S Johansen, L Cozzi, and D R Olsen. A planning comparison of dose patterns in organs at risk and predicted risk for radiation induced malignancy in the contralateral breast following radiation therapy of primary breast using conventional, IMRT and volumetric modulated arc treatment techniques. *Acta Oncol*, 48(4):495–503, 2009.

[241] E Vanetti, A Clivio, G Nicolini, A Fogliata, S Ghosh-Laskar, J Pr Agarwal, Ritu R Upreti, A Budrukkar, V Murthy, D D Deshpande, et al. Volumetric modulated arc radiotherapy for carcinomas of the oro-pharynx, hypopharynx and larynx: a treatment planning comparison with fixed field IMRT. *Radiother Oncol*, 92(1):111–7, 2009.

[242] J Zimmerman, S Korreman, G Persson, H Cattell, M Svatos, A Sawant, R Venkat, D Carlson, and P Keall. Dmlc motion tracking of moving targets for intensity modulated arc therapy treatment-a feasibility study. *Acta Oncol*, 48(2):245–50, 2009.

[243] A van't Riet, A Mak, M Moerland, L Elders, and W van der Zee. A conformation number to quantify the degree of conformality in brachytherapy and external BEAM irradiation: application to the prostate. *Int J Radiat Oncol Biol Phys*, 37(3):731–6, 1997.

[244] I Kawrakow, E Mainegra-Hing, D W O Rogers, F Tessier, and B Walters. The EGSnrc code system: Monte Carlo simulation of electron and photon transport. *NRCC Report PIRS-701, National Research Council Canada, Ottawa*, 2011.

[245] C Scholz. *Development and evaluation of advanced dose calculations for modern radiation therapy.* PhD thesis, Doctoral dissertation, PhD thesis, 2004.

[246] S Kim, C Liu, T Zhu, and J Palta. Photon beam skin dose analyses for different clinical setups. *Med Phys*, 25:860–6, 1998.

[247] P Carrasco, N Jornet, MA Duch, L Weber, M Ginjaume, T Eudaldo, D Jurado, A Ruiz, and M Ribas. Comparison of dose calculation algorithms in phantoms with lung equivalent heterogeneities under conditions of lateral electronic disequilibrium. *Med Phys*, 31:2899–911, 2004.

[248] B Fernandéz. *Aplicación de haces combinados de fotones y electrones modulados para el tratamiento radioterápico conservador de cáncer de mama.* PhD thesis, Department of Fisiología Médica y Biofísica, Faculdad de Medicina, Universidad de Sevilla, Spain, 2012.

[249] E Spezi, DG Lewis, and CW Smith. A dicom-rt-based toolbox for the evaluation and verification of radiotherapy plans. *Phys Med Biol*, 47(23):4223–32, 2002.

[250] J Deasy, A Blanco, and V Clark. Cerr: a computational environment for radiotherapy research. *Med Phys*, 30:979–85, 2003.

[251] W Nelson and Y Namito. The egs4 code system: solution of gamma-ray and electron transport problems. In *Presented at the International Conference on Supercomputing in Nuclear Applications, Mito City, Japan, 12-16 MaR 1990*, volume 1, pages 12–6, 1990.

[252] D Low, W Harms, S Mutic, and J Purdy. A technique for the quantitative evaluation of dose distributions. *Med Phys*, 25:656–61, 1998.

[253] T Depuydt, A Van Esch, and D Huyskens. A quantitative evaluation of IMRT dose distributions: refinement and clinical assessment of the gamma evaluation. *Radiother Oncol*, 62(3):309–19, 2002.

[254] E Spezi and D Lewis. Gamma histograms for radiotherapy plan evaluation. *Radiother Oncol*, 79(2):224–30, 2006.

[255] A Bakai, M Alber, and F Nüsslin. A revision of the γ-evaluation concept for the comparison of dose distributions. *Phys Med Biol*, 48(21):3543–53, 2003.

[256] S Korreman, J Medin, and F Kjaer-Kristoffersen. Dosimetric verification of rapidarc treatment delivery. *Acta Oncol*, 48(2):185–91, 2009.

[257] T Knöös, L Ahlgren, and M Nilsson. Comparison of measured and calculated absorbed doses from tangential irradiation of the breast. *Radiother Oncol*, 7 (1):81–8, 1986.

[258] V Panettieri, P Barsoum, M Westermark, L Brualla, and I Lax. AAA and pbc calculation accuracy in the surface build-up region in tangential beam treatments phantom and breast case study with the Monte Carlo code penelope. *Radiother Oncol*, 93(1):94–101, 2009.

[259] S Yoo, Q Wu, J O'Daniel, J Horton, and F Yin. Comparison of 3d conformal breast radiation treatment plans using the anisotropic analytical algorithm and Pencil Beam convolution algorithm. *Radiother Oncol*, 103(2):172–7, 2012.

[260] T Krieger and O Sauer. Monte Carlo-versus pencil-beam-/collapsed-cone-dose calculation in a heterogeneous multi-layer phantom. *Phys Med Biol*, 50 (5):859–68, 2005.

[261] A Fogliata, E Vanetti, D Albers, C Brink, A Clivio, T Knöös, G Nicolini, and L Cozzi. On the dosimetric behaviour of photon dose calculation algorithms in the presence of simple geometric heterogeneities: comparison with Monte Carlo calculations. *Phys Med Biol*, 52(5):1363–85, 2007.

[262] M Tubiana. Can we reduce the incidence of second primary malignancies occurring after radiotherapy? a critical review. *Radiother Oncol*, 91(1):4–15, 2009.

[263] E Hall and C Wuu. Radiation-induced second cancers: the impact of 3d-crt and IMRT. *Int J Radiat Oncol Biol Phys*, 56(1):83–8, 2003.

[264] A Joosten, F Bochud, S Baechler, F Levi, RO Mirimanoff, and R Moeckli. Variability of a peripheral dose among various linac geometries for second cancer risk assessment. *Phys Med Biol*, 56(16):5131–50, 2011.

[265] L Cozzi, F Buffa, and A Fogliata. Dosimetric features of linac head and phantom scattered radiation outside the clinical photon beam: experimental measurements and comparison with treatment planning system calculations. *Radiother Oncol*, 58(2):193–200, 2001.

[266] R M Howell, S B Scarboro, S Kry, and D Z Yaldo. Accuracy of out-of-field dose calculations by a commercial treatment planning system. *Phys Med Biol*, 55(23):6999–7008, 2010.

[267] X Xu, B Bednarz, and H Paganetti. A review of dosimetry studies on external-beam radiation treatment with respect to second cancer induction. *Phys Med Biol*, 53(13):R193–241, 2008.

[268] N Chofor, D Harder, A Rühmann, K Willborn, T Wiezorek, and B Poppe. Experimental study on photon-beam peripheral doses, their components and some possibilities for their reduction. *Phys Med Biol*, 55(14):4011–27, 2010.

[269] S Kry, U Titt, F Pönisch, D Followill, O Vassiliev, R White, R Mohan, and M Salehpour. A Monte Carlo model for calculating out-of-field dose from a varian 6 mv beam. *Med Phys*, 33:4405–13, 2006.

[270] J Lehmann, R Stern, T Daly, D Rocke, C Schwietert, G Jones, M Arnold, C Siantar, and Z Goldberg. Dosimetry for quantitative analysis of the effects of low-dose ionizing radiation in radiation therapy patients. *Radiat Res*, 165 (2):240–7, 2006.

[271] B Bednarz and X Xu. Monte Carlo modeling of a 6 and 18 mv varian clinac medical accelerator for in-field and out-of-field dose calculations: development and validation. *Phys Med Biol*, 54(4):N43–57, 2009.

[272] D Pierce, Y Shimizu, D L Preston, M Vaeth, and K Mabuchi. Studies of the mortality of atomic bomb survivors report 12, part i cancer: 1950-1990. *Radiat Res*, 146(1):1–27, 1996.

[273] D Preston, Y Shimizu, D Pierce, Ao Suyama, and K Mabuchi. Studies of mortality of atomic bomb survivors report 13: Solid cancer and noncancer disease mortality: 1950-1997. *Radiat Res*, 160(4):381–407, 2003.

[274] D Preston, D Pierce, Y Shimizu, H Cullings, S Fujita, S Funamoto, and K Kodama. Effect of recent changes in atomic bomb survivor dosimetry on cancer mortality risk estimates. *Radiat Res*, 162(4):377–89, 2004.

[275] D Brenner, R Doll, D Goodhead, E Hall, C Land, J Little, J Lubin, D Preston, R Preston, J Puskin, et al. Cancer risks attributable to low doses of ionizing radiation: assessing what we really know. *Proc Natl Acad Sc*, 100 (24):13761–6, 2003.

[276] L Travis, D Hill, G Dores, M Gospodarowicz, F van Leeuwen, E Holowaty, B Glimelius, M Andersson, T Wiklund, C Lynch, et al. Breast cancer following radiotherapy and chemotherapy among young women with hodgkin disease. *JAMA: J Am Med Assoc*, 290(4):465–75, 2003.

[277] L Kenney, Y Yasui, P Inskip, S Hammond, J Neglia, A Mertens, A Meadows, D Friedman, L Robison, and L Diller. Breast cancer after childhood cancer: a report from the childhood cancer survivor study. *Annals Intern Med*, 141 (8):590–7, 2004.

[278] J Perkins, Y Liu, P Mitby, J Neglia, S Hammond, M Stovall, A Meadows, R Hutchinson, Z Dreyer, L Robison, et al. Nonmelanoma skin cancer in survivors of childhood and adolescent cancer: a report from the childhood cancer survivor study. *J Clin Oncol*, 23(16):3733–41, 2005.

[279] W Cahan, H Woodard, N Higinbotham, F Stewart, and B Coley. Sarcoma arising in irradiated bone. *Cancer*, 82(1):8–34, 1998.

[280] M Stovall, S Smith, and M Rosenstein. Tissue doses from radiotherapy of cancer of the uterine cervix. *Med Phys*, 16:726–33, 1989.

[281] R Roychoudhuri, H Evans, D Robinson, and H Møller. Radiation-induced malignancies following radiotherapy for breast cancer. *Brit J Canc*, 91(5): 868–72, 2004.

[282] B Fowble, A Hanlon, G Freedman, N Nicolaou, and P Anderson. Second cancers after conservative surgery and radiation for stages i–ii breast cancer: identifying a subset of women at increased risk. *Int J Radiat Oncol Biol Phys*, 51(3):679–90, 2001.

[283] T Grantzau, L Mellemkjaer, and J Overgaard. Second primary cancers after adjuvant radiotherapy in early breast cancer patients: a national population based study under the danish breast cancer cooperative group (dbcg). *Radiother Oncol*, 106:42–9, 2013.

[284] X Gao, S Fisher, and B Emami. Risk of second primary cancer in the contralateral breast in women treated for early-stage breast cancer: a population-based study. *Int J Radiat Oncol Biol Phys*, 56(4):1038–45, 2003.

[285] L Bertelsen, L Bernstein, J Olsen, and et aL. Effect of systemic adjuvant treatment on risk for contralateral breast cancer in the women's environment, cancer and radiation epidemiology study. *J Natl Cancer Inst*, 100(1):32–40, 2008.

[286] G Freedman, P Anderson, A Hanlon, D Eisenberg, and N Nicolaou. Pattern of local recurrence after conservative surgery and whole-breast irradiation. *Int J Radiat Oncol Biol Phys*, 61(5):1328–36, 2005.

[287] D Brenner. Contralateral second breast cancers: prediction and prevention. *J Natl Cancer Inst*, 102(7):444–5, 2010.

[288] O Abe, R Abe, K Enomoto, K Kikuchi, H Koyama, Y Nomura, K Sakai, K Sugimachi, T Tominaga, J Uchino, and et al. Tamoxifen for early breast cancer: an overview of the randomised trials. *Lancet*, 351(9114):1451–67, 1998.

[289] B Fisher, J Costantino, D Wickerham, C Redmond, M Kavanah, W Cronin, V Vogel, A Robidoux, N Dimitrov, J Atkins, and et al. Tamoxifen for prevention of breast cancer: report of the national surgical adjuvant breast and bowel project p-1 study. *J Natl Canc Inst*, 90(18):1371–88, 1998.

[290] Early Breast Cancer Trialists Collaborative Group. Ovarian ablation in early breast cancer: overview of the randomised trials. *Lancet*, 348(9036):1189–96, 1996.

[291] L Hartmann, D Schaid, J Woods, T Crotty, J Myers, P Arnold, P Petty, T Sellers, J Johnson, S McDonnell, and et al. Efficacy of bilateral prophylactic mastectomy in women with a family history of breast cancer. *N Engla J Med*, 340(2):77–84, 1999.

[292] D Brenner, I Shuryak, Sa Russo, and R Sachs. Reducing second breast cancers: a potential role for prophylactic mammary irradiation. *J Clin Oncol*, 25(31):4868–72, 2007.

[293] J Kurtz, R Amalric, H Brandone, Y Ayme, and J Spitalier. Contralateral breast cancer and other second malignancies in patients treated by breast-conserving therapy with radiation. *Int J Radiat Oncol Biol Phys*, 15(2): 277–84, 1988.

[294] E Obedian, D Fischer, and B Haffty. Second malignancies after treatment of early-stage breast cancer: lumpectomy and radiation therapy versus mastectomy. *J Clin Oncol*, 18(12):2406–12, 2000.

[295] A Khan and B Haffty. The location of contralateral breast cancers after radiation therapy. *The Breast Journal*, 7(5):331–6, 2001.

[296] B Hankey, R Curtis, M Naughton, and J Boice, Jand Flannery. A retrospective cohort analysis of second breast cancer risk for primary breast cancer patients with an assessment of the effect of radiation therapy. *J Natl Canc Inst*, 70(5):797–804, 1983.

[297] P Horn, W Thompson, and S Schwartz. Factors associated with the risk of second primary breast cancer: an analysis of data from the connecticut tumor registry. *J Chronic Dis*, 40(11):1003–11, 1987.

[298] R Parker, P Grimm, and J Enstrom. Contralateral breast cancers following treatment for initial breast cancers in women. *Am J Clin Oncol*, 12(3):213–6, 1989.

[299] J Bernstein, W Thompson, N Risch, and T Holford. Risk factors predicting the incidence of second primary breast cancer among women diagnosed with a first primary breast cancer. *American journal of epidemiology*, 136(8): 925–36, 1992.

[300] B Yadav, S Sharma, F Patel, S Ghoshal, and R Kapoor. Second primary in the contralateral breast after treatment of breast cancer. *Radiother Oncol*, 86(2):171–6, 2008.

[301] E Harvey and L Brinton. Second cancer following cancer of the breast in connecticut, 1935-82. *Natl Canc Inst Monogr*, 68:99–112, 1985.

[302] R Murakami, T Hiyama, A Hanai, and I Fujimoto. Second primary cancers following female breast cancer in osaka, japan—a population-based cohort study. *Jap J Clin Oncol*, 17(4):293–302, 1987.

[303] C Hill-Kayser, E Harris, W Hwang, and L Solin. Twenty-year incidence and patterns of contralateral breast cancer after breast conservation treatment with radiation. *Int J Radiat Oncol Biol Phys*, 66(5):1313–19, 2006.

[304] J Boice, E Harvey, M Blettner, M Stovall, and J Flannery. Cancer in the contralateral breast after radiotherapy for breast cancer. *N Engl J Med*, 326 (12):781–5, 1992.

[305] VE Basco, AJ Coldman, JM Elwood, and ME Young. Radiation dose and second breast cancer. *Brit J Canc*, 52(3):319–25, 1985.

[306] H Storm, M Andersson, J Boice, M Blettner, M Stovall, H Mouridsen, P Dombernowsky, C Rose, A Jacobsen, and M Pedersen. Adjuvant radiotherapy and risk of contralateral breast cancer. *J Natl Canc Inst*, 84(16): 1245–50, 1992.

[307] M Stovall, S Smith, B Langholz, J Boice, R Shore, M Andersson, T Buchholz, M Capanu, L Bernstein, C Lynch, et al. Dose to the contralateral breast from radiotherapy and risk of second primary breast cancer in the wecare study. *Int J Radiat Oncol Biol Phys*, 72(4):1021–30, 2008.

[308] B Fraass, P Roberson, and A Lichter. Dose to the contralateral breast due to primary breast irradiation. *Int J Radiat Oncol Biol Phys*, 11(3):485–97, 1985.

[309] C Kelly, X Wang, J Chu, and W Hartsell. Dose to contralateral breast: a comparison of four primary breast irradiation techniques. *Int J Radiat Oncol Biol Phys*, 34(3):727–32, 1996.

[310] S Chang, K Deschesne, T Cullip, S Parker, and J Earnhart. A comparison of different intensity modulation treatment techniques for tangential breast irradiation. *Int J Radiat Oncol Biol Phys*, 45(5):1305–14, 1999.

[311] Y Borghero, M Salehpour, M McNeese, M Stovall, S Smith, J Johnson, G Perkins, E Strom, J Oh, S Kirsner, et al. Multileaf field-in-field forward-planned intensity-modulated dose compensation for whole-breast irradiation is associated with reduced contralateral breast dose: a phantom model comparison. *Radiother Oncol*, 82(3):324–8, 2007.

[312] J Burmeister, N Alvarado, A Way, P McDermott, T Bossenberger, H Jaenisch, R Patel, and T Washington. Assessment and minimization of contralateral breast dose for conventional and intensity modulated breast radiotherapy. *Med Dosim*, 33(1):6–13, 2008.

[313] Á Gulybán, P Kovács, Z Sebestyén, Rt Farkas, T Csere, G Karácsonyi, K Dérczy, K Hideghéty, and O Ésik. Multisegmented tangential breast fields: a rational way to treat breast cancer. *Strahlenther Onkol*, 184(5):262–9, 2008.

[314] S Saur, LMB Fjellsboe, T Lindmo, and J Frengen. Contralateral breast doses measured by film dosimetry: tangential techniques and an optimized IMRT technique. *Phys Med Biol*, 54(15):4743–58, 2009.

[315] M Hooning, B Aleman, M Hauptmann, M Baaijens, J Klijn, R Noyon, M Stovall, and F van Leeuwen. Roles of radiotherapy and chemotherapy in the development of contralateral breast cancer. *J Clin Oncol*, 26(34):5561–8, 2008.

[316] B Haffty. Radiation therapy and the risk of contralateral breast cancer. *Int J Radiat Oncol Biol Phys*, 56(4):920–1, 2003.

[317] J Pignol, B Keller, and A Ravi. Doses to internal organs for various breast radiation techniques - implications on the risk of secondary cancers and cardiomyopathy. *Radiat Oncol*, 6(5):1–6, 2011.

[318] C Weides, E Mok, W Chang, D Findley, and C Shostak. Evaluating the dose to the contralateral breast when using a dynamic wedge versus a regular wedge. *Med Dosim*, 20(4):287–93, 1996.

[319] S Kry, M Salehpour, D Followill, M Stovall, D Kuban, R White, and I Rosen. The calculated risk of fatal secondary malignancies from intensity-modulated radiation therapy. *Int J Radiat Oncol Biol Phys*, 62(4):1195–203, 2005.

[320] A Bhatnagar, E Brandner, D Sonnik, A Wu, S Kalnicki, M Deutsch, and D Heron. Intensity modulated radiation therapy (IMRT) reduces the dose to the contralateral breast when compared to conventional tangential fields for primary breast irradiation. *Breast Canc Res Treat*, 96(1):41–46, 2006.

[321] I Jurkovic, W Bice, A Sadeghi, M Sims, and B Prestidge. The dosimetric superiority of inverse planned {IMRT} compared to 3d whole breast irradiation techniques. *Int J Radiat Oncol Biol Phys*, 69(3, Supplement):S226, 2007.

[322] CM Ma, M Ding, JS Li, MC Lee, T Pawlicki, and J Deng. A comparative dosimetric study on tangential photon beams, intensity-modulated radiation therapy (IMRT) and modulated electron radiotherapy (mert) for breast cancer treatment. *Phys Med Biol*, 48(7):909–24, 2003.

[323] RJ Epstein, SA Kelly, M Cook, A Bateman, I Paddick, KC Kam, P Dunn, IW Hanham, RG Dale, and PM Price. Active minimisation of radiation scatter during breast radiotherapy: management implications for young patients with good-prognosis primary neoplasms. *Radiother Oncol*, 40(1):69–74, 1996.

[324] R Prabhakar, PK Julka, M Malik, T Ganesh, RC Joshi, PS Sridhar, GK Rath, GS Pant, and S Thulkar. Comparison of contralateral breast

dose for various tangential field techniques in clinical radiotherapy. *Tech Canc Res & Treat*, 6(2):135–8, 2007.

[325] L Marks, E Yorke, A Jackson, R Ten Haken, L Constine, A Eisbruch, S Bentzen, J Nam, and J Deasy. Use of normal tissue complication probability models in the clinic. *Int J Radiat Oncol Biol Phys*, 76(3):S10–S19, 2010.

[326] H Ayata, M Güden, C Ceylan, N Kücük, and K Engin. Comparison of dose distributions and organs at risk (oar) doses in conventional tangential technique (ctt) and IMRT plans with different numbers of beam in left-sided breast cancer. *Rep Pract Oncol Radiother*, 16:95–102, 2011.